Exhumation of blueschist-facies assemblages from Western Turkey : the significance of ^{40}Ar-^{39}Ar ages and excess argon in a HPLT terrain

Thesis

UNRESTRICTED

EXHUMATION OF BLUESCHIST-FACIES ASSEMBLAGES FROM WESTERN TURKEY: THE SIGNIFICANCE OF ^{40}Ar-^{39}Ar AGES AND EXCESS ARGON IN A HPLT TERRAIN

A thesis presented for the degree of Doctor of Philosophy

by

SARAH CHRISTINE SHERLOCK

B.SC. (HONS) CHELTENHAM & GLOUCESTER CHE 1994
M.SC. (RESEARCH) BRISTOL 1995

Department of Earth Sciences
The Open University

October 1998

DATE OF SUBMISSION : 8 OCTOBER 1998
DATE OF AWARD : 11 MARCH 1999

ACKNOWLEDGEMENTS

First and foremost I would like to thank Drs Simon Kelley, Nigel Harris and Aral Okay for excellent supervision and encouragement during the last three years, and Simon especially for fuelling my growing interest in argon. I also thank Handan and Anton for their valuable assistance in the field and more importantly in surviving Sivrihisar.

Simon Inger of CASP is thanked for Rb-Sr ages, Nicolas Arnaud for furnace step-heating assistance and extremely valuable encouragement, Kay Chambers for thin section preparation, Andy Tindle for microprobe assistance, Jo-Anne Wartho for argon-related assistance, and Steve Roberts for Raman specroscopy.

I acknowledge NERC for studentship GT4/95/243/E.

There are many people whom I would like to acknowledge. The past three years would have been a lot less fun and considerably more difficult without the unending support and encouragement of certain people. All have been thanked in person.

ABSTRACT

The Tavsanli Zone of northwest Turkey is a tract of metacherts, metapelites and metabasite lithologies that have undergone a single metamorphic cycle in the lawsonite-blueschist, epidote-blueschist and low-temperature eclogite sub-facies. These deeply subducted rocks which formed during late Cretaceous closure of the Tethys Ocean reached minimum pressures of 24 ± 2 kbar and temperatures of approximately 500° C in the eastern regions, and 20 ± 2 kbar and 400° C in the central and western regions. The difference in metamorphic pressures between the east and west regions of the Tavsanli Zone are attributed to different locations of the rocks within the subducting slab. Syn-subduction exhumation brought the rocks up from depths of 75 km to the base of the continental crust. Metamorphism took place under fluid-absent conditions, in part due to the incorporation of large quantities of water into the lawsonite. Subduction ended by approximately 70 Ma and the ensuing exhumation during continent-continent collision took place by thrusting.

Rb-Sr and ^{40}Ar-^{39}Ar geochronological techniques have been applied to phengites from the Tavsanli Zone and indicate that white mica crystallisation and the onset of exhumation occurred at 79 to 82 Ma. Ultra-violet laser, infra-red laser and furnace step-heating ^{40}Ar-^{39}Ar techniques confirm that the rocks of the Tavsanli Zone contain excess argon, which has probably built up in the grain-boundary network during the single metamorphic cycle. The variable concentrations of excess argon correlate with

lithological type, reflecting low mobility of argon. This is consistent with vapour-absent metamorphism as inferred from metamorphic petrology.

CONTENTS

CHAPTER FOUR - GEOCHRONOLOGY

CHAPTER FIVE – EXCESS ARGON

CHAPTER SIX – SYNTHESIS

CHAPTER SEVEN – CONCLUSIONS AND FURTHER WORK

APPENDICES

A - ^{40}Ar-^{39}Ar techniques

B - ^{40}Ar-^{39}Ar data relating to Chapter Four

LIST OF TABLES

CHAPTER TWO

CHAPTER THREE

CHAPTER FOUR

CHAPTER FIVE

APPENDICES

A – ^{40}Ar-^{39}Ar TECHNIQUES

G – ELECTRON PROBE MICROANALYSIS

H – ELECTRON MICROPROBE DATA

LIST OF FIGURES

CHAPTER ONE

CHAPTER TWO

CHAPTER THREE

CHAPTER FOUR

CHAPTER FIVE

LIST OF PLATES

CHAPTER TWO

LIST OF SAMPLES AND LOCALITIES:

sample	region	locality	lithology
96/234	Orhaneli	Alacaat	metachert
96/252	Orhaneli	Alacaat	metachert
96/12	Tavsanli	Inonu	metachert
96/16	Tavsanli	Dodurga	foliated metabasite
96/27	Tavsanli	Yeniuregil	porphyroblastic metabasite
96/185	Tavsanli	Yeniuregil	metapelite
96/28	Tavsanli	Yeniuregil	foliated metabasite
K380	Tavsanli	Dodurga	metapelite
96/14	Tavsanli	Dodurga	metabasite
96/15	Tavsanli	Dodurga	metabasite
96/48	Akcakaya	Akcakaya	metapelite
97/1	Sivrihisar	Halilbagi	metapelite
96/66	Sivrihisar	Halilbagi	metapelite
96/158	Sivrihisar	Halilbagi	foliated metabasite
96/120	Sivrihisar	Halilbagi	metapelite
96/149	Sivrihisar	Halilbagi	porphyroblastic metabasite
96/134	Sivrihisar	Halilbagi	metapelite
96/135	Sivrihisar	Halilbagi	metapelite
96/139	Sivrihisar	Halilbagi	foliated metabasite
96/162	Sivrihisar	Halilbagi	foliated metabasite
96/117	Sivrihisar	Halilbagi	porphyroblastic metabasite
96/118	Sivrihisar	Halilbagi	porphyroblastic metabasite
96/152	Sivrihisar	Halilbagi	foliated metabasite
96/216	Sivrihisar	Halilbagi	porphyroblastic metabasite
96/159	Sivrihisar	Halilbagi	foliated metabasite
96/69	Sivrihisar	Halilbagi	foliated metabasite
96/67	Sivrihisar	Halilbagi	foliated metabasite

CHAPTER ONE

INTRODUCTION

1.0 Introduction

An improved understanding of the thermal and mechanical processes operating in active subduction zones is fundamental to interpreting the forces that drive plate tectonics. At present the sites of ancient subduction zones can often be identified by the exposure of blueschist- and eclogite-facies metamorphic rocks which indicate that rocks were buried to great depths and subsequently returned to the surface before thermal relaxation was able to take place. The study of such enigmatic rocks which formed under unusually high pressures (10 to 30 kbar) and often temperatures as low as (150° to 450° C) affords insight into the exact nature and timescales of processes operating within the subduction zone and/or convergent setting at the time.

In order to fully understand the tectonic mechanisms governing the formation of a region of high-pressure low-temperature (HPLT) metamorphic rocks and to solve fundamental problems, the pressure-temperature (P-T) constraints and fabric analysis of the petrologist must be integrated with thermochronological constraints from

geochronological analysis.

This brief chapter introduces the blueschist metamorphic facies, the environments of formation of blueschist-facies assemblages, and the mechanisms by which they are exhumed. An introduction to ^{40}Ar-^{39}Ar geochronology outlines the advantages and current limitations of applying such a technique to the interpretation of high-pressure low-temperature (HPLT) rocks. Finally this chapter defines the aims and objectives of the thesis, the overall methodology used in the field and the laboratory, and describes the layout of the thesis as a whole.

1.1 High-pressure low-temperature metamorphic rocks: their formation and exhumation.

1.1.1 Blueschist-facies metamorphic rocks

Blueschist-facies metamorphic rocks are intriguing and unusual for two reasons. Firstly they are crustal rocks that have formed at very high pressures, at depths exceeding the base of the earth's crust and this requires some extraordinary process beyond intracontinental orogeny. Secondly they commonly show no evidence of heating during exhumation to the earth's surface, in many cases preserving pristine HPLT mineralogy. Blueschist-facies mineralogy is formed exclusively under high P-T ratios (Ernst, 1977; Chopin, 1987; Ernst, 1988), requiring an environment where confining pressures are high, and temperatures are low to moderate (Ernst, 1971).

To achieve the low temperatures which will allow blueschist-facies assemblages to crystallise, normal continental geotherms must be depressed. Within stable continental crust at depths of 75 km, temperatures are expected to exceed 750° C but within subduction zones cold oceanic material is transported down the subduction zone, depressing isotherms at depth (e.g. Peacock, 1992; Hacker and Peacock, 1995). The diagnostic minerals of the blueschist-facies are the blue sodic amphibole glaucophane, and lawsonite. The blueschist-facies lies within the P-T range of 150° to 450° C and upwards of 4 kbar (Figure 1.1).

The formation of high and ultra-high pressure rocks is generally regarded as a product of convergent tectonics, most commonly subduction zones and sites of continent-continent collision. HPLT rocks formed in a subduction and continent-continent collision setting seem to display diagnostic P-T histories.

All blueschist-facies assemblages, regardless of their origin, have in common similar prograde P-T paths, under which the rocks pass through zeolite- to prehnite-pumpellyite to blueschist-facies with some assemblages reaching the eclogite-facies (Figure 1.1). Most prograde P-T trajectories have dP/dT gradients approaching 35 to 40° C/kbar, translating to 10° C/km. It is the retrograde path which varies significantly between blueschist belts of different origins. Ernst (1988) has distinguished two types of retrograde path, the Franciscan-type and the Alpine-type. The Franciscan-type, exemplified by the Franciscan complex of California, is characterised by a retrograde path that closely mirrors the prograde path (Figure 1.1). Alpine-type retrograde paths

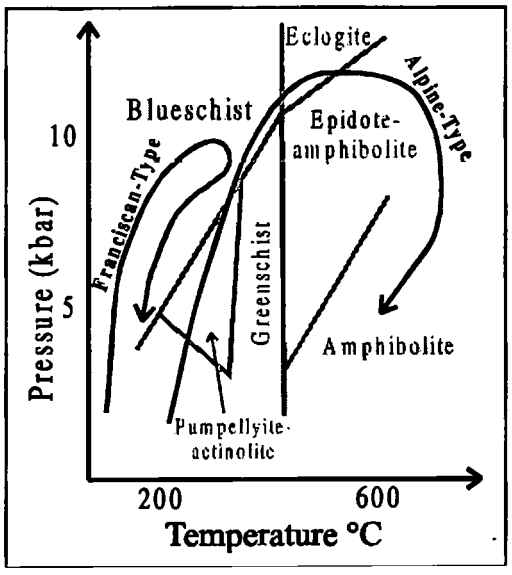

Figure 1.1: Pressure-temperature diagram illustrating the various recognised metamorphic facies and the sub-divisions of the blueschist-facies. The Alpine-type and Franciscan-type P-T paths are shown for comparison (after Ernst, 1988).

experience isothermal decompression or even heating shortly after peak burial conditions, resulting in overprinting by greenschist- or amphibolite-facies assemblages (Figure 1.1). Convergent tectonic style, or the style in which two crustal plates of either continental or oceanic origin meet, governs whether or not a blueschist terrane experiences a Franciscan-type or an Alpine-type retrograde path, and therefore whether or not they experience thermal overprinting. Franciscan-type paths require a subduction environment, and result from retrograde cooling which is facilitated by syn-subduction exhumation (Ernst and Peacock, 1996), thus retaining sufficiently low temperatures to preserve HPLT mineralogy and prevent thermal overprinting. In contrast the Alpine-type retrograde paths are consistent with exhumation during and after the cessation of subduction, and/or a reduction in convergence rates.

1.1.2 Mechanisms of blueschist and eclogite exhumation

Numerous mechanisms have been proposed for the exhumation of blueschists and related HPLT rocks. When considering possible mechanisms It is useful to distinguish between the two terms 'uplift' and 'exhumation' which are commonly misused in the

thermochronology of metamorphic rocks. Whereas uplift strictly refers to the increase in elevation of the Earth's surface (Platt, 1993), 'exhumation' refers specifically to the movement of rocks towards the Earth's surface (England and Molnar, 1990). In HPLT terrains exhumation involves one or more, and commonly a combination, of the following mechanisms: i) external forces applied to the HPLT terrane (e.g. Platt, 1993; Thompson et al., 1997), ii) erosion (Draper and Bone, 1981), iii) density contrasts leading to the buoyant rise of HPLT material (e.g. Cloos, 1982), and iv) extensional tectonics (Dewey, 1988; Andersen et al., 1991; Platt, 1986).

i) Externally applied forces may result in the expulsion of HPLT rocks from the subduction zone. Horizontal compression of less competent lithologies causes vertical extension and uplift, and if denudation is simultaneous then continued extrusion and exhumation will occur for the duration of compression. A transpressive component within a convergent zone behaves similarly with the development of localised uplift due to the vertical expulsion of a weaker zone between two more competent blocks (e.g. Thompson et al., 1997) (Figure 1.2).

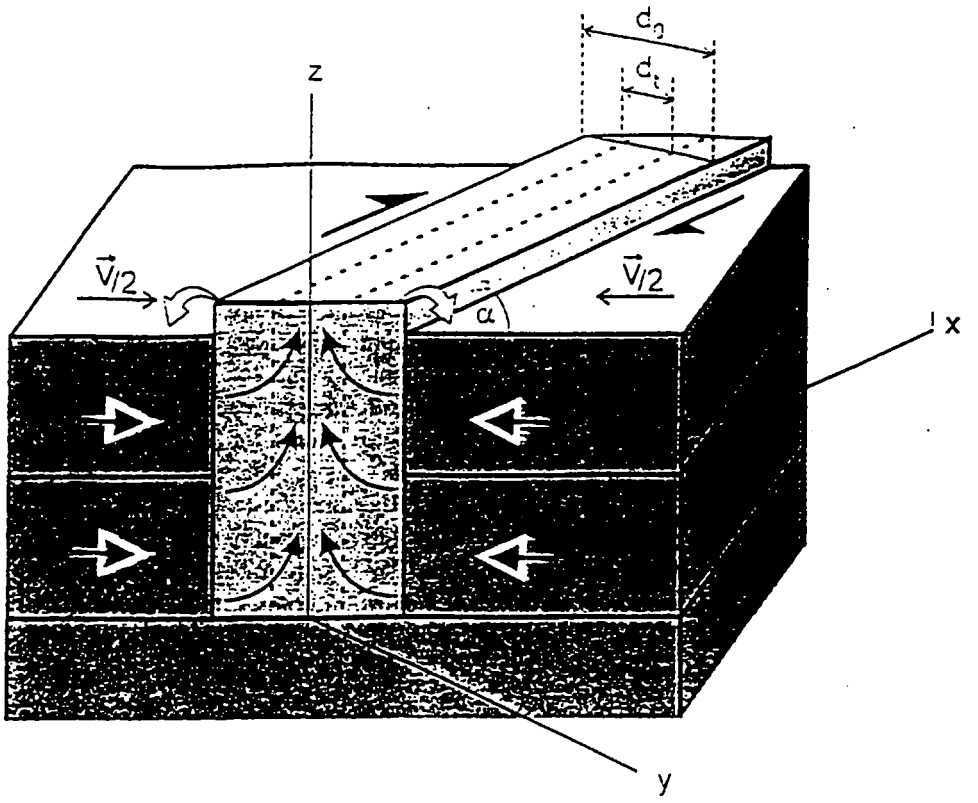

Figure 1.2: Schematic block diagram to illustrate the vertical expulsion of deep crustal material within a convergent setting (From Thompson et al., 1997).

ii) Simple erosion of an orogenic belt may result in the gradual rise of rocks within the crust towards the surface. For the exhumation of HPLT rocks, which have experienced often extreme depths within the crust, this is an insufficient mechanism. Simple erosion models are insufficient to result in the complete removal of overburden. Mass-balance calculations indicate that in many cases the volume of sediment within surrounding basins is unable to account for the volume of sediment removed during erosion (England, 1981). Moreover the thermal consequences of exhumation exclusively by erosion are unrealistically high. A minimum erosion rate of

between 0.04 and 1.4 cm/yr is required to prevent the thermal overprinting of HPLT assemblages, depending on the level of radiogenic heat production (Draper and Bone, 1981), which is beyond any present-day denudation rate.

iii) Buoyancy-driven exhumation is reliant on the buoyancy differences between subducted crustal material and the surrounding mantle material. For example, England and Holland (1979) suggested that eclogitic blocks became entrained within the buoyant upflow of low-density and low-viscosity carbonate-rich material, and were exhumed. The key factor in such a model is the density difference between subducting material and surrounding mantle; if for example dense oceanic crust is undergoing subduction the contrast in density between it and the surrounding mantle is less stark and subducted material is more likely to remain at a constant crustal level. Such a mechanism is successful for either very small volumes of eclogitic HPLT material within a mass of much less dense and lower viscosity material, or for unspecified quantities of low-density continental material. For higher-density eclogitic material it is unfeasible to suggest that it will approach the surface above the base of the continental crust by this mechanism alone, and a second mechanism must be invoked for the final return to the Earth's surface (Platt, 1993).

iv) Extensional tectonics is one of the most commonly cited mechanisms for the exhumation of HPLT rocks within orogenic belts.

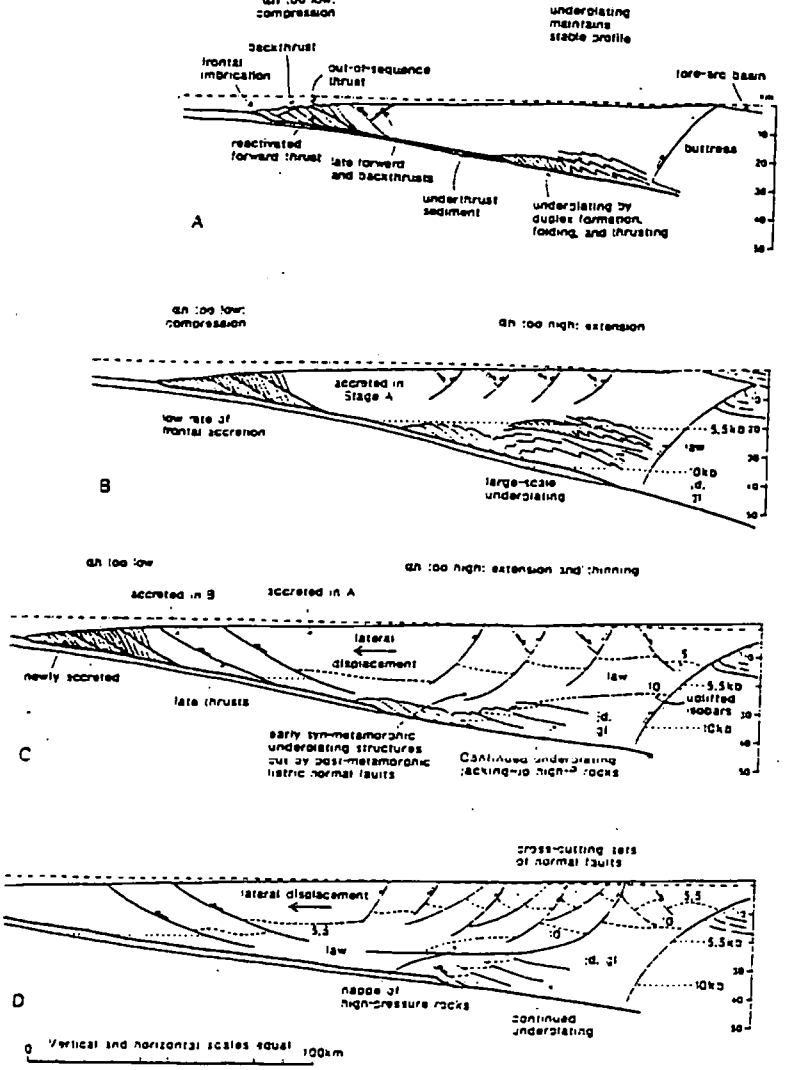

Figure 1.3: Evolutionary model of an accretionary wedge. A: early stage, with frontal accretion dominant, the product of surface slope and wedge thickness which controls the wedge stability and has the term αH, is too low in the frontal region and internal shortening takes place. B: Under conditions such that most sediment is underthrust, the rate of frontal accretion is low, and underplating is the predominant mode of accretion. αH is too high in the rear of the wedge, where extension by normal faulting and ductile flow at depth occurs. HPLT metamorphism takes place in the deeper parts of the wedge. C: Continued underplating and extension have lifted HPLT rocks towards the surface. Extension in the rear of the wedge causes lateral spreading and late thrusting towards the front of the wedge. D: In a mature prism, underplating and extension have brought HPLT rocks to within 15 km of the surface, accessible to future erosion. (from Platt, 1986).

Platt (1986; 1987; 1993) proposed that during subduction the descending material would accrete to the front of the orogenic wedge by folding and thrust imbrication, and material may be accreted to the base of the wedge, or underplated, at depth. The orogenic wedge geometry becomes less stable with the addition of material; with continued underplating extension is initiated within the rear of the orogenic wedge

itself. Within this mechanism material underplated at an early stage may be exhumed during later subduction (Figure 1.3).

A different mechanism for exhuming HPLT rocks following continent-continent collision and accompanying orogenic collapse has been described by Dewey (1988) and applied to the Norwegian Gneiss Region (Andersen et al., 1991).

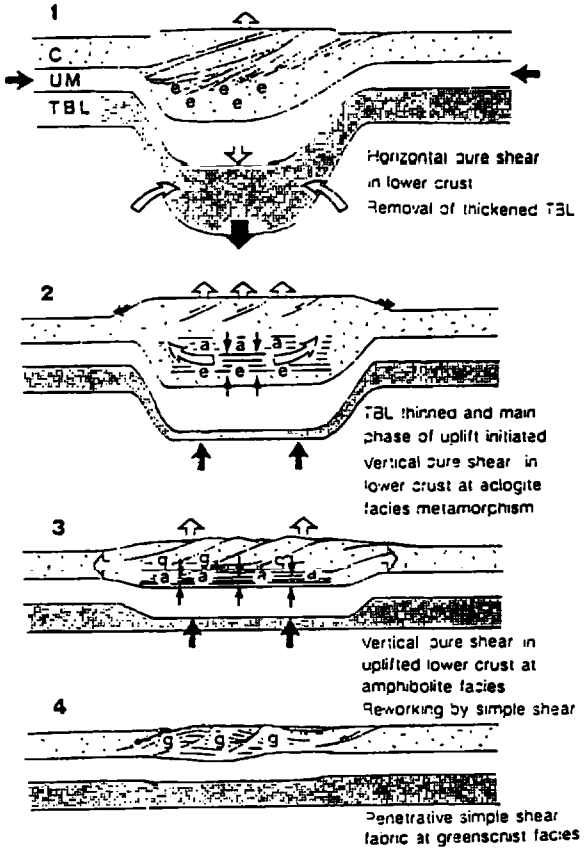

Figure 1.4: The exhumation of the Western Gneiss Region of Norway following continent-continent collision and radial collapse. (From Andersen et al., 1991).

This model suggests that during collision and crustal thickening the thermal boundary conduction layer becomes gravitationally unstable and is removed by convection (England and Houseman, 1988). The subsequent rapid uprising of the geothermal gradient and uplift of the surface cause instability which is then accommodated by

radial collapse (Figure 1.4). Rocks from deep crustal levels are exhumed via major eclogite-facies shear zones, which have been subsequently re-worked and overprinted during exhumation by the higher temperature amphibolite- and greenschist-facies metamorphism.

1.1.3 ^{40}Ar-^{39}Ar geochronology in HPLT assemblages

An understanding of exhumation mechanisms is essential to our understanding of the preservation of blueschists. However an obstacle to determining the rates of formation and exhumation of these rocks is their relatively low temperatures of crystallisation, resulting in fine grain-sizes and chemical and isotopic disequilibrium. ^{40}Ar-^{39}Ar geochronology has been extensively applied to HPLT assemblages since the closure temperature to argon diffusion in white micas, which are common minerals in such rocks, is approximately 350° ± 50° C (Dodson, 1973), and is within the temperature range for the likely exhumation path of many HPLT terranes (Figure 1.1). Most models for the rates and mechanisms of exhumation of HPLT terranes are therefore reliant to some extent on ^{40}Ar-^{39}Ar geochronology. Unfortunately ^{40}Ar-^{39}Ar white mica ages from HPLT terranes are often misleading and are open to misinterpretation due to the problem of excess argon (Li et al., 1994; Arnaud and Kelley, 1995; Ruffet et al., 1995; 1997; Scaillet, 1992; Scaillet 1996; Sherlock et al., submitted a; Sherlock and Arnaud, submitted).

One of the principal assumptions of the ^{40}Ar-^{39}Ar and K-Ar geochronological systems

is that all argon within the system which is not produced by the *in situ* decay of ^{40}K has a $^{40}Ar/^{36}Ar$ ratio of 295.5 (Steiger and Jäger, 1977), which is equal to that of atmospheric argon. In essence, excess argon is ^{40}Ar in a mineral additional to radiogenic $^{40}Ar^*$ produced by potassium decay since the mineral closed to argon diffusion. A primary difficulty is the detection of excess argon. The age spectrum approach associated with furnace step-heating has produced a variety of results for grains contaminated by excess argon. A release pattern common to amphiboles and feldspars, which became known as the 'saddle-shaped' spectra (Figure 1.5a), revealed high initial ages which decreased in medium-temperature steps, and rose again in the high-temperature steps (e.g. Lanphere and Dalrymple, 1971; 1976; Pankhurst et al., 1973; Dalrymple et al., 1975; McDougall and Harrison, 1988). The 'saddle-shaped' spectrum is easily distinguished from a plateau, for which the criteria of three consecutive steps each within error of one another and representing a significant proportion of the total ^{39}Ar released, must be met (Figure 1.5b) (e.g. Dalrymple and Lanphere, 1974; Lanphere and Dalrymple, 1978; Berger and York, 1981a). Some minerals contaminated by excess argon further complicate the problem by giving a flat release spectrum, and often a plateau more reminiscent of a mineral that has no excess argon contamination (Hodges et al., 1994; Ruffet et al., 1995; Sherlock and Arnaud, submitted). Identifying the presence of excess argon with the furnace step-heating technique is further complicated by the breakdown of the mineral during heating *in vaccuo* in addition to the averaging effects of bulk sampling.

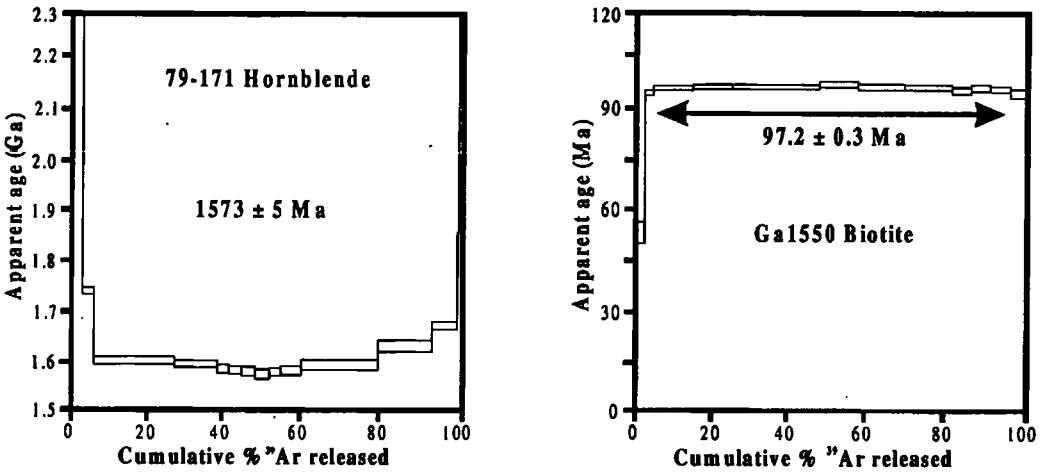

Figure 1.5: ^{40}Ar-^{39}Ar release spectra: a) 'saddle shaped' spectra from hornblende contaminated by excess argon (McDougall and Harrison, 1988), and b) flat plateau from biotite free of excess argon (Tetley, 1978).

The advent of laser-ablation extraction techniques has advanced our understanding of excess argon. The high-spatial resolution afforded by laser extraction techniques has firstly paved the way for single grain and intra-grain analyses, which circumvents the averaging effects of bulk sampling techniques, and secondly enabled *in situ* analyses of 'thick sections' of rocks. This ultimately leads to a much greater understanding of argon systematics in rocks relative to mineral textures and structures.

The best-documented example of widespread excess argon within a HPLT metamorphic belt is the HPLT regions of the European Alps. ^{40}Ar-^{39}Ar furnace step-heated white mica ages provided the first age determinations on the Alpine Dora Maira ultra-HPLT coesite-bearing terrane. Convincing plateau ages of up to 130 Ma were obtained for the HPLT metamorphic event (Monié and Chopin, 1991; Scaillet et al., 1990; 1992), with a range of 40 Ma to 130 Ma, clustering at 60 Ma to 90 Ma.

More recent U-Pb, Sm-Nd and Rb-Sr on a range of minerals gave much younger ages of 34 to 50 Ma for the same metamorphic event (Tilton et al., 1989; 1991; Bowtell et al., 1994; Gebauer et al., 1997). Chopin and Maluski (1980) argued that the closure temperature of argon diffusion in high-pressure white micas is much higher than in lower pressure white micas, and therefore the much older ages are real ages of ultra high-pressure metamorphism. Arnaud and Kelley (1995) applied the Ultra-Violet Laser Ablation Microprobe (UVLAMP) technique to the same lithologies from the Dora Maira, and produced an age range of 40 Ma to 615 Ma from both potassium-rich and potassium-free phases. From this study it became apparent that the previously discounted theory of excess argon in the Alps was in fact the reason for such a wide range of ages for one metamorphic event. The Alpine Dora Maira is the best documented but not the only example of excess argon in high-pressure rocks. Other examples include the Sesia-Lanzo Zone of the western Italian Alps (Pickles et al., 1997; Inger et al., 1996; Reddy et al., 1996; Ruffet et al., 1995), and the Dabie Mountains and Su-Lu terrane of China (Li et al., 1994).

Undetected excess argon has led to erroneous hypotheses for the geological evolution of whole regions, and tectonic interpretation has been borne out of age ranges which may or may not be geologically meaningful.

1.2 Aims and objectives of this study

The broad objective of this thesis is to combine aspects of metamorphic petrology with

a number of ^{40}Ar-^{39}Ar geochronological techniques to elucidate the tectonic history of an extensive belt of HPLT rocks. The field area selected is the Tavsanli Zone of northwest Turkey (Figure 1.6).

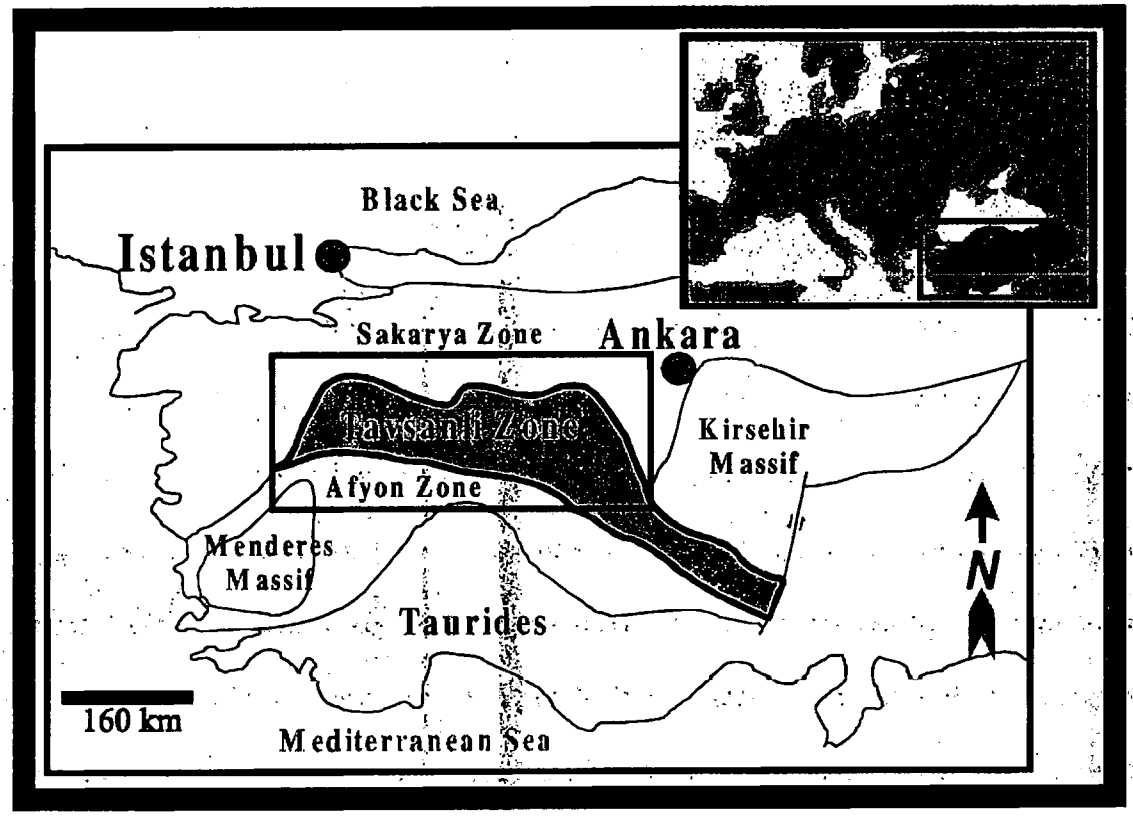

Figure 1.6: Location map of the Tavsanli Zone within Europe and Turkey.

More specifically this thesis has the following aims:

1 To combine metamorphic petrology and detailed geochronology to determine firstly the P-T-t path and secondly the possible exhumation mechanisms responsible for the return of the Tavsanli Zone HPLT rocks to the surface;

2 To use a variety of ^{40}Ar-^{39}Ar geochronological techniques to determine the extent to which excess argon is present within the Tavsanli Zone, and attempt

to understand its origins and evolution;

3 To evaluate the significance of the exhumation of the Tavsanli Zone for the tectonics of the Eastern Mediterranean during the Alpine orogenesis;

1.3 Fieldwork approach and methodology

During two brief field seasons samples were collected from the Tavsanli Zone blueschist belt with a view to understanding the petrological evolution and geochronology of the region. The field area included the previously studied regions of Orhaneli and Tavsanli, and the lesser studied Sivrihisar region, all of which are described in more detail in Chapter 2. The Tavsanli Zone is one of several zones that comprise the Anatolian Plateau, with an average elevation of 1700 m (Figure 1.7).

During the months of May and September the region was generally hot and arid with minor pockets of snow at the highest altitudes. Sampling in the remotest regions in the east was confined to early morning and where possible terminated by early afternoon to avoid maximum temperatures which approached 35° C. Outcrops were restricted to road cuttings in the west and central regions. In the east, however, regions were sampled by following dried stream gullies.

Travelling between regions, which were separated by as much as 200 km, was achieved by hire car, largely on dirt tracks and unmetalled roads. The principal difficulties encountered were navigational, since the topographical maps and the actual

roads rarely coincided. In terms of the rocks collected, where possible garnet-bearing samples have been favoured for their suitability for pressure-temperature studies. The least deformed and most micaceous samples have been selected for geochronological purposes.

Figure 1.7: View of the Tavsanli Zone, looking northward over the village of Halilbagi in the Sivrihisar region.

1.4 Laboratory methodology

The Open University provided the following analytical facilities: Cameca SX100 electron probe microanalyser, ^{40}Ar-^{39}Ar infra-red and ultra-violet laser-probes, and all mineral separation and preparation. In addition I undertook ^{40}Ar-^{39}Ar furnace step-heating at Université Blaise-Pascal, Clermont-Ferrand, France. Rb-Sr analyses were

undertaken at the Department of Earth Sciences, University of Leeds. Micro-Raman spectroscopy was undertaken with Dr Steve Roberts in the Department of Geology at the University of Southampton. Each technique is detailed in the appendices.

1.5 Thesis Layout

Chapter Two places the work of this study within the context of its regional importance in terms of the Tethyan region of the Alpine-Himalayan chain, with a detailed description of the geological setting of the field area, including field descriptions and petrography.

Chapter Three details the metamorphic evolution of the two pristine regions of HPLT regions of the Tavsanli Zone. The P-T evolution is based on both detailed metamorphic petrology and thermobarometry and provides an insight into the processes taking place during exhumation. This comprises two submitted manuscripts, co-authored by Nigel Harris, Aral Okay and Simon Kelley, the second of which concentrates on a specific mineralogical problem unique to samples from the Sivrihisar region. A third section discusses the evidence both for and against the likelihood that parts of the Tavsanli Zone were once an ultra-high pressure metamorphic region.

Chapter Four details the geochronology of the pristine HPLT regions of the Tavsanli Zone. From this and preliminary P-T estimates it has been possible to propose rates and mechanisms for the exhumation of the Tavsanli Zone HPLT rocks. This is also a

submitted manuscript with Simon Kelley, Simon Inger (Leeds), Nigel Harris and Aral Okay (Istanbul).

Chapter Five describes in detail the problem of excess argon in the Tavsanli Zone, and its implications for the interpretation of the argon data. This also includes a submitted manuscript based on the ^{40}Ar-^{39}Ar furnace step-heating results from Tavsanli Zone rocks, which have highlighted an inherent flaw in the way in which argon data is graphically represented. The manuscript is co-authored by Nicolas Arnaud of Clermont-Ferrand. A second manuscript co-authored by Simon Kelley is a detailed account of excess argon in the Tavsanli Zone.

Chapter Six provides a brief discussion of the aims and objectives addressed within this thesis together with proposals for future research directions. In view of the fact that this thesis incorporates five submitted manuscripts a certain amount of repetition has been unavoidable, largely in terms of introductory statements and analytical techniques.

Co-authors on the submitted manuscripts have been essential in establishing laboratory techniques and in the field for supervision and co-operation. With the exception of the four Rb-Sr analyses performed by Dr Simon Inger at Leeds University all the analyses presented here are the author's own work, as are the interpretation of these results and the final written manuscript.

CHAPTER TWO

THE TAVSANLI ZONE

2.0 Geological setting

2.0.1 The Tethys Ocean

The Tavsanli Zone is the result of the consumption of the Tethys Ocean during the Cretaceous.The Tethys Ocean was a major ocean formed within the eastward-widening gap between the Laurasian and Gondwana continents after the Carboniferous. The Tethys did not experience a simple evolution, because continental fragments rifted from both Laurasian and Gondwanan margins during the Permo-Triassic generating new oceanic crust (Sengör, 1987; Ricou, 1994; Stampfli, 1996). Moreover, the absence of any pre-Jurassic subduction-accretion complexes and ophiolites led to the subdivision of Tethys into Neo- and Palaeo-Tethys (Smith, 1973). It has been further argued by Sengör (1979; 1984; 1987) that during the Triassic, in the Mediterranean region a continental fragment rifted from the northern Gondwanan

margin, and moved north. This northward drifting fragment, named the Cimmerian continent, led to the closure of the Palaeo-Tethys and the opening of the Neo-Tethys. The whole Tethys gradually began diminishing after the late-Triassic during which time the Atlantic Ocean began to open and the Gondwanan continents were dispersed.

The plate boundary between Gondwana and Laurasia comprise multiple sutures arising from the diminishing Neo-Tethys and collision of the micro-continental fragments. The final closure of the Tethys took place at varying intervals along its length during the early Mesozoic. In Turkey the final coalition of the micro-continents into a single landmass occurred as late as the Eocene (e.g. Okay and Tüyüz, in press). The highly deformed southern margin of the Laurasian continent and deformed northern margin of the Gondwanan continents delineate the site of the complex Tethys Ocean. Mountain ranges associated with the Tethys ocean closure are outlined in Table 2.1.

SOUTHERN MARGIN OF EURASIA		NORTHERN MARGIN OF GONDWANA
New Guinea;	Zagros Belt, Iran;	Far Eastern ranges of Asia;
Eastern Indonesian tectonic zones;	Taurides, Anatolides and Pontides of Turkey;	Tien Shan;
Western Indonesian tectonic zones;	Greek Hellenides;	Caucasus;
Indo-China mountains;	Italian Appenines;	Carpathians;
Himalayas;	Sicilian Thrust Belt;	Pyrenees;
Salt Range, Pakistan;	Tell and Atlas of northern Africa;	Alps;
Oman Mountains;	Betic Cordillera of Spain;	

Table 2.1: Major orogenic belts associated with the southern and northern margins of the Tethys Ocean.

2.0.2 Blueschists in the Alpine-Himalayan orogen

The distribution of blueschist facies metamorphic rocks in the Alpine-Himalayan orogen has been described by Okay (1989). Figure 2.1 is a simplified version of the Tethyan sutures, focussing on the Alpine-Himalayan orogen, upon which the distribution of major blueschist occurrences is marked.

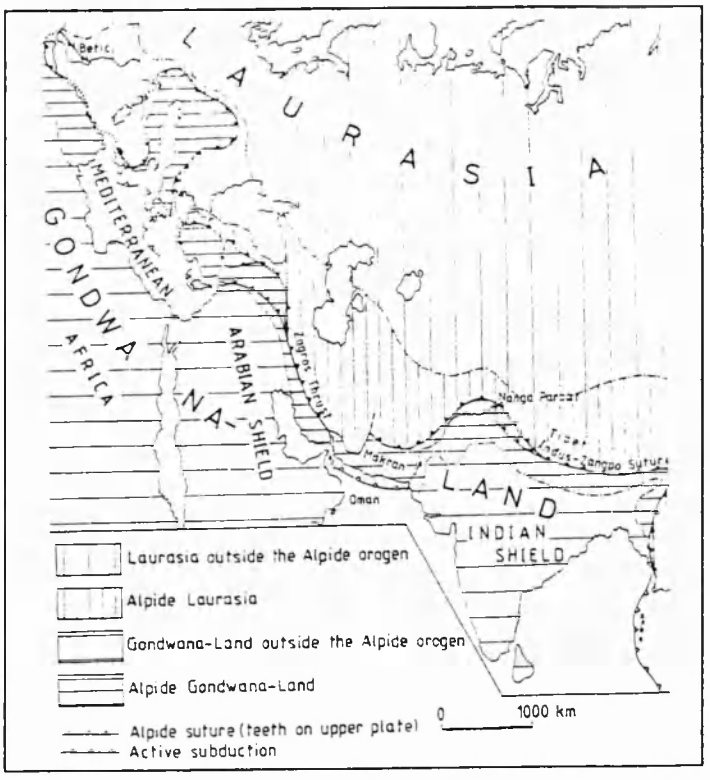

Figure 2.1: The Alpine-Himalayan orogenic belt and Tethyan sutures, and the locations of major blueschist occurrences (after Okay, 1989).

Over 80% of the known occurrences are between Spain and western Turkey. This may reflect the state of current research, which is more comprehensive in the Mediterranean regions, or it may be a real feature (Okay, 1989). The blueschists in northwest Turkey are one of the largest exposures in the Alpine-Himalayan chain.

2.0.3 The micro-continental framework of Turkey

2.0.3.1 Introduction

The complex tectonic framework of Turkey is traditionally sub-divided into six major continental fragments: Istanbul Zone, Sakarya Zone, Tavsanli Zone, Afyon Zone, Anatolide-Tauride Block, and Kirsehir Massif. These are stratigraphically, structurally and metamorphically distinct from one another, and amalgamated during the Alpine orogeny (e.g. Okay et al., 1998). On a broader scale Turkey may be sub-divided into the Pontides, Anatolides and Taurides. Table 2.2 briefly describes the geology of the sub-divisions of each of these three major units.

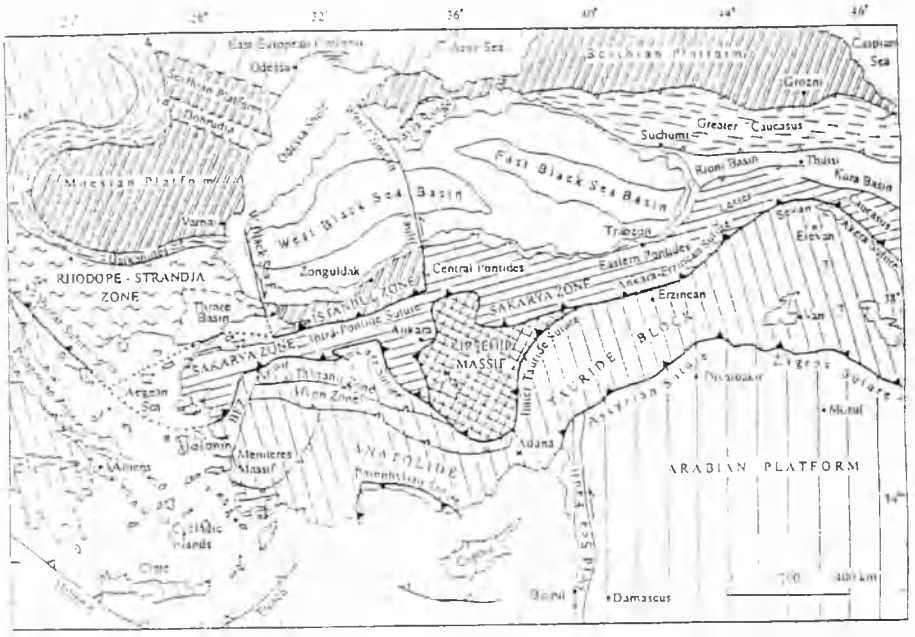

Figure 2.2: Tectonic map of Turkey which illustrates the major microcontinental fragments and Tethyan sutures (Okay and Tüyüz, in press, modified after Sengor et al., 1984; Okay, 1989 and Okay et al., 1994). Sutures are shown by heavy lines with the polarity of the former subduction zones indicated by filled triangles. Heavy lines with open triangles represent active subduction zones. The Late Cretaceous oceanic crust in the Black Sea is shown by grey tones. Small open triangles indicate the vergence of the major fold and thrust belts. BFZ denotes the Bornova Flysch Zone.

Figure 2.2 shows in detail both the continental fragments and the major tectonic boundaries within Turkey and the surrounding Mediterranean regions. In brief the Pontides are considered to show Laurasian characteristics (Okay, 1986; Okay et al., 1998), with less intense Alpine deformation and no post-Jurassic regional

metamorphism (Okay, 1986). The Anatolide-Tauride block, which covers most of southern Turkey including the Tavsanli Zone, is both strongly deformed by Alpine deformation and extensively metamorphosed (Okay, 1986).

The micro-continental fragments of Turkey are separated by Tethyan sutures. The Sakarya zone, which is the southernmost unit of the Pontides, is separated from the Tavsanli Zone, the northernmost unit of the Anatolide-Tauride block, by the major Izmir-Ankara-Erzincan suture. This 2000 km long suture represents the boundary between Laurasia and Gondwana. The final collision, forming the Izmir-Ankara-Erzincan suture, took place in the early-Palaeocene in the west and late-Palaeocene in the east (Okay and Tüyüz, in press). Figure 2.3 is a south-north cross section across western Turkey, showing the relationships between some of the major tectonic units, described in Table 2.2.

In the south the Alanya Nappes and Antalya Unit are thrust northwards and overly the dome of the Geyidag Unit. Northwards of this dome structure all tectonic units form a southward-thrusted imbricate stack, within which the Tavsanli Zone is mapped as two thrust slices, named the Orhaneli Unit and the Ovacik Unit. The Tavsanli Zone is tectonically overlain by the southward-thrusted ophiolite.

Table 2.2: Sub-divisions of the three major tectonic zones in Turkey.

Pontides	Kirsehir Massif	Anatolide-Tauride Block
Rhodope-Strandj Zone In the Turkish Thrace region metamorphic basement is intruded by Permian granites, and is overlain by Triassic sediments. Folding, thrusting and regional metamorphism followed in the mid-Jurassic, with later deposition of conglomerates and shallow marine lithologies. Finally subduction-related andesitic volanics and granodiorites are emplaced (e.g. Sengör and Yilmaz, 1981). **Istanbul Zone** Small continental fragment of Precambrian crystalline basement overlain by Ordovician to Carboniferous sediments deformed in the Hercynian orogeny (e.g. Gurur et al., 1997), overlain by early-Triassic sediments. Collision with the Sakarya Zone took place in the early-Eocene (Okay and Tüyüz, in press). **Sakarya Zone** Contains widespread Triassic subduction-accretion complexes which are in the Alpine-Himalayan chain form a metamorphosed and highly deformed basement overlain by lower-Jurassic to Eocene sediments. The Nilufer Unit is a dominant feature and comprises a thick metabasite-marble-phyllite sequence with exotic eclogite (Monie and Okay, 1997) and HPLT lenses (Monod et al., 1996).	Cretaceous metmorphic and granitic rocks, varying from greenschist to granulite facies, tectonically overlain by a late-Cretaceous accretionary complex.	Gondwanan in characteristics, during the late-Cretaceous continent-continent collision this block was in the footwall and is more strongly deformed and metamorphosed than the Pontides. The emplacement of ophiolite and accretionary complex material during the Senonian resulted in HPLT metamorphism (Okay and Tüyüz, in press), and during Palaeocene collision resulted in a south-southeast verging imbricate pile. Continued compression has resulted in metamorphism and deformation to different extents within different nappe piles: **Tavsanli Zone** Cretaceous blueschist belt with discrete pods of low-temperature facies eclogite material. Afyon Zone and Menderes Massif Palaeocene and Eocene respectively Barrovian-type metamorphic belts.

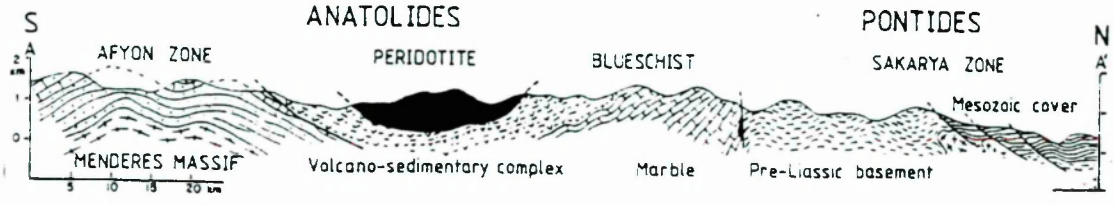

Figure 2.3: Cross-section through northwest Turkey (after Okay, 1986).

2.0.3.1 The Tavsanli Zone

The Tavsanli Zone is a roughly linear east-west trending belt outcropping in the central northern regions of Anatolia (Figure 2.4). To the north the Tavsanli Zone is bounded by the Izmir-Erzincan-Ankara suture, separating it from the Sakarya Zone of the Pontides. To the south it is divided from the Afyon Zone of the Anatolide-Tauride block by a major southward-directed thrust. The Zone itself extends for almost 300 km in length, and in width varies along its length from approximately 80 to 150 km. The Tavsanli Zone itself represents northward subducted oceanic crustal and sedimentary material.

The Orhaneli and Ovacik units are easily distinguished. The Orhaneli Unit has undergone a pervasive recrystallisation and the development of layer-parallel

schistosity, with the formation of a strong lineation and isoclinal folding. The Ovacik Unit, has suffered erosion and is not observed ubiquitously throughout the Tavsanli Zone. Where present, the Ovacik Unit is an imbricated and strongly deformed volcano-sedimentary unit, comprising intercalated basic volcanics, radiolarian cherts, pelagic shales and limestones and pods of serpentinite. Although in the field the rocks of the Ovacik Unit appear to be unmetamorphosed. The Ovacik Unit has in fact undergone incipient blueschist facies metamorphism at pressures of up to 8 kbar, and regional metasomatism (Okay, 1980a, b; Okay, 1982), whereby HPLT mineralogy has grown within the amygdales and veins of the basic volcanic lithologies.

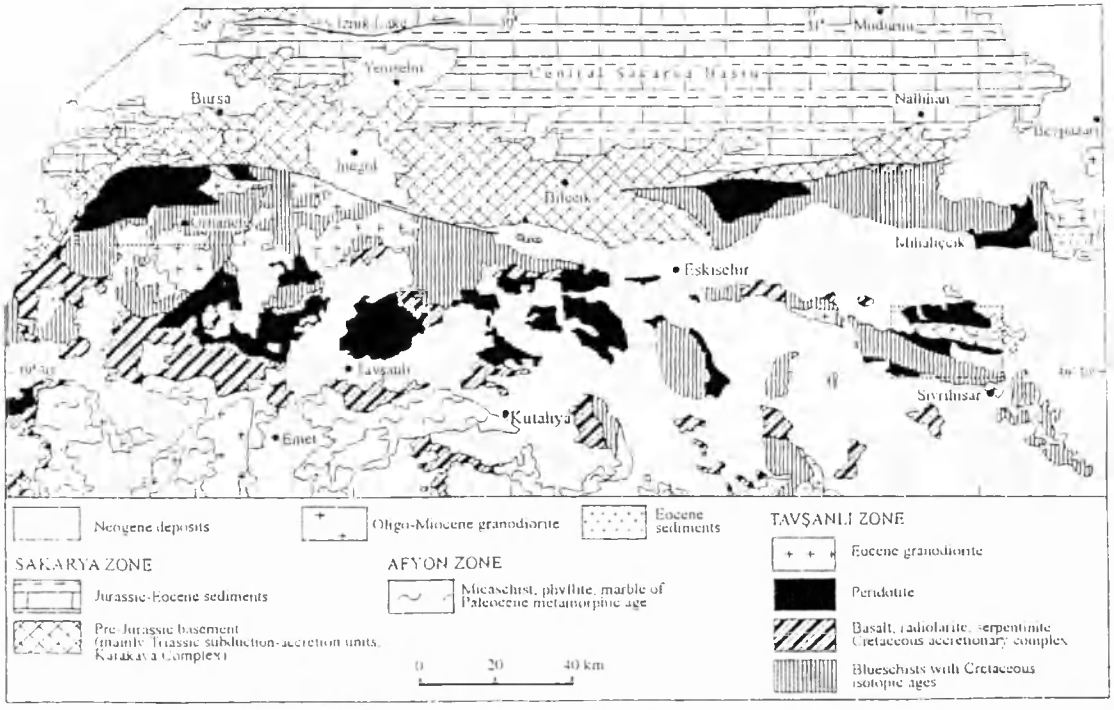

Figure 2.4: Generalised geological map of the Tavsanli Zone (Okay and Tüyüz, in press), the dotted box south of Bursa represents the study area of Okay and Kelley (1994) and Okay and Tüyüz (in press).

2.0.3.2 Previous petrological studies of the Tavsanli Zone

Studies of the HPLT metamorphism in the Tavsanli Zone have centred on the western region of Orhaneli, and the central region of Tavsanli (Figure 2.4).

The HPLT metamorphic rocks of the Orhaneli Unit have been extensively studied by Lisenbee (1971) and Okay and Kelley (1994). The subduction-related calc-alkaline rocks intrusive into the Tavsanli Zone HPLT rocks and the surrounding thermal aureole have been studied by Harris et al. (1994). In the Orhaneli Unit, pressures of metamorphism have been constrained by the equilibrium assemblage chloritoid + glaucophane + paragonite + chlorite + quartz and are 20 ± 2 kbar at 430° ± 30° C. Maximum and minimum temperatures are constrained by the absence of garnet in either the micaschists or the metabasites, and by the chloritoid-glaucophane equilibrium (Okay and Kelley, 1994).

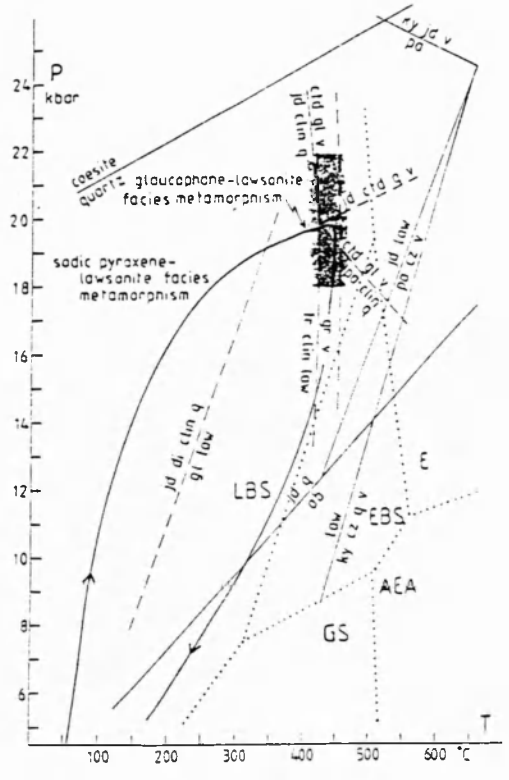

Figure 2.5: Pressure-Temperature path for the Orhaneli region (Okay and Kelley, 1994).

The P-T evolution of the Tavsanli Zone has thus far been based upon these estimates, with peak blueschist facies metamorphism taking place at 88 Ma (Okay and Kelley, 1994; Harris et al., 1994; Okay et al., 1998; Okay and Tüyüz, in press), followed by a

steep retrograde path, which remains within the blueschist-facies, avoiding recrystallisation within the greenschist-facies (Figure 2.5).

The Tavsanli region of the Tavsanli Zone (Figure 2.4), which lies immediately south of the Izmir-Ankara-Erzincan suture and 60 km east of the Orhaneli region by, has also been extensively studied (Okay, 1980a, b; Okay, 1982). The rocks of the Orhaneli Unit all contain the assemblage glaucophane-lawsonite (Okay, 1980a, b) and therefore lie within the lawsonite-blueschist sub-facies. The blueschists of the Orhaneli Unit in the same region show evidence for an initial static recrystallisation in metabasite lithologies resulting from low shear stresses in the subducting slab (Okay, 1980b). The rocks of the Ovacik Unit in the Tavsanli region have undergone incipient blueschist-facies metamorphism (Okay, 1982). Conditions of the incipient metamorphism in the Ovacik Unit are in the range 5 to 8 kbar and 150 to 200° C, based on the absence of jadeite and zeolites and the presence of albite, lawsonite and aragonite (Okay, 1982). The Tavsanli region has also been briefly studied by Kaya (1972; 1981), reporting the range of blueschist-facies mineral assemblages and paragenetic relationships.

Other regions of the Tavsanli Zone have been studied much less extensively. The petrology of the Mihalliccik region in the northeast Tavsanli Zone (Figure 2.4) was described by Cogolu (1967), who notes a northward increase in grade based on the assemblages lawsonite, lawsonite-crossite and lawsonite-epidote. A small area south of Eskisehir was briefly described by Lunel (1967) and Monod et al. (1991) as containing lawsonite-blueschist sub-facies assemblages. Further east, the petrology and

metamorphism within the Sivrihisar region (Figure 2.4) has been described by Gautier (1984), and Kulaksiz (1981). The P-T estimates for lawsonite-glaucophane assemblages range from 200° to 350° C and 5 to 8 kbars, and for what is described as the transitional zones 350° to 470° C and 4 to 6 kbars (Kulaksiz, 1981).

2.0.3.3 Previous geochronology of the Tavsanli Zone

Estimates of the age of geological events in the Tavsanli Zone, from deposition of the sediments in the Orhaneli Unit to the age of HPLT metamorphism and exhumation of the blueschists, have been inferred from regional geological constraints and scattered isotopic ages.

The deposition age of the Orhaneli and Ovacik Units is unclear. Palaeontological evidence suggests that the Ovacik Unit was deposited in the late-Jurassic to early-Cretaceous (Servais, 1981). Based on the stratigraphic correlation between the Orhaneli Unit and the Afyon Zone of Okay (1984) the age of deposition of the Orhaneli Unit is late-Palaeozoic to early-Mesozoic.

Estimates for the age of blueschist facies metamorphism range from pre-Carboniferous (Lisenbee, 1971), to Jurassic (Kaya, 1972); Bingol (1976) proposed late Cretaceous to early Pliocene subduction and HPLT metamorphism. K-Ar phengite ages of 65 and 82 Ma from the Sivrihisar region (Cogolu and Krummenacher, 1967) provide the first

isotopic determinations. Much higher precision ^{40}Ar-^{39}Ar white micas ages of 88 to 71 Ma (Okay and Kelley, 1994), 87 ± 3 Ma (Okay et al., 1998) and a glaucophane age of 108 Ma (Harris et al., 1994) have been obtained from blueschists in the Orhaneli region.

2.0.3.4 Previous models for the exhumation of the Tavsanli Zone

A model for the exhumation of the Tavsanli Zone has only recently been considered. The P-T-t path and low geothermal gradient of 5° C/km described by Harris et al. (1994) was considered to result from underplating of cold material under the blueschists during exhumation by normal faulting, in conjunction with a slower rate of subduction, associated with the subduction of continental material. Normal faulting was suggested as a likely mechanism for exhuming the blueschists beneath the overlying peridotite sheet (Okay and Kelley, 1994). A minimum exhumation rate of 2mm/yr (Harris et al., 1994) precludes the possibility that exhumation could have taken place purely by isostatic uplift since there is no evidence for the greenschist-facies overprinting which would be inevitable under such conditions (Harris et al., 1994). The 20 Ma age range of 88 Ma to 108 Ma from the blueschists of the Orhaneli region may be a result of syn-subduction and differential cooling and uplift of discrete tectonic units (Harris et al., 1994). A similar scenario has been reported for blueschist-assemblages of Sifnos in Greece where younger blueschist ages are found closest to the detachment zone (Wijbrans et al., 1993). In the case of the Tavsanli Zone an equivalent detachment is considered to be the interface between the blueschists and

overlying peridotite (e.g. Harris et al., 1994).

The proposed model for the exhumation of the Tavsanli Zone is based on the P-T-t data from the Orhaneli region of Okay and Kelley (1994) and Harris et al. (1994), and on new ^{40}Ar-^{39}Ar white mica ages from the Orhaneli region similar to those reported by Okay and Kelley (1994) (Figure 2.6a). The blueschists are said to have formed during subduction in the late Cretaceous, and undergone exhumation in the late-Cretaceous to early Palaeogene (Figure 2.6b). In this model the upper crustal parts of the subducted slab are detached from the basement and incorporated in the hanging-wall of the subduction zone. The blueschists consequently rise buoyantly back up the subduction zone by virtue of the density differences between the crustal material and surrounding mantle. Thermal relaxation of the ascending material and thermal overprinting of the blueschist facies assemblages is avoided by the underplated cold material and the temperature of the overlying wedge. Subduction zone shallowing due to the detachment of the oceanic lithosphere root may have resulted in a rise in the mantle wedge, thinning by ductile flow in the lower part, accompanied by extensional faulting in the upper part, to bring the rocks to the surface (Okay et al., 1998).

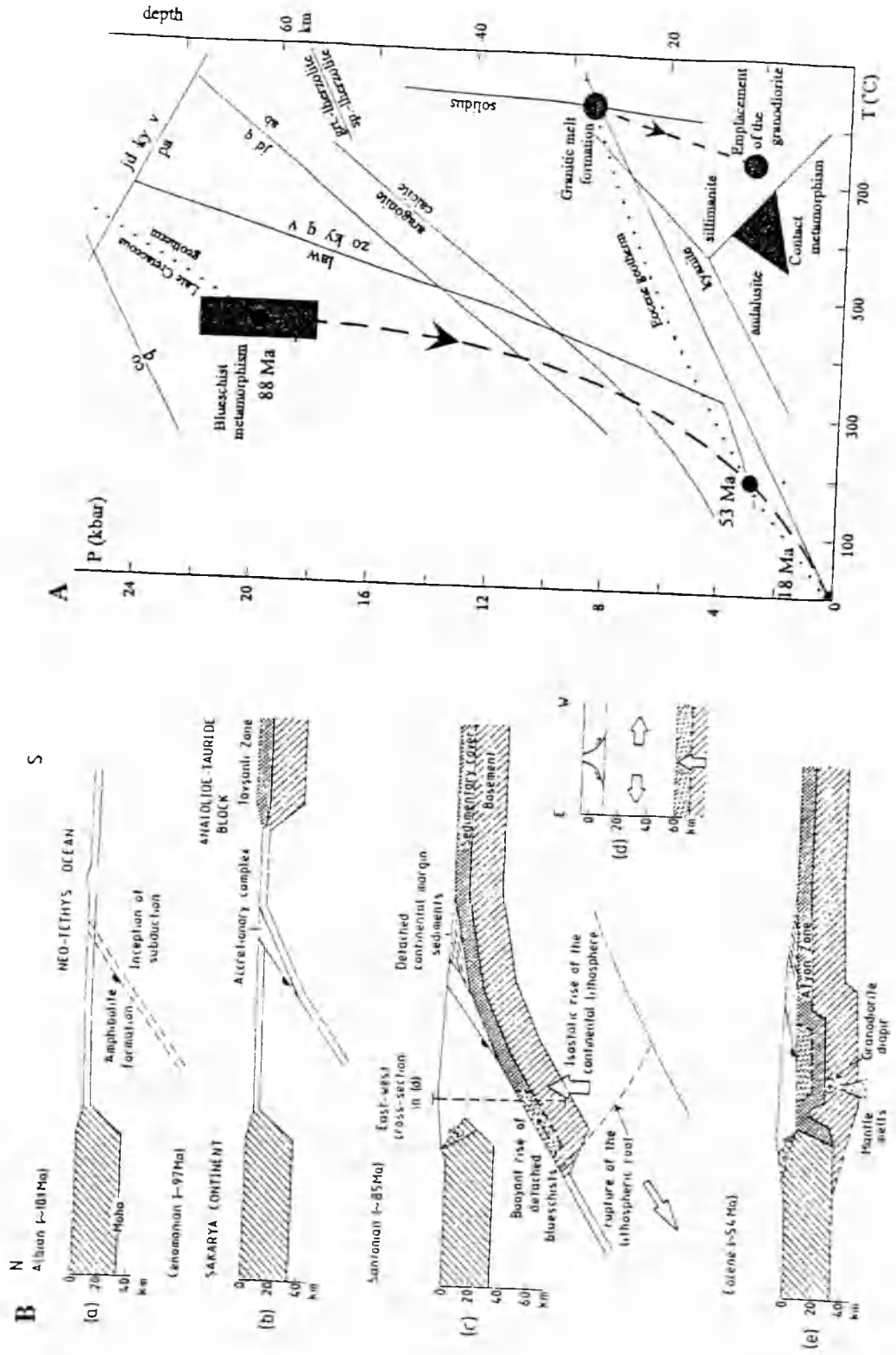

Figure 2.6: Exhumation model for the Tavsanli Zone: a) Pressure-Temperature-time path (Okay et al., 1998), and b) four stages of the evolution of the Tavsanli Zone (Okay and Tüyüz, in press).

2.1 The Field area

In the following sections the areas from which samples were collected are described, in addition to descriptions of each lithological type in the field and petrography. Four regions of the Tavsanli Zone were studied, Orhaneli, Tavsanli, Akcakaya and Sivrihisar, from west to east (Figure 2.7).

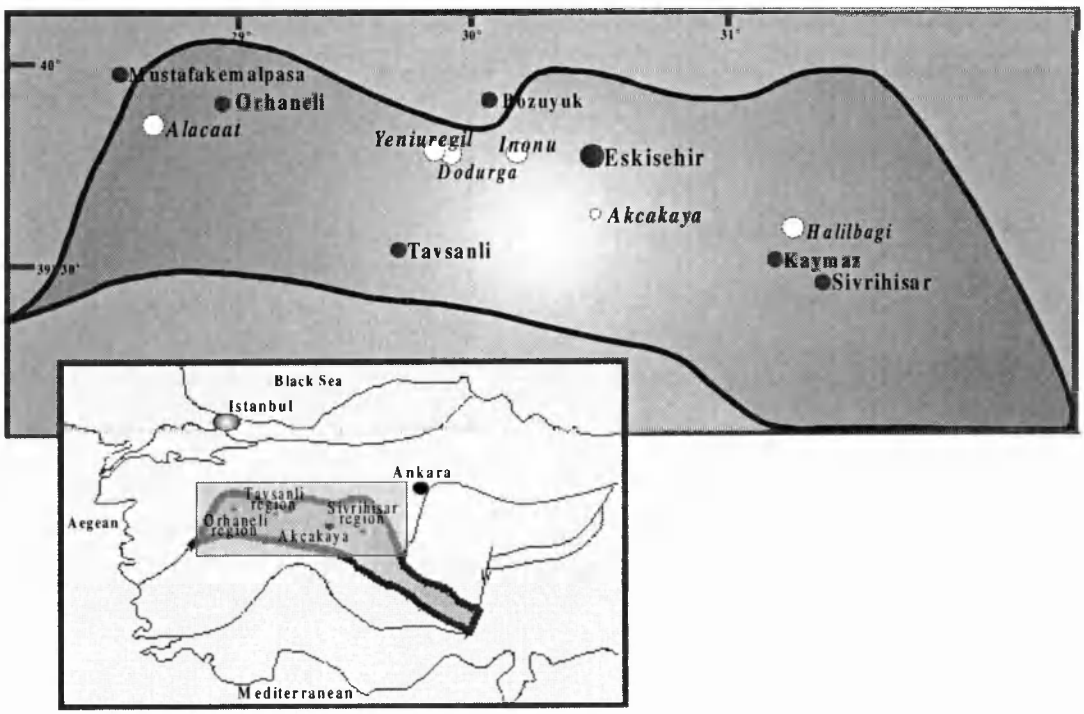

Figure 2.7: Location map for the Tavsanli Zone field area. White circles indicate sample collection sites, black circles are places referred to in the text for location purposes.

2.1.1 Orhaneli region:

2.1.1.1 Aliova River section, Alacaat.

Eight samples were collected from the road cutting following the Aliova River, to the east of Alacaat village which is approximately 30 km southeast of Mustafakemalpasa (Figure 2.7). The outcrop was poorly exposed, friable and heavily weathered (Plate 2.3.1a). The rocks form part of the lower-most Orhaneli Unit, and are predominantly micaceous metacherts and quartz-rich metapelites with the assemblage quartz + phengite + hematite; metacherts and metapelites are differentiated on the basis of either quartz or phengite being the dominant mineral. All samples are strongly foliated, the main penetrative foliation is flat-lying with local dip variations of up to 30 ° to the north or south due to late-stage regional warping. The samples from the Orhaneli region are texturally and mineralogically simple; quartz + phengite predominate with minor lawsonite + hematite. Quartz is the dominant phase and varies in grain size from coarse and platy to fine grain-sized aggregates or 'stringers' associated with high-strain regions. Phengite is second in abundance to quartz, and forms phengite-rich layers of up to 10 mm in thickness separated by quartz-rich domains. The abundance of phengite-rich domains varies locally and sample collection was biased towards the most phengitic horizons for the purposes of ^{40}Ar-^{39}Ar geochronology. Plate 2.3.1b is a photomicrograph of sample 96/234, representative of the least altered quartz micaschist from this locality. Phengites are elongated and formed during the development of the penetrative foliation. Deformation associated with this event has caused the localised reduction in quartz grain-sizes in high-strain areas. Lawsonite is fine grained and forms tabular prisms within the phengite rich domains. Hematite

forms fine grained cubes dispersed throughout the phengite-rich domains. Most of the samples collected are severely weathered resulting in fine grained alteration products.

2.1.2 Tavsanli region

The Tavsanli region lies in the central Tavsanli Zone, near to the villages of Tavsanli, Inonü, Dodurga and Yeniuregil (Figure 2.7), and south of the Izmir-Ankara suture by 50 kilometres. The dominant lithology of phengite-rich metapelite, was preferentially sampled for the purposes of ^{40}Ar-^{39}Ar geochronology.

2.1.2.1 Inonü

Inonü, meaning 'caves in front of' is situated 20 km southeast of Bözüyuk (Figure 2.7). Massive HPLT marbles are in contact with blueschist-facies metapelites and metabasites. Eight samples have been collected from the main east-west road cutting, within close proximity to the concordant marble contact. Outcrops are less weathered and friable than in the Aliova River section in the Orhaneli region (Plate 2.3.2a); all share a flat-lying dominant foliation locally affected by regional warping.

2.1.2.1.1 Metapelite

Metapelites are characterised by the assemblage quartz + phengite + glaucophane + lawsonite ± titanite. Samples are dominated by quartz with phengite-rich bands of up

to 5 mm in thickness though more commonly restricted to 1 to 2 mm in thickness (Plate 2.3.2b). The main foliation comprises elongate phengite grains, some of which are kinked. Glaucophane grains are aligned within the main foliation and are optically zoned with lilac cores and darker blue/purple rims (Plate 2.3.2c). Lawsonite is less abundant than glaucophane, forming elongate and tabular grains that are aligned within the main foliation. Titanite is an accessory mineral that is also aligned within the main foliation. A subsequent and less intense deformation event has resulted in the crenulation of the main foliation, with the kinking of some phengite grains and the occasional boudinage of glaucophane grains.

2.1.2.1.2 Metabasite

Metabasites are less prevalent than metapelites. They are compositionally zoned, with sodic-pyroxene rich domains and lawsonite-rich domains (Plate 2.3.2d). The overall assemblage is sodic-pyroxene + lawsonite + sodic-amphibole + phengite. The metabasites are foliated, pyroxenes from sodic-pyroxene rich domains being aligned within the main foliation. The less common sodic-amphiboles, lawsonite and phengite are also present within sodic-pyroxene domains but are far less common. Lawsonite-rich domains are less common than sodic-pyroxene rich domains, and comprise lawsonite + phengite. Lawsonites are squat prismatic idioblasts reaching a maximum of 100 μm in diameter. Phengites are elongate and reach a maximum diameter of 50 μm. Minor sodic-pyroxene occurs within the lawsonite-rich domains. Texturally the earliest assemblage is the main foliation which comprises sodic-pyroxene + sodic-

amphibole + lawsonite + phengite. There are no earlier phases included within any grains, and further, there is no evidence for any deformation subsequent to the main foliation.

2.1.2.2 Dodurga

Six samples were collected from a road cutting near to Dodurga Reservoir, approximately 25 km southwest of Bözuyük, near to the village of Dodurga. Fine grain-sized metabasites outcrop along a roadcutting (Plate 2.3.2e).

2.1.2.2.1 Foliated metabasite

Metabasites contain the assemblage lawsonite + sodic-amphibole + sodic-pyroxene ± phengite ± garnet ± titanite (Plate 2.3.2f). The earliest distinguishable assemblage is quartz + lawsonite, the latter being preserved as rare inclusions within garnet where present. Garnets are rare; where present grains are sub-idiomorphic and are up to 250 μm in diameter. The main penetrative foliation is dominated by idoblastic tabular lawsonite grains, up to 200 μm in diameter. Sodic-amphibole is less abundant; grains are optically zoned but to a lesser extent than those from pelitic lithologies described from Inonü. Rims are ferro-glaucophane-rich with glaucophane cores. Sodic-pyroxene is less abundant than sodic-amphibole, with a finer grain-size, and is aligned within the main foliation. Phengite is the least common mineral aligned within the main foliation. Grains are elongate and reach a maximum diameter of 50 μm. The only accessory

phase present is titanite; grains are elongate sub-idiomorphic and aligned within the main foliation.

2.1.2.3 Yeniuregil

Twelve samples from the Yeniuregil section were collected from a road cutting spanning approximately 200 metres in length, 5 km from the Dodurga locality, near to Yeniuregil village (Figure 2.7). A series of intercalated massive poorly-foliated metabasites, finer grain-sized foliated metabasites, and metapelites outcropped over a distance of 200 metres along a road cutting. A penetrative foliation is common to all outcrops, though it is less dominant within the more competent massive metabasite lithologies. The flat-lying foliation strikes east-west, though large-scale regional warping causes local dip variations of up to 20°. Most outcrops are compositionally banded, and the more foliated metabasites have a blue-green banded appearance attributed to either sodic-amphibole or sodic-pyroxene rich domains (Plate 2.3.2g). The massive metabasites contain lawsonite-rich bands (Plate 2.3.2h). Metapelites are the least common lithology and are generally weathered and friable.

2.1.2.3.1 Massive porphyroblastic metabasite

Outcrops of massive porphyroblastic metabasite are less well foliated and massive. Lawsonite is sufficiently coarse grain-sized to be visible to the naked eye. Metabasites have the general assemblage lawsonite + sodic-amphibole + sodic-pyroxene ±

phengite. Lawsonite is the dominant mineral and reaches 1 mm in diameter; grains are idioblastic squat prisms and are inclusion-free. Lawsonite idioblasts represent the earliest phase (Plate 2.3.2i), and are wrapped by the main foliation. The main foliation comprises fine grain-sized sodic-amphibole and less common and finer-grained sodic-pyroxene. Phengite grains are rare, fine- to medium grain-sized, and where present are aligned within the weakly developed foliation with sodic-amphibole.

2.1.2.3.2 Metapelite

Metapelites are found within bands up to 1 metre in width intercalated within metabasite outcrops. Metapelites are micaceous and friable, and are often weathered (Plate 2.3.2j). The general assemblage is quartz + phengite + sodic-amphibole ± lawsonite ± titanite (Plate 2.3.2k). The earliest assemblage is preserved as rare quartz inclusions within sodic-amphibole. The lithology is dominated by fine- to coarse-grained quartz; the main penetrative foliation comprises fine- to medium-grained elongated phengite grains, up to 100 μm in diameter. Micaceous bands vary from 5 mm to 15 mm in width. Sodic-amphibole is less common than phengite; grains are elongated and aligned within the main foliation, and are optically zoned with lilac-blue cores and dark blue rims. Lawsonite is less abundant than sodic-amphibole and, where observed, forms fine-grained, elongated tabular grains aligned within the main foliation. Titanite is a fine-grained accessory mineral which is also aligned within the main foliation.

2.1.2.3.3 Foliated metabasite

The foliated metabasite lithology is segregated into sodic-amphibole rich or sodic-pyroxene rich domains. Plate 2.3.2l is of the sodic-amphibole rich variety, with the assemblage lawsonite + sodic-amphibole + sodic-pyroxene ± phengite ± titanite. Lawsonite is the earliest mineral and varies from fine- to coarse-grained tabular idioblasts which are inclusion-free. The main foliation is either sodic-amphibole rich with minor sodic-pyroxene, or sodic-pyroxene-rich with minor sodic-amphibole. The dominant mineral is generally fine- to medium-grained and aligned with the foliation. Sodic-amphiboles are optically zoned with lilac-blue cores and deep-blue rims. Phengite is less common than either sodic-amphibole or sodic-pyroxene. Grains are aligned within the main foliation and are finer-grained than sodic-amphibole.

2.1.3 Akcakaya

Akcakaya neither belongs to the Tavsanli region nor the Sivrihisar region, but is located geographically between the two. Akcakaya is a small village which is approximately 30 km south of Eskisehir (Figure 2.7). The outcrops are dominated by a strongly foliated and fine-grained micaceous metapelite lithology and metacherts which are free of micaceous material (Plate 2.3.3a). Samples were biased towards the micaceous lithology for the purposes of ^{40}Ar-^{39}Ar geochronology.

2.1.3.1 Metapelite

The metapelite lithology has the finest grain-size collected within the Tavsanli Zone, comprising an assemblage of white mica + lawsonite. The dominant foliation results from aligned white mica, up to 10 μm in diameter, and lawsonite which forms elongated tabular grains (Plate 2.3.3b). The white mica-rich foliation is weakly crenulated by a subsequent deformation event, resulting in an undulating appearance.

2.1.4 Sivrihisar region

The Sivrihisar region lies at the eastern extremity of the field area, 70 km east of Eskisehir (Figure 2.7). Outcrop near to the village of Halilbagi, northwest of Sivrihisar by 25 km, consists of a series of intercalated blueschist- and low-temperature eclogite-facies metabasites, metapelites and metacherts. A thick marble sequence underlies the HPLT rocks, beneath which is a monotonous series of lower-grade and less well-preserved schists. The dominant penetrative foliation is concordant throughout the sequence of lower-grade schists, marble and high-grade blueschist and eclogite facies rocks.

2.1.4.1 Halilbagi

Halilbagi is a small village approximately 15 km northeast of Kaymaz (Figure 2.7). Outcrops were not as well exposed as in previously described localities. Samples were

collected from dried stream gulleys up to 2 km from the roadside southeast of Halilbagi village (Plate 2.3.4a). Sample collection was biased towards micaceous lithologies for the purposes of ^{40}Ar-^{39}Ar geochronology, and towards garnet-bearing lithologies for the purposes of thermobarometric analysis.

2.1.4.1.1 Low-grade metapelite

The low-grade metapelitic lithology, termed the 'Sivrihisar greenschist' by Gautier (1984), is the lowest stratigraphic horizon sampled in the Sivrihisar region. This lithology is heavily weathered and friable (Plate 2.3.4b), with the assemblage quartz + lawsonite + chlorite ± white mica ± calcite ± unidentified alteration products. Quartz is the dominant mineral, and is fine- to medium-grained and locally highly strained. Lawsonite is fine- to medium-grained and is both squat and tabular, and also elongated tabular in form. The dominant foliation is defined by aligned lawsonite grains, and white mica, where present. Chlorite forms fine-grained 'clots' and is associated with amorphous aggregates of a brown and ultra fine-grained alteration product. Calcite calcite forms amorphous regions and is associated with chlorite/alteration product.

2.1.4.1.2 Metachert

Metacherts are quartz-rich and foliated, with the assemblage quartz + phengite + lawsonite (Plate 2.3.4c). Fine- to medium-grained quartz which has been variably strained is the dominant mineral. The dominant foliation comprises phengite and minor

lawsonite. Phengite grains are elongated and aligned, with a maximum diameter of 100 μm. Lawsonite is generally finer grained than phengite, and is elongated and tabular and aligned within the main foliation. A subsequent deformation has resulted in a weakly developed strain-slip cleavage of re-orientated phengite grains.

2.1.4.1.3 Foliated metabasite

The foliated metabasite is more ubiquitous than the metachert. Outcrops are banded, with blue bands dominated by sodic-amphibole and green bands dominated by sodic-pyroxene (Plate 2.3.4d). The overall assemblage in the foliated metabasite is garnet + sodic-amphibole + sodic-pyroxene + lawsonite ± phengite ± epidote ± titanite ± quartz (Plate 2.3.4e). The earliest minerals which can be distinguished are quartz and lawsonite inclusions within pre-kinematic garnet. Pre-kinematic lawsonite has also been identified. Such grains are fragmented and boudinaged, and wrapped around by the main foliation. Garnets are pre- to syn-kinematic and are commonly fragmented in high-strain zones. Garnets are abundant in very fine-grained quartz + lawsonite + sodic-amphibole inclusions, which in high-strain zones define an earlier fabric oblique to the dominant foliation. In high-strain zones garnet rims are concordant with and include sodic-amphibole and sodic-pyroxene aligned with the main foliation. The main foliation comprises sodic-amphibole + sodic-pyroxene ± lawsonite ± phengite, with strong compositional banding into either sodic-pyroxene or sodic-amphibole rich domains. Lawsonite is fine-grained and common to both compositional domains. The main foliation has been strongly deformed, in places isoclinally, resulting in a weakly

developed axial planar strain-slip cleavage of reorientated phengite.

2.1.4.1.4 Metapelite

Metapelites are quartz- and phengite-rich and have the overall assemblage quartz + phengite + sodic-amphibole + sodic-pyroxene (Plate 2.3.4f). Quartz is fine- to medium-grained and displays varying degrees of strain. The main dominant foliation is dominated by elongated phengite grains which reach a maximum of 70 μm in diameter. Sodic-amphiboles are aligned within the main foliation; grains are finer-grained than phengite and are optically zoned with lilac-blue cores and darker-blue rims. Where present, sodic-pyroxene is aligned with the main foliation, grains are of similar grain-sizes to sodic-amphibole. Lawsonite is fine-grained, elongate and tabular, and aligned within the main foliation. A subsequent deformation event has deformed the main foliation, resulting in a weakly developed crenulation and strain-slip cleavage of reorientated white micas.

2.1.4.1.5 Massive porphyroblastic metabasite

The main foliation in the porphyroblastic metabasite is less strongly developed due to the greater competency of the lithology (Plate 2.3.4g). Within the assemblage lawsonite + sodic-pyroxene + sodic-amphibole ± garnet ± phengite ± epidote ± titanite, four progressively developed mineral growths are distinguished. Pre-kinematic garnet and clinopyroxene porphyroblasts form the earliest assemblage (Plate 2.3.4h).

Both are heavily fractured with cores abundant in ultra-fine grained inclusions, too fine-grained to identify. Garnet and sodic-pyroxene sub-idioblasts are wrapped by the foliation, which comprises fine-grained sodic-pyroxene, sodic-amphibole, minor lawsonite and sparse white mica. Fine-grained idioblastic epidote grains, together with lawsonite idioblasts, form aggregates within pressure shadows around pre-kinematic garnet and clinopyroxene porphyroblasts. A second porphyroblastic lawsonite growth has formed subsequent to the main foliation development. Coarse lawsonite idioblasts overgrow the foliation and consequently contain, often coarse-grained, inclusions of sodic-amphibole, sodic-pyroxene, and less commonly epidote.

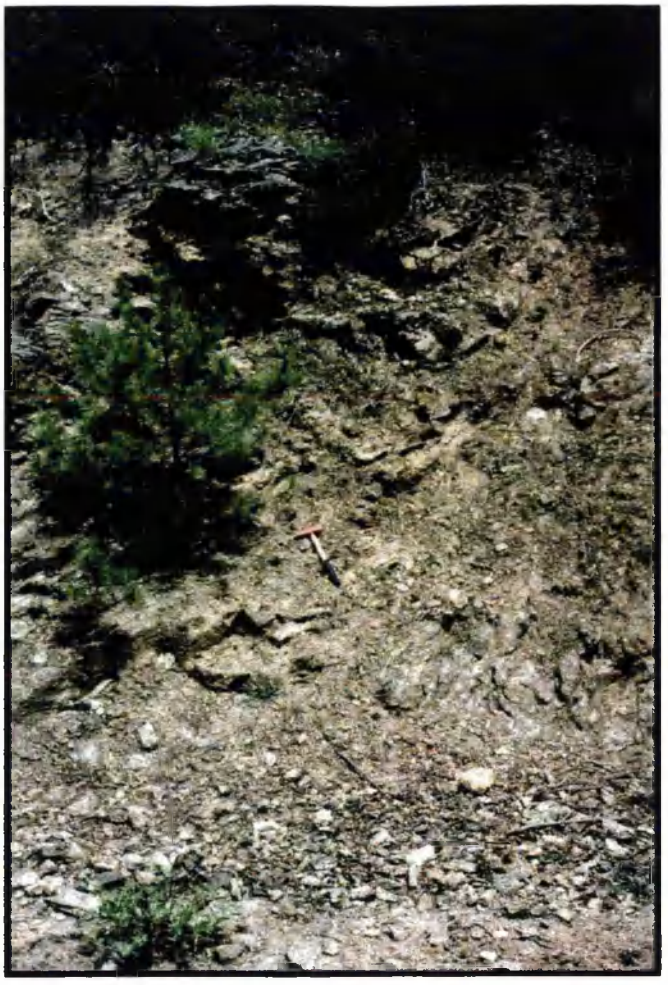

Plate 2.3.1a: Outcrop of phengitic metachert along the Aliova River section near Alacaat Village in the Orhaneli region.

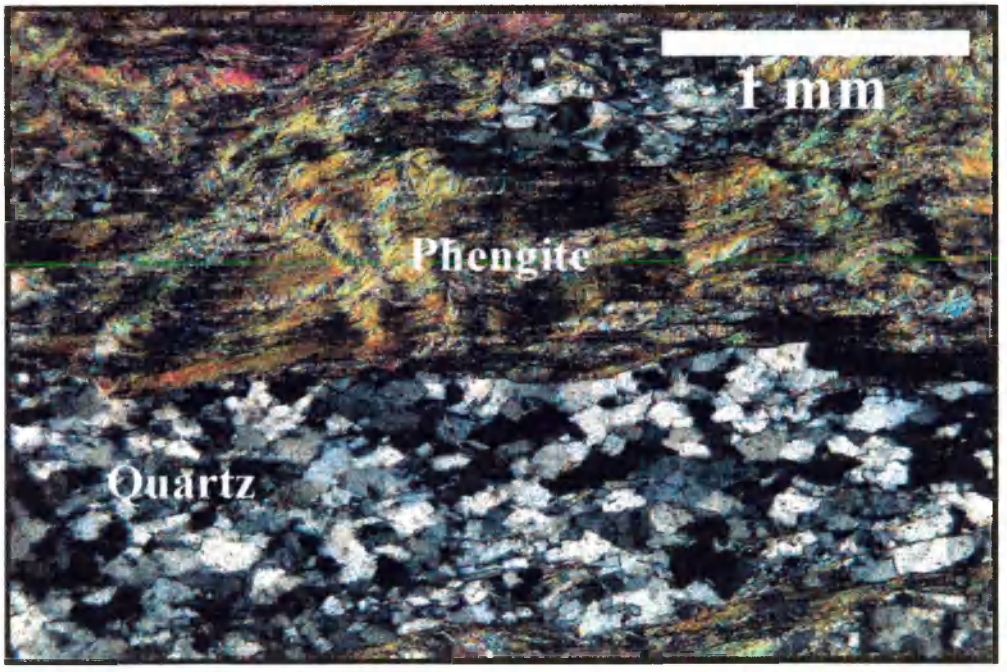

Plate 2.3.1b: Photomicrograph of metachert sample 96/234 from the Aliova River section in the Orhaneli region.

Plate 2.3.2a: Blueschist-facies metabasite outcrop in Inonü, within the Tavsanli region. Dr Jo-Anne Wartho for scale.

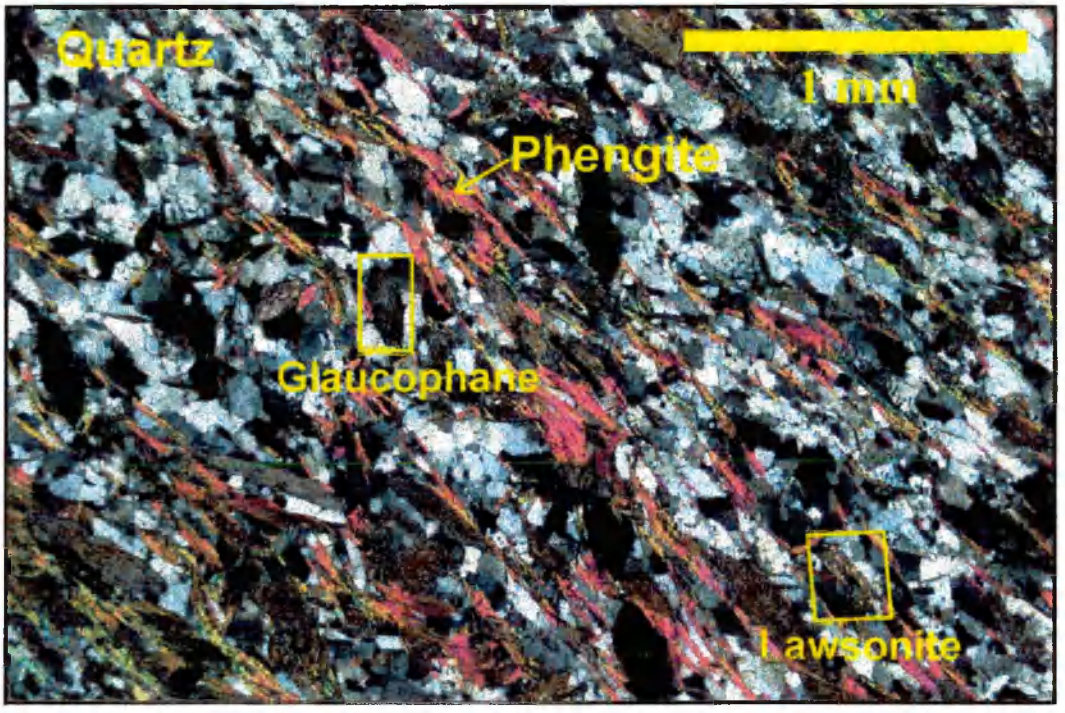

Plate 2.3.2b: Photomicrograph of sample 96/12 from Inonü metapelite, Tavsanli region.

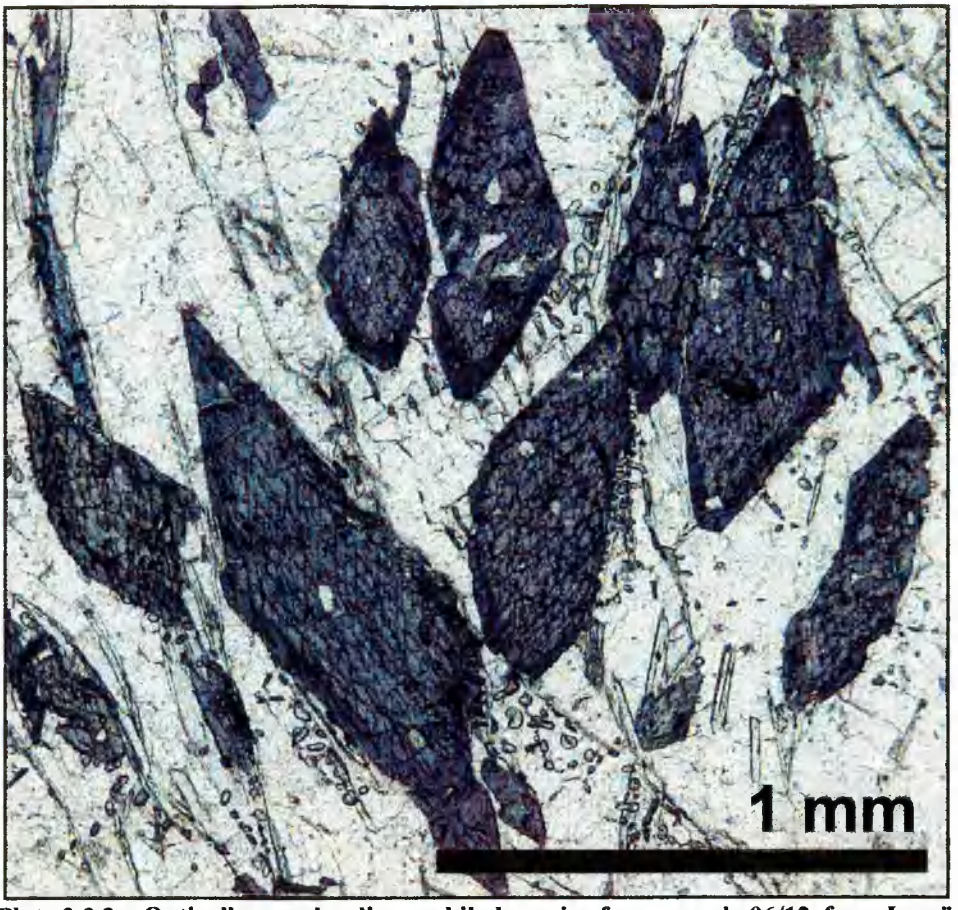

Plate 2.3.2c: Optically zoned sodic-amphibole grains from sample 96/12, from Inonü, the Tavsanli region.

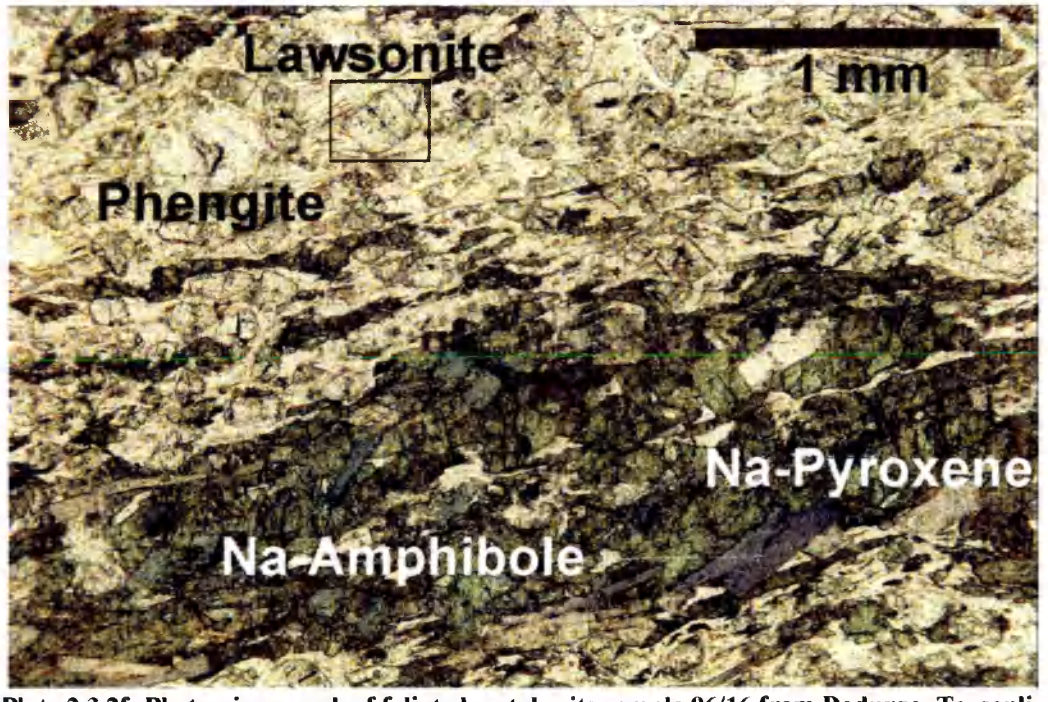

Plate 2.3.2f: Photomicrograph of foliated metabasite sample 96/16 from Dodurga, Tavsanli region.

Plate 2.3.2e: Blueschist outcrop along a road-cutting overlooking Dodurga reservoir, near Dodurga in the Tavsanli region.

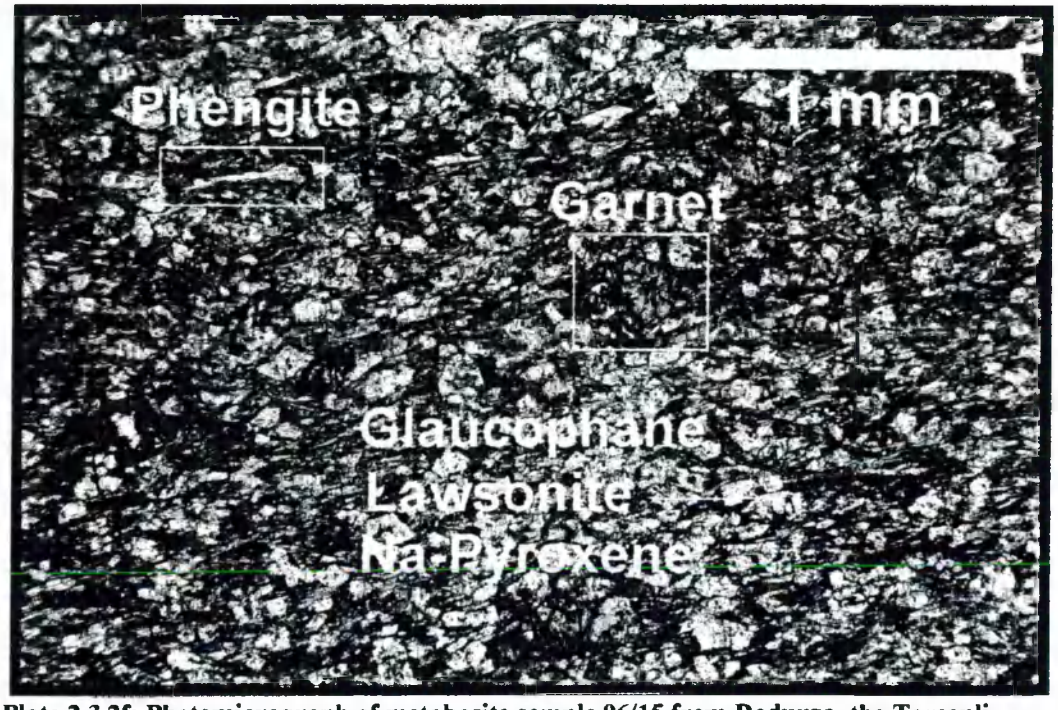

Plate 2.3.2f: Photomicrograph of metabasite sample 96/15 from Dodurga, the Tavsanli region.

Plate 2.3.2g: Compositionally banded field photograph of foliated metabasite in Yeniuregil, Tavsanli region.

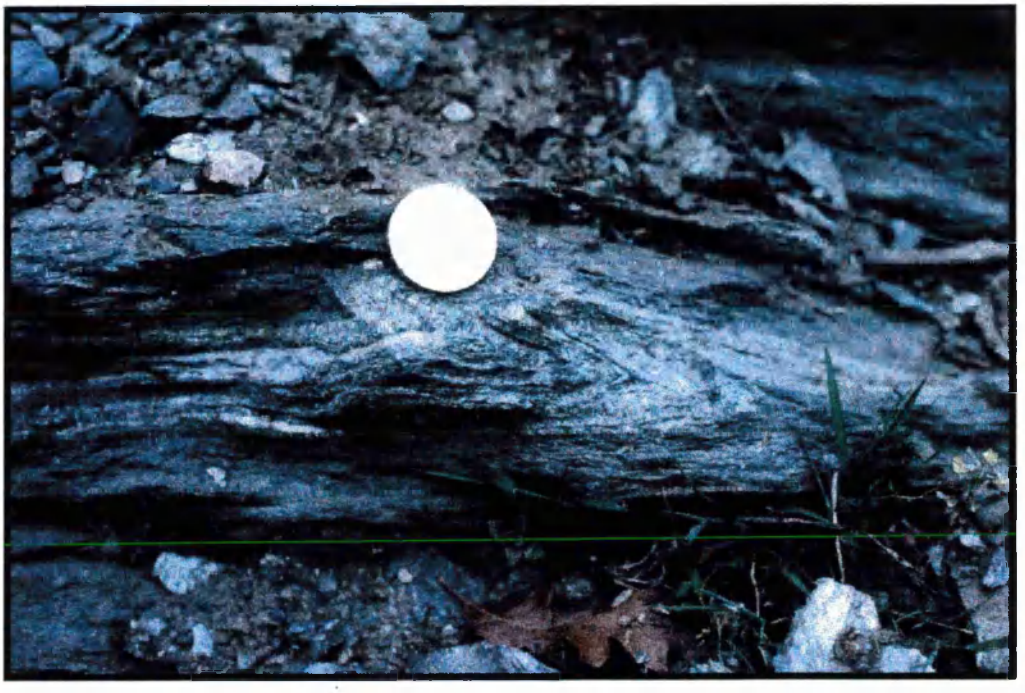

Plate 2.3.2h: Field photograph of lawsonite rich band in metabasite outcrop, Yeniuregil, Tavsanli region.

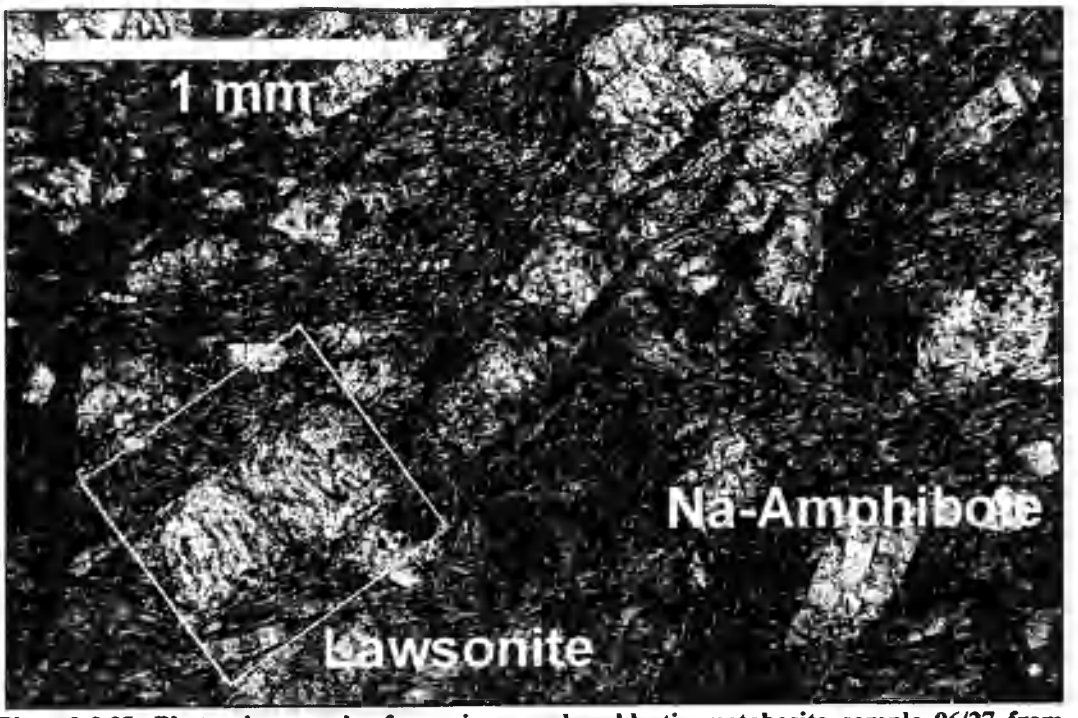

Plate 2.3.2I: Photomicrograph of massive porphyroblastic metabasite sample 96/27 from Yeniuregil, Tavsanli region.

2.3.2j: Field photograph of metapelite bands within metabasite outcrops in Yeniuregil, the Tavsanli region

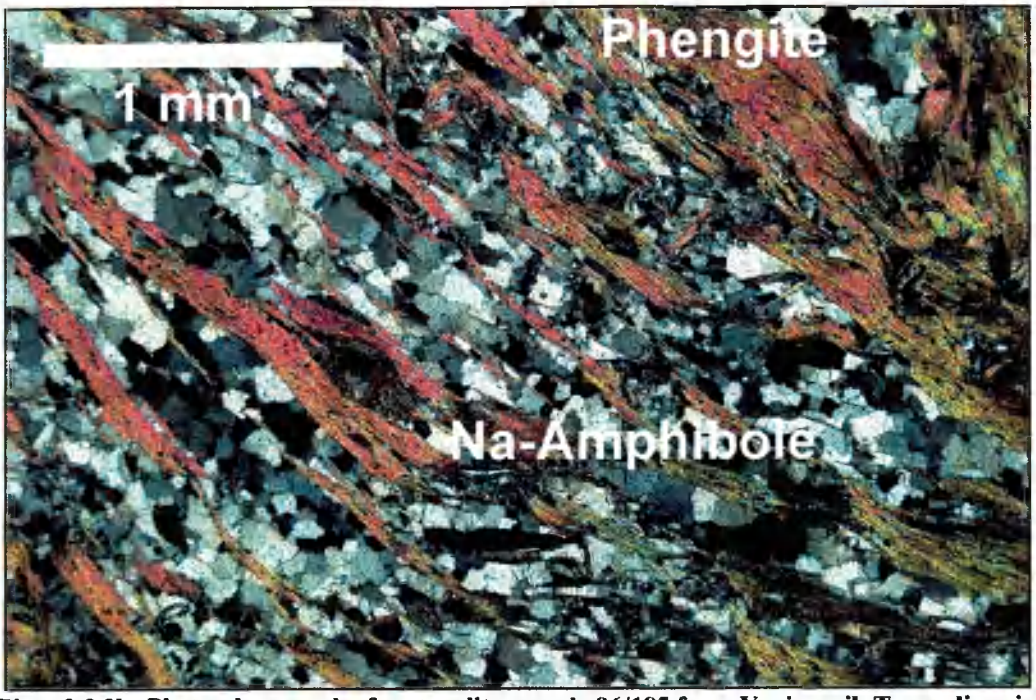

Plate 2.3.2k: Photomicrograph of metapelite sample 96/185 from Yeniuregil, Tavsanli region.

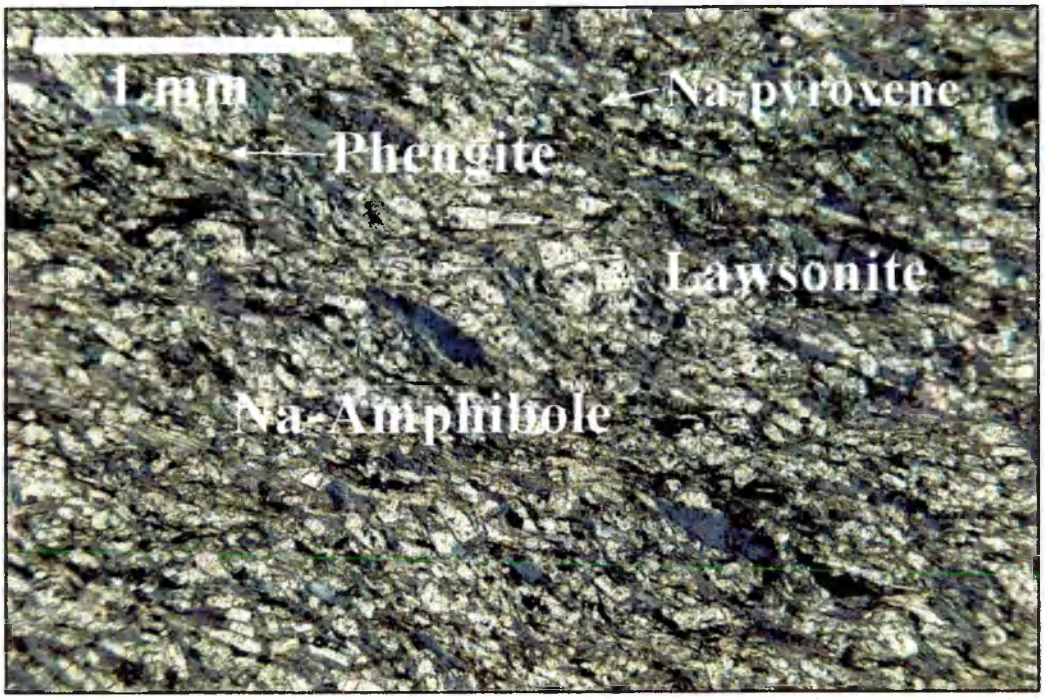

Plate 2.3.2l: Photomicrograph of sodic-amphibole-rich foliated metabasite sample 96/28 from Yeniuregil, Tavsanli region

Plate 2.3.3a: Field photograph of metapelite outcrop in Akcakaya.

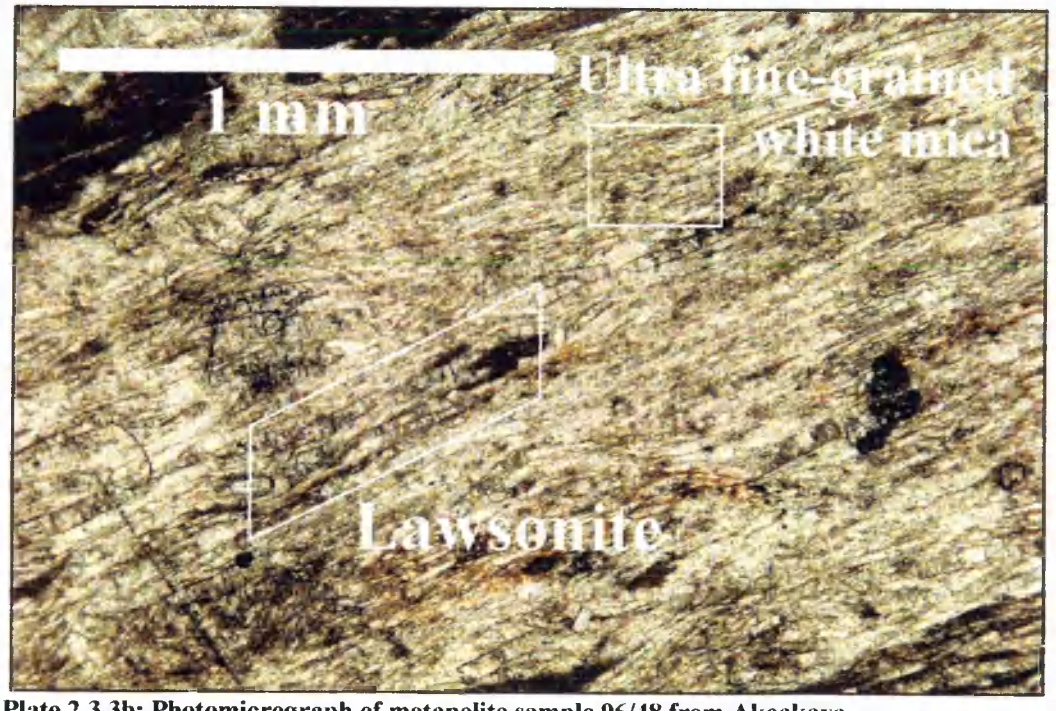

Plate 2.3.3b: Photomicrograph of metapelite sample 96/48 from Akcakaya.

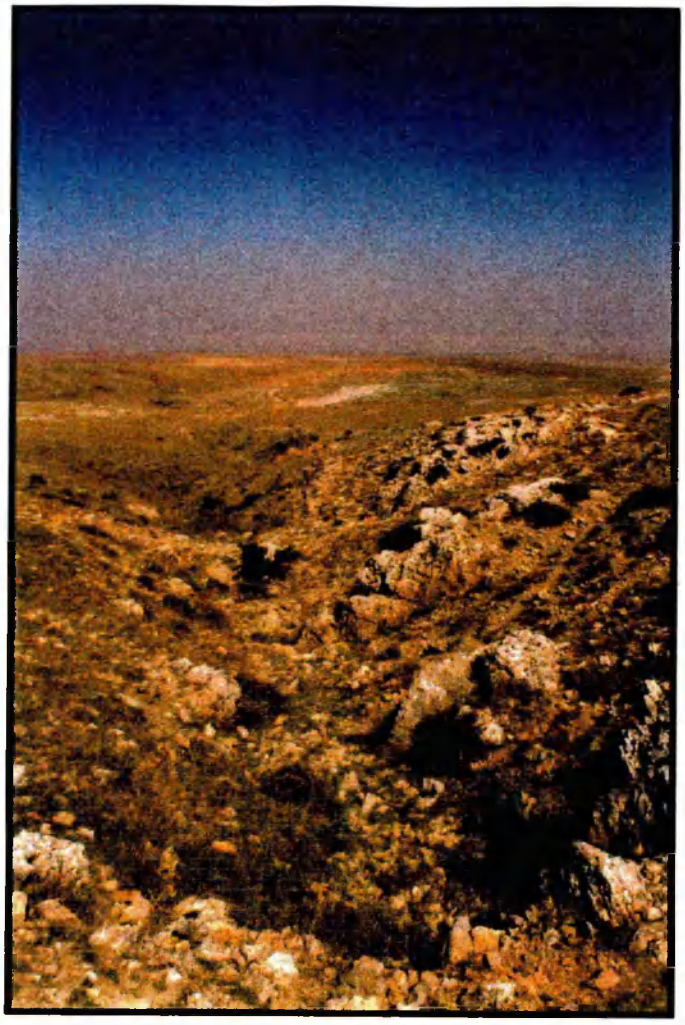

Plate 2.3.4a: Field photgraph of outcrop in Halilbagi, in the Sivrihisar region.

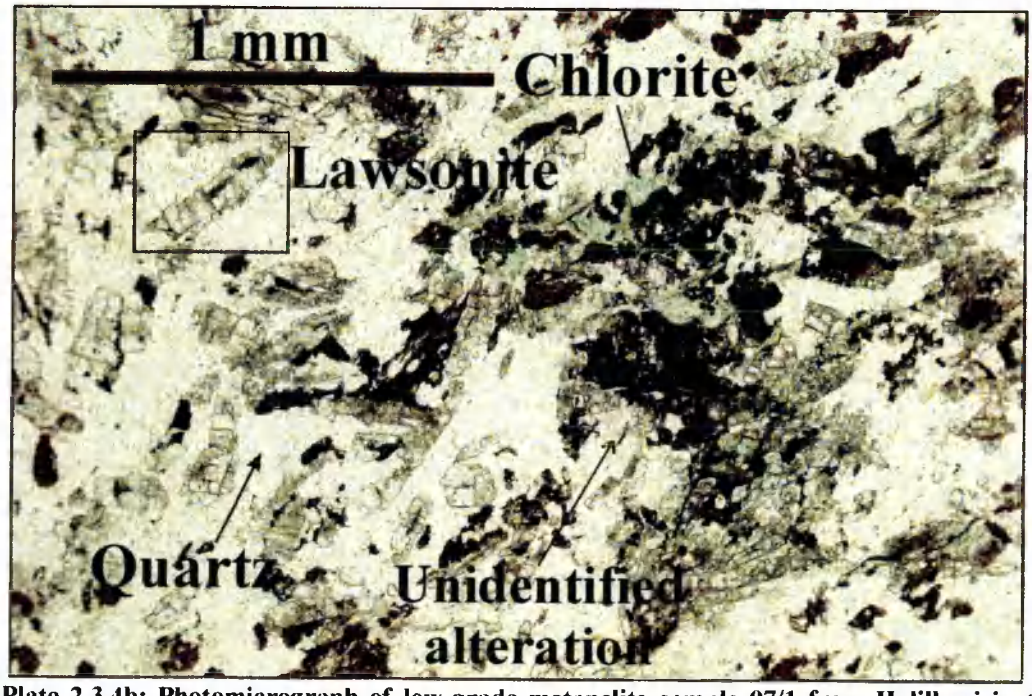

Plate 2.3.4b: Photomicrograph of low-grade metapelite sample 97/1 from Halilbagi in the Sivrihisar region.

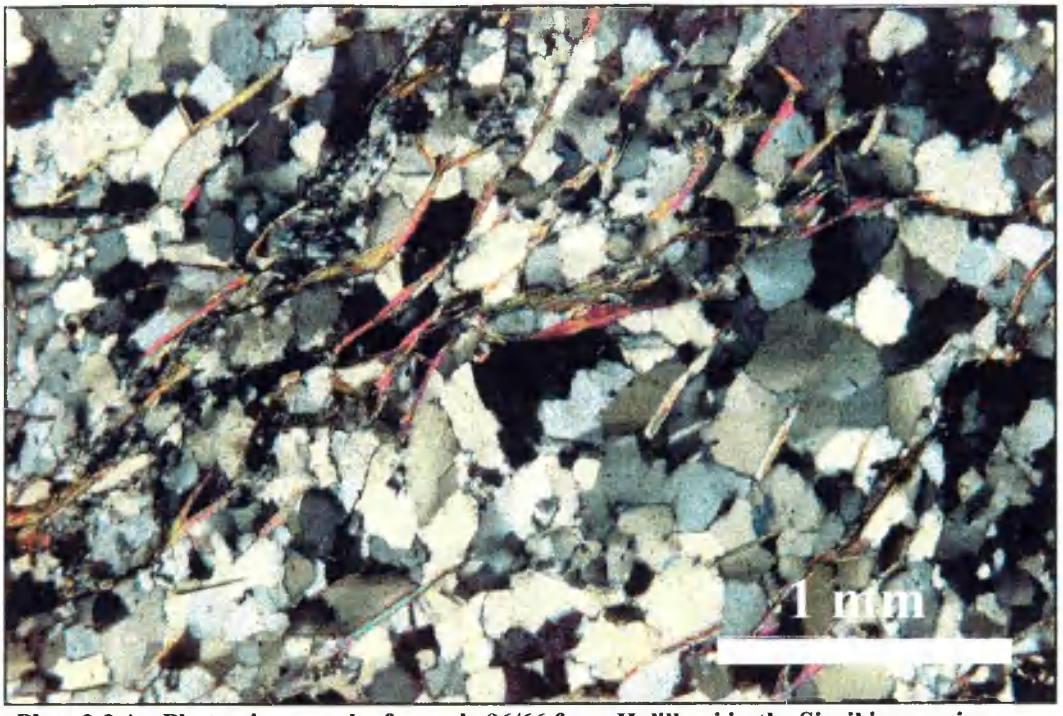

Plate 2.3.4c: Photomicrograph of sample 96/66 from Halilbagi in the Sivrihisar region.

Plate 2.3.4d: Field photograph of blue/green banded foliated metabasite outcrop in Halilbagi, within the Sivrihisar region.

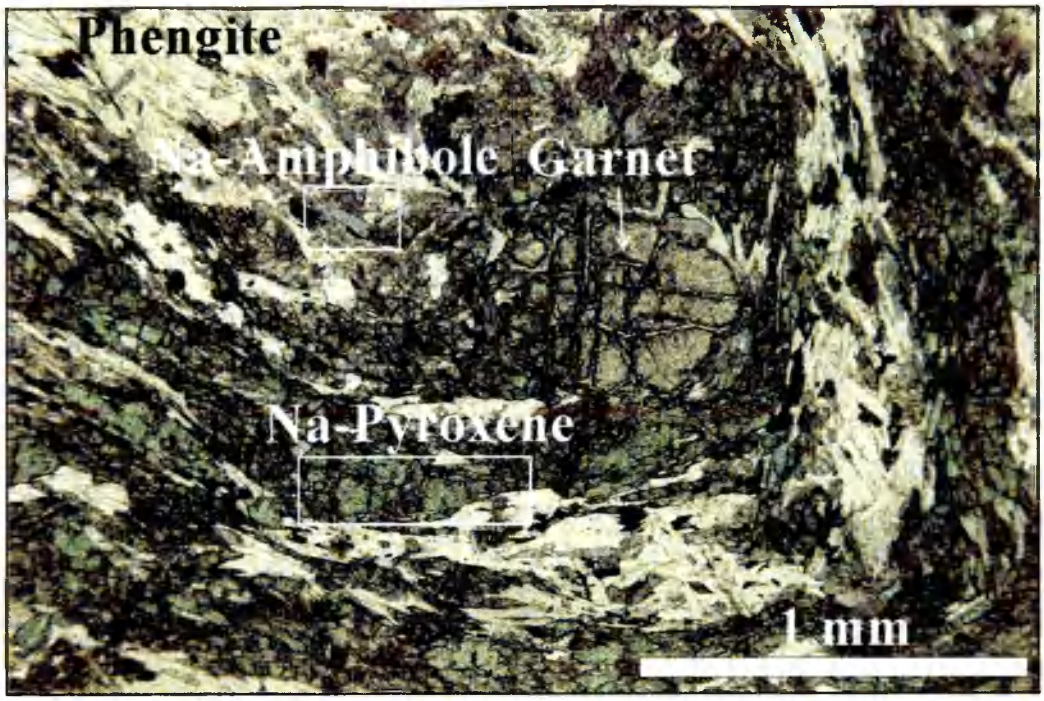

Plate 2.3.4e: Photomicrograph of foliated metabasite sample 96/158 from Halilbagi in the Sivrihisar region.

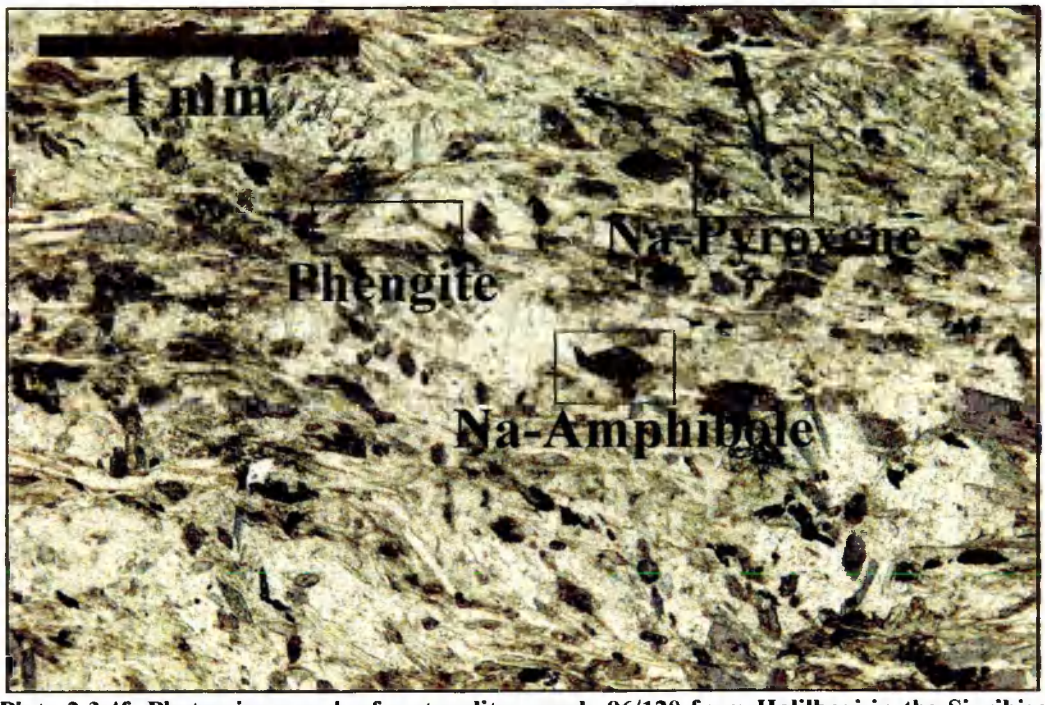

Plate 2.3.4f: Photomicrograph of metapelite sample 96/120 from Halilbagi in the Sivrihisar region.

Plate 2.3.4g: Field photograph of porphyroblastic metabasite from Halilbagi, in the Sivrihisar region.

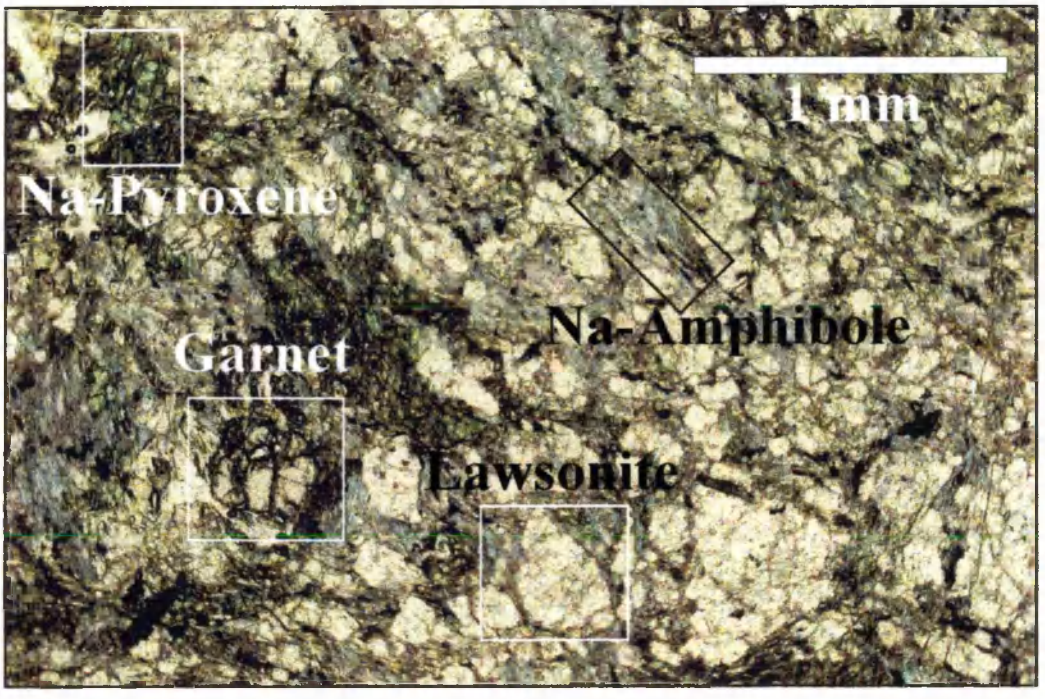

Plate 2.3.4h: Photomicrograph of porphyroblastic metabasite sample 96/149 from Halilbagi in the Sivrihisar region.

CHAPTER THREE

METAMORPHIC EVOLUTION

3.0 Outline of Chapter Three

The following chapter comprises two submitted papers. The first paper describes the metamorphic evolution of the blueschist- and low-temperature eclogite-facies rocks of the Tavsanli Zone and an interpretation of the Pressure-Temperature paths. The second paper describes oscillatory zoning in lawsonites, unique to the metabasites in the Sivrihisar region. An additional section details the evidence for possible ultrahigh-pressure metamorphism of the Halilbagi region of Sivrihisar.

3.1 Thermobarometry and P-T evolution of Tethyan high- pressure metamorphism: the Tavsanli Zone, NW Turkey.

3.1.1 Introduction

The formation, exhumation and preservation of high-pressure low-temperature (HPLT) assemblages have long been enigmatic and the subject of debate, not least in terms of the mechanisms responsible for their return to the surface from depths greater than the base of the continental crust. The diversity of tectonic settings in which these rocks are formed attest to the diversity of exhumation mechanisms including buoyancy forces (e.g. England and Holland, 1979; Cloos, 1982) or by extension (Platt, 1986; 1987; 1993), and in many cases a combination of several mechanisms may operate together (Platt, 1993).

Research in many areas of HPLT metamorphism shows that Pressure-Temperature (P-T) paths associated with HPLT rocks follow two broad trends. Those resulting exclusively from subduction are characterised by a retrograde path closely mirroring the prograde path, termed the Franciscan Type after the Franciscan complex, California (Ernst, 1988). HPLT rocks formed in a collisional setting, such as the Western Gneiss region of Norway, display a more 'looped' P-T path with almost isothermal decompression resulting in often extensive overprinting of HPLT assemblages by either greenschist- or amphibolite-facies metamorphism (e.g. Cloos, 1982; Thompson and England, 1984). In many cases, however, the HPLT rocks can be attributed to a combination of both subduction and collision-related tectonic processes, such as the Sesia Zone in the Western Alps (e.g. Pognante, 1991; Avigad, 1996) resulting in more complex P-T paths recorded by different tectonic units. The Tavsanli Zone of NW Turkey is a region of HPLT metamorphic rocks for which the timing of metamorphism and the process of exhumation is now well constrained

(Sherlock et al., submitted a). The Tavsanli Zone is approximately 250 km in length, and 100 km across at its widest (Figure 3.1), and is the largest expanse of Tethyan blueschist-facies rocks (Okay, 1989). A comparison of P-T paths from the best exposed regions of pristine rocks from this region affords a greater understanding of Tethyan subduction and metamorphism within an eastern Mediterranean tectonic context.

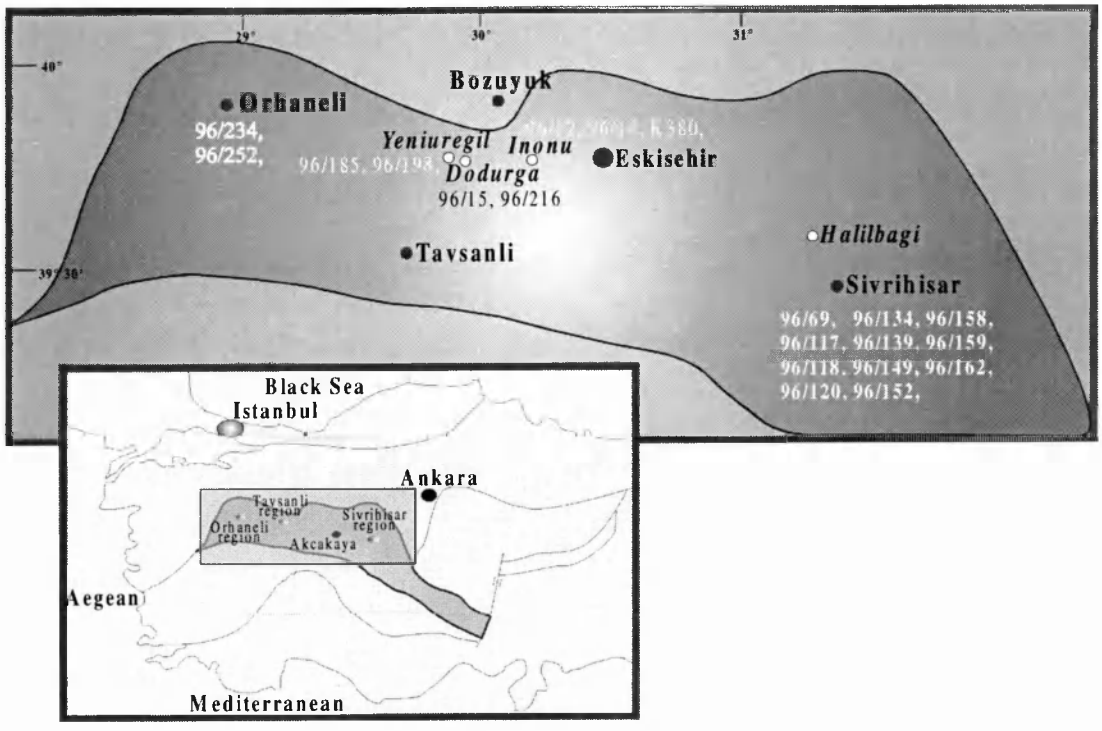

Figure 3.1: Location map for the samples collected from the Tavsanli Zone.

3.1.2 Geological setting

The Tavsanli Zone HPLT rocks lie in an east-west trending major Tethyan Izmir-Ankara suture. The suture represents the site of a major northward-directed subduction zone, one of a number responsible for the consumption of the Tethyan ocean during the Alpide orogeny (Okay, 1989). Given the plate configurations and relative plate motion directions for the African and European plates, subduction is inferred to have been oblique until approximately 65 Ma (Dewey et al., 1989). Thereafter convergence remained northward-directed but became orthogonal following continent-continent collision and the cessation of subduction. Final collision was diachronous, consuming the westward-narrowing Tethys earlier in the west than in the east (Okay and Tüyüz, in press).

The Tavsanli Zone HPLT belt comprises both sedimentary and volcanic rocks which represent remnants of the metamorphosed passive continental margin of the Anatolide-Tauride platform that have been exhumed from different crustal levels. Intrusive into the HPLT rocks are a series of 53 ± 3 Ma calc-alkaline subduction-related granitoid plutons exposed from the Orhaneli region in the west (Harris et al., 1994; Okay et al., 1998) to the Sivrihisar region some 200 km eastward (Sherlock et al., Submitted a).

Neogene cover obscures large regions of HPLT rocks, though the three best exposed areas of Orhaneli, Tavsanli and Sivrihisar (Figure 3.1) provide ample outcrop and lithological variety for a detailed study of the HPLT metamorphism. The principal aim

of this work is to assess the conditions of metamorphism and P-T evolution of two areas of pristine HPLT rocks within the Tavsanli Zone and compare with the existing P-T data for the Tavsanli Zone which is primarily based on the Orhaneli region (Okay and Kelley, 1994; Harris et al., 1994; Okay et al., 1998) and reconnaissance studies further east (Kulaksiz, 1981; Gautier, 1984). We present new thermobarometric and petrographical data from the Tavsanli and Sivrihisar regions in the central and east Tavsanli Zone (Figure 3.1).

To date, the Orhaneli region in the west of the Tavsanli Zone has provided the best documented study of blueschist-facies metamorphism. The P-T path of those blueschists follows a clockwise trajectory, reaching peak metamorphic conditions of 430 ± 30° C and 20 ± 2 kbar (Okay and Kelley, 1994). The whole P-T trajectory lies within the lawsonite-blueschist sub-facies. Conditions of metamorphism in the eastern regions of the Tavsanli Zone are less well understood and no previous attempt has been made to constrain their P-T evolution. Within the Sivrihisar region P-T estimates for lawsonite-glaucophane assemblages range from 200° to 350° C and 5 to 8 kbars, and for the transitional zones 350° to 470° C and 4 to 6 kbars (Kulaksiz, 1981).

Blueschist- and low-temperature eclogite-facies samples have been selected to constrain both the prograde and retrograde history of the Tavsanli Zone rocks, and underwent rapid syn-subduction exhumation (Sherlock et al., submitted a). At approximately 65 Ma subduction ceased and exhumation continued during continent-continent collision by southward-directed thrusting (Sherlock et al., submitted a).

Thermobarometric and fabric analyses from a number of lithological types are used to constrain the P-T conditions that link with the established chronological evolution of the Tavsanli Zone.

3.1.3 Lithological descriptions

Four main lithological types occur within the Tavsanli and Sivrihisar regions: metachert, metapelite, foliated metabasite and massive porphyroblastic metabasite. Mineral assemblages for all four lithological types are given in Table 3.1.

	Qtz	Phen	Laws	Amph	Pyx	Grt	Epi	Tite	Hem	Chl	Calc
Metachert											
96/234	×	×	×								
96/252	×	×	×						×		
Metapelite											
K380	×	×	×	×							
96/12	×	×	×	×							
96/69	×	×	×	×	×	×	×	×		×	
96/120	×	×	×	×							
96/134	×	×	×	×							
96/185	×	×	×	×							
96/198	×	×	×	×							
Foliated Metabasite											
96/14		×	×	×	×			×			
96/139		×	×	×	×			×			
96/152		×	×	×	×			×		×	×
96/158		×	×	×	×	×		×			
96/162		×	×	×	×			×			
Porphyroblastic Metabasite											
96/15		×	×	×	×	×					
96/117		×	×	×	×		×			×	×
96/118		×	×	×	×		×			×	×
96/149		×	×	×	×	×	×	×			
96/159		×	×	×	×	×		×			
96/216		×	×	×	×		×	×		×	×

Table 3.1: Mineral assemblages for samples from all lithological types.

3.1.3.1 Metachert

Metacherts are dominated by medium- to coarse-grained quartz with rare fine- to medium-grained fragmented feldspar. Three stages of mineral growth can be distinguished:

i The dominant feature is the main penetrative foliation which comprises inclusion-free lawsonite + phengite ± titanite (Figure 3.2).

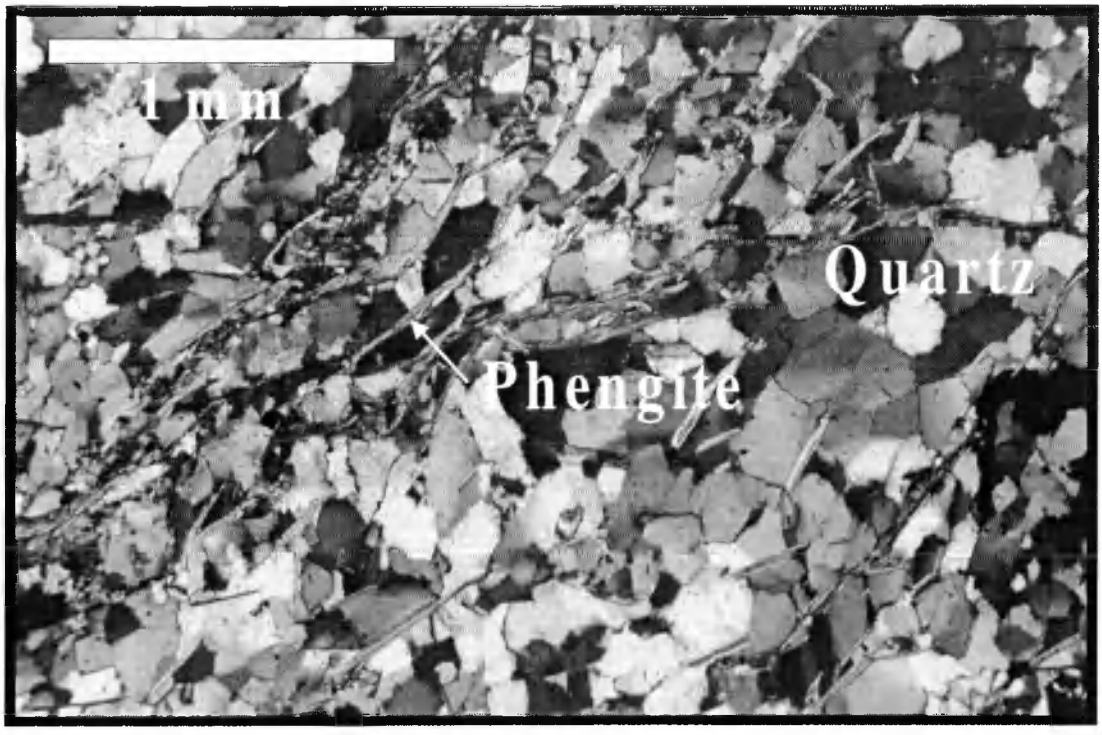

Figure 3.2: Photomicrograph of metachert sample 96/234 from the Orhaneli region.

Fine-grained idioblastic lawsonites are aligned in the foliation, phengites are inclusion-free and of a coarser grain-size than lawsonite. Fine-grained titanite grains are also aligned within the main foliation where present.

ii The dominant foliation was weakly crenulated in a subsequent and less intense deformation event, resulting in a non-penetrative strain-slip cleavage of re-oriented white micas.

3.1.3.2 Metapelite

Metapelites are dominated by the penetrative foliation (Figure 3.3), within the overall assemblage phengite + sodic-amphibole + lawsonite + quartz ± sodic-pyroxene ± garnet ± titanite, four stages of mineral growth can be distinguished:

i An earlier foliation comprising quartz and lawsonite is preserved as fine-grained inclusions within cores of sodic-amphiboles, and where present within cores of garnet.

ii The dominant foliation is defined by aligned sodic-amphibole + lawsonite + phengite. Where present, sodic-pyroxene is aligned in the main foliation and forms domains which include minor lawsonite and sodic-amphibole, separated from sodic-amphibole-rich domains by fine- to medium-grained quartz bands. The rims of pre-kinematic garnets preserve sodic-amphibole and occasionally sodic-pyroxene + phengite inclusions, which are concordant with the main foliation. Sodic-amphibole is

optically zoned with deep-blue rims and lilac-blue cores. Sodic-pyroxenes are not optically zoned and are generally finer-grained than sodic-amphibole. Lawsonite are elongated sub-idioblastic and finer grained than sodic-amphibole. Phengites are finer-grained than lawsonite and are elongate with a maximum diameter of 50 μm.

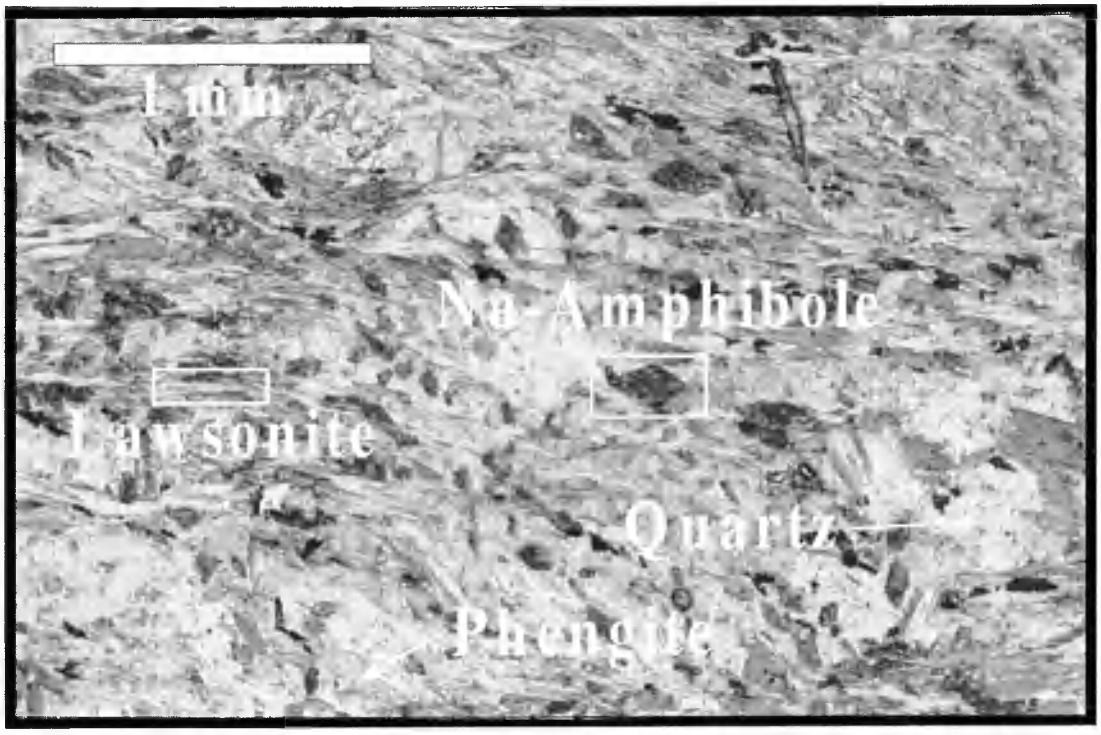

Figure 3.3: Photomicrograph of metapelite, sample 96/12 from the Tavsanli Region.

iii The dominant foliation has been deformed producing a weakly developed strain-slip cleavage of re-orientated white mica.

3.1.3.3 Foliated metabasite

Metabasites contain the assemblage lawsonite + sodic-pyroxene + sodic-amphibole ± garnet ± phengite ± titanite. In the Tavsanli region garnet is absent with the exception

of sample 96/15. Garnet is ubiquitous in the Sivrihisar region. Within the foliated metabasite four progressive mineral growth stages have been identified:

i The earliest assemblage of quartz + lawsonite is preserved as inclusions in garnet cores. Pre-kinematic lawsonite is fragmented and boudinaged. Subsequent sodic-amphibole and quartz have grown within pressure shadows around lawsonite, and in cracks in lawsonite associated with deformation. The pre-kinematic lawsonite is wrapped by the main foliation.

ii Where present, garnets are pre- to syn-kinematic and commonly fragmented in high-strain zones (Figure 3.4).

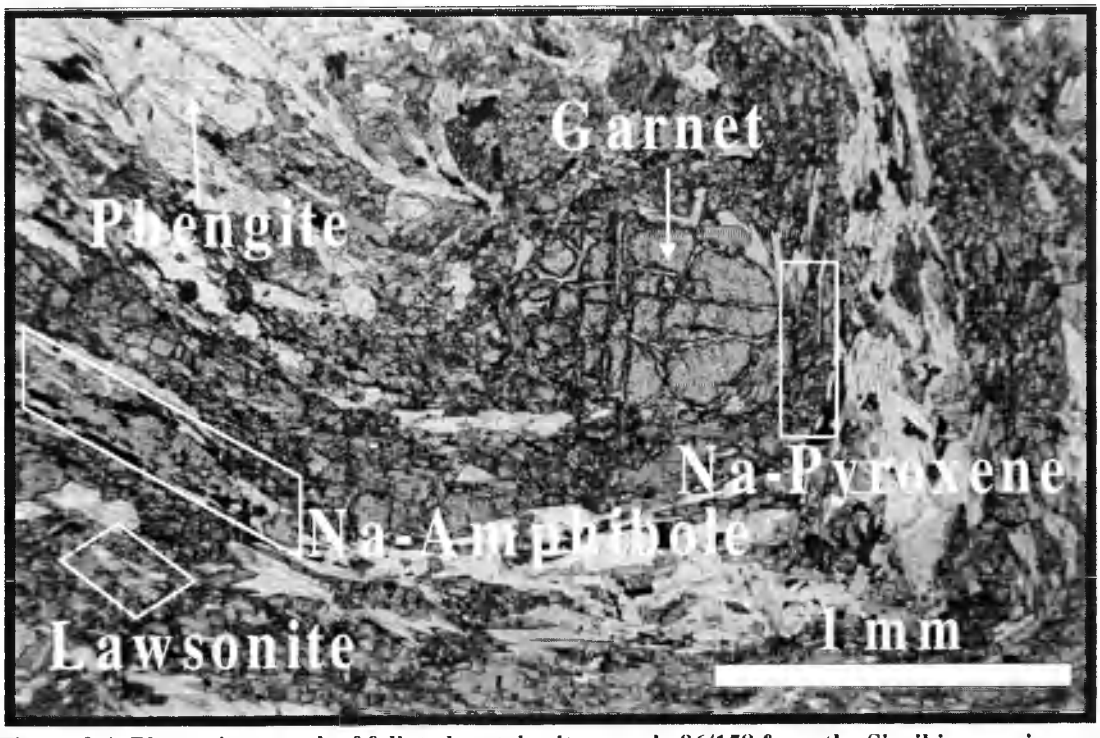

Figure 3.4: Photomicrograph of foliated metabasite sample 96/158 from the Sivrihisar region.

Within the garnets are abundant quartz + lawsonite + sodic-amphibole inclusions which in high-strain zones define an earlier oblique foliation. However garnet rims are

concordant with, and include sodic-amphibole and sodic-pyroxene defining the later foliation (Figure 3.5).

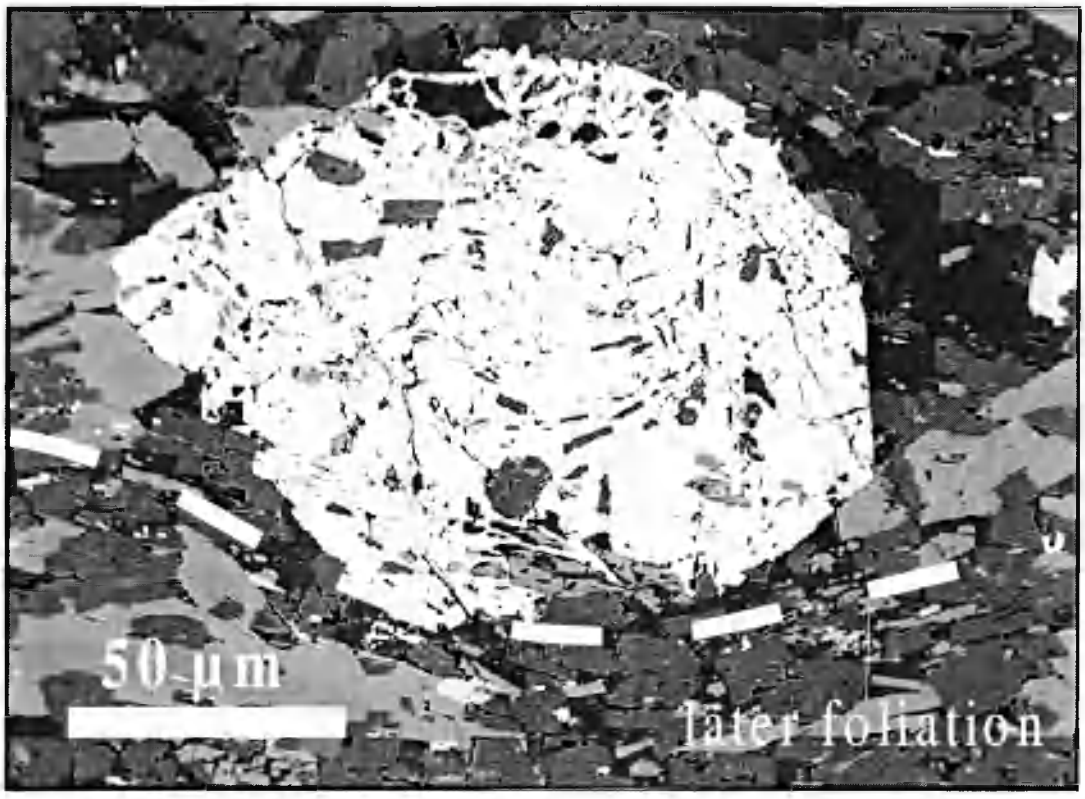

Figure 3.5: Backscattered electron image of a garnet in sample 96/158 illustrating porphyroblast-foliation relationships.

iii The penetrative foliation is the dominant feature, comprising sodic-amphibole + sodic-pyroxene + lawsonite + white mica, with strong compositional segregation resulting in amphibole-rich and pyroxene-rich domains. Within the foliation, fine-grained tabular lawsonite is ubiquitous. Fine-grained phengite is also present but is less abundant than either sodic-pyroxene or sodic-amphibole.

iv The main foliation has been folded, in places isoclinally, resulting in a weakly developed axial planar crenulation cleavage of reorientated white micas.

3.1.3.4 Porphyroblastic metabasite

The main foliation in the porphyroblastic metabasite is weakly developed due to the greater competency of the lithology (Figure 3.6). Within the assemblage lawsonite + sodic-pyroxene + sodic-amphibole ± garnet ± phengite ± epidote ± titanite, four progressively developed mineral growth events are distinguished:

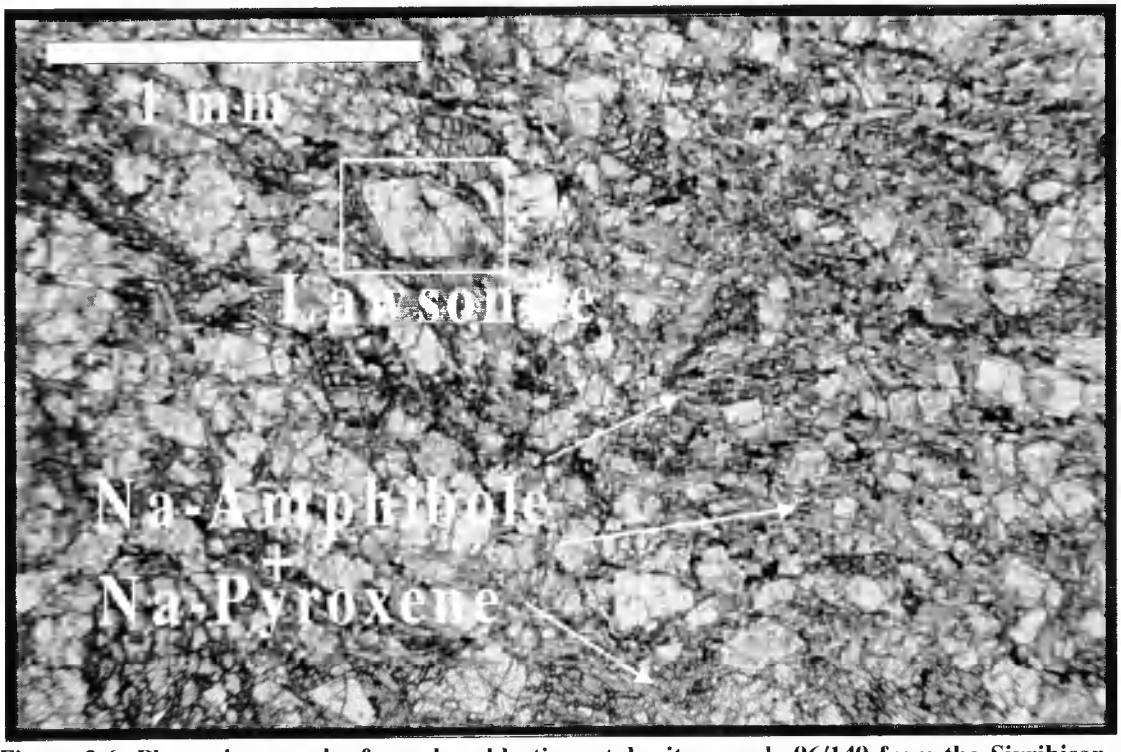

Figure 3.6: Photomicrograph of porphyroblastic metabasite sample 96/149 from the Sivrihisar region.

i Pre-kinematic garnet and clinopyroxene porphyroblasts form the earliest assemblage, both are heavily fractured with cores abundant in ultra-fine grained inclusions, too fine grained to identify.

ii Garnet and sodic-pyroxene sub-idioblasts are wrapped by the weakly developed foliation, which comprises fine-grained sodic-pyroxene, sodic-amphibole,

minor lawsonite, and sparse white mica. Fine-grained idioblastic epidote grains, together with lawsonite idioblasts, form aggregates within pressure shadows around the pre-kinematic garnet and clinopyroxene porphyroblasts.

iii A second porphyroblastic lawsonite growth has formed syn- to post-main foliation development (Figure 3.7)

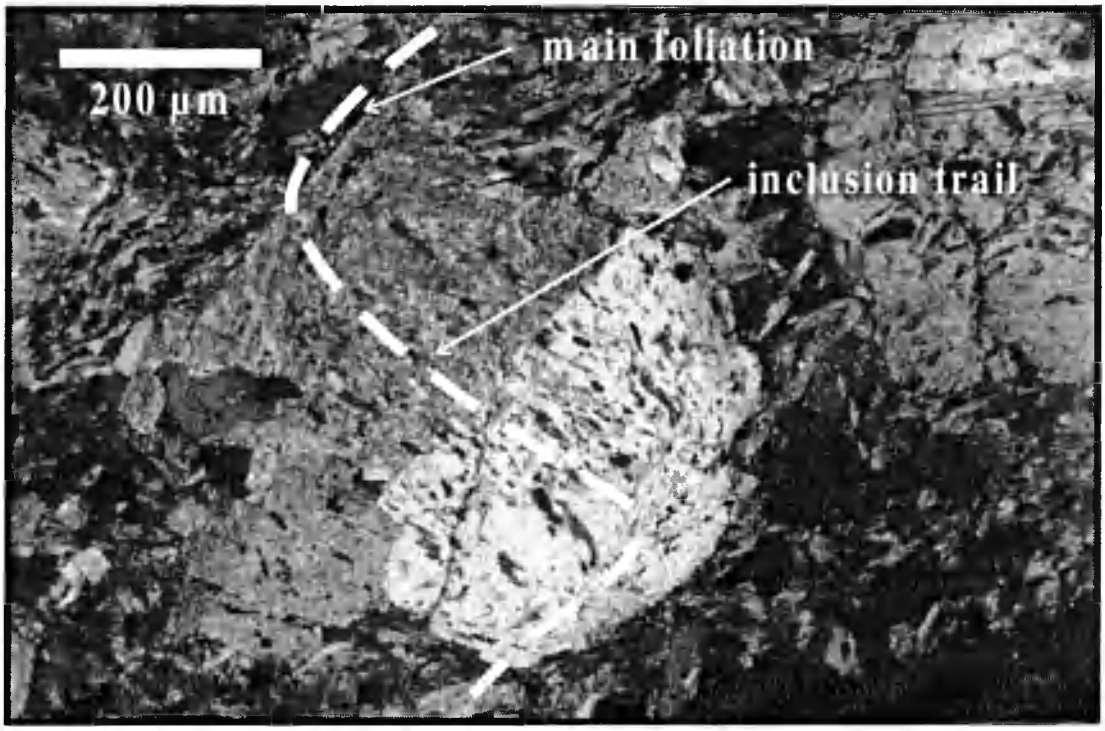

Figure 3.7: Lawsonite porphyroblast in sample 96/149 containing sodic-amphibole, sodic-pyroxene and rare epidote inclusions.

Coarse lawsonite idioblasts overgrow the foliation and consequently contain often coarse-grained inclusions of sodic-amphibole, sodic-pyroxene and less commonly epidote.

3.1.4 Mineral Chemistry

Mineral compositions have been determined using a Cameca SX100 electronprobe microanalyser at the Open University, with a 20 kV accelerating voltage, 20 nA beam current and a spot size of 10 microns. Representative analyses of selected minerals from all lithologies are presented in Tables 3.2 to 3.6.

3.1.4.1 Garnet

Garnets in metachert and metabasite samples from Sivrihisar are almandine-rich and concentrically chemically zoned (Figure 3.8). Garnet in sample 96/158 displays strong concentric zoning in Fe, Mg, Ca and Mn. X-ray maps display a Mn-rich, Fe-poor core (Figure 3.8). A chemically distinct region lies between the core and the rim regions of the garnets, which is Fe-rich and Mn-poor, with a minor increase in Ca and Mg. Rims are lower in Fe with an increase in Mn and a corresponding decrease in Mg and Ca.

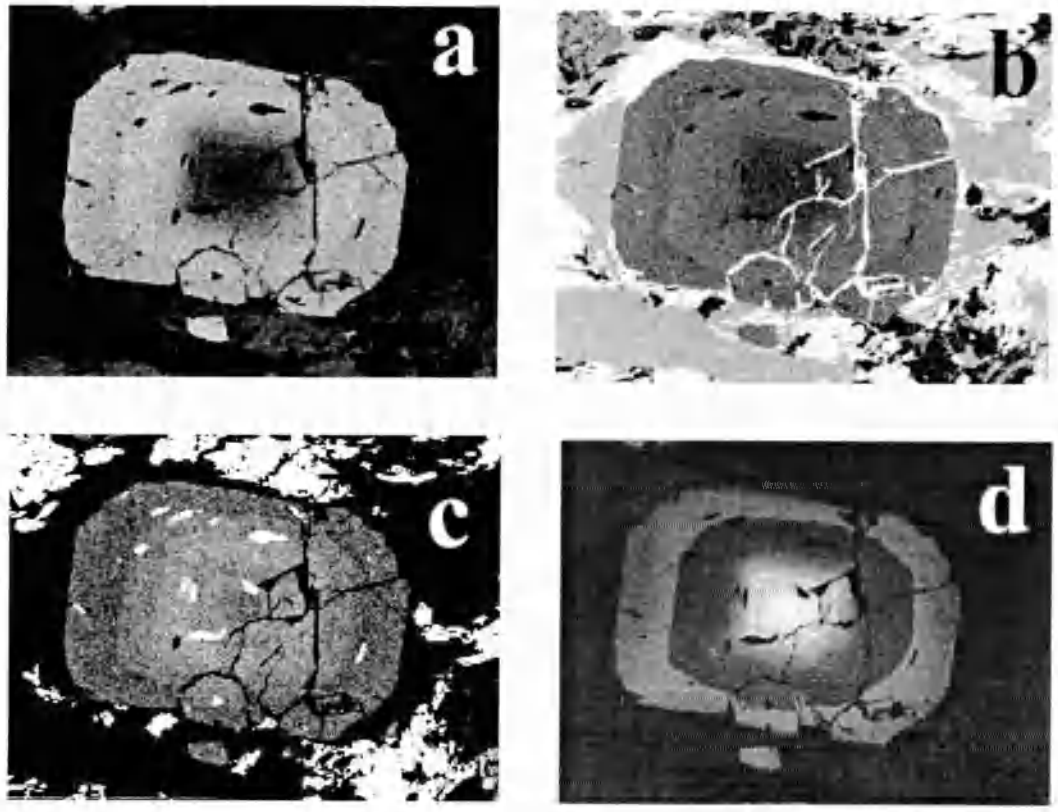

Figure 3.8: X-ray maps of concentrically-zoned garnet from sample 96/158 from the Sivrihisar region: a) Fe, b) Mg, c) Ca and d) Mn.

Garnets are rare within the metabasites of the Tavsanli region and have only been observed in a single sample of the porphyroblastic metabasite (sample 96/15). These are fine-grained and are more weakly zoned than garnets from Sivrihisar. Garnets are almandine-rich ($Alm_{(60-66)}$) with a grossular component of $Grs_{(24-26)}$ and pyrope and spessartine components of $Py_{(05-08)}$ and $Spss_{(03-09)}$.

	96/15	96/158	96/159	96/69
SiO_2	37.51	37.15	37.43	37.63
TiO_2	0.39	0.15	0.13	0.32
Al_2O_3	20.38	20.66	21.04	19.49
Cr_2O_3	0.03	0.11	0.13	0.02
MgO	1.67	1.25	2.09	1.15
CaO	9.15	9.94	10.11	24.79
MnO	2.61	6.13	3.18	6.68
FeO	29.54	24.91	26.77	10.09
Na_2O	0	0	0	0.00
K_2O	0	0	0	0.00
Total	101.27	100.30	100.88	100.17
Si	2.98	2.98	2.97	3.04
Ti	0.02	0.01	0.01	0.02
Al	1.91	1.95	1.97	1.86
Cr	0.00	0.01	0.01	0.00
Mg	0.20	0.15	0.25	1.67
Ca	0.78	0.85	0.86	0.14
Mn	0.18	0.42	0.21	0.58
Fe	1.97	1.67	1.77	0.69
Na	0.00	0	0	0.00
K	0.00	0	0	0.00
Total	8.04	8.03	8.04	7.99
XAlm	0.63	0.54	0.57	0.22
XPyr	0.06	0.05	0.08	0.54
XGross	0.25	0.28	0.28	0.04
XSpss	0.06	0.14	0.07	0.19

Table 3.2: Average garnet analyses for representative garnet-bearing samples.

3.1.4.2 Amphibole

Amphiboles are sodic, and according to the classification of Leake et al. (1997) are glaucophane and ferro-glaucophane with an occasional magnesio-riebeckite component, (Figure 3.9). Fe^{2+} and Fe^{3+} were calculated according to the method of Okay (1980).

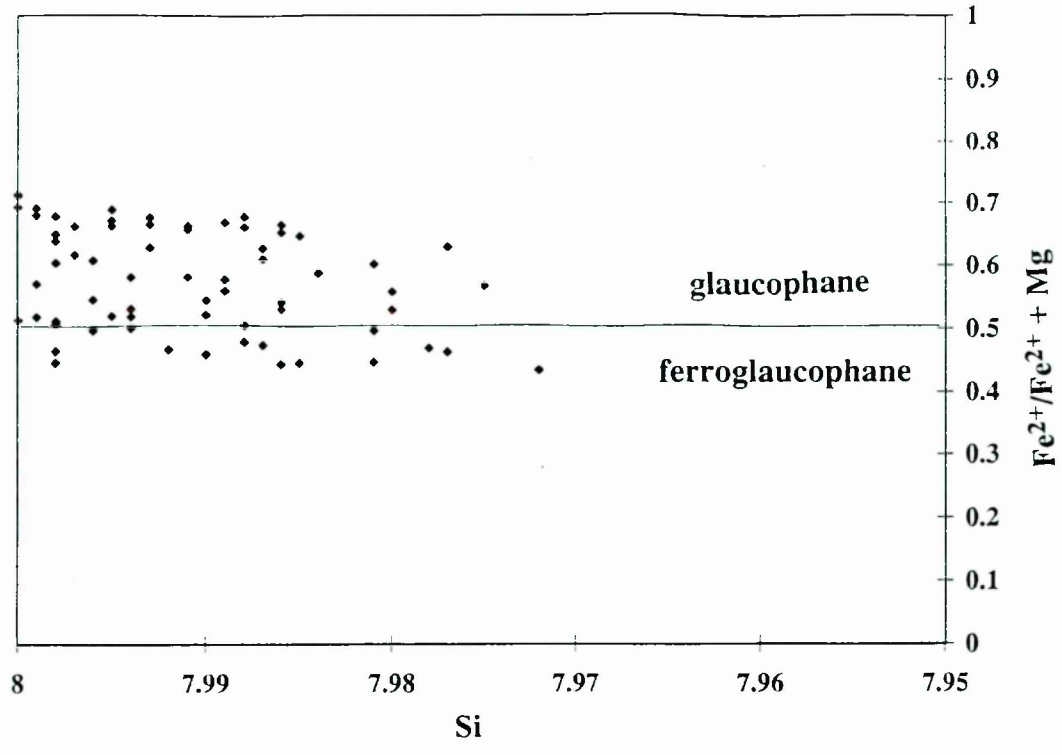

Figure 3.9: Amphibole compositions according to the classification of Leake et al. (1997).

Individual grains display complex optical and chemical zoning, with lilac-blue cores and deeper-blue rims. Backscatter electron (BSE) imaging reveals distinctly more complex zoning features (Figure 3.10). Rims show increased $Fe_{(total)}$ and Ca, with a corresponding decrease in Mg. Core regions are patchily zoned, a feature which cannot be attributed to major element zonation. The relationship between Fe^{2+}, Fe^{3+} and $Fe_{(total)}$ within cores and rims is not simple. Within the rims Fe^{2+} behaves as $Fe_{(total)}$ described above but Fe^{3+} decreases though by a lesser extent than Fe^{2+} increases. Within the cores Fe^{2+} and Fe^{3+} mirror each other in an almost 1:1 ratio. Na^{2+} and Mn^{2+} are minor components which co-vary in an almost oscillatory fashion throughout both cores and rims.

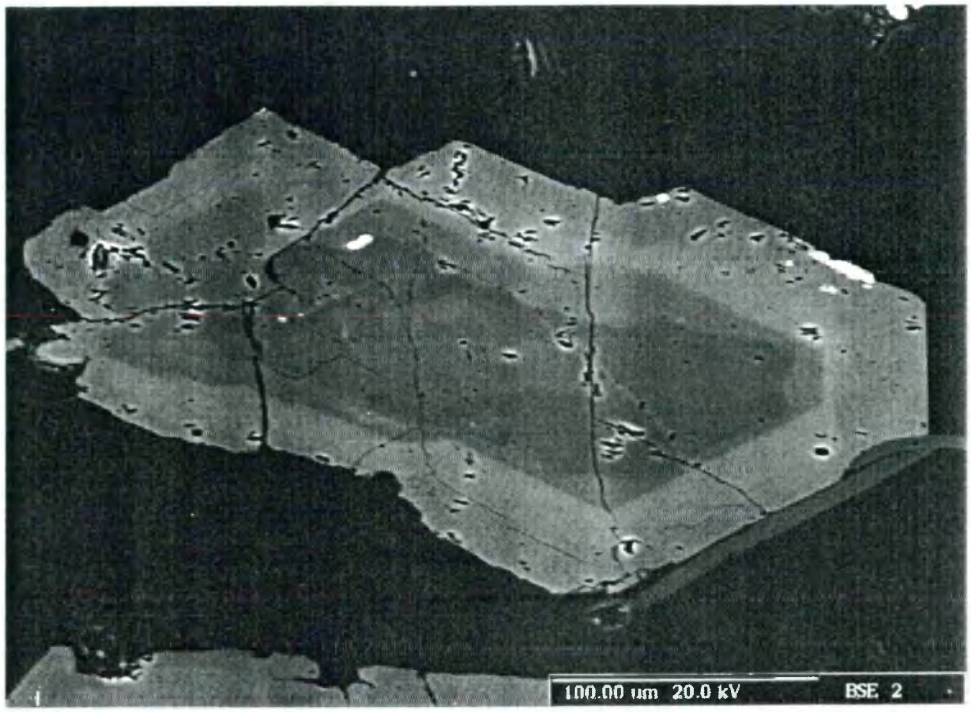

Figure 3.10: BSE image of complex zoning in sodic-amphibole from sample 96/12.

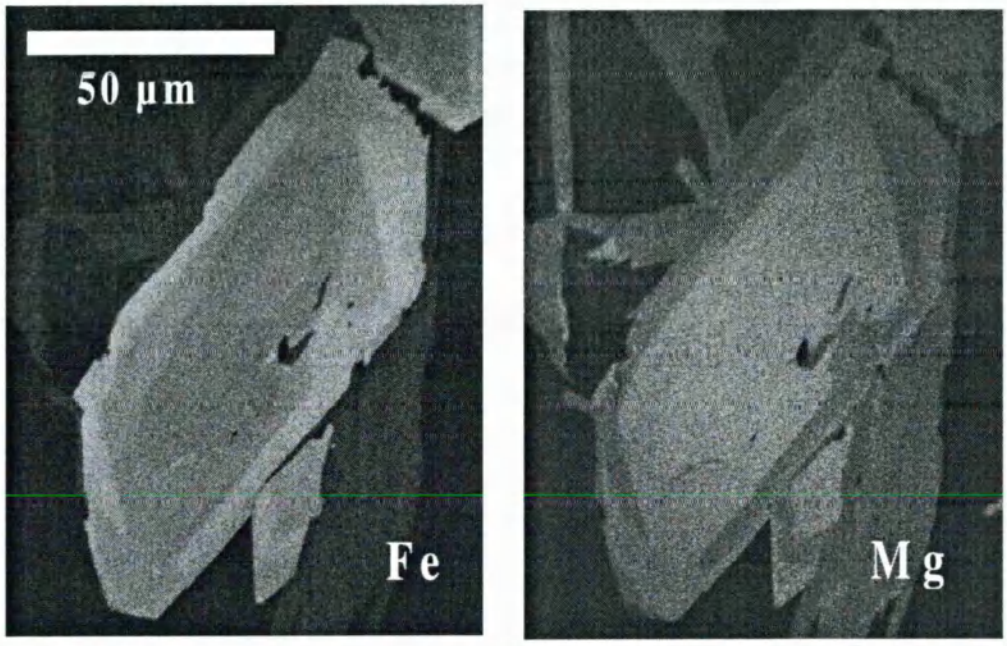

Figure 3.11: X-ray maps of sodic-amphibole from sample K380: a) Fe(total), and b) Mg.

X-ray maps of both Fe(total) and Mg^{2+} display distinct core/rim differences (Figure 3.11 a, b). Cores are Mg-rich and Fe-poor, rims are Fe-rich and Mg-poor. The boundary between core and rim in terms of Mg is much more distinct than for Fe.

	96/12	K380	6/15	96/185	96/139	96/149	96/159	96/69
SiO_2	57.27	55.79	57.59	56.95	57.09	57.66	56.92	57.18
TiO_2	0.00	0.00	0	0	0.02	0	0.02	0.00
Al_2O_3	6.83	4.71	6.78	4.83	6.00	7.21	5.37	5.93
MgO	9.36	8.68	10.29	10.27	16.45	12.18	13.40	8.71
CaO	0.37	0.38	1.20	0.69	0.13	3.38	5.46	0.10
MnO	0.18	0.15	0.03	0.27	1.37	0.13	0.04	0.53
FeO	9.49	11.2	9.41	8.18	5.20	9.89	10.58	11.95
Fe_2O_3	7.57	10.1	6.46	10.03	5.94	2.08	1.89	7.79
Na_2O	7.03	7.03	6.61	6.76	6.61	5.15	4.22	6.32
K_2O	0.02	0.07	0.04	0.03	0.03	0.03	0	0.03
Total	97.37	97.10	97.77	97.00	98.27	97.50	97.70	97.76
Si	8.15	8.01	8.13	8.20	7.99	8.05	8.00	8.08
Ti	0	0.00	0	0	0.00	0	0.00	0.00
Al	1.14	0.80	1.13	0.82	0.99	1.18	0.89	0.99
Mg	1.98	1.86	2.17	2.21	1.84	2.54	2.82	1.85
Mn	0.06	0.02	0.00	0.11	0.01	0.51	0.83	0.01
Fe^{2+}	1.11	1.34	1.10	0.03	0.60	1.15	1.40	1.41
Fe^{3+}	0.80	1.09	0.68	0.96	0.61	0.22	0.20	0.83
Ca	1.95	0.06	0.18	0.03	0.21	0.02	0.01	0.08
Na	0.04	1.96	1.81	1.89	1.79	1.39	1.14	1.73
K	1.94	0.01	0.01	0.01	0.00	0.01	0	0.00
Total	15.25	15.02	15.22	15.34	15.04	15.06	15.13	14.87

Table 3.3: Average amphibole analyses for representative samples

3.1.4.3 White mica

White micas are of the Si-rich phengite variety and are in the range Si = 3.50 to 3.79 (p.f.u.). Most analyses do not lie on the ideal muscovite-celadonite mixing line (Figure 3.12) due to the interference of Fe^{3+} substitution. The calculation of Fe^{3+} in phengite is

not possible on a stoichiometric basis (e.g. Carswell et al., 1997), and can only be inferred from the non-ideal behaviour of the data in Figure 3.12. Also apparent from Figure 3.12 is that the Tschermak exchange ([Mg, Fe^{2+}]^{vi}, Si^{iv} = Al^{vi}, Al^{iv}) in addition to Fe^{3+}-Al^{vi} substitution has taken place in most phengites.

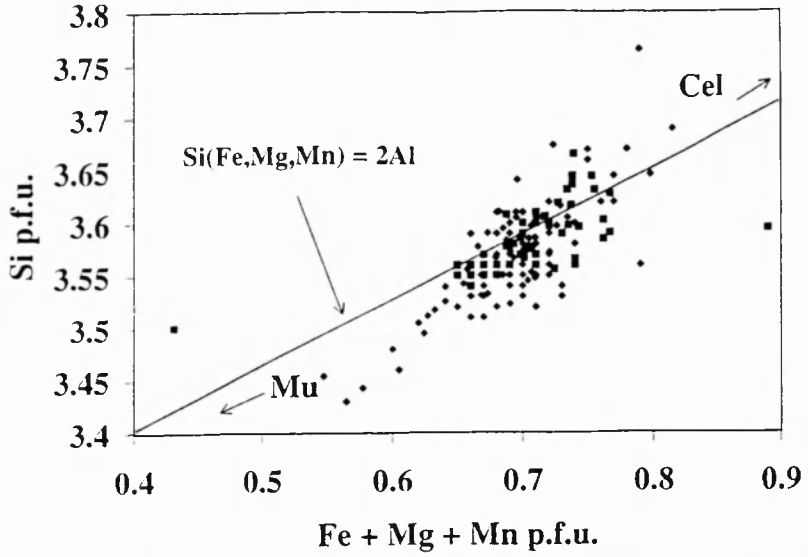

Figure 3.12: Compositional diagram of phengite illustrating both Tschermak and Fe^{3+} substitution.

	96/12	96/15	96/185	96/198	K380	96/139	96/149	96/158	96/159	96/69	96/117	96/118
SiO_2	51.8	52.62	52.21	52.42	52.03	53.35	52.18	52.00	53.80	52.66	49.38	49.38
TiO_2	0.1	0.14	0.09	0.08	0.09	0.12	0.13	0.20	0	0	0.15	0.15
Al_2O_3	22.3	21.21	21.78	22.14	21.90	20.92	21.62	22.40	22.14	22.20	21.34	21.34
MgO	4	4.33	4.23	4.14	4.02	4.66	4.62	4.27	4.81	4.56	4.71	4.71
MnO	0	0.02	0	0.06	0.07	0.02	0.05	0.00	0.01	0.02	0.02	0.02
FeO	4.8	4.87	0.05	4.59	5.33	4.53	4.18	0.41	4.41	4.12	4.38	4.38
Na_2O	0.1	0.11	4.67	0.08	0.07	0.12	0.15	0.10	0.17	0.13	0.08	0.08
K_2O	10.8	10.95	0.11	10.81	10.51	10.98	10.60	11.00	11.03	10.69	11.16	11.16
Total	94.1	94.27	10.98	94.33	94.02	95.25	93.52	94.10	96.38	94.39	91.32	91.32
Si	3.60	7.21	94.13	3.58	3.57	3.61	3.58	3.60	3.59	3.58	3.51	3.51
Ti	0.00	0.02	3.58	0.00	0.00	0.01	0.01	0.00	0	0	0.01	0.01
Al	1.80	3.42	0.00	1.78	1.77	1.67	1.75	1.80	1.74	1.78	1.79	1.79
Mg	0.40	0.88	1.76	0.42	0.41	0.47	0.47	0.40	0.48	0.46	0.50	0.50
Mn	0.00	0	0	0.00	0.00	0.00	0.00	0.00	0.00	0.00	0.00	0.00
Fe	0.30	0.00	0.43	0.26	0.31	0.26	0.24	0.20	0.25	0.23	0.26	0.26
Na	0.00	0.56	0.00	0.01	0.01	0.02	0.02	0.00	0.02	0.02	0.01	0.01
K	0.90	0.03	0.27	0.94	0.92	0.95	0.93	1.00	0.94	0.93	1.01	1.01
Total	7.01	1.91	0.01	7.00	7.00	7.01	7.01	7.00	7.02	7.00	7.09	7.09

Table 3.4: Average phengite analyses from representative samples.

3.1.4.4 Pyroxene

Pyroxenes are generally augitic with the jadeite component in the range $Jd_{(19-36)}$ for the Sivrihisar region, and $Jd_{(18-33)}$ from the Tavsanli region.

	96/15	96/149	96/152	96/158	96/159	96/69
SiO_2	54.85	55.23	55.11	55.19	55.45	55.29
TiO_2	0.02	0.04	0.09	0	0.03	0.03
Al_2O_3	5.21	6.02	4.98	5.63	4.86	6.32
MgO	7.33	8.24	8.81	8.00	8.15	4.88
CaO	13.33	13.65	13.53	13.40	14.41	9.18
MnO	0.02	0.06	0.17	0.07	0.10	0.30
Fe_2O_3 (i)						
Fe_2O_3 (ii)						
FeO	12.64	10.26	10.65	11.47	11.98	14.36
Na_2O	6.75	6.14	5.99	6.54	6.21	8.64
Total	100.17	99.64	99.34	100.30	101.19	98.99
Si	2.04	2.04	2.05	2.04	2.04	2.04
Ti	0.00	0.00	0.00	0	0.00	0.00
Al	0.23	0.26	0.22	0.24	0.21	0.29
Mg	0.41	0.44	0.49	0.44	0.45	0.29
Ca	0.53	0.45	0.54	0.53	0.57	0.39
Mn	0.00	0.54	0.01	0.00	0.00	0.47
Fe^{3+} (i)						
Fe^{3+} (ii)						
Fe^{2+}	0.39	0.00	0.33	0.35	0.37	0.01
Na	0.49	0.32	0.43	0.47	0.44	0.66
Total	4.09	4.05	4.06	4.07	4.08	4.15
Jd	0.23	0.26	0.22	0.24	0.21	0.29
Ac	0.26	0.06	0.21	0.22	0.23	0.37
Aug	0.51	0.68	0.57	0.53	0.56	0.34

Table 3.5: Average clinopyroxene analyses from representative samples.

The Fe^{3+} component has been estimated in omphacites using (i) a standard charge balance procedure (e.g. Droop, 1987), and (ii) the procedure of Cawthorn and

Collerson (1974), which maximises the jadeite component relative to acmite - thus making the assumption that the omphacites are low in Al^{iv}.

3.1.4.5 Lawsonite, epidote and titanite

Lawsonite compositions vary little from the ideal formula in samples from the four lithologies from either Tavsanli or Sivrihisar. In some metabasite samples unusually high Cr^{3+} is reported in lawsonites which are oscillatory zoned (Sherlock and Okay, submitted) but this is not common to all lithologies.

	96/117	**96/118**	**96/149**	**96/216**
SiO_2	37.22	36.96	36.85	38.02
TiO_2	0.00	0	0	0
Al_2O_3	22.07	23.36	22.65	23.02
Cr_2O_3	0.00	0	0	0
MgO	0.01	0	0.01	0.02
CaO	23.05	25.01	22.78	22.96
MnO	0.30	0.16	0.23	0.31
Fe_2O_3	13.55	12.99	13.62	13.96
Total	96.20	98.48	96.14	98.29
Si	3.03	2.95	2.99	3.02
Ti	0.00	0	0	0
Al	2.12	2.2	2.17	2.16
Cr	0.00	0	0	0
Mg	0.00	0	0	0
Ca	2.01	2.14	1.99	1.96
Mn	0.21	0.01	0.02	0.02
Fe^{3+}	0.83	0.78	0.83	0.83
Total	8.00	8.07	8	7.99

Table 3.6: Average mineral compositions of epidotes from representative samples.

3.1.5 Conditions of metamorphism

3.1.5.1 NCMASH partial petrogenetic grid

Metamorphic conditions have been determined using three pertinent equilibria calculated for minerals within the NCMASH system. Mineral formulae and associated activities are represented in Table 3.7.

	Formulae	Activities	
		96/69	**96/149**
gl	$Na_2Mg_2Al_2(Si_8O_{22})[H_2O]_2$	0.0242	0.054
law	$CaAl_2Si_2O_7(OH)_2.H_2O$	1.0	1.0
cz	$Ca_2Al_3Si_3O_{12}(OH)$	0.69	1.0
di	$CaMgSi_2O_6$	0.272	0.433
jd	$NaAlSi_2O_6$	0.279	0.259
hed	$CaFeSi_2O_6$	0.163	0.158
alm	$Fe_2Al_2Si_3O_{12}$	0.144	0.17
py	$Mg_2Al_2Si_3O_{12}$	0.000848	0.00124
gr	$Ca_2Al_2Si_3O_{12}$	0.00617	0.0202
mu	$K_2Al_4(Si_6Al_2O_{20})[OH]_4$	0.261	0.25
cel	$Na_2Al_4(Si_6Al_2O_{20})[OH]_4$	0.331	0.334
qtz	SiO_2	1.0	1.0
H_2O	H_2O	0.3	0.3

Table 3.7: Mineral formulae and activities used to calculate equilibria for metapelite sample 96/69 and metabasite sample 96/149. Activities calculated using Ax software (T. J. B. Holland).

The lawsonite-blueschist and epidote-blueschist sub-facies boundaries, and the lawsonite-blueschist and low-temperature eclogite sub-facies boundaries have been calculated for metapelite and metabasite lithologies from the Tavsanli Zone following

Evans (1990) (Figure 3.13). The four calculated reactions are given in Table 3.8.

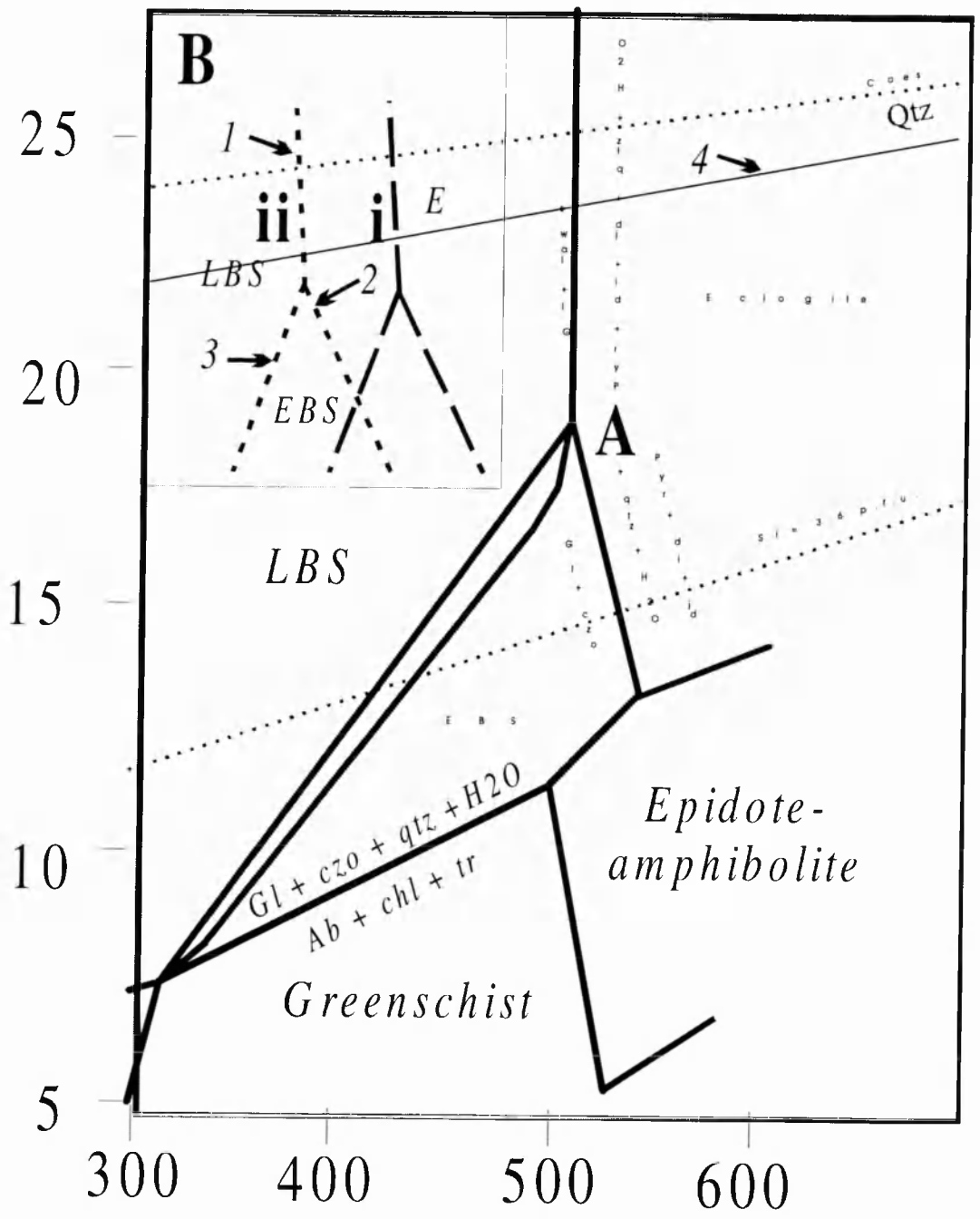

Figure 3.13: P-T diagram illustrating the sub-facies boundaries computed by Evans (1990) (A), with the reactions 1 to 3 of this study highlighted in box B. Abbreviations LBS = lawsonite-blueschist sub facies, and EBS = epidote-blueschist sub-facies. The quartz-coesite transition equilibrium is after Bohlen and Boettcher (1982), the Si in phengite isopleth is according to Massonne and Schreyer (1987). aH_2O = 0.5 for A, and aH_2O = 0.2 for B. i = metabasite sample, ii = metapelite sample.

Where garnet is present in the Sivrihisar rocks the transition from the lawsonite-blueschist sub-facies to the low-temperature eclogite sub-facies is marked by the 'garnet-in' reaction 1. Reaction 2 marks the boundary between the low-temperature eclogite sub-facies and the epidote-blueschist sub-facies, and the appearance of clinozoisite in some Sivrihisar samples. Reaction 3 marks the transition between the epidote-blueschist sub-facies and the lower temperature lawsonite-blueschist sub-facies observed within epidote-bearing assemblages from Sivrihisar. Reaction 4 is calculated for garnet-bearing samples from the Sivrihisar region and is an effective barometer since it has a flat slope in P-T space.

No.	Reaction
1	$4gl + 3law = 3py + 3di + 8jd + 7qtz + 10H_2O$
2	$9py + 12di + 26jd + 19qtz + 16H_2O = 13\ gl + 6cz$
3	$cz + jd + py + qtz + H_2O = gl + law$
4	$py + gr + ccl = di + mu$

Table 3.8: Equilibria calculated for samples 96/69 and 96/149.

Reactions 1 to 3 are strongly temperature dependent and highly sensitive to aH_2O. All end-members are independent of iron and are thus unaffected by the Fe^{3+} content of clinopyroxenes. Reaction 4 is a strongly pressure dependent equilibrium, independent of water activity and iron end-members. Comparison of reactions 1 to 3 calculated for the Sivrihisar rocks, with those computed by Evans (1990), illustrate the effect that increased aH_2O on these equilibria. The petrogenetic grid of Evans (1990) assumes $aH_2O = 0.5$ (Figure 3.13). Water activity is difficult to assess in these rocks, and a

value of $aH_2O = 0.2$ has been assigned based on the positioning of the triple point of reactions 1 to 3, relative to the average pressures obtained using reaction 4, which is *independent* of H_2O. Points *i* and *ii* (Figure 3.13) are calculated for the porphyroblastic metabasite sample 96/149 and the metapelite sample 96/69 respectively, both from the Sivrihisar region. Both *i* and *ii* are approximately 3 kbar higher than the same equilibria calculated by Evans (1990), *i* is 100° C and *ii* 150° C lower than Evans (1990), due to the lower aH_2O. The temperature variations observed between the lithologies are within a ± 50° C error and may be apparent differences rather than real differences.

3.1.5.2 Thermometry

Garnet-clinopyroxene and garnet-phengite thermometry has been applied to suitable assemblages to determine temperatures of metamorphism. Both garnet-clinopyroxene and garnet-phengite thermometry are strongly dependent on Fe^{2+}-Mg^{2+} partitioning. For garnet-phengite thermometry the calibrations of Krogh and Raheim (1978) and Green and Hellman (1982) have been applied; for garnet-clinopyroxene thermometry the calibrations of Ellis and Green (1979), Powell (1985) and Krogh (1988) have been applied. For peak temperatures the highest XMg(grt), lowest XNa(cpx) and lowest XSi(phen) have been chosen from mineral pairs to minimise the likelihood of using points within minerals which reflect equilibration at lower temperatures during exhumation.

The results of the garnet-clinopyroxene thermometry vary significantly with different methods of Fe^{3+} recalculation (Table 3.9). All temperatures which are estimated assuming that all Fe is ferric, are considerably higher than for temperatures estimated following Fe^{3+} calculation in pyroxene according to Cawthorn and Collerson (1974) and Droop (1987) (Table 3.9). Temperature estimates obtained using garnet-phengite thermometry cover a wider temperature range than garnet-pyroxene thermometry (Table 3.10) and is probably due to the inestimable Fe^{3+} within phengite.

In summary temperatures from garnet-clinopyroxene and garnet-phengite thermometry are highly variable, both between calibrations and between samples, as is often observed in HPLT rocks (e.g. Carswell et al., 1997). The spread of temperature estimates in both garnet-clinopyroxene and garnet-phengite calibrations can be attributed to the varying amounts of Fe^{3+} in both clinopyroxene and phengite (Table 3.9). To a certain extent this can be rectified using recalculation methods in clinopyroxenes (see section 3.1.4.4), but cannot be accounted for in phengites.

(Sivrihisar)	**Fe(total) = Fe^{2+}**	**Cawthorn and Collerson (1974)**	**Droop (1987)**
Ellis and Green (1982)	642° - 928° C	482° - 646° C	452° - 641° C
Powell (1985)	623° - 915° C	462° - 625° C	429° - 620° C
Krogh (1988)	542° - 608° C	429° - 600° C	400° - 600°C

(Tavsanli)	**Fe(total) = Fe^{2+}**	**Cawthorn and Collerson (1974)**	**Droop (1987)**
Ellis and Green (1982)	705° - 715° C	498° - 507° C	456° - 463° C
Powell (1985)	685° - 695° C	476° - 484° C	433° - 440° C
Krogh (1988)	444° - 453° C	441° - 452° C	404° - 412° C

Table 3.9: Results of garnet-clinopyroxene thermometry for Sivrihisar samples 96/159, 96/159, 96/149, 96/69, and a single Tavsanli sample – 96/15 -over the pressure range of 18 to 26 kbar using both all iron as ferric, and Fe^{3+} calculated according to Cawthorn and Collerson (1974) and Droop (1987).

	18 - 26 kbar (Sivrihisar)	**18 - 26 kbar** (Tavsanli)
Krogh & Raheim (1978)	460° - 708° C	520° - 565° C
Green and Hellman (1982)	481° - 680° C	535° - 559° C

Table 3.10: Results of garnet-phengite thermometry from Sivrihisar samples samples 96/159, 96/159, 96/149, 96/69, and a single Tavsanli sample – 96/15.

The three garnet-clinopyroxene calibrations have been applied with varying effects. Temperatures using both Ellis and Green (1982) and Powell (1985) exceed garnet-clinopyroxene temperatures using Krogh (1988) by over 100° C, and are also significantly higher than garnet-phengite estimates. Krogh (1988) accounts for Ca^{2+} in the garnet mineral lattice which significantly affects Tavsanli Zone garnets, and is a likely cause of the overestimation of temperatures from Ellis and Green (1982) and Powell (1985). The garnet-phengite temperatures of Green and Hellman (1982) and

Krogh and Raheim (1978) are lower than garnet-clinopyroxene temperature estimates, though are still higher than expected for the Tavsanli Zone according to Okay and Kelley (1994) and Okay et al. (1998). The proportion of Fe^{3+} in phengite is inestimable. If, however, all Fe is assumed ferric in phengites in sample 96/149 then the temperature using both Krogh and Raheim (1974) and Green and Hellman (1982) is 600° C at 23 kbar, whilst assuming Fe(total)=Fe^{2+}(0.6), Fe^{3+}(0.4) the temperature at 23 kbar is reduced to 530° C. Garnet-clinopyroxene and garnet-phengite thermometry indicate that temperatures for the Sivrihisar region are a maximum of 500° to 550° C ± 50° C. Garnet-clinopyroxene thermometric estimates for the Tavsanli region are lower by between 50° and 100° C, but garnet-phengite estimates for the Tavsanli region are within error of those obtained for the Sivrihisar region.

3.1.5.3 Barometry

Metamorphic pressures have been calculated using the garnet-clinopyroxene-phengite barometer of Waters and Martin (1993), which is based on the equilibrium: pyrope + 2grossular = 6 diopside + 3phengite, and uses the self-consistent thermodynamic dataset of Holland and Powell (1998). To avoid retrograde re-equilibration at lower pressures, the highest XCa(grt), XNa(cpx) and XSi(phen) points have been chosen from mineral pairs. Results of garnet-clinopyroxene-phengite barometry are presented in Table 3.11.

(Sivrihisar)	**Fe(total) = Fe^{2+}**	**Cawthorn and Collerson (1974)**	**Droop (1987)**
Waters and Martin (1993)	27.7 to 33.6 kbar	23.0 to 26.9 kbar	19.4 to 26.9 kbar
(Tavsanli)	**Fe(total) = Fe^{2+}**	**Cawthorn and Collerson (1974)**	**Droop (1987)**
Waters and Martin (1993)	23.0 to 23.2 kbar	17 kbar	13.8 to 14 kbar

Table 3.11: Garnet-clinopyroxene-phengite barometric estimates for Sivrihisar (samples 96/158, 96/159, 96/149 and 96/69) and a single Tavsanli Zone sample (96/15) over a temperature range of 400° to 550° C.

Pressure estimates for the Tavsanli Zone are less complex than temperature estimates, but results are still highly sensitive to Fe^{3+} recalculation methods (Table 3.11).

3.1.5.4 Pitfalls of thermobarometry in Tavsanli Zone rocks

Thermobarometry in HP-LT rocks is complicated by the major element chemical heterogeneity resulting from both the low temperatures and limited fluid levels during formation, and also by the difficulty in assessing aH_2O. The specific problems encountered whilst attempting to assess the thermobarometric conditions of the Tavsanli Zone samples are the uncertainty surrounding the water activity, the uncertainty surrounding the ratio of ferric to ferrous iron in a variety of minerals, and the strong major element chemical zoning in garnet.

Garnet-clinopyroxene and garnet-phengite thermometers are readily applied to HP-LT rocks since garnet, phengite and clinopyroxene are all relatively common, and only two of the three are required to extract temperatures. The disadvantages are, however, the reliance upon the exchange of Fe^{2+} and Mg^{2+}. Fe^{3+} may be present within garnet, clinopyroxene and phengite but no thermodynamic data is available for the Fe^{3+}-bearing end-members so that it is impossible to take account of them in thermometric equations. If however a percentage of Fe^{2+} is assumed to be Fe^{3+} in a given mineral then the temperatures obtained are erroneously elevated. The garnet-phengite method assumes that all iron in phengite is Fe^{2+}, though according to figure 3.12 there is a significant proportion of Fe^{3+} within phengite. The same is true of garnet-clinopyroxene thermometry in that all iron is assumed to be Fe^{2+}, which according to the various recalculation methods applied to clinopyroxene microprobe analyses is not the case. In the event that the percentage of Fe^{2+} is reduced to accommodate a proportion of Fe^{3+}, the estimated temperatures rise.

The garnet-phengite-clinopyroxene barometer is extremely sensitive to Fe^{3+} in clinopyroxene. The pressures vary within one sample by 8 kbar depending on whether all iron is assumed to be Fe^{2+}, or whether an assumption is made on the amount of Fe^{3+} in clinopyroxene, based on the various Fe^{3+} recalculation methods (see section 3.1.1.4). Both the temperatures and pressures calculated using methods that are heavily dependent on iron-bearing phases are only as good as the Fe^{3+} estimation will allow. In the absence of Mössbauer spectroscopy, which enables a quantitative assessment of the Fe^{2+}/Fe^{3+}, it is reasonable to assume that all temperatures calculated

in samples known to contain Fe^{3+} are maximum temperatures.

The Thermocalc approach (Holland and Powell, 1998) avoids the problem of Fe^{2+}/Fe^{3+} estimation to a certain extent by accounting for all components in all the phases which are in equilibria. The problems in applying this technique to the rocks of the Tavsanli Zone, and indeed other HP-LT rocks, is the difficulty in assessing exactly which phases are in equilibrium. A further problem, which has proved more pertinent in the Tavsanli Zone rocks, is the assessment of aH_2O. Reaction 4 on figure 3.13 is a barometer which has the advantage of avoiding hydrous phases such as lawsonite, epidote and amphiboles, which are very sensitive to aH_2O. Reactions 1, 2 and 3 however do not avoid such phases and are problematic. The three sub-facies boundaries that have been calculated (Figure 3.13, Table 3.8) are highly sensitive to aH_2O, and in the absence of an independent reaction such as reaction 4, could be positioned anywhere between 350° C and 600° C depending on the assumed aH_2O.

Finally the success of both Fe^{2+}/Mg^{2+} exchange thermometry and Thermocalc are dependent on understanding which minerals, or parts of minerals, are in equilibrium. The best estimate of peak conditions possible in strongly zoned minerals where equilibrium may or may not be represented, it to choose the highest XMg(grt), lowest XNa(cpx) and lowest XSi(phen) points (Carswell et al. 1997). It must be stressed, however, that the results may only be considered maximum estimates.

3.1.6 P-T paths

The general form of the P-T path may be determined on the basis of the observed parageneses and mineral growth sequences in metachert/metapelite and metabasite samples (Figure 3.14).

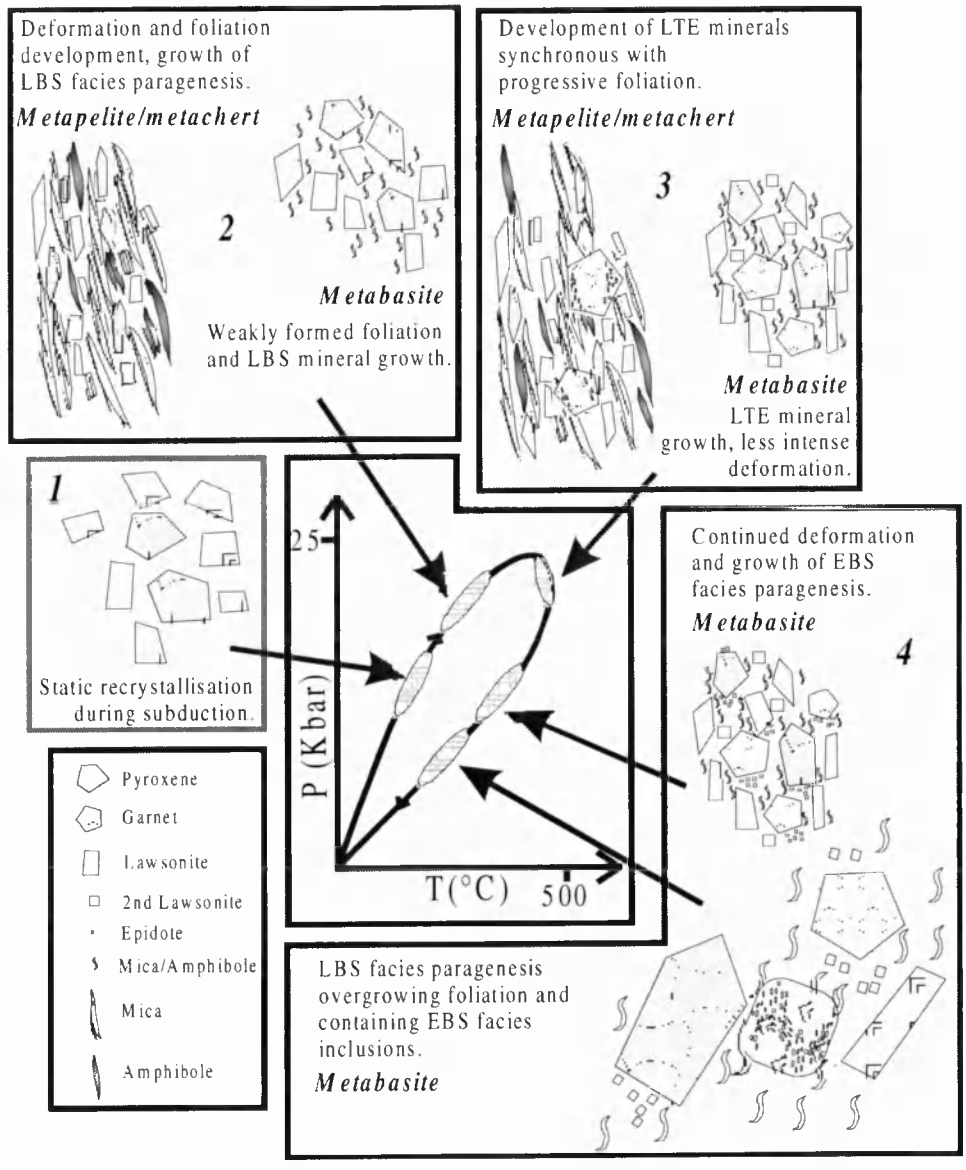

Figure 3.14: Schematic summary of the assemblages and textures used to determine the form of the P-T path.

From static recrystallisation in the subducting slab, the rocks then undergo deformation in the lawsonite-blueschist sub-facies where lawsonite and glaucophane grow and are observed as inclusions within subsequent low-temperature eclogite facies minerals. In the metapelites, where deformation is more intense, garnet rims grow synchronous with deformation and include sodic pyroxene, sodic amphibole and lawsonite. Textural evidence for a passage through the epidote-blueschist sub-facies is in the form of ultra fine-grained epidote forming in the pressure shadows of garnet and pyroxene porphyroblasts in the metabasite lithology. Subsequent to this lawsonite porphyroblasts which contain inclusions of epidote, sodic-amphibole and sodic-pyroxene overgrow the main foliation and serve as evidence for the rocks passing from the epidote-blueschist sub-facies into the lawsonite-blueschist sub-facies.

From this combined approach it is possible obtain a P-T path in a region where Fe^{3+} is variable and aH_2O is difficult to estimate. In calculating the three reactions which correspond to the lawsonite-blueschist/low-temperature eclogite-facies/epidote-blueschist sub-facies boundaries it is possible to track the evolution of Tavsanli and Sivrihisar samples without depending on estimates of absolute pressure and temperature. This approach is advantageous in avoiding Fe end-members, and is based upon the most recent internally consistent thermodynamic data set (Holland and Powell, 1998). The transition from the lawsonite-blueschist into the low-temperature eclogite sub-facies, corresponding to the 'garnet-in' reaction, is crossed with increasing pressure and temperature at approximately 400° C in the Sivrihisar samples, and 350° to 375° C in the Tavsanli sample (Figure 3.15).

Minimum peak pressures are 23 kbar, as is indicated by reaction 4 on Figure 3.13 and Figure 3.15. From textural relations (see section 3.1.3) it is apparent that phengite growth occurred post-peak pressure, and is likely to have partially re-equilibrated at lower pressures during uplift. Estimated pressures are therefore a minimum, a feature common to many high and ultra-high pressure metamorphic terranes (e.g Okay, 1993). Peak temperatures in Sivrihisar are a maximum of 550° C based on thermometric estimates and more qualitatively, on the upper stability limit of natural glaucophane (Maresch, 1977) which is a mineral common to each stage of the metamorphic evolution. Samples in both the Sivrihisar and Tavsanli regions have moved down-temperature and pressure into the lawsonite-blueschist sub-facies. Some Sivrihisar samples such as 96/69 and 96/149 show evidence of passing through the epidote-blueschist sub-facies.

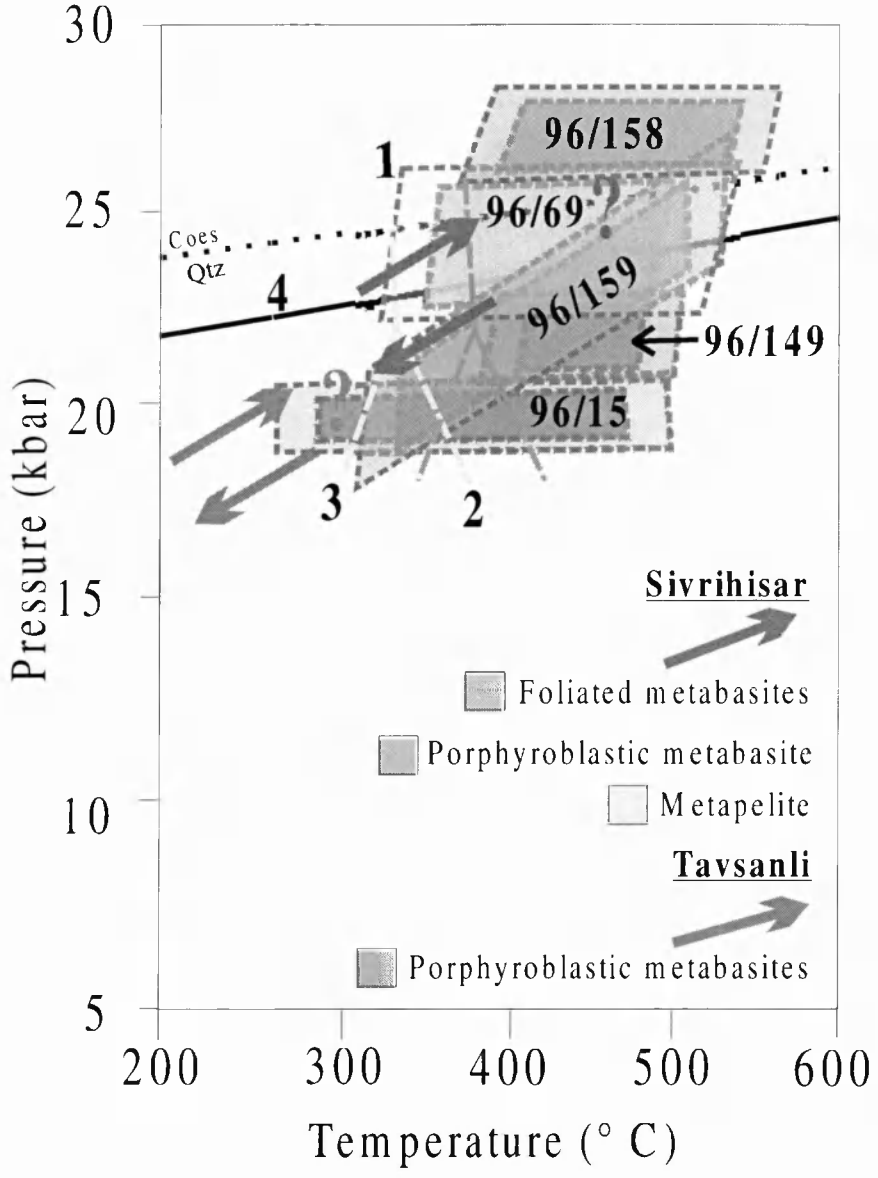

Figure 3.15: P-T boxes and sub-facies boundaries for the Sivrihisar and Tavsanli regions.

Petrographic observations and the reaction equilibrium in the NCMASH system, place conditions of metamorphism in the Sivrihisar region in the range 20 to 24 kbar and 420° to 380° C for the basites, and 400° to 350° C for the metapelite. The same approach applied to the single garnet-bearing sample from the Tavsanli region

suggests that return to the lawsonite-blueschist sub-facies took place at approximately 375° to 400° C and 18 to 20 kbar.

3.1.7 Discussion

Both the Tavsanli and Sivrihisar regions have undergone a single Franciscan-type PT path (Figure 3.16).

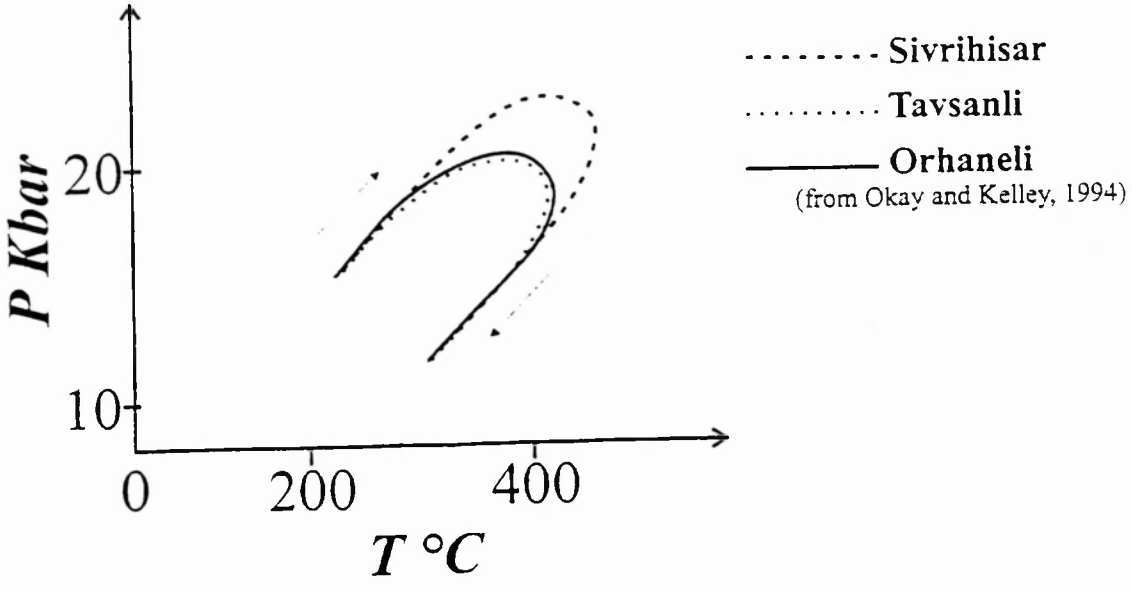

Figure 3.16: P-T paths for the Sivrihisar and Tavsanli regions, with the Orhaneli P-T path of Okay and Kelley (1994) for comparison.

Steady-state conditions and low shear stresses within the subduction zone are necessary to achieve the high dP/dT ratio observed within the Tavsanli Zone (e.g. Peacock, 1992; 1996). Steady state conditions only fully develop within a subduction

zone after 5 to 20 Ma of subduction (Peacock, 1996) and thus if subduction initiated at approximately 100 Ma (Sengör and Yilmaz, 1981; Okay et al., 1998) and white mica crystallisation occurred at 80 Ma (Sherlock et al., submitted a), subduction must have been taking place for at least 20 Ma, which is sufficient for steady-state conditions to have developed.

From an amalgamation of petrographic relationships, thermobarometric estimates and the positioning of pertinent reaction equilibria in PT space, it is evident that the retrograde P-T paths of both the Tavsanli and Sivrihisar regions closely mirror the prograde path. This is consistent with syn-subduction exhumation and 'retrograde refrigeration' which is necessary to maintain the depressed geotherms within the subduction zone and prevent a temperature increase during exhumation (Ernst and Peacock, 1996).

3.1.8 Conclusions

All three regions of the Tavsanli Zone have undergone a single clockwise, Franciscan-type P-T evolution which is characterised by a low dT/dP ratio, and consistent with syn-subduction exhumation and retrograde refrigeration. An initial lawsonite-blueschist sub-facies static recrystallisation consistent with low shear stresses within the subduction zone is observed in some lithologies, whilst peak conditions were achieved in the lawsonite-blueschist sub-facies or the low-temperature eclogite sub-

facies. The retrograde path illustrates the absence of heating following peak burial conditions, which requires the 'retrograde refrigeration' achieved by syn-subduction exhumation.

3.2 Oscillatory-zoned chrome lawsonite in the Tavsanli Zone of Northwest Turkey.

3.2.1 Introduction

Lawsonite is a mineral found within a variety of metavolcanic and metasedimentary lithologies, that have undergone high-pressure low-temperature (HPLT) conditions of metamorphism. Recent experiments have shown that lawsonite is stable to 120 kbar and 960° C - conditions which occur in the subducting slab (Schmidt, 1995). The general structure of lawsonite as $CaAl_2[Si_2O_7](OH)_2.H_2O$ was first determined by Wickmann (1947), and later redefined by Bauer (1978). Lawsonite rarely deviates from the ideal composition, and experiences no changes in the lattice structure during subduction (Comodi and Zanazzi, 1996). To our knowledge there is only one other reported occurrence of chromium lawsonite, within a Cr-rich metagabbro in the Piemont zone, western Alps (Mevel and Kienast, 1980). Within the Tavsanli Zone of northwest Turkey oscillatory zoned lawsonite occurs within blueschist-facies metabasites from a small region of high-pressure low-temperature (HPLT) rocks.

The aim of this paper is to describe a first occurrence of Cr in lawsonite from the Tavsanli Zone in northwest Turkey, and more importantly the first occurrence of oscillatory zoning recorded in lawsonite. Oscillatory zoning is commonly described in magmatic minerals such as pyroxenes and feldspars (Shore and Fowler, 1996). Both extrinsic and intrinsic mechanisms have invoked oscillatory zoning in magmatic minerals. Extrinsic mechanisms require differences in pressure, temperature or chemical composition in a convecting magma chamber or solution (e.g. Bowen, 1928). Intrinsic mechanisms invoke a feedback mechanism between a growing crystal and narrow fluid margin, which is depleted in growth constituents with respect to the bulk liquid, at the crystal-fluid interface (e.g. Shore and Fowler, 1996).

3.2.2 Occurrences of oscillatory zoning in metamorphic minerals

Mechanisms for oscillatory zoning in metamorphic minerals are less well documented. Oscillatory zoned prehnite and epidote from an active geothermal field in Costa Rica is thought to be the result of fluctuations of $a(Fe^{3+})$ in the fluid due to rapid changes in redox state in the fluid (Yardley et al., 1991). Oscillatory zoned pyroxenes from Fraser Mine, western Australia, may be due to externally imposed changes in the composition of an infiltrating fluid, or due to changes in the rate of fluid flow (Yardley et al., 1991). Oscillatory zoned pyroxene from a bedded rock unit within the Connemara marble have grown metasomatically due to the interaction of infiltrating quartz-saturated fluid with dolomite (Yardley et al., 1991). Garnets in skarn deposits have been described in

a contact metamorphic environment as a result of complex epitaxial growth in addition to changing fluid compositions (Jamtveit, 1991; Jamtveit et al., 1993). Finally, complex oscillatory zoned plagioclase is described in a calcic pelitic schist from South Stafford, Vermont, which preserves almost an entire compositional range of plagioclase compositions from core to rim, due at least in part to plagioclase overgrowing a heterogeneous matrix of crenulated muscovite (Menard and Spear, 1996).

3.2.3 Geological setting

The lawsonites described here are found within the Tavsanli Zone of northwest Turkey. The Tavsanli Zone is an east-west trending linear tract of HPLT rocks, lying south of the major Izmir-Ankara suture (Figure 3.17). The suture is one of many found within the Alpine-Himalayan orogenic chain and represents the site of a major northeast-directed oblique subduction zone responsible for the consumption of the Tethys Ocean during the Cretaceous (Okay, 1989). The Tavsanli Zone comprises sedimentary and volcanic rocks, which have been metamorphosed in the blueschist- and low-temperature eclogite-facies, and are subducted remnants of the passive continental margin of the Anatolide-Tauride platform. Rb-Sr white mica ages for the subduction-related HPLT metamorphic event are approximately 80 Ma (Sherlock et al., submitted). Pressures and temperatures of metamorphism are estimated to be in the region of 24 kbar and 400° to 450° C (Sherlock et al. submitted b).

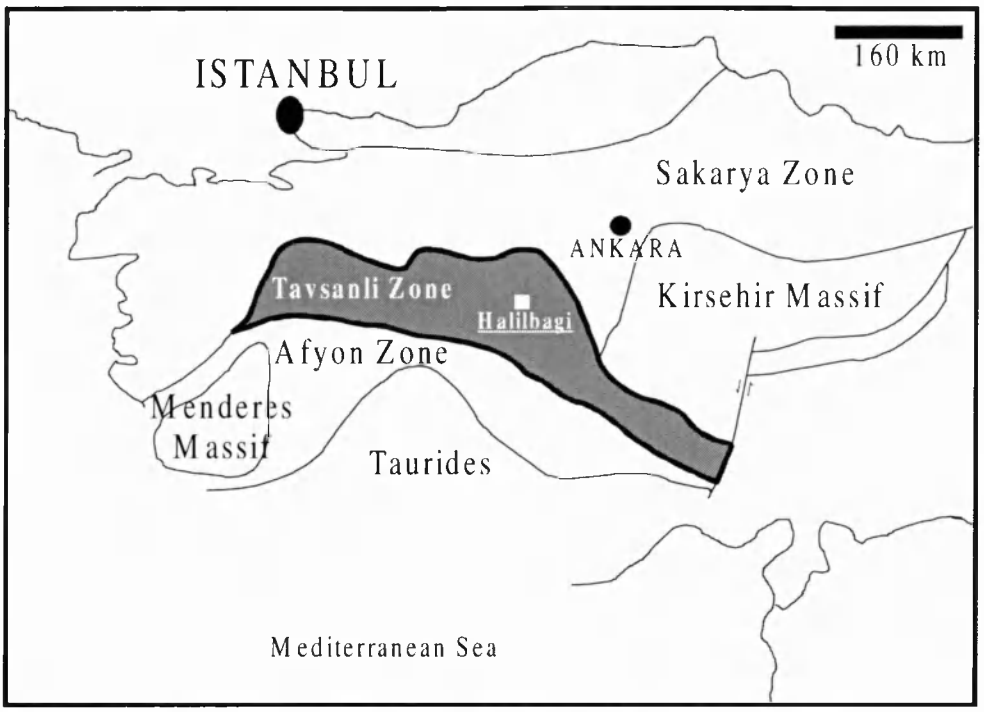

Figure 3.17: Location map of Halilbagi, in the Tavsanli Zone.

Within the Halilbagi region in the east of the Tavsanli Zone (Figure 3.17) there is a small region of intercalated marble, metachert, foliated metabasites, metapelites and poorly foliated porphyroblastic metabasites that have undergone HPLT metamorphism. From these metabasic lithologies with a volcanic protolith have been collected which contain the unusual oscillatory zoned Cr-lawsonite.

3.2.4 Sample description

Samples 96/152 and 96/67 are foliated metabasites with the assemblage lawsonite ± clinopyroxene ± sodic amphibole + white mica + apatite + calcite + chlorite ± titanite + talc. Within sample 96/152 pre-kinematic lawsonites and clinopyroxenes are sub-

idioblastic and reach a maximum diameter of 500 microns. White mica and a second clinopyroxene are finer grained and form the dominant fabric which wraps the lawsonite and clinopyroxene grains. Apatite is a common accessory mineral, and there is evidence of late alteration in the form of fine-grained chlorite, talc and calcite. Sample 96/67 is a compositionally banded metabasite, with bands rich in sub-idioblastic lawsonite of up to 300 microns in diameter, and fine-grained sodic amphibole and white mica. Titanite is a common accessory phase and fine-grained talc is a late alteration product.

Average chemical analyses are presented in Table 3.12, and have been determined using a Cameca SX100 electronprobe microanalyser at the Open University, with a 20 kV accelerating voltage, 20 nA beam current and a spot size of 10 microns.

3.2.5 Mineral chemistry

Amphiboles in sample 96/67 reach a maximum of 150 microns in diameter and are both optically and chemically zoned. Average compositions are glaucophane and are chrome-free; grains have lilac blue cores and dark blue rims corresponding to glaucophane-rich cores and ferroglaucophane rims after the amphibole classification of Leake et al. (1997). Fe^{3+} in amphibole has been determined according to the recalculation method of Okay (1980b). The core-rim optical zoning observed in amphiboles corresponds to decreasing Mg^{2+} and increasing Fe^{2+} from core to rim, with

an overall decrease in Al^{3+} and corresponding increase in Fe^{3+}. In sample 96/152 the pre-kinematic sub-idioblastic clinopyroxenes are more augitic and with a jadeite component of $Jd_{(21)}$, whilst later syn-kinematic clinopyroxenes are much finer grained, less augitic and with a higher jadeite component of $Jd_{(23)}$. Both clinopyroxene generations contain Cr; pre-kinematic grains contain an average of 0.30 wt %, whereas syn- to post-kinematic grains have a lower concentration of 0.19 wt %. Syn- to post-kinematic white micas, which are aligned with the main foliation are phengitic, with average Si = 3.70 and 3.58 in samples 96/152 and 96/67 respectively.

	Amph	**Cpx**		**Law**		**Mica**		**Talc**	
	67	**152 (1)**	**152 (2)**	**152**	**67**	**152**	**67**	**152**	**67**
SiO_2	56.65	54.79	54.36	37.05	39.30	57.33	52.65	60.15	61.78
Al_2O_3	5.83	4.83	5.40	26.25	25.00	14.83	21.82	0.70	0.68
Cr_2O_3	0.00	0.33	0.19	3.62	6.40	0.07	0.30	0.04	0.01
Fe_2O_3	7.48	7.52	9.36	0.00	0.00	0.00	0.00	0.00	0.00
FeO	13.3	3.52	2.04	1.41	1.90	4.80	3.86	6.13	6.83
MnO	0.29	0.18	0.16	0.04	0.03	0.03	0.04	0.05	0.14
MgO	7.74	9.87	8.50	0.00	0.03	13.52	4.81	24.77	27.22
CaO	0.68	12.39	13.40	16.72	16.90	0.00	0.02	1.73	0.03
Na_2O	6.20	6.13	6.57	0.03	0.01	0.22	0.08	0.59	0.03
K_2O	0.04	0.01	0.00	0.00	0.01	6.73	10.86	0.03	0.01
Total	98.27	99.48	99.98	87.97	89.72	97.50	94.44	94.11	96.73
Si	8.05	2.01	1.99	3.20	3.27	3.70	3.58	7.96	7.94
Al	0.98	0.21	0.23	2.67	2.44	1.15	1.75	0.11	0.11
Cr	0.00	0.01	0.01	0.25	0.43	0.00	0.02	0.01	0.00
Fe^{3+}	0.81	0.21	0.26	0.00	0.00	0.00	0.00	0.00	0.00
Fe^{2+}	1.58	0.11	0.06	0.10	0.14	0.13	0.22	0.68	0.73
Mn	0.04	0.01	0.01	0.00	0.00	0.00	0.00	0.01	0.02
Mg	1.04	0.54	0.46	0.00	0.00	1.32	0.48	4.89	5.21
Ca	0.10	0.48	0.52	1.43	1.50	0.00	0.00	0.25	0.01
Na	1.71	0.44	0.47	0.00	0.00	0.03	0.01	0.15	0.01
K	0.00	0.00	0.00	0.00	0.00	0.57	0.94	0.01	0.00
Total	14.90	4.00	4.01	7.65	7.78	6.91	6.92	14.07	14.01
Jd		21	23						
Ac		23	24						
Aug		56	53						

Table 3.12.: Representative chemical analyses of minerals from samples 96/152 and 96/67.

Micas in sample 96/152 do not contain measurable Cr; whereas micas in sample 96/67 contain (on average) 0.3 wt %.

3.2.6 Chrome lawsonite

Lawsonites are idioblastic to sub-idioblastic squat prismatic grains, compositionally ideal with the exception of the presence of Cr^{3+}. On average sample 96/67 has twice the abundance of Cr – 6.40 wt. % - compared with 3.62 wt. % in sample 96/152. In both samples 96/67 and 96/152 Cr^{3+} is oscillatory zoned and varies antithetically with Al. Figure 3.18 illustrates the Cr^{3+}-Al^{3+} substitution in lawsonites from both samples.

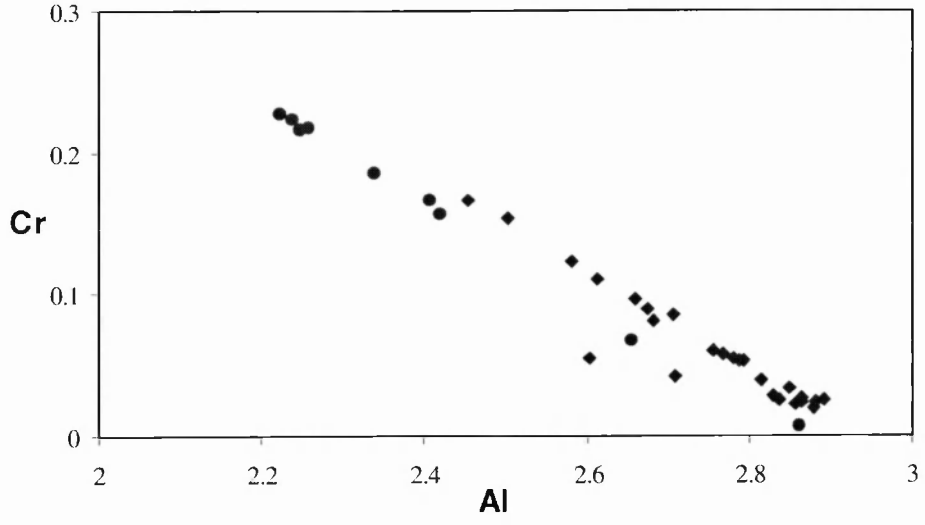

Figure 3.18: Al^{3+}/Cr^{3+} substitution diagram plotted for lawsonites from samples 96/67 (circles) and 96/152 (squares).

In both samples oscillatory zoning is concentric. In sample 96/152 oscillatory zoning in lawsonite persists from core to rim (Figure 3.19a). In sample 96/67 cores are oscillatory zoned with a monotonically zoned outer margin (Figure 3.19b). In both

samples Cr^{3+} and Al^{3+} co-fluctuate on a sub-10 micron level. There are no further compositional variations, lawsonite is either ideal or it contains Cr^{3+}.

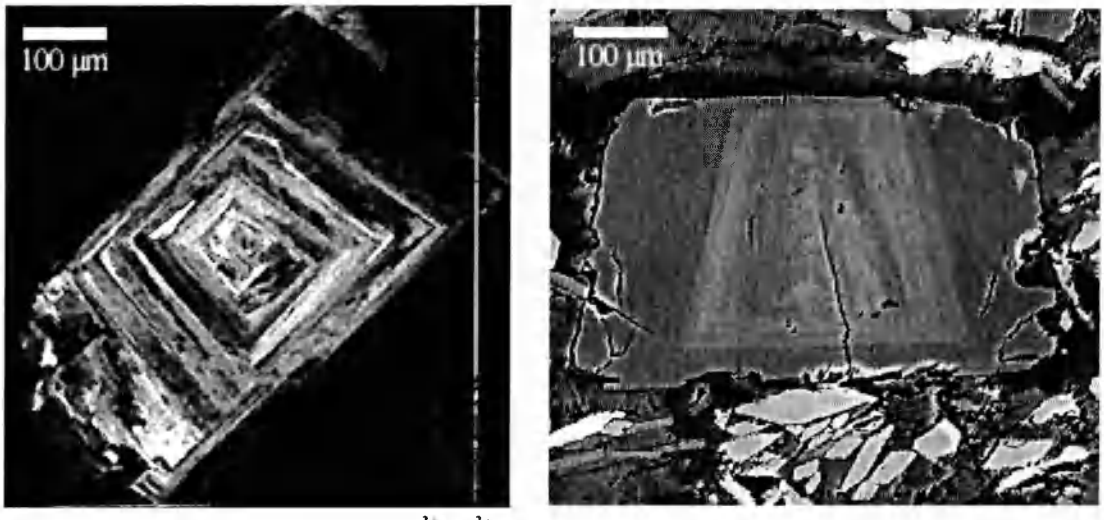

Figure 3.19: Images of oscillatory Cr^{3+}/Al^{3+} zoning in lawsonite in a) X-ray map of Cr, sample 96/152 and b) backscattered electron image, sample 96/67.

3.2.7 Discussion

Within the Tavsanli Zone the only lawsonites which are oscillatory zoned are those within metabasites characterised by a high bulk Cr_2O_3. The pre-kinematic pyroxenes were originally igneous, and were topotactically replaced by sodic pyroxene during the static recrystallisation in the subducting slab (Okay, 1980a). Cr^{3+} is likely to have been inherent in the igneous pyroxene. Pre-kinematic lawsonite is therefore likely to have been formed during the same static event during subduction. Since coexisting phases show no significant zoning the oscillatory zoning in lawsonite is unlikely to be the result of rapidly changing externally controlled parameters such as pressure and temperature. Detailed P-T analyses suggest that steady-state conditions prevailed

during subduction (Sherlock et al., submitted b) which preclude any rapid or fluctuating changes in temperature and pressure as a possible mechanism. In this case the Cr in lawsonite will have originated from chromite grains in the protolith, with the oscillatory zoning resulting from fluid/rock interaction.

Fluids originating from the subduction and consequent dehydration of sediments and volcanics may well have interacted with lawsonite during growth. In particular Cr^{3+} originated from chromites within the volcanic protoliths, which then substituted for Al^{3+} in lawsonite. The oscillatory nature of the zoning may have been achieved by local fluid buffering by chromite grains and slow equilibration at the fluid-crystal interface. A second mechanism may be a result of fluctuating fO_2. Oxygen fugacity is a locally buffered component (e.g. Chinner, 1960; Greenwood, 1975). Previous studies in the Tavsanli Zone illustrate that changing fO_2 determines the Fe^{2+}/Fe^{3+} ratio in the sodic amphiboles (Okay, 1980b), producing the same compositional zoning as is observed in amphiboles in sample 96/67, indicative of reduction during amphibole growth. It may be possible that the Cr^{2+}/Cr^{3+} is similarly affected and whilst fluid is oxidising a high Cr^{3+}/Al^{3+} substitution is facilitated in lawsonite.

Syn-kinematic phengites in sample 96/67 and clinopyroxene in sample 96/152 contain minor quantities of Cr^{3+} which may be a result of later remobilisation of Cr^{3+} during the higher temperatures following peak-pressure conditions, and associated with the onset of exhumation.

3.2.8 Conclusions

The first recorded oscillatory zoning in lawsonite occurs in metabasite lithologies from the Halibagi region of the Tavsanli Zone in northwest Turkey. Cr^{3+}/Al^{3+} substitution is responsible for the zoning. Fluids, which most likely originate from the dehydration of subducting sediments and volcanic rocks are either locally buffered by chromite in the volcanic protolith, or changes in fO_2 which have already been described in the Tavsanli Zone (Okay, 1980b) may be responsible for fluctuations in $a(Cr^{3+})$. Sodic pyroxenes which formed topotactically from pre-existing magmatic pyroxenes do not display oscillatory zoning, it has been suggested that hydrous phases such as amphibole and in this case lawsonite, are more highly susceptible to fO_2 fluctuations than anhydrous phases such as pyroxene (Okay, 1980b). Adjacent lawsonite-bearing metachert and metapelite lithologies neither contain any Cr^{3+} or oscillatory zoned lawsonites. It is suggested that oscillatory zoning in lawsonite is a primary metamorphic feature culminating from quantities of Cr^{3+} in the protolith and local fluid conditions.

3.3 Are parts of the Tavsanli Zone relic ultra-high pressure metamorphic fragments?

3.3.1 Introduction

Ultra-high pressure metamorphic terrains are characterised by the presence of coesite. Coesite is a rare high-pressure silica polymorph indicative of crustal rocks having been buried to depths of 100 km within the crust and rapidly exhumed. There are few reported ultra-high pressure (UHP) metamorphic terrains and as yet there are no reported occurrences related to the subduction of the Tethys Ocean. The Western Gneiss region of Norway, the Kokchetav region in Kazakhstan, Dabie Shan of Eastern China, the Western Alps and the Bohemian massif, Eastern Europe are the known occurrences of UHP metamorphic rocks. The common denominators are that these crustal rocks are cold and dry supracrustal rocks that have undergone high-temperature metamorphism and often anatexis prior to UHP metamorphism (Coleman and Wang, 1995).

In the following sections, evidence is presented and discussed both for and against the hypothesis that the rocks in Halilbagi from the Sivrihisar region of the Tavsanli Zone have undergone UHP metamorphism.

3.3.2 The significance of coesite in metamorphic terranes

Coesite is the ultra-high pressure SiO_2 polymorph and the quartz/coesite transition is a solid-solid phase transformation which is a flat-lying and strongly pressure dependent equilibrium in P-T space. The position of the equilibrium in P-T space has been experimentally determined (Figure 3.20), and although well-constrained at

temperatures above 500° C and pressures of 26 kbar (Bose and Ganguly, 1995), only Bohlen and Boettcher (1982) have constrained the phase transition below these pressures and temperatures.

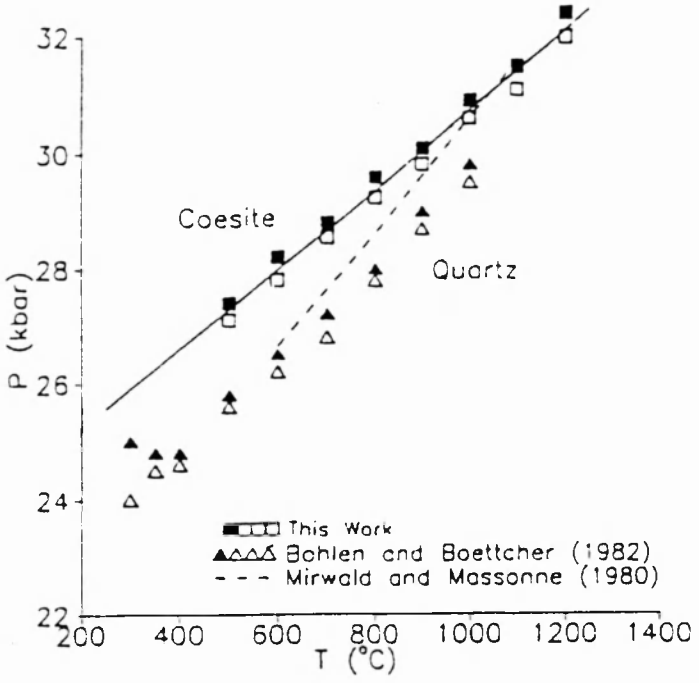

Figure 3.20: Experimentally determined quartz-coesite equilibrium, from Bose and Ganguly (1995).

Coesite in crustal rocks was first recorded as relic inclusions in garnet in whiteschists from the Western Alps by Chopin (1984). Prior to this all naturally occurring examples had only been found in association with impact craters (e.g. Chao et al., 1960). Coesite has currently been identified as relic inclusions in clinopyroxene from the Western Gneiss Region of Norway (Smith, 1984; Wain, 1997), in zircon grains from the Kokchetav Massif, Northern Kazakhstan (Sobolev et al., 1991), and in two regions of the Dabie Shan Mountains, China (Okay et al., 1989; Wang et al., 1989). In the Tavsanli Zone coesite has not been reported, and the maximum pressures of metamorphism have always been regarded as 20 ± 2 kbar (Okay and Kelley, 1994,

based on rocks from the Orhaneli region) significantly lower than the quartz/coesite transition.

3.3.3 Thermobarometric evidence for ultra-high pressures in the Tavsanli Zone?

Sherlock et al. (submitted b) detail the thermobarometric evolution for the rocks of the Tavsanli Zone. There is no *a priori* reason to suspect that the rocks of either the Orhaneli region in the west or the Tavsanli region in the central Tavsanli Zone have ever achieved pressures within the coesite stability field. The rocks from the Sivrihisar region, however, yield a range of barometric estimates, many of which are in the coesite stability field. Table 3.11 on page 88 lists the pressures determined for the Sivrihisar region using the Waters and Martin (1993) garnet-clinopyroxene-phengite barometer. Pressures are strongly dependent on the Fe^{2+}/Fe^{3+} ratio, and are in the range 27.7 to 33.6 kbar assuming no Fe^{3+}, 23.0 to 26.9 kbar using Fe^{3+} the recalculation method of Cawthorn and Collerson (1974), and 19.4 to 26.9 kbar using the Fe^{3+} recalculation method of Droop (1987). In the absence of an accurate determination of the Fe^{2+}/Fe^{3+} ratio it is only possible to infer that pressures assuming no Fe^{3+} are maxima, while the lower estimates using the methods of both Cawthorn and Collerson (1974) and Droop (1987) are minima. Pressures estimated using the strongly pressure-dependent reaction 4 in Table 3.8 on page 83 are a minimum of 23 kbar. All pressures are calculated using equilibria which are strongly dependent on phengite, and according to textural observations phengite is a retrograde phase. So on this basis also, all calculated equilibria must be considered as minimum estimates (e.g.

Okay, 1993). The pressure ranges straddle the quartz/coesite transition in the temperature range 400° to 500° C.

3.3.4 Optical evidence for ultra-high pressures in the Tavsanli Zone?

Sample 96/69 is a low-temperature eclogite facies metapelite, with the assemblage quartz + garnet + sodic-amphibole + sodic-pyroxene + lawsonite + phengite + chlorite. The metapelite is strongly foliated and has undergone subsequent deformation, resulting in tight folding of the main foliation. The main foliation is defined by aligned sub-idiomorphic to idiomorphic sodic-amphibole, sodic-clinopyroxene, lawsonite and minor phengite. Poikiloblastic garnets of up to 600 μm diameter contain an inclusion suite predominantly of quartz with minor apatite, sodic-amphibole and lawsonite. Garnet is almandine-rich ranging from 51-56 mol % of the end-member, the remainder being 21-26 mol % spessartine and 18-29 mol % grossular and 4-10 mol % pyrope. Reverse growth zoning is preserved within garnet, indicating that temperatures were not sufficiently high for homogenisation. The coarsest α-quartz inclusion (approximately 100 μm in diameter) contains a 20 μm inclusion of SiO_2 which is higher in both density and relief than the surrounding quartz, and displays the feathery texture observed in coesite relics and described by Chopin (1984) (Figure 3.21). Figure 3.22 is a photograph of the 20 μm SiO_2 inclusion in reflected light, and illustrates the higher relief of the 20 μm inclusion in comparison to the 100 μm host quartz inclusion. The higher density of the 20 μm SiO_2 inclusion is illustrated by the backscattered electron image, Figure 3.21.

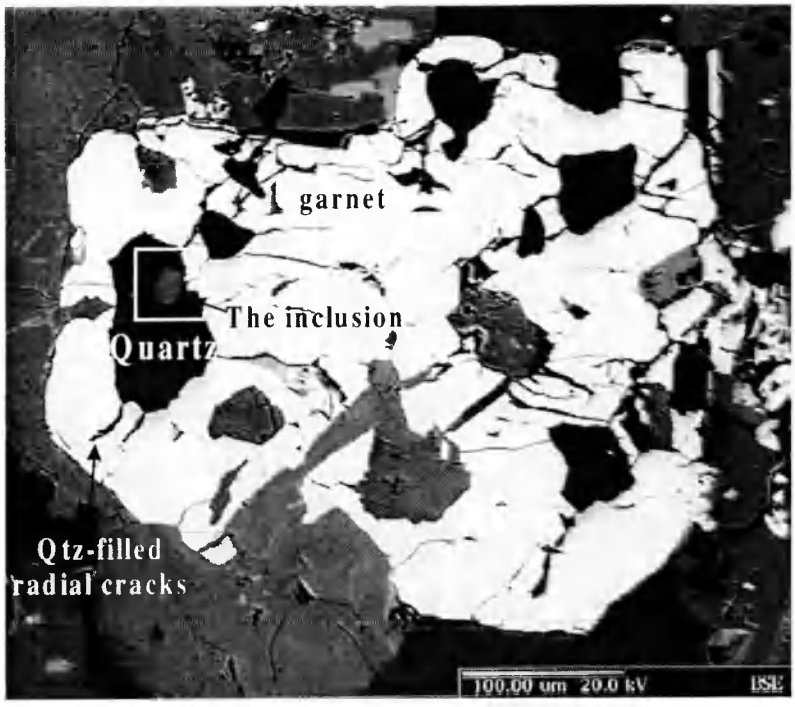

Figure 3.21: Backscattered electron image of garnet in sample 96/69 with quartz inclusion containing the 20 μm SiO_2 inclusion.

A diagnostic feature common to all reported relic coesite are radial cracks surrounding the host inclusion, which are filled with α-quartz rather than a late alteration product such as chlorite or white mica. In sample 96/69 radial cracks surrounding quartz inclusions are filled with quartz (Figure 3.21).

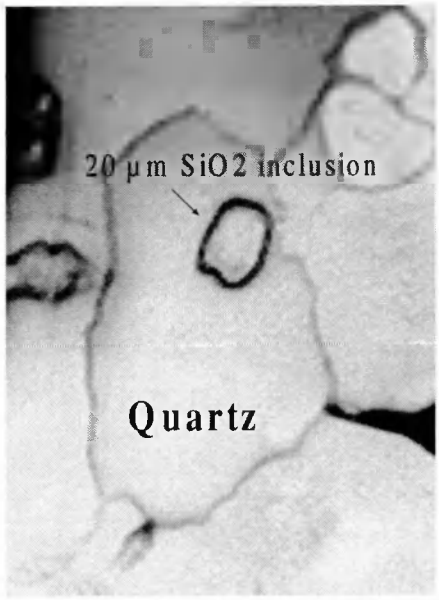

Figure 3.22: Photograph in reflected light of the 20 μm SiO_2 inclusion within the quartz inclusion shown in figure 3.21.

The traditional view of this has been that it is unequivocal proof of the prior existence of coesite.

During rapid decompression radial cracks form in response to the contrasting elastic properties of quartz and garnet, and the large volume increase of the inclusion which takes place during the phase transition from coesite to quartz (van Der Molen et al., 1986).

Wendt et al. (1993) state that radial cracks around quartz are not indicative of a phase transformation from coesite to quartz, and they may occur when initial inclusion pressures are greater than 10 kbar. The appearance of radial cracks is dependent on the component of isothermal compressibility within the retrograde P-T path (Figure 3.19). Either the radial cracks in the Sivrihisar samples occurred at high pressures and as a result of the coesite to quartz transition, or they occurred at low pressures conforming to the model of Wendt et al. (1993).

3.3.5 Microraman spectroscopy of sample 96/69 from the Tavsanli Zone

Historically quartz and coesite have been differentiated using Raman spectroscopy. Micro-Raman spectroscopy has been applied at the University of Southampton Department of Geology, to the 20 μm inclusion within the α-quartz inclusion with garnet. The analysed regions within the quartz inclusions in garnets from sample 96/69 are all α-quartz.

3.3.6 Discussion

There is evidence both for and against the rocks from the Sivrihisar region of the Tavsanli Zone experiencing UHP metamorphic conditions. Thermobarometry is problematic in HPLT assemblages due to the chemical disequilibrium and the strong mineral zoning inherent in a low-temperature and low-aH_2O system (e.g. Carswell et al., 1997). The range of pressure estimates obtained from the Sivrihisar rocks of the Tavsanli Zone attest to this. The fact remains that the pressure estimates straddle the coesite/quartz phase transition equilibria and are not conclusive. Similarly the presence of quartz-filled radial cracks around quartz inclusions within garnet are inconclusive. Regarding the physical evidence for the existence, or not, of coesite in the Sivrihisar rocks there are a number of obvious differences between the Sivrihisar rocks and the confirmed UHP metamorphic terrains. Firstly there is only one possible coesite relic out of a more than representative number of thin sections and samples. In the Western Gneiss region of Norway there have been occurrences reported in a number of outcrops spanning a wide region (Wain, 1997). Another problem is the monocrystallinity of the quartz inclusion which contains the 20 μm SiO_2 inclusion. In all other reported occurrences, the α-quartz inclusions that either contain relics or in which relics have been entirely pseudomorphed, the α-quartz is polycrystalline. The monocrystalline α-quartz inclusion which contains the 20 μm SiO_2 inclusion barely exceeds the diameter of *one* of the grains within the polycrystalline aggregates, and is therefore a fraction of the size of the α-quartz inclusions described in the previously reported UHP terranes. A second observation is the temperature differences between

the Tavsanli Zone and reported UHP terrains. The Tavsanli Zone is of a much lower temperature than the reported UHP terrains. Temperatures have not exceeded 475° C in the Sivrihisar region. In the Dora Maira coesite-bearing terrain of the Alps temperatures are estimated to be 700° C (e.g. Chopin, 1984; Chopin et al., 1993), are 700° to 850° C for the Western Gneiss Region of Norway (Lappin and Smith, 1978) are greater than 900° C in the Kokchetav Massif in Kazakhstan (Sobolev et al., 1991), and in the Central Dabie mountains of China temperatures are estimated at 850° C (Carswell et al., 1997). The fine-grained nature of the α-quartz inclusions in the Tavsanli Zone could be attributed to the low temperatures experienced, and the possibility that it is kinetically unfavourable for an inclusion no greater than 100 μm in diameter to grow polycrystalline.

From the Micro-Raman spectroscopy it is apparent that the 20 μm inclusion within α-quartz is α-quartz. This does not explain however why the 20 μm is SiO_2 in composition, determined by both Energy Dispersive spectrometers and Wavelength Dispersive spectrometers, and is both higher relief according to a reflected light image of the polished section, or higher in density according to the Backscattered electron image. There is no reason to doubt the Micro-Raman spectroscopy technique however.

The proof required for a metamorphic region to be designated UHP is the existence of coesite. As yet no coesite has been discovered within the Tavsanli Zone. This is not to say that the rocks have never experienced the coesite stability field. Owing to the

difficulty in preserving coesite, and given the fine-grained nature of the low-temperature eclogite facies rocks it is unlikely, if it was once present, that coesite has been preserved.

CHAPTER FOUR

GEOCHRONOLOGY

4.0 Outline of Chapter Four.

Previous geochronological studies of the Tavsanli Zone have raised a number of key questions, without answers to which an understanding of the rates and timescales of its tectonic evolution is severely compromised. This chapter details the problems raised by previous geochronological studies of the Tavsanli Zone, the approach adopted in order to tackle these problems, the results of such a study, and then finally a synthesis of the new geochronology. This chapter is a manuscript in its entirety, entitled "^{40}Ar-^{39}Ar and Rb-Sr geochronology of high-pressure metamorphism and exhumation history of the Tavsanli Zone, NW Turkey" submitted to Contributions to Mineralogy and Petrology on the 6th March, 1998. This manuscript is co-authored by Simon Kelley who has provided supervision in the Open University Argon-Argon laboratory, Simon Inger who performed Rb-Sr analyses on the four Tavsanli Zone sample at the University of Leeds, Nigel Harris and Aral Okay who provided expertise in the field.

4.1 Introduction

Blueschist-facies assemblages are extraordinary not only for providing evidence of low temperatures, of less than 500° C at crustal depths in excess of 75 km, but also for their preservation during exhumation from such deep crustal levels. The mechanisms responsible for the exhumation of high-pressure low-temperature (HP-LT) metamorphic rocks and the tectonic rates required for their preservation are the subject of continued debate (e.g. Platt, 1993; Beaumont et al. 1996; Hynes et al. 1996). Dating HP-LT assemblages is problematic because the low peak temperatures experienced do not reset many commonly used isotope systems, and partly because the most commonly used ^{40}Ar-^{39}Ar white mica ages are open to misinterpretation. Insight into the processes may be afforded by high resolution, multi-system geochronological analysis, without which the mechanisms and rates of exhumation of pristine HP-LT rocks will remain largely conjectural.

Studies from a range of HP-LT assemblages from the European Alps to the Dabie Shan of China have established that white mica ages within HP-LT assemblages often yield ages older than are geologically realistic. The age of HP-LT metamorphism in the Alps provides a comprehensive example, where ^{40}Ar-^{39}Ar step-heating and laser spot ages yielded plateau ages of 110 to 130 Ma for the high-pressure metamorphic event (e.g. Monie and Chopin, 1991; Scaillet et al. 1990), contrasting with Rb-Sr, Sm-Nd, U-Pb and Lu-Hf ages of *ca.* 34 to 66 Ma (e.g. Tilton et al. 1991; Inger et al. 1996; Gebauer et al. 1997; Duchene et al. 1997). Arnaud and Kelley (1995) and Scaillet (1996) demonstrated that the old ^{40}Ar-^{39}Ar ages were an artifact of excess argon, resulting from the incorporation of a non-radiogenic ^{40}Ar. Nonetheless relatively small variations in white mica ages from some blueschist assemblages appear to be tectonically significant, underpinning proposed exhumation models for blueschists

(Wijbrans et al. 1990). Clearly the interpretation of white mica ages even within HP-LT terranes can not be unequivocal and it is important to distinguish the role of excess argon before attempting models for the exhumation of HP-LT assemblages.

This study is an investigation of the conditions and timing of high-pressure metamorphism in an extensive and largely pristine blueschist-facies belt from NW Turkey. New chronological data have been obtained combining the high spatial resolution ^{40}Ar-^{39}Ar UVLAMP, infra-red laser spot ages and furnace step-heating techniques, compared with Rb-Sr white mica ages. The UVLAMP extraction technique has enabled detailed intra-grain analysis of minerals in order to distinguish isotopic heterogeneities (Kelley et al. 1994). Fine-grained lithologies are unsuited to such a technique, to which the lower spatial resolution infra-red laser is more readily applicable. Furnace step-heating has been applied to white micas for comparison with intra-grain analyses, and to investigate the relationship between bulk-sampling techniques and laser extraction. Rb-Sr white mica ages have also been obtained primarily as an estimate of white mica crystallisation rather than cooling ages since the Tavsanli Zone rocks have not been heated sufficiently to exceed the closure temperatures of the Rb-Sr system in white micas.

In applying both the Rb-Sr and ^{40}Ar-^{39}Ar techniques we aim not only to distinguish between geologically meaningful ^{40}Ar-^{39}Ar age ranges and those which may be an artefact of excess argon, but also to assess the timing of crystallisation of the white micas, which is not possible using the ^{40}Ar-^{39}Ar system. In addition to data from HP-LT assemblages a ^{40}Ar-^{39}Ar plateau age has been obtained for hornblende from a single granodiorite intrusive into the blueschist facies rocks, in order to constrain the post-HP-LT facies history of the region.

4.2 Geological Setting

The Tavsanli Zone of Northwest Turkey is a passive continental margin sequence which has undergone subduction resulting in high-pressure metamorphism at unusually low temperatures (Okay, 1984). The zone forms a coherent tract of blueschist and low-temperature eclogite facies metamorphic rocks of up to 40 km wide and 250 km in length (Fig. 4.1); for such an expansive region of HPLT rocks, it remains poorly understood in terms of its thermal evolution and exhumation history.

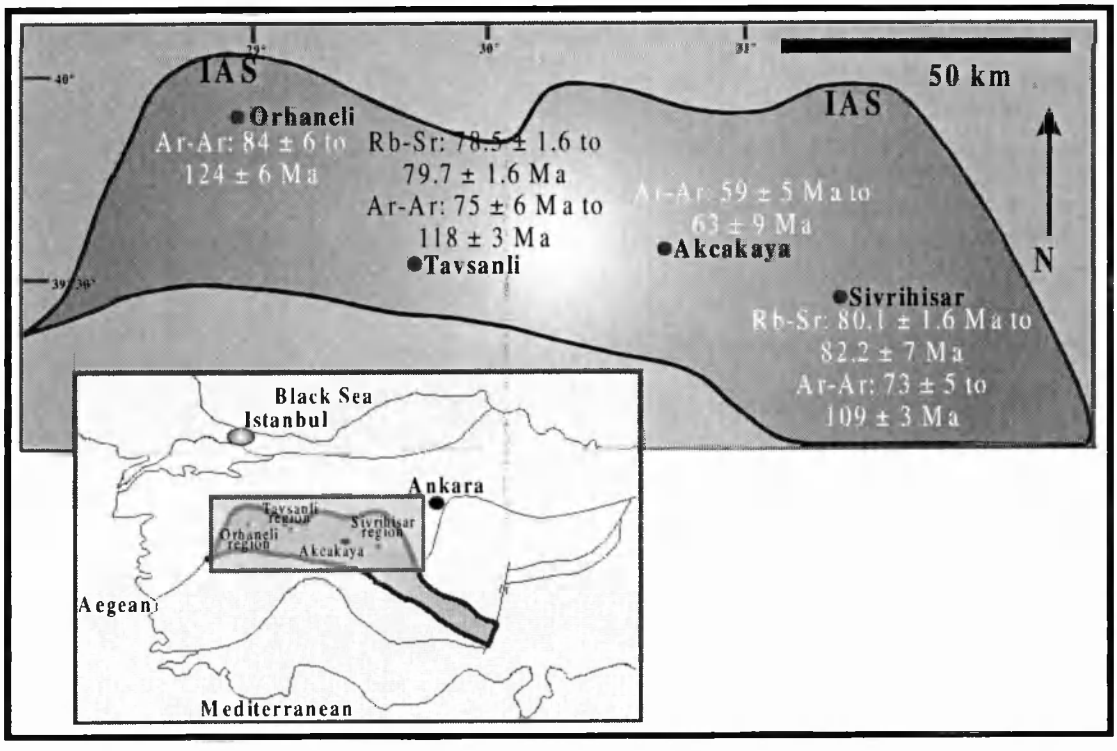

Figure 4.1: Location map of the Tavsanli Zone and the four sample locations in northwest Turkey. IAS = the Izmir-Anakara Suture.

The Tethyan Izmir-Ankara suture, that marks the northern boundary of the Tavsanli Zone, formed in response to the northward subduction of the Tethyan oceanic lithosphere, culminating in continental collision between the northern plate and the passive southern plate, now represented by the Late Cretaceous blueschists of the

Tavsanli Zone (Sengör and Yilmaz, 1981). An accretionary complex, or tectonic melange, overlies a thick marble, metachert and metaclastic sequence derived from a passive continental margin, all of which have undergone various degrees of HPLT metamorphism and form a sequence reaching over 5 km in thickness (Okay, 1984). The accretionary complex comprises intercalated and highly tectonised basic metavolcanic rocks, metachert and metashale lithologies displaying evidence of moderate metamorphism, with maximum pressures estimated at only 8 kbar (Okay, 1980).

Previous geochronological studies within the Tavsanli Zone report two K-Ar white mica ages from blueschists of 82 Ma and 65 Ma (Cogolu and Krummenacher, 1967) and ^{40}Ar-^{39}Ar white mica ages of 89 to 71 Ma (Okay and Kelley, 1994; Okay et al., 1998) and a ^{40}Ar-^{39}Ar glaucophane age of 108 Ma (Harris et al., 1994) for the high-pressure blueschist facies metamorphism. Until now it has not been established whether these age ranges are geologically significant or an artifact of excess argon. The Orhaneli and Topuk granodiorites within the western regions of the Tavsanli Zone yielded ^{40}Ar-^{39}Ar hornblende plateau ages of 48 Ma to 53 Ma (Harris et al., 1994) for intrusion into the blueschists.

Samples analysed are from the unit of intercalated blueschist- and low-temperature eclogite-facies marble, metabasite and metachert lithologies outcropping in the Orhaneli, Tavsanli Akcakaya and Sivrihisar regions, forming a west-east transect of the belt (Figure 4.1). The granodiorite was sampled from within the Sivrihisar region. The extensively studied Orhaneli region in the Western part of the Tavsanli Zone comprises metapelites, metapsammites and rare metabasites (Okay and Kelley, 1994; Okay et al., 1998). The Tavsanli, Akcakaya and Sivrihisar regions within the central Tavsanli Zone comprise intimately associated metabasite and metachert lithologies,

with peak metamorphic conditions reaching the epidote-blueschist facies in the Tavsanli and Akcakaya region and low-temperature eclogite facies in the Sivrihisar region.

4.3 Metamorphic history

The Orhaneli, Tavsanli and Sivrihisar regions of the Tavsanli Zone comprise metabasite, metachert and marble lithologies, all of which underwent an initial static recrystallisation probably during subduction. Recrystallisation was in the low-temperature medium-pressure lawsonite-blueschist sub-facies, with the partial to complete pseudomorphing of augite by sodic-pyroxene (Okay, 1980) and development of lawsonite. Peak conditions within the low-temperature eclogite sub-facies were subsequently attained in the Tavsanli and Sivrihisar regions, with coexisting garnet + omphacite.

Peak conditions in the Tavsanli and Sivrihisar regions are based on both petrographic observations and calculations using the garnet-omphacite-phengite barometer of Waters and Martin (1993) which gave results of 18 ± 2.5 and 24 ± 2.5 kbar respectively. Temperature estimates are based on both petrographic observations and thermobarometric estimates using the garnet-clinopyroxene Fe^{2+}/Mg^{2+} exchange calibrations of Ellis and Green (1979), Powell (1985) and Krogh (1988), and garnet-phengite Fe^{2+}/Mg^{2+} exchange calibrations of Krogh and Raheim (1978) and Green and Hellman (1982). The most important conclusion from the application of these thermometers is that neither the Tavsanli or Sivrihisar rocks have exceeded 550° C. In contrast, further west within the Orhaneli region, peak temperatures were not high enough to generate garnet and the rocks stayed within the lawsonite-blueschist subfacies. From petrographical observations it is clear that the rocks have not

exceeded the lawsonite-blueschist sub-facies. Detailed studies from the Orhaneli region indicate a single clockwise high-pressure metamorphic event in the Late Cretaceous culminating in peak pressures and temperatures of 20 ± 2 kbar and 430 ± 30° C in the Orhaneli region (Okay and Kelley, 1994).

The main penetrative foliation is a retrograde feature common to all three regions, with the assemblage phengite + glaucophane + lawsonite ± omphacite ± garnet ± epidote progressively developing. During exhumation the rocks pass from the low-temperature eclogite sub-facies to the lawsonite-bluechist sub-facies with some assemblages just entering the epidote-blueschist sub-facies. Samples from Orhaneli have a main retrograde foliation of phengite + glaucophane + lawsonite. Sample 96/48 from Akcakaya, near to Sivrihisar, differs from both Sivrihisar and Tavsanli in that the retrograde foliation of white mica + lawsonite is significantly finer-grained, rarely exceeding 50 microns. No greenschist-facies mineralogy is observed within these samples which suggests that the rocks never passed through the greenschist-facies field.

The later stages of the P-T evolution are not well constrained by the assemblages of Okay and Kelley (1994). Petrographic observations from samples from the Sivrihisar and Tavsanli regions show evidence of 'retrograde refrigeration' (Ernst and Peacock, 1996), or cooling during exhumation.

4.4 Geochronology

The maximum age of the blueschist-facies metamorphism is established as 'late-Cretaceous' by the earlier geochronological estimates, the minimum age by the intrusive Eocene granodiorites (Harris et al., 1994). ^{40}Ar-^{39}Ar phengite and

glaucophane ages spanning the range 88 Ma to 108 Ma (Okay and Kelley, 1994; Harris et al., 1994) compare with K-Ar ages of 82 Ma and 65 Ma (Cogolu and Krummenacher, 1967). Within this study high-resolution ^{40}Ar-^{39}Ar and Rb-Sr white mica ages have been combined from the Tavsanli Zone HPLT metamorphic event in order to establish the geological validity of these age ranges.

4.4.1 Analytical techniques

High-spatial resolution ^{40}Ar-^{39}Ar white mica ages were obtained using the Ultra-Violet Laser Ablation Microprobe extraction technique. For a detailed account of the technique see Reddy et al. (1997), samples were monitored using the GA1550 biotite standard with an age of 97.9 Ma (McDougall and Harrison, 1988). The calculated J value for the samples was 0.00583, and results were corrected for blanks, ^{39}Ar decay and neutron-induced interference reactions. The correction factors used were: $(^{39}Ar/^{37}Ar)Ca$ = 0.00067, $(^{36}Ar/^{37}Ar)Ca$ = 0.000255, $(^{40}Ar/^{39}Ar)K$ = 0.048 based on analyses of Ca and K salts. Furnace step-heating was carried out at Clermont-Ferrand, for the experimental procedure see Arnaud et al. (1993). A J value of 0.016952 and correction factors of $(^{39}Ar/^{37}Ar)Ca$ = 0.002341, $(^{36}Ar/^{37}Ar)Ca$ = 0.0003127, $(^{40}Ar/^{39}Ar)K$ = 0.00 were used. Step-heating with an Infra-red laser was performed on amphiboles from the Sivrihisar granite, standard magnetic separation followed by handpicking resulted in a high-purity hornblende separate. The sample was step heated using the Infra-red laser, for the experimental procedure see Kelley et al. (1994).

Samples were crushed and sieved for Rb-Sr analysis and minerals separated by standard magnetic and heavy liquid methods. Micas were separated by adherence to paper, and where impurities were not quartz separates were further purified by hand

picking. For a detailed account of the analytical procedure and error propagation see Inger et al. (1996).

Electronprobe microanalyses were obtained with a Cameca SX100, using operating conditions of 20 kV accelerating voltage, 20 nA beam current and both 10 and 20 um beam sizes. Elements were analysed with four wavelength-dispersive detectors.

Appendices A, C and G detail the techniques described above.

4.5 Results

4.5.1 Rb-Sr white mica ages

Four samples, 96/12, 96/134, 96/198 and 96/158 from two pristine HP-LT assemblages from the Tavsanli and Sivrihisar regions yield white mica ages of 78.5 ± 1.6 to 82.8 ± 1.7 Ma (Table 1). Samples 96/12 and 96/198 are from the Tavsanli region metachert and penetratively foliated metabasite lithologies. White mica ages of 78.5 ± 1.6 Ma and 79.7 ± 1.6 Ma were obtained from samples 96/12 and 96/198 from the Tavsanli area. Ages from samples 96/134 and 96/158 from the Sivrihisar region some 130 km east of Tavsanli are marginally older, with a white mica age of 80.1 ± 1.6 Ma and an isochron age of 80.1 ± 2.6 Ma from the metachert 96/134, and from the penetratively foliated metabasite 96/158 a white mica age of 82.8 ± 1.7 Ma.

4.5.2 ^{40}Ar-^{39}Ar white mica ages

4.5.2.1 High resolution UVLAMP

High spatial resolution argon data using the UVLAMP has been collected from eight samples from Orhaneli, Tavsanli and Sivrihisar. A detailed study has been made of fine- to medium-grained phengites, the coarsest of which reached approximately 250 x 90 microns, and of very low-potassium glaucophane grains. (Average compositions Table 4.1).

From the Orhaneli region sample 96/234 phengites gave an age range of 84 ± 6 Ma to 124 ± 6 Ma (Appendix B.1). Phengite ages from the four samples 96/12, 96/185, 96/198 and K380 from the Tavsanli region yielded an age range of 75 ± 6 Ma to 118 ± 3 Ma. Ages have been obtained from both whole single phengite grains, and from sequential traverses across single coarser phengite grains. Samples 96/198 and K380 from Tavsanli contain phengite grains up to 100 microns in diameter, and intra-grain age variations were determined by detailed grain profiling. Figures 4.2a and 4.2b illustrate that core regions of the coarsest grain size in samples 96/198 and K380 yield ages of 86 ± 3 Ma and 94 ± 6 Ma respectively, with ages increasing towards the rims to 111 ± 3 Ma and 110 ± 3 Ma. Single phengite grains from sample 96/12 yielded ages ranging from 75 ± 6 Ma to 89 ± 1 Ma. Sample 96/185 is finer-grained and single phengite grains gave an age range of 102 ± 4 to 118 ± 3 Ma. Glaucophane grains analysed from all four samples contained very little argon (Appendix B.1), with such large uncertainties the ages are meaningless.

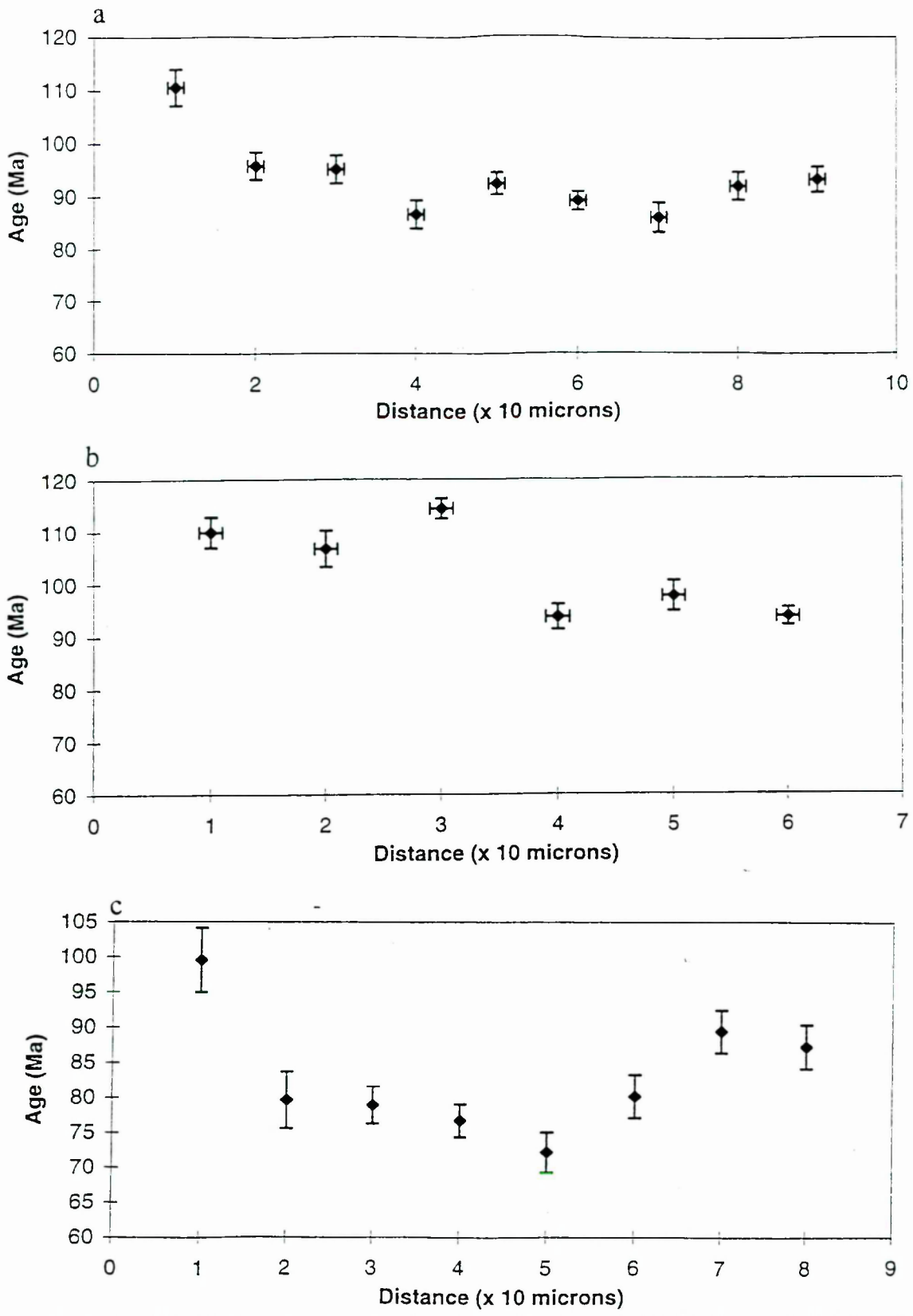

Figure 4.2: UVLAMP traverses across phengite grains a) sample 96/198, b) sample K380, and c) sample 96/158.

Phengites and glaucophanes were analysed from the three samples from the Sivrihisar region, 96/120, 96/134, and 96/158, (Appendix B.1). The metachert sample 96/158 was coarse enough for detailed intra-grain analysis; Figure 4.2c illustrates a core age

of 73 ± 5 Ma, and a rim age of 100 ± 6 Ma. Single phengite grains from the same sample fell within the range of 83 ± 2 Ma and 107 ± 3 Ma. Sample 96/134 yielded an intra-grain age range of 98 ± 3 Ma to 109 ± 3 Ma from core and rim respectively, and single phengite grains gave a range of 78 ± 2 Ma to 105 ± 2 Ma. Phengite ages from single grains in sample 96/120 are in the range 86 ± 4 Ma to 105 ± 5 Ma. A glaucophane 'age' of 109 ± 7 Ma was obtained from sample 96/158, most likely the result of phengite inclusions or intergrowths within the amphibole. Glaucophanes from 96/134 and 96/120 did not yield age data (Appendix B.1).

4.5.2.2 IR laser spot analyses

Two samples were analysed using an Infra-red laser which produced spots of approximately 100 μm in diameter; results are presented in Appendix F.2. Spot analyses of single *in situ* phengite grains from the Tavsanli region (sample K380, see Appendix B.2) yielded an age range of 92 ± 11 Ma to 192 ± 8 Ma. Ages from fine-grained sample 96/48 from Akcakaya are 'whole rock' ages. From microprobe analyses it is apparent that the potassium budget of the rock is dominated by fine-grained phengites (< 20 μm), thus the age range 59 ± 5 Ma to 63 ± 9 Ma are considered to reflect white mica ages.

4.5.2.3 *IR laser step-heating*

Figure 4.3 is the release spectra for hornblende separate from the granodiorite intruding the HPLT assemblages near to Sivrihisar, plotted from the data in Appendix B.3. The plateau age of 53 ± 3 Ma is consistent with the ^{40}Ar-^{39}Ar age range obtained from both the Topuk and Orhaneli granodiorties in the west (Harris et al., 1994) and is

indicative of a magmatic event distributed over distances of >100 km for a duration of less than 6 Ma.

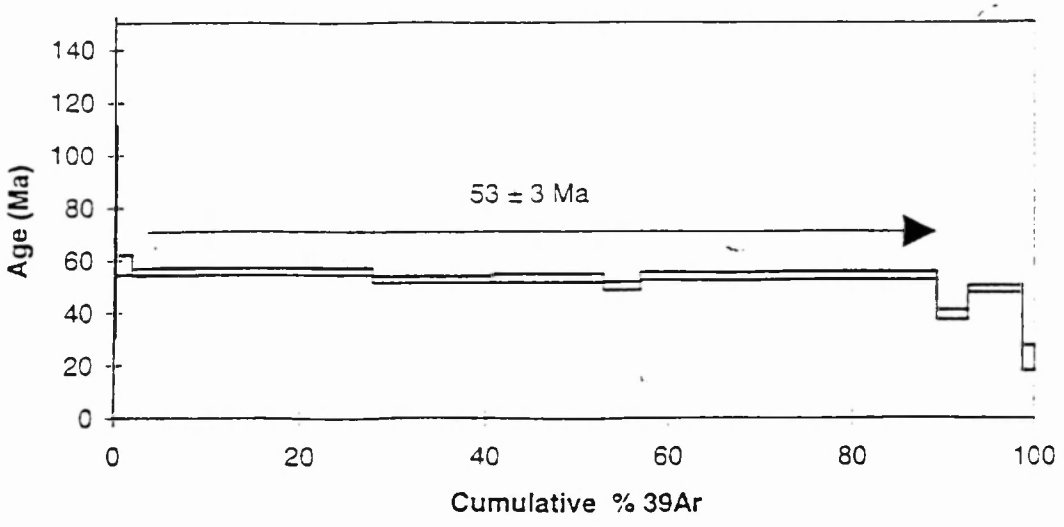

Figure 4.3: Infra-red laser step-heating spectra of Sivrihisar granodiorite hornblende separate.

4.5.2.4 Furnace step-heating

Phengite from sample 96/12 and glaucophanes from samples 96/12 and 96/134 from the Tavsanli and Sivrihisar regions respectively were analysed (Appendix B.4). A well-defined plateau age of 86.5 ± 1.2 Ma was obtained from the 96/12 phengite (Figure 4.4a), which comprised 7 steps and 97% of the ^{39}Ar released, and the total fusion age for the sample is 85.9 ± 1.2 Ma. Although Figure 4.4a appears to be a well-defined plateau for 69/12 phengite, when compared with the Rb-Sr and laser ^{40}Ar-^{39}Ar ages it is clearly more than 6 Ma too old and outside the errors, as is the total fusion age. The phengite plateau age is considered to be an artifact of excess argon on the grounds that it is significantly higher than the Rb-Sr white mica ages for the same sample, as

has been discovered in phengites from the Sezia Lanzo Zone in the European Alps (Inger et al., 1996).

The amphibole spectra do not yield plateau ages; sample 96/134 from the Sivrihisar area has a total fusion age of 154 ± 3 Ma, sample 96/12 from Tavsanli has a total fusion age of 118 ± 2 Ma. Figures 4.4b and 4.4c illustrate that both amphibole spectra display the same characteristics, with an increase in age within the first three steps, followed by an overall decline. The K/Ca ratios (Figures 4.4d and 4.4e) suggests that this represents the early outgassing of mica inclusions in the amphibole, followed by a release pattern more consistent with an amphibole that has an excess argon component. The first step in Figure 4.4d have a K/Ca ratio of 3.3, steps 2 to 7 show a marked reduction to between 0.3 and 0.8. The same is true of sample 96/12 with a more pronounced drop in K/Ca ratio from 8.5 in step 2 to between 0.5 and 1.0 in steps 3 to 10. The data from these amphiboles do not correspond to a geological event, since the initial steps are dominated by this release from mica inclusions which mask any signal from the low-K amphibole. To derive a plateau age, three or more concordant steps must represent a significant proportion of total ^{39}Ar released (e.g. Dalrymple and Lanphere, 1974). These criteria are not met by these amphiboles due to the non-pervasive contamination of excess argon in both samples.

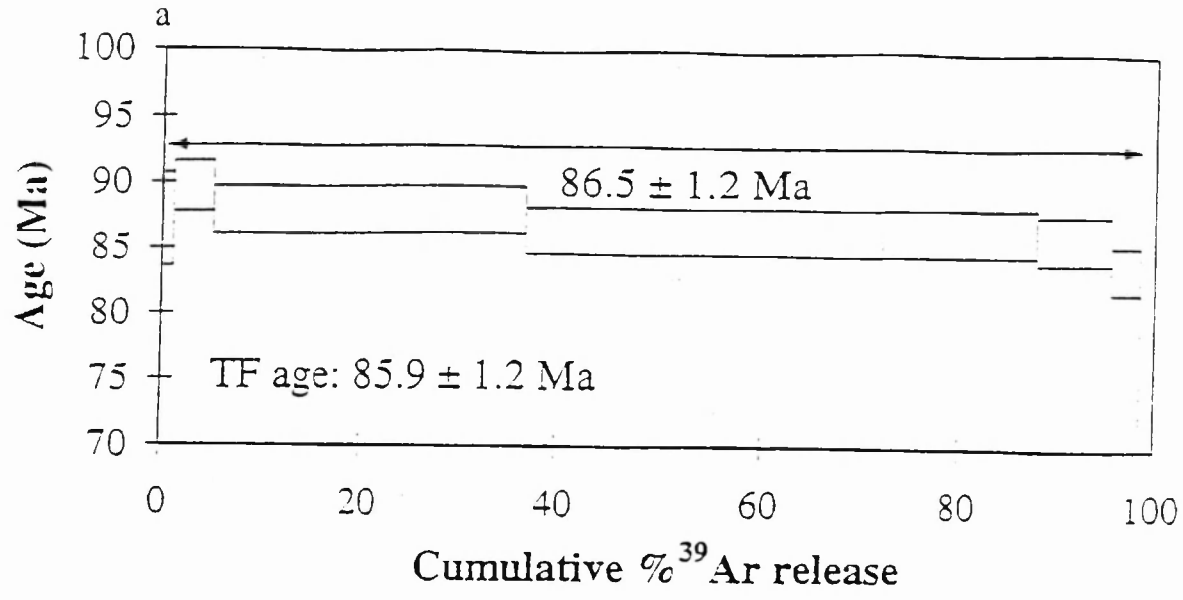

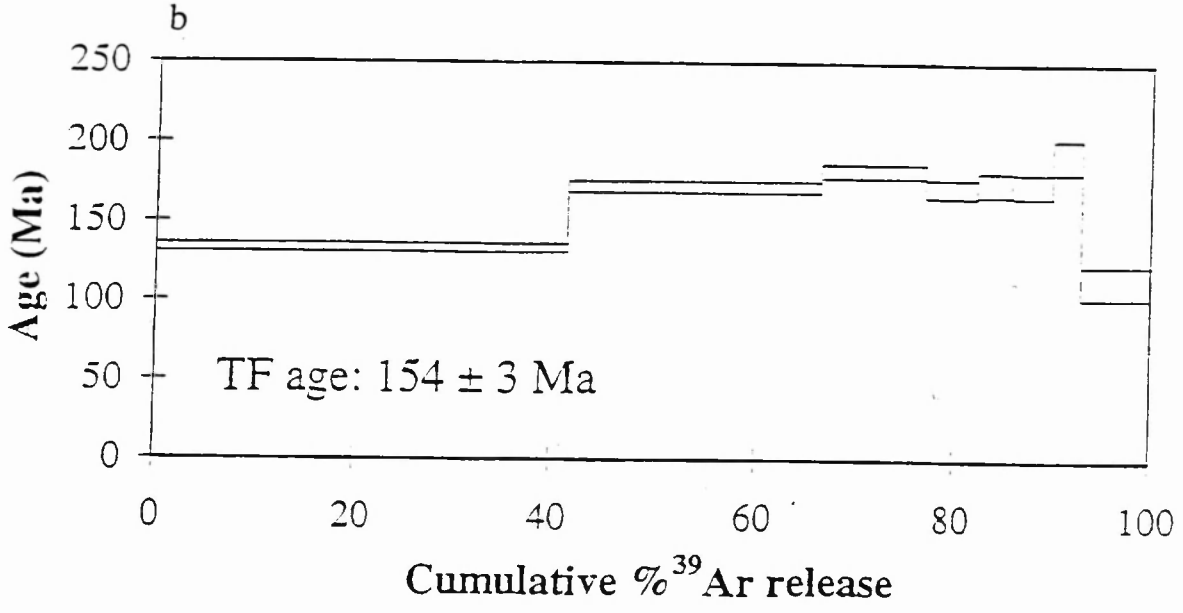

Figure 4.4: Furnace step-heating release spectra for a) phengite from sample 96/12, b) sodic-amphibole from sample 96/134.

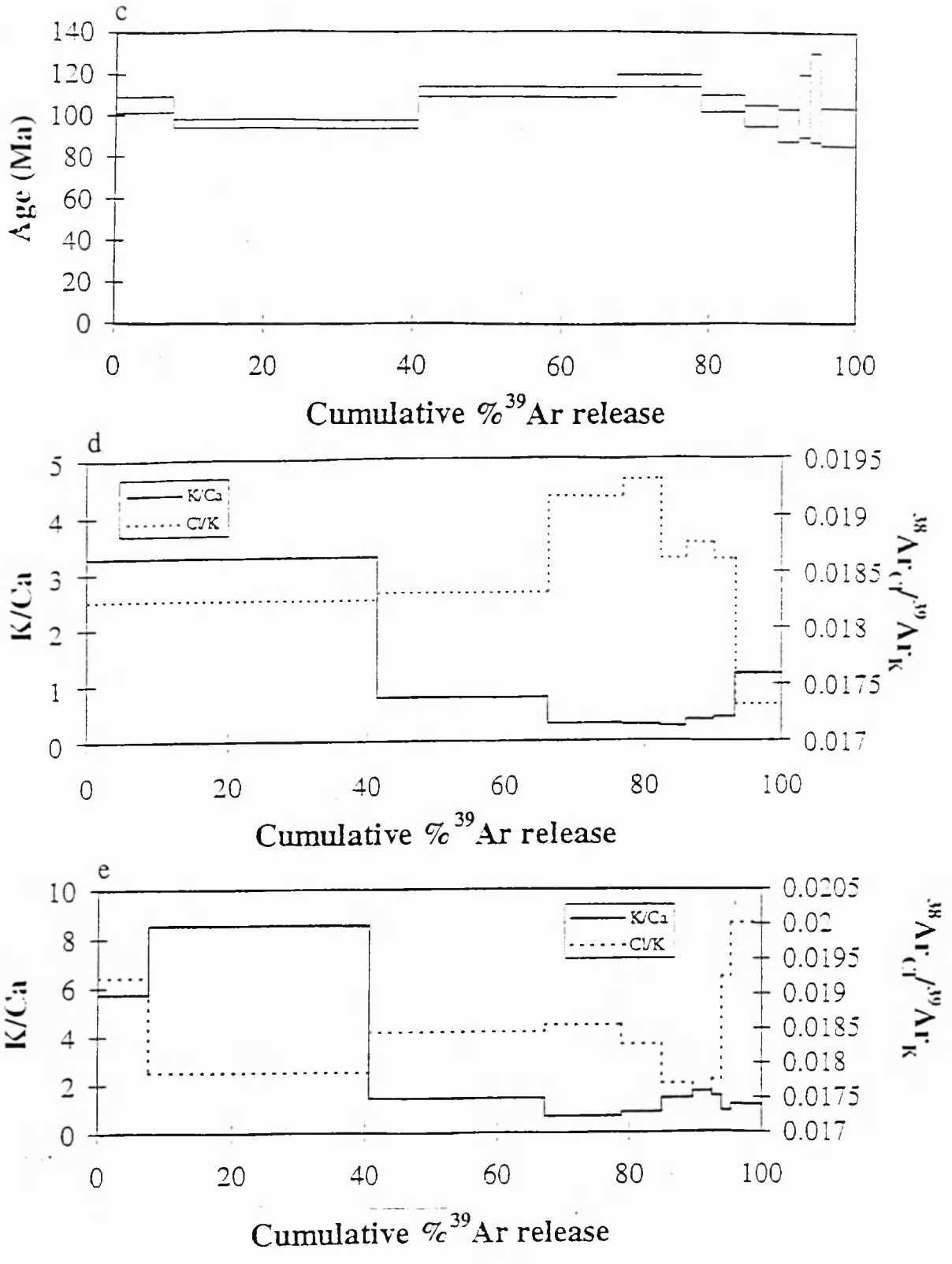

Figure 4.4 continued: c) sodic-amphibole from sample 96/12, d) K/Ca ratios from sodic-amphibole in sample 96/12, and e) K/Ca ratios for sodic-amphibole in sample 96/12.

	96/134		96/158		K380	
	phengite	glaucophane	phengite	glaucophane	**phengite**	glaucophane
SiO2	51.90	57.29	52.00	57.56	54.20	55.76
TiO2	0.01	0.00	0.20	0.00	0.10	0.00
Al2O3	22.70	5.84	22.40	5.13	19.50	4.64
Cr2O3	0.00	0.00	0.00	0.00	0.00	0.00
FeO (total)	4.38	16.62	4.10	16.53	6.25	20.38
MnO	0.10	0.16	0.00	0.23	0.10	0.31
MgO	4.50	10.49	4.30	10.34	4.20	8.77
CaO	0.00	0.53	0.00	0.58	0.00	0.51
Na2O	0.20	6.91	0.10	6.68	0.30	6.83
K2O	11.10	0.03	11.00	0.18	10.01	0.03
Total	94.90	97.92	94.11	97.24	94.67	97.27
Si	3.53	8.01	3.56	8.23	3.69	8.00
Ti	0.00	0.00	0.01	0.00	0.01	0.00
Al	1.82	0.96	1.81	0.86	1.57	0.79
Cr	0.00	0.00	0.00	0.00	0.00	0.00
Fe (total)	0.24	1.84	0.23	1.98	0.35	2.33
Mn	0.01	0.02	0.00	0.03	0.01	1.88
Mg	0.46	2.19	0.44	2.20	0.44	0.08
Ca	0.00	0.08	0.00	0.09	0.00	0.08
Na	0.03	1.87	0.01	1.85	0.04	1.90
K	0.96	0.00	0.96	0.03	0.87	0.00
Total	7.04	14.99	7.02	15.28	6.99	15.01
	96/12		**96/198**		**96/234**	**SivG**
	phengite	glaucophane	phengite	glaucophane	phengite	amphibole
SiO2	51.80	56.86	52.40	57.18	51.90	45.74
TiO2	0.10	0.05	0.10	0.00	0.10	0.92
Al2O3	22.30	6.76	22.20	5.93	22.20	7.83
Cr2O3	0.00	0.02	0.00	0.00	0.00	0.00
FeO (total)	4.8	16.86	4.60	18.96	05.56	15.64
MnO	0.00	0.17	0.10	0.10	0.00	0.70
MgO	4.20	9.08	4.10	8.71	4.40	12.3
CaO	0.00	0.47	0.00	0.53	0.00	12.06
Na2O	0.10	6.91	0.10	6.32	0.20	1.17
K2O	10.80	0.02	10.80	0.03	10.80	0.74
Total	94.14	97.19	94.42	97.76	94.17	97.10
Si	3.56	8.14	3.57	8.07	3.55	6.81
Ti	0.01	0.00	0.01	0.00	0.01	0.10
Al	1.80	1.14	1.79	0.99	1.79	1.38
Cr	0.00	0.00	0.00	0.00	0.00	0.00
Fe (total)	0.28	2.02	0.26	2.13	0.26	1.85
Mn	0.00	0.02	0.01	0.01	0.00	0.09
Mg	0.41	1.93	0.42	1.83	0.45	2.73
Ca	0.00	0.07	0.00	0.08	0.00	1.93
Na	0.01	1.92	0.01	1.73	0.03	0.34
K	0.95	0.01	0.94	0.00	0.94	0.14
Total	7.01	15.25	7.00	14.87	7.02	15.42

Table 4.1: Average mineral compostions

4.6 Geological implications of the new age data

4.6.1 Excess argon in the Tavsanli Zone

Previous attempts to understand the geochronology of the Tavsanli Zone have been distorted by the heterogeneous distribution of excess argon which is evident from macroscopic to microscopic scales. This has affected K-Ar and ^{40}Ar-^{39}Ar ages from white micas and glaucophanes in the Tavsanli Zone in a way similar to that seen in the European Alps (e.g. Scaillet et al., 1992; 1996; Arnaud and Kelley, 1995; Inger et al., 1996). Excess argon within the Tavsanli Zone has not been previously considered, given the regional geological constraints and a small age range. The age range of 70 ± 1.2 to 88.5 ± 0.5 Ma was considered to reflect geological events (Okay and Kelley, 1994; Harris et al., 1995). The age ranges reported by Cogolu and Krummenacher (1967) and Okay and Kelley (1994) are similar to this new data. The ^{40}Ar-^{39}Ar age range of 72 ± 3 to 124 ± 6 Ma obtained with the UVLAMP are both older and younger than Rb-Sr ages in the Tavsanli and Sivrihisar regions. Although there are no Rb-Sr ages for the Orhaneli region, the presence of excess argon is inferred from the similarity of isotopic characteristics of Orhaneli phengites and phengites from the Tavsanli and Sivrihisar regions.

Infra-Red laser spot ages of phengites in sample K380 from the Tavsanli region further confirm the presence of excess argon (Appendix B.2), where ages of up to 192 Ma have been obtained. The Infra-Red laser has a larger spot size and has a tendency to average isotopically distinct regions in grains which are as small as 120 μm in diameter. Results represent a mixture of real ages, possibly from core regions free of excess argon, and older rims contaminated by excess argon. When samples analysed

by furnace-step heating are compared with the high spatial resolution UVLAMP extraction technique it becomes apparent that the bulk sample technique results in an age which is an average of the low core ages and high rim ages which are evident from the high spatial resolution UVLAMP. The analysis of phengite and low-potassium minerals with the UVLAMP indicates either i) that only phengites are contaminated by excess ^{40}Ar or ii) that the concentration of excess argon is higher in the phengites than in the low-potassium amphiboles. The step-heated glaucophane ages are likely to be an artefact of excess argon from mica inclusions and intergrowths since with a bulk separate analysis technique it is not possible to avoid the effects of mica inclusions. Several attempts have been made to obtain meaningful chronological information from low-potassium amphiboles (e.g. Sisson and Onstott, 1986), which often yield age data reflecting phengite inclusions or microscopic phengite intergrowths, as is illustrated by the sodic amphibole analyses presented here. The contamination of phengite by excess argon is to a lesser extent than phengites from other HPLT areas, exemplified by the Dabie Shan of China (Li et al., 1994) and Dora Maira in the Western Alps (Arnaud and Kelley, 1995), where intra-grain ages are consistently older than those yielded by all other isotopic systems (Scaillet et al., 1992; Inger et al., 1996; Reddy et al., 1996).

4.6.2 P-T-t evolution of the Tavsanli Zone

Closure temperature (T_c) estimates have been calculated for Tavsanli Zone white micas. In the absence of satisfactory kinetic data for Ar diffusion in the Si-rich phengitic white micas, the data of Hames and Bowring (1994) for muscovitic white micas has been applied using the closure equation of Dodson (1973). Given that the diffusion parameters are poorly constrained for high-pressure white micas, the proposed Tc within this study may be subject to large uncertainties. Estimates of T_c

based on an average cooling rate of 10° C/Km are 400 ± 50° C for the coarsest phengite grain size, (~ 100 μm). For the finest-grained material analysed with the infra-red laser, T_c is approximately 290 ± 50° C for the 20 μm diameter grains, based on the same cooling rate. HP-LT phengite crystallisation during exhumation of the Tavsanli Zone occurred within the timespan of 79.7 ± 1.6 to 82.8 ± 1.7 Ma during the development of the penetrative retrograde foliation, post-peak metamorphism. The youngest ^{40}Ar-^{39}Ar ages provide the best estimates for the time at which the samples passed through T_c of 400 ± 50° C and 290 ± 50° C, at 72 Ma and 60 Ma respectively.

If petrographical observations, thermobarometric estimates and the new geochronological data are combined, it is possible to describe a P-T-t path for the Tavsanli Zone rocks. From the petrographical observations it is apparent that the rocks of the Tavsanli Zone underwent a prograde path within the lawsonite-blueschist sub-facies. Peak metamorphic conditions were achieved within the low-temperature eclogite sub-facies, and the rocks returned along a retrograde P-T path which closely mirrors the prograde path in form, within the lawsonite-blueschist sub-facies. On this basis it is possible to constrain the form of the P-T path using the sub-facies stability fields of Schliestedt (1990), with peak metamorphic conditions constrained by thermobarometric estimates (Fig. 4.5). Time, t, is constrained by the new geochronological data. The phengites crystallised at temperatures of approximately 500 ± 50° C, thus the *ca* 80 Ma Rb-Sr white mica ages reflect the time of crystallisation during the retrograde part of the P-T path, post-peak metamorphic conditions (Fig. 4.5). By 72 Ma the rocks had cooled to 400 ± 50° C, based on the youngest UVLAMP ^{40}Ar-^{39}Ar white mica ages from the coarsest-grained phengites. From the infra-red laser analysis of much finer-grained phengites it is apparent that at 60 Ma the rocks were at temperatures of 290 ± 50° C (Fig. 4.5).

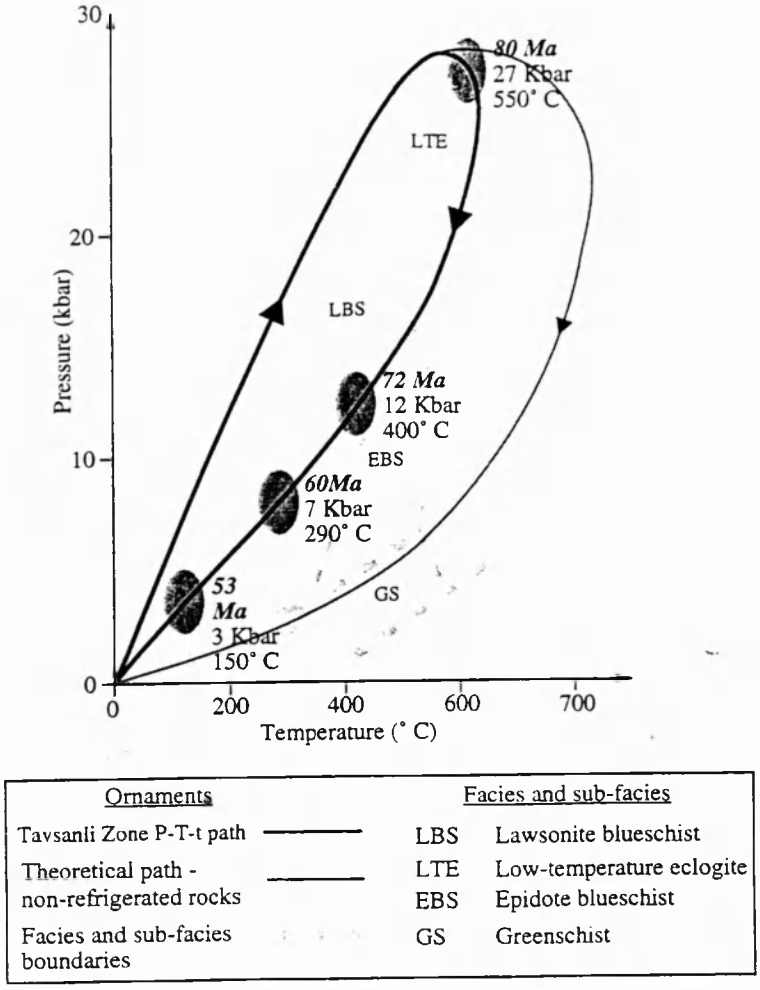

Figure 4.5: P-T-t path for the Tavsanli Zone blueschist- and low-temperature-eclogite facies rocks.

The final constraint on the P-T-t path comes from the granodorite aureole, where intrusion at 51 to 53 Ma occurred, at pressures of approximately 3 kbar (Harris et al. 1994).

It is possible to infer mechanisms for the exhumation of the HP-LT rocks on the basis of the P-T-t information in Figure 4.5. The retrograde P-T trajectory path passes from

the low-temperature eclogite sub-facies into the lawsonite-blueschist sub-facies, indicative of cooling during exhumation. Figure 5 presents both the P-T-t path for the Tavsanli Zone rocks and a theoretical path for deeply subducted rocks undergoing post-subduction exhumation (Hacker and Peacock, 1995). In order to achieve the cooling during exhumation, syn-subduction exhumation is required (e.g. Rubie, 1984; Platt, 1986; Okay and Kelley, 1994; Ernst and Peacock, 1996). HP-LT material is underplated and accreted to the base of the hangingwall, and cooled by conductive heat loss to both the hangingwall and lower subducting plate, a process described as 'retrograde refrigeration' (e.g. Platt, 1986; Platt, 1987; Platt, 1993). The most likely mechanism for the subsequent exhumation of HP-LT rocks is mechanical exhumation back up the subduction zone by underplating, from maximum depths of 75 km.

At approximately 65 Ma the oblique northeast directed convergence of African and European plates changed to northward directed orthogonal convergence (Dewey et al. 1989). The implications of this for the exhumation of the Tavsanli Zone rocks are that at approximately 65 Ma subduction ceased and continent-continent collision ensued (e.g. Okay et al. 1998). Syn-subduction exhumation is no longer viable and exhumation must have taken place by some other mechanism. From 72 Ma to 53 Ma, an average rate of exhumation of approximately 1.5 mma^{-1} can be inferred based on the P-T-t estimates in Figure 4.5. It is during this time that subduction ceases, and an alternative mechanism of exhumation must have become operative. Exhumation at an approximate rate of 1.5 mma^{-1} exceeds that predicted by any simple erosion model (Draper and Bone, 1981) and an additional tectonic mechanism is probably required during this period of post-collisional crustal shortening. Alternatives include: i) crustal shortening accommodated by the southward-directed thrusts which exhumed the blueschists, or ii) backsteepening of the suture during collision. There is no direct evidence from this study to favour either model.

The calc-alkaline granitoids emplaced into the Tavsanli Zone were generated at the base of the crust at temperatures of approximately 950° C at 53 Ma, and emplaced into HP-LT rocks at a depth of approximately 10 km (Harris et al. 1994). No overprinting is observed in HP-LT rocks presently exposed in the Tavsanli Zone which were already at upper crustal levels whilst thermal relaxation took place at depth; thus rocks likely to have experienced overprinting lie beneath the present erosion level. Such temperatures in the lower crust could not be generated less than 20 Ma after collision by radiogenic heat build up (England and Thompson, 1984). Okay et al. (1998) have suggested heating due to slab-breakoff (Davies and von Blackenberg 1995) though there is no surficial evidence of basalt eruption due to decompression melting which might ensue from such a process.

4.7 Conclusions

This study highlights the importance of the high spatial resolution UVLAMP technique. Detailed profiling of coarse phengite grains enables us to see past excess argon in a HP-LT terrain, providing excess argon is a non-pervasive feature. By combining a range of ^{40}Ar-^{39}Ar and Rb-Sr isotope techniques we conclude:

1 Rb-Sr dating of white micas indicate that phengite crystallisation which post-dates the peak of HP-LT metamorphism occurred at 79.7 ± 1.6 to 82.8 ± 1.7 Ma.

2 The analysis of phengite and sodic-amphibole indicate the presence of excess argon. The previous Ar-Ar ages of Okay and Kelley (1994) and Harris et al. (1994) are probably an artifact of excess argon, and only the cores of coarse phengite grains yield true cooling ages in the Tavsanli Zone rocks.

3 The Tavsanli Zone HP-LT rocks underwent syn-subduction exhumation and cooling, followed by exhumation along southward-directed thrusts to the surface.

4 When the P-T path derived from mineral assemblages is combined with mineral chronometry a minimum exhumation rate of 1.5 mma-1 is determined for the period between 72 and 53 Ma.

5 Granodiorites intruded HP-LT rocks in the eastern end of the Tavsanli Zone at 53 Ma synchronous with similar intrusions emplaced into the western extent of the belt reported by Harris et al. (1994).

Finally we suggest that Ar-Ar data from white micas in HP-LT terrains should be approached with caution before being used in any geological interpretation.

CHAPTER FIVE

EXCESS ARGON

5.0 Outline of Chapter Five

When attempting to apply ^{40}Ar-^{39}Ar geochronological techniques to HPLT metamorphic terranes, many, if not all, are found to suffer from the problem of 'excess argon'. The Tavsanli Zone provides excellent opportunities for studying this problem, with an abundance of micaceous rocks that are well characterised and have only experienced a single metamorphic cycle, removing many of the problems inherent in studying polymetamorphic terranes. The absence of crystallisation in either the amphibolite- or greenschist-facies during exhumation also precludes the complexities associated with full and partial resetting of the argon system. This chapter comprises two manuscripts, the first of which is co-authored by Simon Kelley who has provided supervision in the Argon-Argon laboratory at The Open University, the second is co-authored by Nicolas Arnaud who provided supervision in the Argon-Argon laboratory in Clermont-Ferrand, France.

5.1 Excess argon in HP-LT rocks: a UVLAMP study of phengite and K-free minerals.

5.1.1 Introduction

High- and ultra-high-pressure metamorphic rocks formed in convergent settings often originate from deep crustal levels, and generally survive an elaborate P-T-t return path to the surface. The exhumation of these high-temperature/low-pressure (HPLT) metamorphic rocks has been the subject of debate. A comprehensive understanding of the mechanisms of exhumation is subject to knowledge of rates of cooling from HPLT conditions. A major complication however is isotopic disequilibrium, which is prevalent in rocks with low water activities and low temperatures of formation. Most importantly the closure temperature concept applied to ^{40}Ar-^{39}Ar white mica ages assumes that radiogenic $^{40}Ar^*$ from the decay of K in white micas is isotopically equilibrated with argon within the whole rock at high temperatures but is retained within the mica at low temperatures. In rocks with both low temperatures and low water activities, the extrinsic parameters responsible for the equilibration of argon are reduced in effect and result in the heterogeneous distribution of argon within the system, thus reducing the effectiveness of the ^{40}Ar-^{39}Ar technique.

Despite the apparent problems, ^{40}Ar-^{39}Ar geochronology is commonly applied to white micas in HPLT rocks. White micas are often abundant in HPLT rocks, and with a high-potassium content are well suited to the ^{40}Ar-^{39}Ar technique. Ideally, in higher-temperature assemblages cooling ages are obtained. In lower-temperature assemblages which crystallised in temperatures similar to the closure temperature of argon diffusion in white micas (approximately 350° C, Dodson, 1973) white mica ages may be interpreted as crystallisation ages. Although in a large number of

regions and tectonic settings the ^{40}Ar-^{39}Ar technique has proved reliable and consistent, an array of results indicating excess argon have been produced from unaltered micas in HPLT rocks (Scaillet et al., 1990; 1992; Arnaud and Kelley, 1995; Ruffet et al., 1995; 1997; Scaillet, 1996; Reddy et al., 1996; Pickles et al., 1997; Boundy et al., 1997; Sherlock et al., submitted, a; Sherlock and Arnaud, submitted). Excess argon is common to both pristine and altered or overprinted micas and is largely responsible for the variable success of ^{40}Ar-^{39}Ar geochronology in HPLT rocks. Excess ^{40}Ar, additional to radiogenic $^{40}Ar^*$, may be incorporated into the mineral lattice during or after mineral growth, resulting in apparent ages older than the true age of the mineral. In many cases white mica ages which have been considered reliable, and which have been used to generate tectonothermal models (e.g. Rubie, 1984; Duchene et al., 1997), have subsequently been found to be an artefact of excess argon. In order to distinguish meaningful from problematic age data the isochron approach has historically been used (e.g. Dalrymple and Lanphere, 1974; Lanphere and Dalrymple, 1978; Berger and York, 1981a; Heizler and Harrison, 1988). This approach enables us to identify the presence of the additional ^{40}Ar component, which results in a deviation of the ^{40}Ar-^{36}Ar ratio from an atmospheric value of 295.5 (Steiger and Jäger, 1977). However, in some examples this approach can indicate no excess argon contamination, this only becomes apparent from Rb-Sr white mica dating (Inger et al., 1996; Ruffet et al., 1997; Sherlock et al., submitted a; Sherlock and Arnaud, submitted). The ^{40}Ar-^{39}Ar plateaux ages of up to 110 Ma for high-pressure metamorphism in the Dora Maira of the western European Alps (e.g. Monie and Chopin, 1991; Scaillet et al., 1990; 1992) are one such well-documented example of the effects of excess argon. In the high-pressure rocks of the Alpine Dora Maira, although the ^{40}Ar-^{39}Ar white

mica plateaux are convincingly flat they are not geologically meaningful but an artefact of prevalent and pervasive excess argon (Arnaud and Kelley, 1995). Rb-Sr, Sm-Nd and U-Pb ages of *ca.* of 35 Ma to 40 Ma for the same metamorphic event further corroborate this (e.g. Tilton et al., 1991; Bowtell et al., 1994; Gebauer et al., 1997).

A similar problem may exist in the Greek Cyclades. A large number of K-Ar and ^{40}Ar-^{39}Ar geochronological studies have revealed age ranges for the various islands (Table 5.1).

Island	Isotopic system	Age ranges	Reference
Ios	K-Ar phengite	82 to 26 Ma	Henjes-Kunst and Kreutzer (1982)
	^{40}Ar-^{39}Ar glaucophane	120 to 100 Ma	Maluski et al. (1981)
Naxos	K-Ar white mica	38 to 11 Ma	Wijbrans and McDougall (1986, 88)
	^{40}Ar-^{39}Ar white mica	40Ar to 18 Ma	
Sifnos	K-Ar white mica	48 to 41 Ma	Altherr et al. (1979)
	Rb-Sr white mica	41 to 33 Ma	
	^{40}Ar-^{39}Ar white mica	42 to 30	Wijbrans et al. (1990)
Syros	^{40}Ar-^{39}Ar, phengite and paragonite	53 to 37 Ma	Maluski et al. (1987)
Tinos	^{40}Ar-^{39}Ar white mica	44 to 31 Ma	Bröcker et al. (1993)
	Rb-Sr white mica	39 to 29 Ma	Bröcker and Franz (1998)

Table 5.1: Comparison of ^{40}Ar-^{39}Ar and K-Ar with Rb-Sr age determinations of HPLT metamorphism in the Cycladic Islands, Greece.

The variation in K-Ar, ^{40}Ar-^{39}Ar and Rb-Sr ages from these Greek Cycladic islands has been variably interpreted. The interpretations are: partial resetting resulting from heterogeneous fluid migration in Tinos (Bröcker et al., 1993; 1998), differential uplift and cooling rates in Sifnos (Wijbrans et al., 1990); and mixing between coexisting phengite and muscovite resulting in complex spectra, with characteristics of both mica populations, in Naxos (Wijbrans and McDougall, 1986). In the most recent and comprehensive ^{40}Ar-^{39}Ar and Rb-Sr study in the

Cyclades, excess argon is considered as a possible mechanism for the ^{40}Ar-^{39}Ar ages being persistently older than Rb-Sr ages. However, given the small age differences between the two systems it is considered to be of limited, or perhaps no importance (Bröcker and Franz, 1998). Altherr et al. (1979) concluded that Rb-Sr ages, which were persistently younger than K-Ar ages, were a result of the less-well preserved samples having a disturbed Rb-Sr system. This observed relationship, in addition to the ages presented in Bröcker and Franz (1998), may be interpreted as the less-well preserved samples suffering from excess argon contamination and yielding older ^{40}Ar-^{39}Ar ages, rather than younger Rb-Sr ages.

In this study we have chosen the Tavsanli Zone of NW Turkey (Figure 5.1), a relatively little studied region of HPLT metamorphic rocks, to investigate excess argon in a simple geological system. In contrast to previous studies, the Tavsanli Zone of NW Turkey has only undergone a single subduction-exhumation metamorphic cycle (Sherlock et al. submitted a). The implications of this are that the system is simple in that: i) samples contain a single generation of white mica and have not been thermally overprinted, and ii) there are no relic assemblages from previous metamorphic events which would give rise to memory effects within the argon isotopic system.

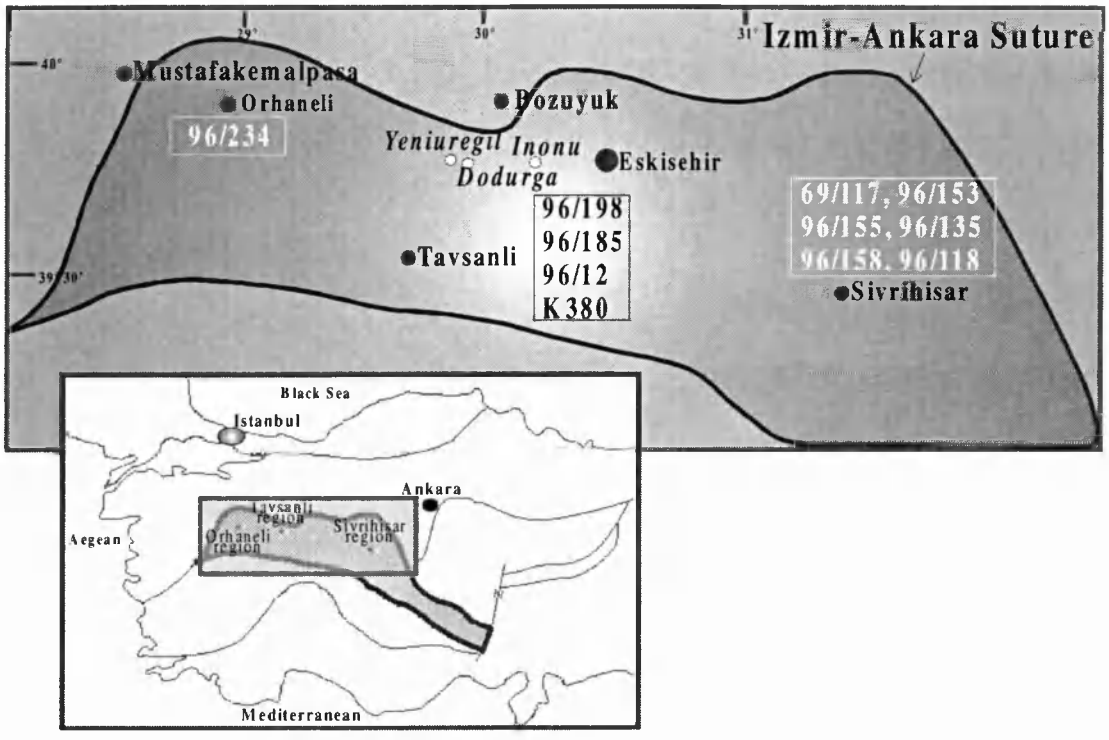

Figure 5.1: Location map of the Tavsanli Zone and sample localities.

5.1.2 Excess argon in the Tavsanli Zone?

Previous geochronological estimates of the age of HPLT metamorphism have raised a number of key questions. The first isotopic age determinations were K-Ar white mica ages of 65 and 82 Ma from the Sivrihisar region (Cogolu and Krummenacher, 1967). Higher precision ^{40}Ar-^{39}Ar white mica ages of 89 to 71 Ma (Okay and Kelley, 1994) and 97 Ma (Okay et al., 1998), and a sodic-amphibole age of 108 Ma (Harris et al., 1994) have been determined from the HPLT rocks in the Orhaneli region. The narrow age ranges reported by Cogulu and Krummenacher (1967) and Okay and Kelley (1994) raised the key question of whether or not they are real and geologically significant, or whether they are an artefact of excess argon. The most recent age determinations for the Tavsanli Zone

HPLT metamorphism are Rb-Sr white mica ages of 79.7 to 82.8 Ma and ^{40}Ar-^{39}Ar white mica and sodic-amphibole ages of 60 to 192 Ma (Sherlock et al., submitted a; Sherlock and Arnaud, submitted). These studies showed that excess argon is responsible for the reported age ranges, and that the white micas from Tavsanli and Sivrihisar crystallised within a much narrower age range than was previously thought. The small ^{40}Ar-^{39}Ar and K-Ar age ranges, comparable to those ranges presented in table 5.1, are an artefact of excess argon (Sherlock et al., submitted a). These ranges are neither too broad or too old to be geologically impossible, and detection of excess argon in similar rocks poses a problem in many HPLT terranes.

A number of key questions have arisen from the preliminary studies (Okay and Kelley, 1994; Harris et al., 1994; Okay et al., 1998): i) is there a regional variation in the distribution of excess argon which may be attributed to a geological event, ii) are there variations in the distribution of excess argon according to lithological type, mineral type and chemistry, deformation and grain size or the thermal history of the rocks; iii) is it possible to assess the relative timing of excess argon contamination; and iv) what are the possible sources of excess argon in the Tavsanli Zone?

In order to understand excess argon in the Tavsanli Zone a detailed investigation of white micas and K-free minerals in rocks from three areas has been carried out using the high spatial resolution UVLAMP (Ultra Violet Laser Ablation microprobe). Samples have been collected from Orhaneli, Tavsanli and Sivrihisar, spatially distributed west to east across the length of the Tavsanli Zone and varying

in distance southwards from the main Tethyan suture (Figure 5.1). The coarsest grain-sized phengites have been chosen for detailed intra-grain UVLAMP profiling.

5.1.3 Geologic setting

Blueschist- and low-temperature-eclogite-facies rocks form an east-west trending linear belt situated south of a major Tethyan suture. The suture represents the site of a major-northward dipping subduction zone, one of a number responsible for the consumption of the Tethys Ocean during the Alpide orogeny. The tract of HPLT rocks, the Tavsanli Zone, is 250 km long and 40 km wide (Figure 5.1) and comprises metamorphosed continental margin sequence rocks. The Tavsanli Zone is stratigraphically uncomplicated and is traditionally sub-divided into the Orhaneli Unit which is concordantly overlain by the Ovacik Unit, and finally tectonically overlain by an ophiolitic peridotite nappe which has not undergone HPLT metamorphism (Okay, 1986). The Orhaneli Unit has attained HPLT conditions. Subduction took place in an oblique convergent setting during the early Cretaceous, followed by syn-subduction exhumation and white mica crystallisation between 79.7 ± 1.6 and 82.8 ± 1.6 Ma (Rb-Sr white mica, Sherlock et al., submitted a). In the Orhaneli Unit, the maximum temperatures attained are considered to be 430°C in the Orhaneli region (Okay and Kelley, 1994), and 450° C and 550° C in the Tavsanli and Sivrihisar regions respectively (Sherlock et al., submitted a; Sherlock et al., submitted b). The Ovacik Unit has only experienced incipient blueschist-facies metamorphism of up to 200° C and 8 kbar, and is thought to represent a tectonic melange or accretionary wedge (Okay 1982; 1984; 1986). The pristine HPLT assemblages of the Orhaneli Unit have returned from

crustal depths in excess of 70 km to the surface without experiencing thermal overprinting in the greenschist- or amphibolite-facies, due to the refrigeration effects of syn-subduction exhumation (Sherlock et al., submitted a, b).

5.1.4 Sample petrography

A suite of metachert, metapelite and metabasite samples have been studied petrographically using standard thin section and electronprobe microanalyser techniques. Ten samples have been analysed in detail from the Orhaneli, Tavsanli and Sivrihisar regions, the most phengite-rich having been chosen for their suitability to the ^{40}Ar-^{39}Ar technique.

Metacherts and metapelites have relatively simple mineralogies. Sample 96/234 from the Kocasu River valley near to Orhaneli (Figure 5.1) is a blueschist-facies phengite-rich metachert with the assemblage quartz + phengite ± lawsonite ± hematite. Phengite, and where present lawsonite, define the main penetrative foliation. Samples 96/12, 96/185, 96/198 and K380 from the Tavsanli region (Figure 5.1) are blueschist-facies metapelites and commonly have the assemblage quartz + phengite + sodic amphibole + lawsonite. The phengite, sodic-amphibole and lawsonite define the main foliation, which is weakly crenulated in samples 96/12, 96/185 and K380, and in places isoclinally folded in sample 96/198. The rocks of the Sivrihisar region are predominately metabasites and are more mineralogically complex than metachert and metapelite lithologies. 96/158 from the Sivrihisar region (Figure 5.1) is a low-temperature eclogite-facies lithology which has the assemblage garnet + sodic pyroxene + sodic amphibole + phengite +

lawsonite + quartz + titanite. The main foliation comprises sodic pyroxene + sodic amphibole + phengite + lawsonite and has been isoclinally folded. Samples 96/117 and 96/118 from the Sivrihisar region (Figure 5.1) are from a single outcrop which displayed petrographical evidence of late-stage fluid influx parallel to the foliation. Both samples are lawsonite-metabasites with the assemblage lawsonite + phengite + sodic amphibole + sodic pyroxene. Sample 96/117 is green in appearance due to late-stage epidote, and calcite and chlorite alteration. Samples 96/153 and 96/155 are also lawsonite-metabasites from the Sivrihisar region (Figure 5.1) but are finer grain-sized than samples 96/117 and 96/118, with a less well-developed foliation. Sample 96/134 is a metapelite from the Sivrihisar region (Figure 5.1) with the assemblage phengite + quartz + sodic-amphibole + titanite.

5.1.5 White micas in the Tavsanli Zone

The white micas which have been analysed are of varying grain sizes ranging from 30 μm to 100 μm in diameter. Grain sizes are generally coarser in the Sivrihisar region than in the Orhaneli or Tavsanli regions. In all three regions white micas are of the Si-rich phengite variety and have Si contents in the range 3.42 to 3.79 (p.f.u.) (Table 5.2). Most analyses do not lie on the ideal muscovite-celadonite mixing line and both the Tschermak exchange ($[Mg, Fe^{2+}]^{iv}$, $Si^{vi} = Al^{vi}$, Al^{iv}) and Fe^{3+}-Al^{3+} substitution has occurred in most phengites analysed (Sherlock et al., in submitted b). Compositionally the phengites do not vary between either the different regions or different lithologies, though samples 96/117 and 96/118 from the Sivrihisar region show some variation in K/Na ratios. Sample 96/117 shows petrographic evidence for alteration due to foliation-parallel fluid influx, in the

form of fine-grained chlorite and calcite. Phengites in sample 96/117 have lower K/Na ratios than phengites in the pristine equivalent sample 96/118 which displays no petrographical evidence of fluid infiltration.

	96/234	96/198	K380	96/185	96/12	96/134	96/153	96/155	96/158	96/117
SiO_2	51.9	52.42	52.03	52.21	51.8	51.9	52.01	52.13	52.00	49.32
TiO_2	0.1	0.08	0.09	0.09	0.1	0.01	0.01	0	0.20	0.13
Al_2O_3	22.2	22.14	21.90	21.78	22.3	22.7	22.35	22.63	22.40	21.70
MgO	4.41	4.14	4.02	4.23	4	4.5	4.23	4.12	4.27	0.04
MnO	0	0.06	0.07	0	0	0.1	0	0	0.00	4.78
FeO	5.56	4.59	5.33	0.05	4.8	4.38	5.32	4.96	4.93	0.02
Na_2O	0.2	0.08	0.07	4.67	0.1	0.2	0.01	0.1	0.10	4.11
K_2O	10.8	10.81	10.51	0.11	10.8	11.1	10.69	10.85	11.00	0.10
Total	94.18	94.33	94.02	10.98	94.1	94.9	94.62	94.79	94.90	0.00
Si	3.55	3.58	3.57	94.13	3.6	3.53	3.54	3.53	3.60	91.27
Ti	0.01	0.00	0.00	3.58	0	0	0	0.01	0.00	3.50
Al	1.79	1.78	1.77	0.00	1.8	1.82	1.81	1.79	1.80	0.01
Mg	0.45	0.42	0.41	0	0.4	0.46	0.42	0.44	0.40	0.00
Mn	0	0.00	0.00	0.43	0	0.01	0	0	0.00	0.51
Fe	0.26	0.26	0.31	0.00	0.3	0.24	0.23	0.25	0.20	0.00
Na	0.03	0.01	0.01	0.27	0	0.03	0.01	0.01	0.00	0.24
K	0.94	0.94	0.92	0.96	0.9	0.96	0.96	0.95	1.00	0.01
Total	7.02	7.00	7.00	7.02	7.01	7.04	6.97	6.98	7.00	7.09

Table 5.2: Representative phengite analyses from samples analysed.

5.1.6 Experimental methods

High-spatial resolution ^{40}Ar-^{39}Ar white mica ages were obtained using the Ultra-Violet Laser Ablation Microprobe (UVLAMP) extraction technique. For a detailed account of the technique see Reddy et al. (1997) and Appendix A. Samples were monitored using the GA1550 biotite standard with an age of 97.9 Ma (McDougall and Harrison, 1988). The calculated J value for the samples was 0.00583 ± 0.000029, and results were corrected for blanks, ^{39}Ar decay and neutron-induced interference reactions. The correction factors used were: ($^{39}Ar/^{37}Ar$)Ca = 0.00067,

$(^{36}Ar/^{37}Ar)Ca = 0.000255$, $(^{40}Ar/^{39}Ar)K = 0.048$ based on analyses of Ca and K salts. All samples were irradiated at the RisØ National Laboratory, Denmark.

5.1.7 Results

Phengites and K-free phases have been analysed using the UVLAMP. Results are presented in Tables E.1 to E.11 in Appendix E.

5.1.7.1 UVLAMP intra-grain and whole phengite analyses

18 detailed intra-grain analyses were performed on phengite with additional ages from finer grain-sized single phengite grains.

5.1.7.1.1 Orhaneli region

From the Orhaneli region traverses 1 and 2 in phengites from sample 96/234 gave intra-grain age ranges of 94 ± 5 to 125 ± 9 Ma and 106 ± 5 to 124 ± 6 Ma. The two phengites analysed were approximately 100 μm and 40 μm in diameter respectively. Traverse 1 is asymmetric but broadly concave with a core to rim age increase (Figure 5.2).

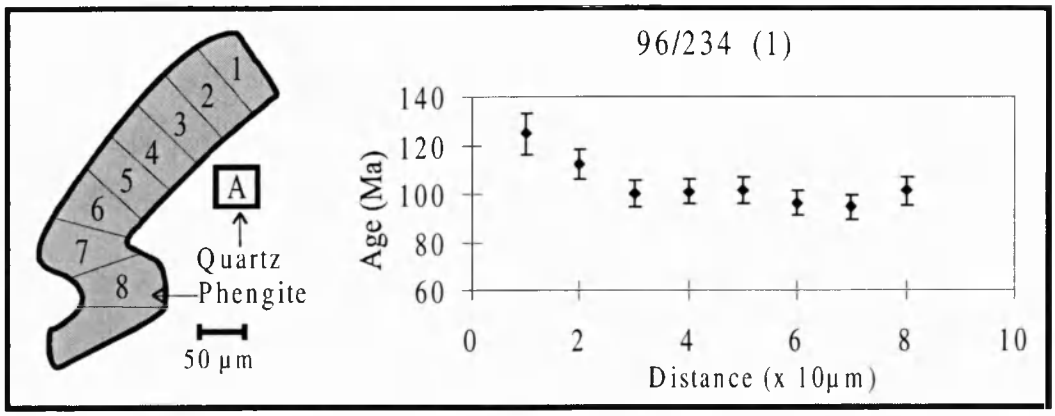

Figure 5.2: UVLAMP traverse 1 across phengite grain in sample 96/234 from the Orhaneli region.

Traverse 2 is irregular with no systematic increase in age from core to rim (Figure 5.3). Quartz analysis A on figure 5.2 corresponds to quartz analysis A in table E.1.

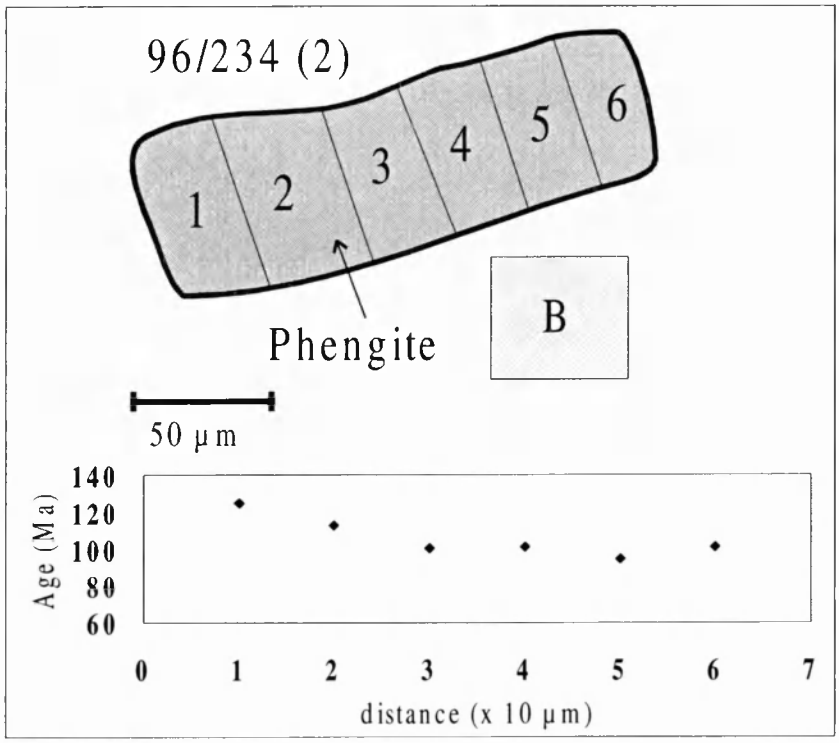

Figure 5.3: UVLAMP traverse 2 from sample 96/234 from the Orhaneli region.

Single finer grain-sized phengites yielded ages of 84 ± 6 and 154 ± 7 Ma. Points 1 and 3 in traverse 1 and points 3 to 6 in traverse 2 have elevated $^{37}Ar/^{39}Ar$ ratios which most likely correspond to analyses which have incorporated adjacent

lawsonite or inclusions of lawsonite. Quartz analysis B on figure 5.3 corresponds to analysis B in table E.1.

5.1.7.1.2 Tavsanli region

Four samples were analysed from the Tavsanli region. Traverses 3 and 4 from sample 96/198 are from phengites 100 μm and 70 μm in diameter; traverse 3 yielded an age range of 86 ± 3 to 111 ± 3 Ma (Figure 5.4), traverse 4 an age range of 93 ± 4 to 123 ± 7 Ma (Figure 5.5). In traverse 3 there is an increase in age asymmetrically towards one rim, but in traverse 4 there is no systematic age variation. Quartz analyses C and D on figures 5.4 and 5.5 correspond to analyses C and D in table E.2. Amphibole analyses A, B and C on figures 5.4 and 5.5 correspond to amphibole analyses A, B and C in table E.2. Phengite analysis A on figure 5.5 corresponds to phengite analysis A in table E.2.

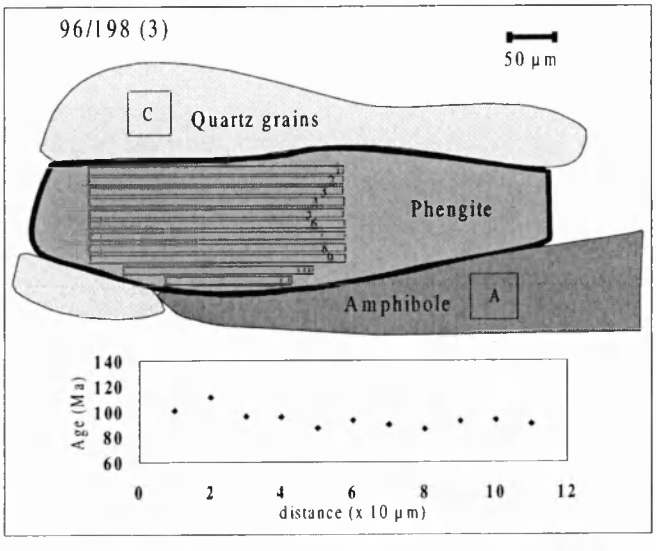

Figure 5.4: UVLAMP traverse 3 from sample 96/198 from the Tavsanli region.

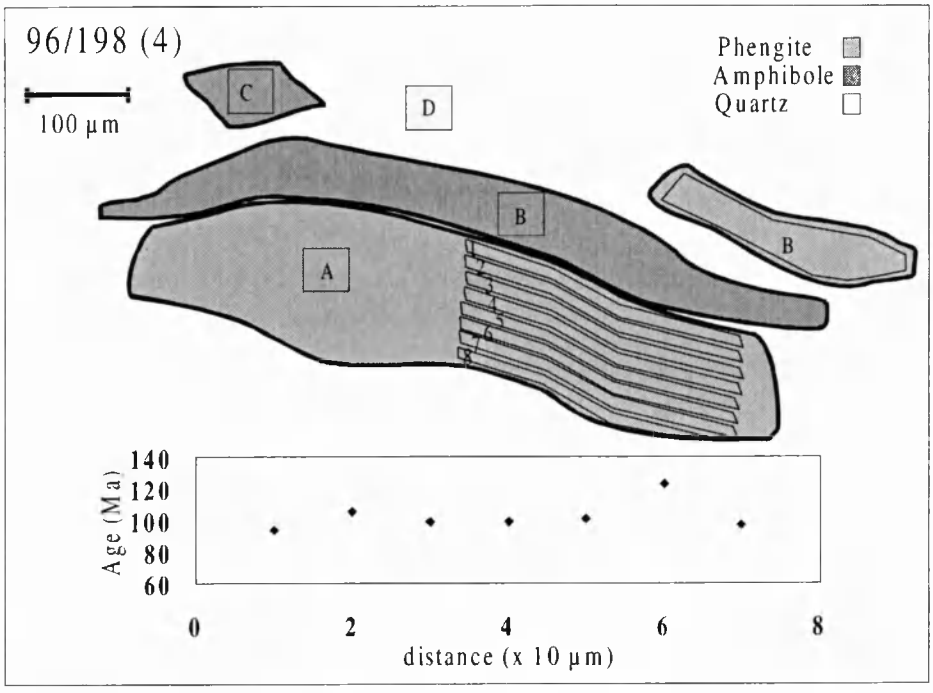

Figure 5.5: UVLAMP traverse 4 from sample 96/198 from the Tavsanli region.

Traverses 5, 6 and 7 are also from sample 96/198 but from finer grain-sized phengites of between 30 µm and 40 µm in diameter.

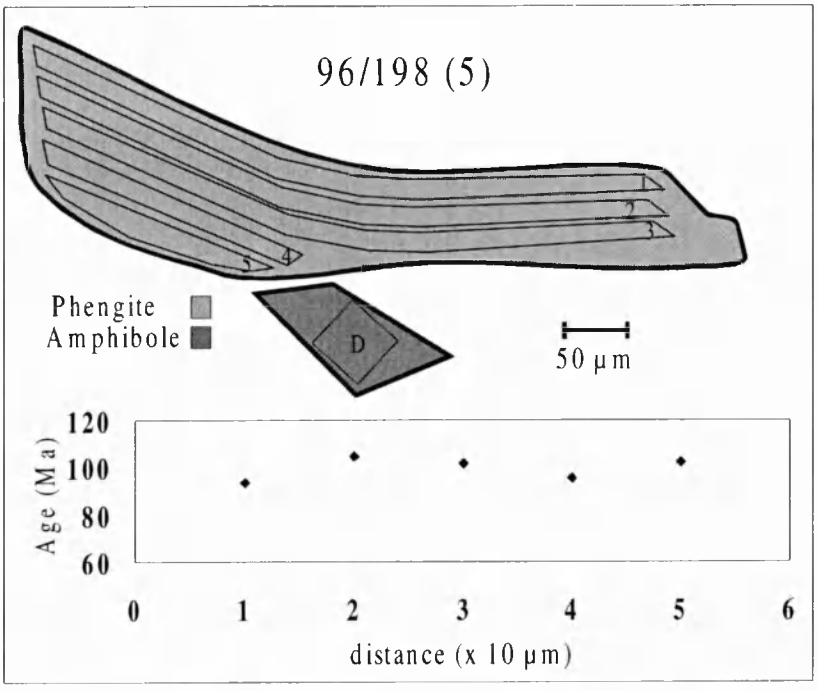

Figure 5.6: UVLAMP traverse 5 from sample 96/198 from the Tavsanli region.

The age ranges were 95 ± 3 to 104 ± 3 Ma, 95 ± 5 to 104 ± 3 Ma and 96 ± 3 to 97 ± 4 Ma (Figures 5.6, 5.7, 5.8). Point 2 of traverse 5 has an elevated $^{37}Ar/^{39}Ar$ ratio and is most likely due to included or adjacent lawsonite. Amphibole analysis D on figure 5.6 corresponds to amphibole analysis D in table E.2.

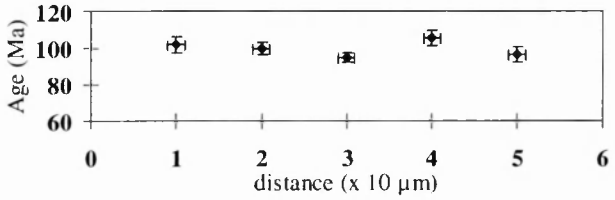

Figure 5.7: UVLAMP traverse 6 from sample 96/198 from the Tavsanli region.

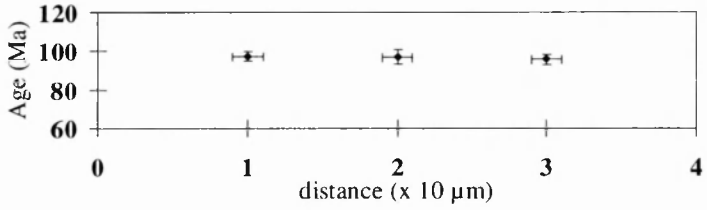

Figure 5.8: UVLAMP traverse 7 from sample 96/198 from the Tavsanli region.

Four single phengite grains of 30 µm in diameter were analysed and gave an age range of 95 ± 3 to 105 ± 2 Ma. In sample K380 traverse 8 gave an age range of 91 ± 20 to 159 ± 15 Ma, with an asymmetric age increase from core to one rim (Figure 5.9).

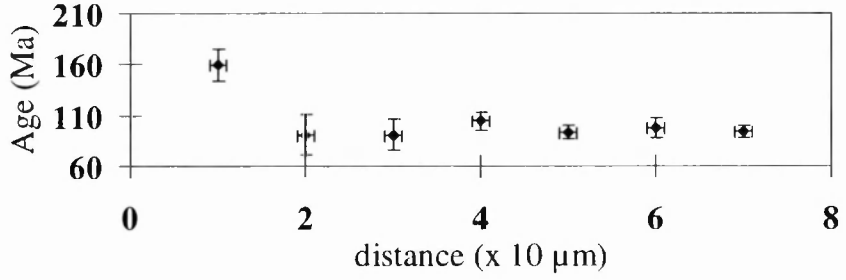

Figure 5.9: UVLAMP traverse 8 from sample K380 from the Tavsanli region.

Points 1, 3 and 6 of traverse 8 have elevated $^{37}Ar/^{39}Ar$ ratios which are attributed to lawsonite included in the phengite.

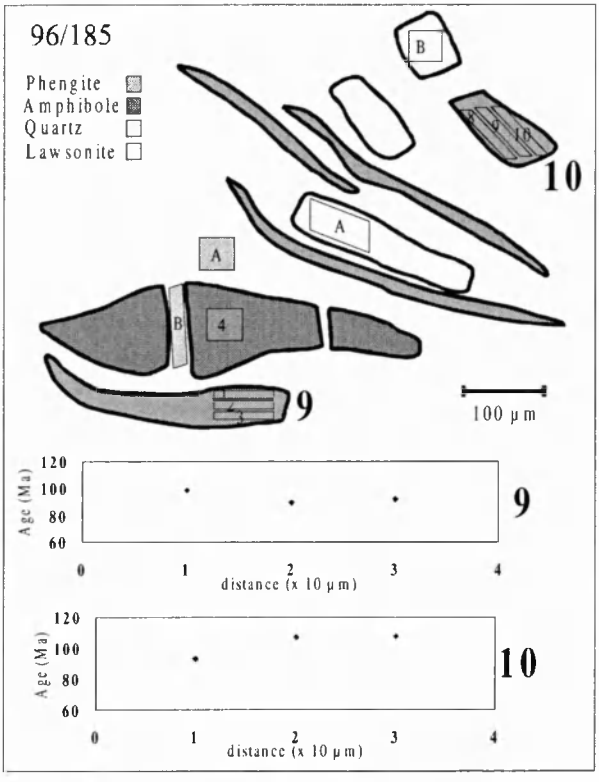

Figure 5.10: UVLAMP traverses 9 and 10 from sample 96/185 from the Tavsanli region.

Traverses 9 and 10 are from sample 96/185, and the coarsest-grain sized phengites of approximately 50 µm in diameter yielded intra-grain age ranges of 90 ± 4 to 99 ± 7 Ma and 93 ± 3 to 108 ± 3 Ma (Figure 5.10). Point 3 on traverse 10 has a high $^{37}Ar/^{39}Ar$ ratio due to the analysis of adjacent lawsonite. Single finer grain-sized phengites gave ages of 91 ± 5 to 105 ± 3 Ma. Quartz analyses A and B on figure 5.10 correspond to analyses A and B in table E.3. Amphibole analyses A on figure 5.10 corresponds to amphibole analysis A in table E.3. In sample 96/12 phengites do not exceed 30 µm in diameter, and traverse 11 yielded an intra-grain age range of 75 ± 6 to 79 ± 5 Ma (Figure 5.11). Point 1 on traverse 11 has a high $^{37}Ar/^{39}Ar$ ratio due to the analysis of lawsonite. Single finer grain-sized micas in sample 96/12 yielded ages which were between 78 ± 3 and 89 ± 1 Ma, the grain which

yields the lowest age has a high $^{37}Ar/^{39}Ar$ ratio, and is likely to be due to the incorporation of included or adjacent lawsonite.

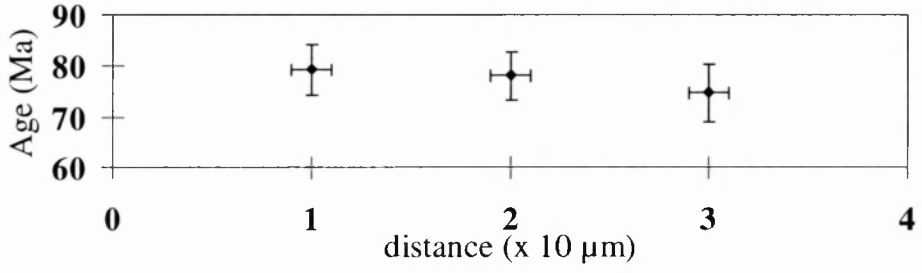

Figure 5.11: UVLAMP traverse 11 from sample 96/12 from the Tavsanli region.

5.1.7.1.3 Sivrihisar region

Samples from the Sivrihisar region are coarser grained and six samples have been analysed. Traverses 12 and 13 from samples 96/153 and 96/155 respectively, gave intra-grain age ranges of 100 ± 4 to 120 ± Ma and 78 ± 3 to 96 ± 3 Ma (Figures 5.12 and 5.13).

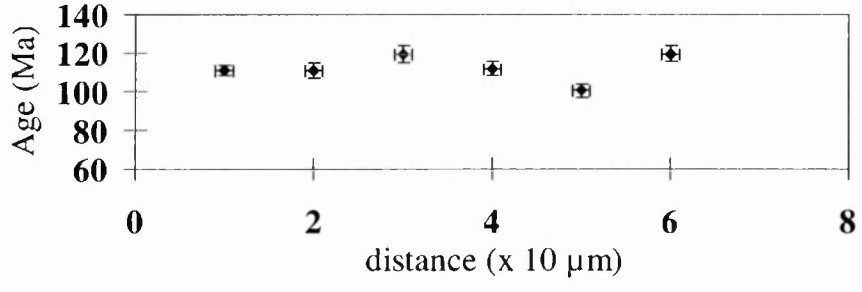

Figure 5.12: UVLAMP traverse 12 from sample 96/153 from the Sivrihisar region.

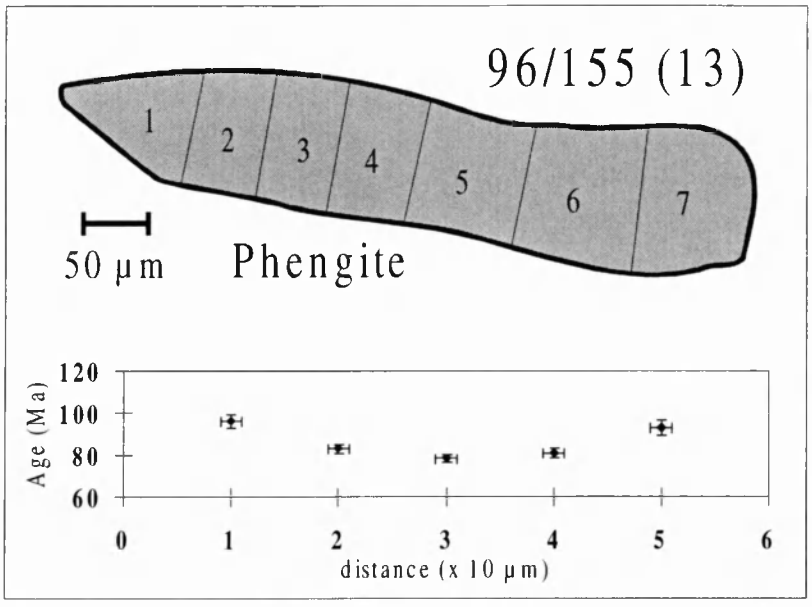

Figure 5.13: UVLAMP traverse 13 for sample 96/155 from the Sivrihisar region.

Traverse 12 yielded no systematic age range while traverse 13 yielded a concave traverse systematically increasing from core to both rims. Points 2, 4 and 5 of traverse 12 have high $^{37}Ar/^{39}Ar$ ratios due to the influence of adjacent or included lawsonite. In sample 96/155 single fine grain sized phengite yielded ages of 111 ± 11 Ma, 112 ± 4 Ma and 82 ± 2 Ma Point 3 on traverse 13 has a high ^{37}Ar-^{39}Ar ratio and is due to the incorporation of lawsonite in the mica analysis. Single phengite grains in sample 96/153 gave an age range of 82 ± 2 Ma to 112 ± 4 Ma, two of which have very high $^{37}Ar/^{39}Ar$ ratios and may either be due to lawsonite or epidote adjacent to the phengites. Traverses 14 and 15 from samples 96/117 and 96/118 gave age ranges of 78 ± 4 to 85 ± 5 and 79 ± 4 to 89 ± 5 Ma. In neither case were there any systematic age increases (Figures 5.14 and 5.15).

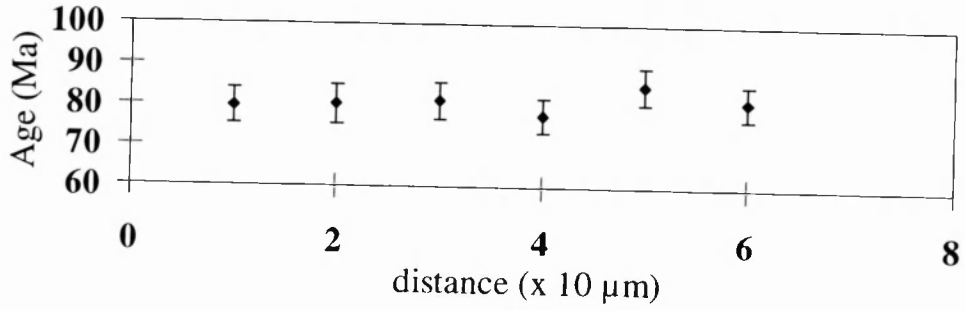

Figure 5.14: UVLAMP traverse 14 from sample 96/117 from the Tavsanli region.

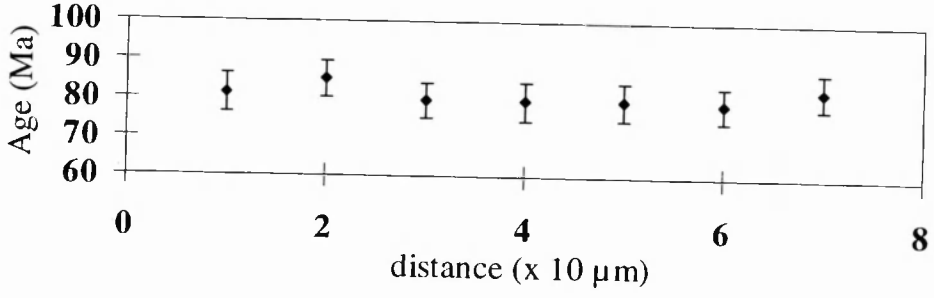

Figure 5.15: UVLAMP traverse 15 from sample 96/118 from the Sivrihisar region.

In sample 96/158 the coarsest phengite grain, with a diameter of approximately 100 µm, yielded an asymmetric concave traverse 16 (Figure 5.16). The age range obtained is 72 ± 3 to 100 ± 5 Ma, with ages increasing towards the rims. Two 50 μm^2 pits ablated within the remaining grain from which traverse 16 was taken, gave ages of 74 ± 2 and 80 ± 2 Ma. Traverse 17 is from a finer grain-sized phengite some 40 µm in diameter, and gave an age range of 82 ± 3 to 87 ± 4 Ma (Figure 5.17).

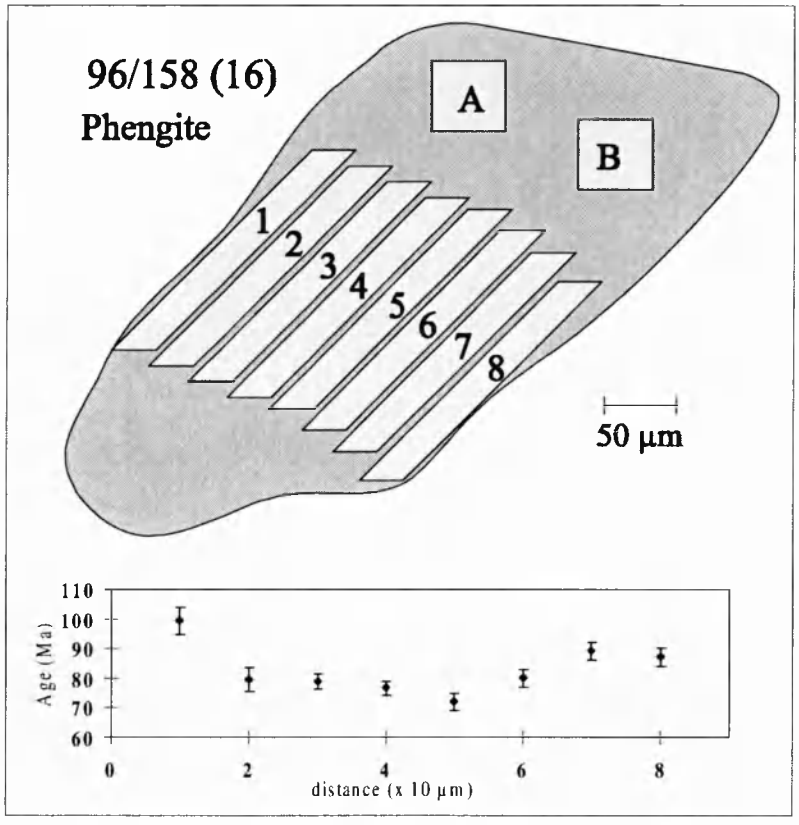

Figure 5.16: UVLAMP traverse 16 from sample 96/158 from the Sivrihisar region.

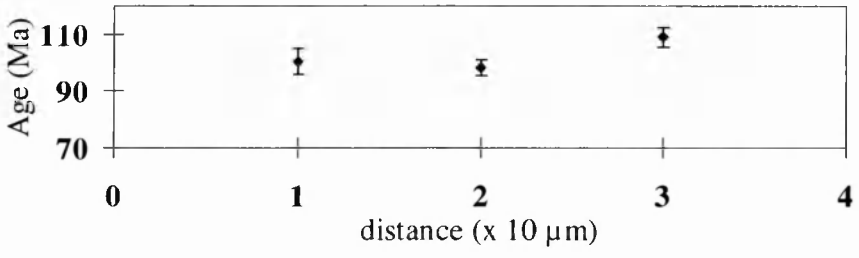

Figure 5.17: UVLAMP traverse 17 from sample 96/158 from the Sivrihisar region.

Points 1 and 2 on traverse 17 have elevated $^{40}Ar/^{39}Ar$ ratios, attributable to an incorporation of either lawsonite, epidote or clinopyroxene within the analysis. Single finer grain-sized phengites gave ages of 83 ± 2 to 107 ± 3 Ma. In sample 96/135 the maximum grain size of phengites is 50 µm in diameter, from which traverse 18 gave an age range of 98 ± 3 to 109 ± 3 (Figure 5.18).

Single finer grain-sized phengites gave ages between 98 ± and 129 ± 87 Ma.

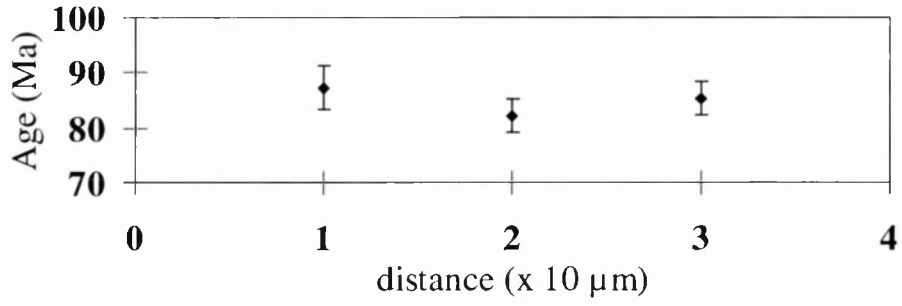

Figure 5.18: UVLAMP traverse 18 from sample 96/135 from the Sivrihisar region.

5.1.7.2 UVLAMP analysis of potassium-free minerals

Where applicable, quartz, sodic-amphibole, lawsonite and garnet have been analysed. The results are within Tables E.1 to E.11.

5.1.7.2.1 Quartz

Quartz analysed in sample 96/234 from Orhaneli gave apparent ages of 109 ± 6 to 1506 ± 561 Ma, though most analyses showed only ^{40}Ar at background levels. Four out of six quartz analyses have high $^{37}Ar/^{39}Ar$ ratios which are most likely a result of analysing adjacent fine-grained lawsonite. Two out of six analyses have high $^{38}Ar/^{39}Ar$ ratios indicative of fluid inclusions containing Cl-rich brines (e.g. Cumbest et al., 1994). The high $^{38}Ar/^{39}Ar$ analyses correspond to quartz analyses with the highest $^{40}Ar/^{39}Ar$ ratios. These grains are also from the high-strain regions. In the Tavsanli region, quartz in samples 96/198 contains minor amounts of ^{40}Ar, with a single analysis yielding an apparent age of 724 ± 36 Ma. Quartz in sample

96/185 contains much greater concentrations of ^{40}Ar, the two apparent ages obtained are 467 ± 44 and 348 ± 281 Ma. A quartz analysis in an unstrained region contains no argon. The second quartz analysis from a high-strain region has high $^{40}Ar/^{39}Ar$, $^{38}Ar/^{39}Ar$, $^{37}Ar/^{39}Ar$, and $^{36}Ar/^{39}Ar$, indicative of atmospheric argon enriched in excess ^{40}Ar in addition to Cl-derived argon from fluid inclusions. The elevated $^{37}Ar/^{39}Ar$ ratio is most likely due to adjacent fine-grained lawsonite.

5.1.7.2.2 Sodic-amphibole

In sodic-amphibole analyses from sample 69/12 from the Tavsanli region, five out of eight have very high ^{40}Ar-^{39}Ar ratios, with apparent ages of 1818 ± 826 and 157 ± 130 Ma. Sodic-amphibole in sample 96/185 yields an apparent age of 676 ± 383 Ma. In the Sivrihisar region amphibole analysed in sample 96/158 contained significant ^{40}Ar and yielded an apparent age of 109 ± 7 Ma. Lawsonite has been analysed in sample 96/185 from the Tavsanli region, and had a high $^{40}Ar/^{39}Ar$ ratio and an apparent age of 117 ± 17.

5.1.7.2.3 Garnet

Garnet in sample 96/158 from the Sivrihisar region contained no ^{40}Ar. There is no garnet in samples from either the Orhaneli or Sivrihisar regions for comparison.

5.1.7.3 Relative concentrations of excess argon in phengite and K-free minerals.

An estimation of the quantity of excess ^{40}Ar has been made in all minerals based on the ^{40}Ar-^{39}Ar ratio required to yield an age of 80 Ma, which is the Rb-Sr age of white mica crystallisation (Sherlock et al., submitted a), and a maximum ^{40}Ar-^{39}Ar age for the phengite. The estimated excess ^{40}Ar concentrations are therefore a minimum, though they provide a comparative means of assessing inter- mineral variations.

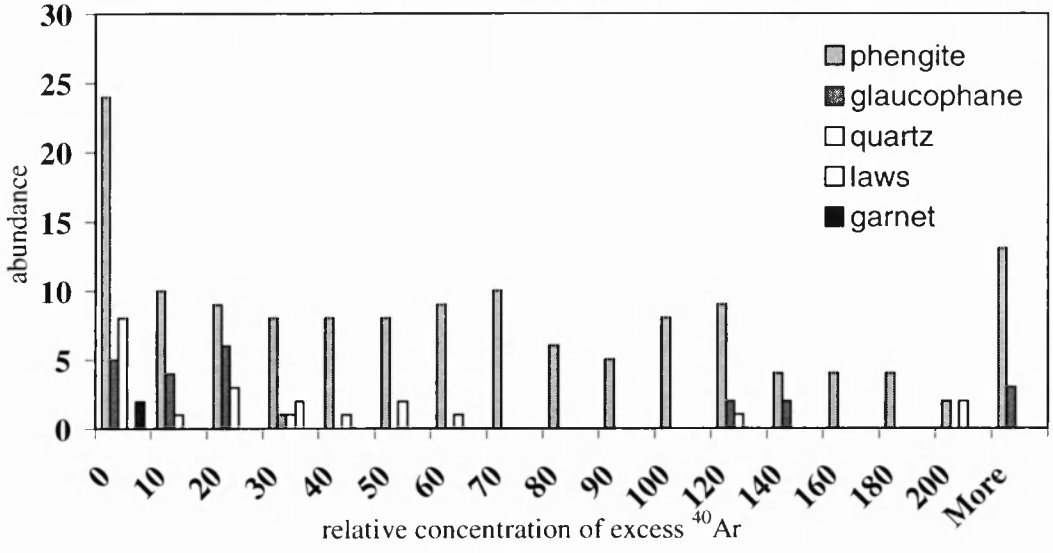

Figure 5.19: Relative concentrations in cc x 10^{-12} of excess 40Ar in all minerals analysed with the UVLAMP.

From figure 5.19 it is apparent that there is a range of concentrations of excess argon within phengite, with a high relative abundance of both high concentrations (greater than 200) and low concentrations (less than 10). Quartz also yields a range of concentrations, with the majority between 0 and 70, and a minor population at 200. Glaucophane follows a similar trend, with concentrations either in the range 0 to 30, or 120 to greater than 200. Lawsonites are between 30 and 40, and two analyses of garnet indicate no excess argon. Phengite contains the highest concentrations of excess argon, and covers the broadest range of excess argon

concentrations. Excess argon is not homogenously distributed among all minerals. High concentrations of excess argon in amphibole and quartz may result from fluid inclusions, indicating the main mineral reservoir for excess argon in HPLT rocks is phengite

5.1.8 Discussion

5.1.8.1 Regional distribution of excess argon in the Tavsanli Zone

Excess argon is prevalent within all three regions of the Tavsanli Zone. This is apparent from the comparison of the ^{40}Ar-^{39}Ar white mica ages with Rb-Sr white mica ages from the same samples (Sherlock et al., submitted a). The ^{40}Ar-^{39}Ar white mica ages are up to 30 Ma older than Rb-Sr white mica ages (Sherlock et al., submitted a; Sherlock and Arnaud, submitted). Within the Orhaneli region, phengites of varying grain sizes are pervasively contaminated by excess argon. The mean ages for traverses 1 and 2 are 36 and 24 Ma older than Rb-Sr white mica ages for the same metamorphic event. In the Tavsanli region excess argon is also pervasive. The mean ages for phengite traverses 3 to 10 are in the range 93 ± 4 Ma to 103 ± 7 Ma, 13 to 23 Ma older than Rb-Sr white mica ages from the same locality. The mean age is noticeably lower in sample 96/12 which has a mean age of 77 ± 2 Ma for traverse 11. In the Sivrihisar region excess argon is prevalent though not consistently pervasive in coarse phengite, in that much lower ages are obtained from the cores of some grains. Traverses 13 to 17 have mean ages in the range 81 ± 2 Ma to 86 ± 7 Ma, which are between 0 Ma and 4 Ma older than Rb-Sr white mica ages from the same region. Samples 96/153 and 96/135 are the

exception to this and for traverses 12 and 18 mean ages are 112 ± 6 Ma and 103 ± 5 Ma, 20 Ma and 11 Ma older than Rb-Sr white mica ages for the same locality.

5.1.8.2 Excess argon and lithological variation

In the metachert sample 96/234, excess argon is prevalent and pervasive within both phengite and quartz. The mean age for phengite traverses are 116 ± 10 and 104 ± 10 Ma, which is older than the initiation of subduction in the region (Yilmaz and Sengör, 1981). Quartz analyses are variable in isotopic composition. Of those with high $^{40}Ar/^{39}Ar$ ratios, many but not all have high $^{38}Ar/^{39}Ar$ ratios indicative of fluid-inclusions rich in chlorine in addition to excess ^{40}Ar. All the metapelites, with the exception of sample 96/12, are contaminated pervasively by excess argon and yield ages up to 24 Ma older than Rb-Sr ages. The mean ages for intra-grain phengite traverses within the metapelites are between 94 ± 7 Ma and 104 ± 23 Ma. Sample 96/12 differs in that excess argon is non-pervasive in the phengite, and the mean intra-grain traverse age is 77 ± 2 Ma. In metapelite samples generally, quartz and sodic-amphibole contain variable concentrations of excess argon, which is not detected in many analyses. The ^{38}Ar-^{39}Ar concentrations are variable. In quartz there is evidence of some influence of chlorine-rich brines. In sodic-amphibole chlorine in fluid inclusions and chlorine in the mineral lattice are indistinguishable. In metabasite samples much younger ages are found within cores of the coarsest phengites, and excess argon is not always pervasive, with a higher frequency of younger ages in phengite cores than in either the metachert or metapelite samples. Mean ages for intra-grain phengite traverses are 81 ± 2 Ma to 86 ± 7 Ma, with the

exception of sample 96/153 which has a mean age of 112 ± 6 Ma. Excess argon is apparent in sodic-amphibole, but there is no excess argon in garnet.

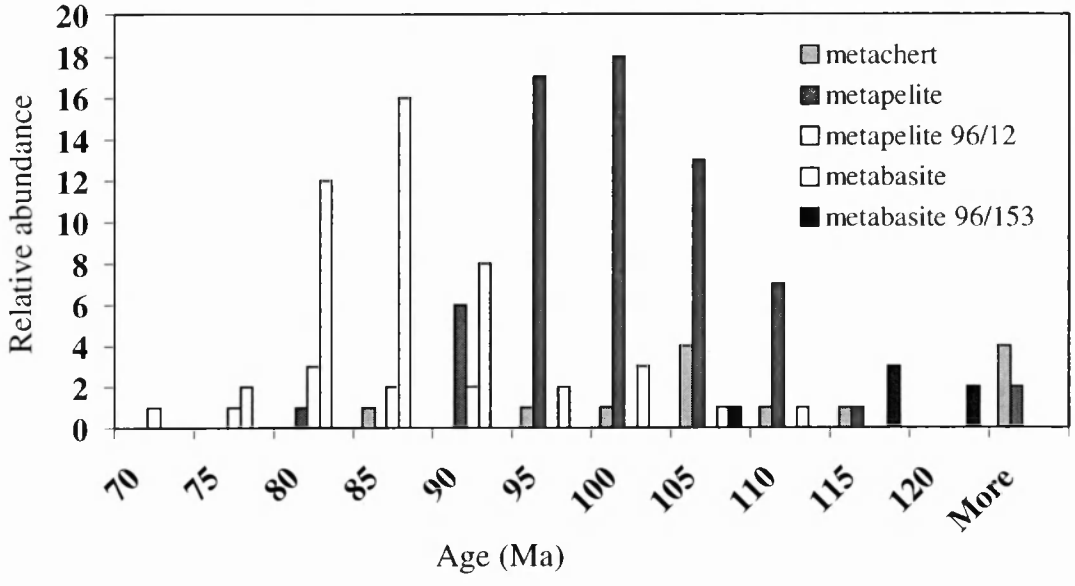

Figure 5.20: Distribution of UVLAMP ^{40}Ar-^{39}Ar phengite ages versus lithological type

Figure 5.20 illustrates the relationship between apparent ^{40}Ar-^{39}Ar phengite age and lithological type. Metabasite samples yield a normal distribution curve with a peak within the 85 to 90 Ma interval. Metapelites also form a normal distribution curve and peak within the 100 to 105 Ma interval. Metachert phengite ages are more widely distributed with two peaks at 105 to 110 Ma and greater than 125 Ma. Samples 96/12 (metapelite) and 96/153 (metabasite) are exceptions to these observed trends (Figure 5.20). Sample 96/12 yields low apparent phengite ages which are comparable to those from the metabasites, and sample 96/153 yields apparent phengite ages which are much older than those of other metabasites and more comparable to those from the metacherts and metapelites.

It is apparent from figure 5.20 that excess argon is heterogeneously distributed among different lithological types. Excess argon is far more pervasive and of greater concentrations in both the metachert and the metapelites, and apparent phengite ages are higher, than in the metabasites. The concentration of excess argon and therefore the extent of excess argon contamination, appears to be controlled by lithological type. The correlation of excess argon with the K_2O content of the lithology is reminiscent of the situation in some dry granulite rocks where excess argon was shown to correlate with K_2O (Foland, 1979) and indicated near closed system behaviour for argon.

5.1.8.3 Excess argon and phengite mineral chemistry.

White mica chemistry has formed the basis of previous discussions of argon retentivity and excess argon in metamorphic rocks. Chopin and Maluski (1980) suggested that white micas with higher celadonitic components are much more retentive of argon than lower pressure muscovites, challenging the traditional view of the blocking temperature concept and stating that the blocking temperature must be significantly higher in more celadonitic white micas, hence the older Alpine ^{40}Ar-^{39}Ar ages. Scaillet et al. (1992) found evidence for increasing retentivity of argon with increasing Mg content in white mica. Dahl (1996), based on ionic porosity arguments, stated that argon retentivity should increase with increasing K/Na ratios with increasing pressure. Phengites in rocks from all three areas studied in the Tavsanli Zone, covering all lithologies, lie in a restricted compositional range. The differences observed in the amount and pervasive nature of the excess argon in Tavsanli Zone cannot be attributed to variations in K/Na

ratios. There are also no significant variations in the ferromagnesian components of the phengites. The likelihood of a significantly higher closure temperature for argon in phengitic white mica compared with muscovite has been discounted as a possible reason for the ^{40}Ar-^{39}Ar ages in the Tavsanli (Sherlock and Arnaud, submitted).

5.1.8.4 Excess argon and deformation

In the metachert from the Orhaneli region, the analyses which have been made in the vicinity of the kinks in phengites do not correspond to the oldest ages, and therefore the highest excess argon concentrations. In Traverse 2 the two analyses which directly correspond to the kink are the lowest ages, 94 ± 5 Ma and 96 ± 6 Ma - the other six analyses all exceeding 100 Ma. In the same sample, excess argon is heterogeneously distributed in quartz. This may be attributed to quartz deformation structures, with excess argon associated with high-strain zones. The same is also true of high- and low-strain quartz in sample 96/185, with the excess argon associated with high-strain zones in quartz. During deformation subsequent to foliation development amphiboles have been extended and boudinaged, leaving extensional cracks within which quartz has recrystallised. Two analyses have been made of the recrystallised quartz for comparison with matrix quartz. One contained excess argon, the second did not. The same is true of the platy matrix quartz which was analysed for comparison.

5.1.8.5 Excess argon and foliation-parallel fluid ingress

Samples 96/117 and 96/118 are from a single lawsonite-metabasite outcrop in the Sivrihisar region. Samples were separated by as much as 30 cm distance. Sample 96/117 green in appearance, sample 96/118 blue in appearance. Both samples have undergone the same thermal history and have the same assemblage but sample 96/117 has additional calcite and chlorite resulting from fluid influx parallel to the foliation prior to the second deformation event. Detailed intra-grain UVLAMP analysis of phengites in both samples reveal that excess argon is prevalent in both samples, and has neither been introduced or removed by late-stage fluids during exhumation.

5.1.9 Timing of excess argon contamination

5.1.9.1 Qualitative assessment

On the basis of the relationships between excess argon and geological and mineralogical observations it is possible to say something of the relative timing of excess argon contamination. Detailed intra-grain phengite analysis suggests that younger cores reflect close to 'real' ages and that rims have been much more greatly affected by excess argon at some point during the later stages of phengite growth, during foliation development. The analysis of the deformed phengite from Orhaneli suggests that excess argon contamination took place prior to the second deformation event. Excess argon *loss* is associated with the mica deformation due to crenulation, similar to results from white micas in Dora Maira (Scaillet et al., 1992; 1996) and contrasting with previous studies which have reported excess argon *gain* under such circumstances (Reddy et al., 1996). Excess argon is also

linked to quartz-deformation which appears to be synchronous with foliation development. The analysis of sodic-amphibole and quartz in extensional cracks in sodic-amphibole reveals little or no excess argon within sodic-amphibole, and no discernible differences between the low-strain matrix and subsequent deformation-related quartz. The implications are that either excess argon preferentially partitions into phengite over sodic-amphibole, or (less likely given other constraints, Dahl, 1996) sodic-amphibole is less retentive of excess argon than phengite.

Excess argon has contaminated phengites during the formation of the main penetrative foliation, prior to the second deformation event. The contamination of phengite by excess argon does not seem to be associated with either peak metamorphic conditions or the late fluids which ingress preferentially along the foliation in the Sivrihisar region.

5.1.9.2 Quantitative assessment

An intra-grain phengite UVLAMP age profile has been modelled using the DIFFARG software (Wheeler, 1996) in order to quantitatively assess the timing and duration of excess argon contamination. The software is capable of simulating argon diffusion profiles and bulk ages of individual mineral grains for any thermal history and grain boundary argon history. The intra-grain traverse 13 from sample 96/155 has been modelled using the DIFFARG software (Figure 5.21), and reveals a number of key points regarding the excess argon evolution of the Tavsanli Zone rocks. Even in this case the apparent excess argon introduction history is complex.

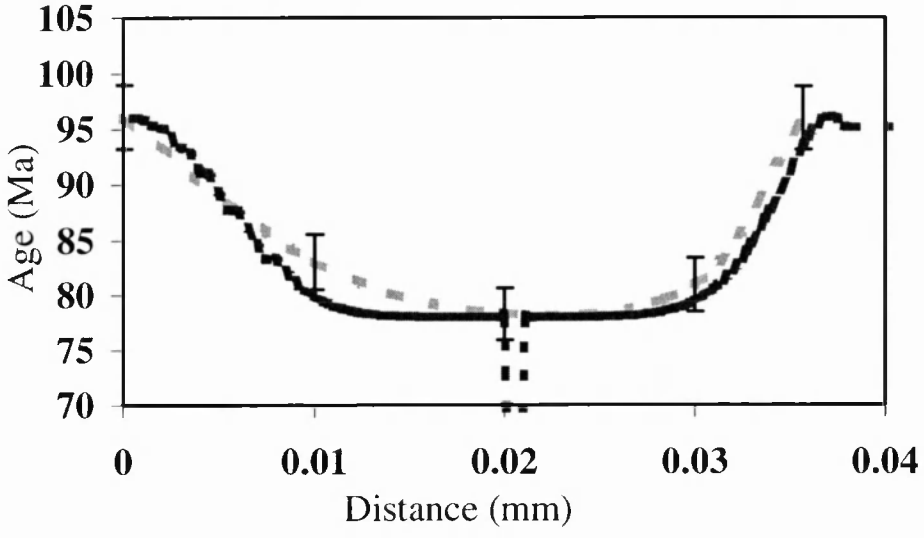

Figure 5.21: Modelling of UVLAMP profile 13 from sample 96/155 using the DIFFARG software of Wheeler (1996).

The thermal history of the white micas input into DIFFARG was derived from Sherlock et al. (submitted a). Modelling the intra-grain phengite age ranges reveals that in order to achieve apparent ages in the cores of 78 Ma (Figure 5.21), excess argon has to be present at the grain boundary at 330° C, causing an apparent grain edge age of 8 Ma rather than 0 Ma. The implications of this are that there has to have been an initial concentration of ^{40}Ar in the grain boundary network, right from the inception of phengite growth, but only sufficient to raise the apparent age from 0 Ma to 8 Ma. Failing this, ages older than 60 Ma cannot be achieved in phengite cores, regardless of thermal history or grain size. It is a requirement that an additional pulse of excess argon enters the mineral lattice and remains there whilst temperatures are in the region of 300° to 320° C. If this additional pulse of excess argon is introduced into the system at higher temperatures, diffusion is sufficiently fast and the balance of argon loss/argon gain, in an effectively open system, is such that the preservation of older ages in the white mica grain is impossible. If excess

argon is introduced at temperatures lower than 300° C then the preserved age distribution is homogeneous from core to rim, and ages are significantly older than those measured in the Tavsanli Zone. The duration of the additional supply of excess argon is of great importance. If the pulse exceeds 1 Ma in duration then the modelled apparent age ranges are much older than the measured intra-grain age ranges.

5.1.10 A model for excess argon in the Tavsanli Zone HPLT rocks

A model for the Tavsanli Zone must account for: i) an initial concentration of excess argon in the grain boundary network prior to phengite growth, ii) ages which are an artefact of excess argon contamination but are neither geologically absurd or sufficiently erratic to be obvious in themselves, iii) higher concentrations of excess argon in metacherts and metapelites than in metabasite lithologies, and iv) an additional influx of excess argon within the temperature range 300° to 330° C.

In a rock which contains potassium, radiogenic argon begins accumulating immediately the rock becomes a closed system, regardless of the status of individual minerals within the rock. During the single metamorphic cycle experienced by the Tavsanli Zone HPLT rocks, potassium-bearing minerals break recrystallise and grow within a progressively evolving paragenesis in response to the transient pressure and temperature conditions. In the absence of fluids fluxing during cooling, the rocks have experienced very low aH_2O (Sherlock et al., submitted b) and remained effectively a closed system. Radiogenic argon is

produced continuously, and since minerals may individually produce argon, the concentration of excess argon builds up in the grain boundary network. In order to calculate K-Ar or ^{40}Ar-^{39}Ar ages it is commonly assumed that argon is lost from a mineral whilst at temperatures which exceed its closure temperature. In other words a hypothetical 'infinite reservoir' (e.g. Dodson, 1973) is assumed, and argon is considered to 'vanish' from the rock. A similar assumption has been made for the Rb-Sr system, recently addressed by Jenkin (1997), in which plagioclase forms a 'sink' for the Sr which would otherwise have been considered 'lost' from the system. In the case of the Tavsanli Zone the HPLT rocks remain in a low-temperature and low-water activity system (Sherlock et al., submitted b) with no extrinsic parameters to render the rocks an 'open' system. This is not an uncommon scenario and is consistent with the observations of Phillipot (1993), whereby fluid movements are often severely restricted in HPLT conditions. In the absence of externally-derived fluids from either adjacent tectonic units or from the mantle for example, and fast fluid-pathways such as major faults or shear zones, there is no mechanism to remove this excess argon from the grain boundary network. The ages which are an artefact of excess argon are neither geologically absurd for the evolution of the Tavsanli Zone, or widely erratic and, may be explained in terms of the relatively young protolith age (maximum sediment age of mid-Jurassic; Livermore and Smith, 1985) and mono-metamorphic history. Within the Alpine Dora Maira for example, where peak high-pressure metamorphism is considered to be at around 35 Ma (Gebauer et al., 1997), ^{40}Ar-^{39}Ar ages white mica ages, which are an artefact of excess argon, are commonly 90 Ma though they can be as old as 130 Ma. Higher concentrations of excess argon are apparent in the Dora Maira, which is most likely due to the age and complexity of the protolith,

Hercynian metagranites and basement which have subsequently undergone ultra-high pressure metamorphism (e.g. Chopin et al., 1991; Biino and Compagnoni, 1992; Henry et al., 1993). Within such a protracted evolution as the Alpine Dora Maira, greater concentrations of excess argon may accumulate in the grain boundary network over time and produce older ages. The observation that metabasites contain lower concentrations of excess argon than metacherts and metapelites may be explained in terms of the *in situ* production of excess argon. The metabasites are less potassic than metacherts and metapelites and, therefore, produce less radiogenic argon throughout their evolution. The additional influx of excess argon responsible for the elevated rim ages in phengites is more difficult to explain geologically, and may best be explained in terms of dynamic recrystallisation, since at temperatures of 300° to 330° C the rocks are still plastically deforming.

5.1.11 Conclusions

From this detailed study of HPLT rocks from the Tavsanli Zone a number of key observations are made:

1. Excess argon varies with lithology. In the simplest metachert assemblages excess argon in phengite is more pervasive, and has higher concentrations, whereas in the metabasites excess argon in phengite is both less pervasive, and of a lower concentration. This observation cannot be explained by phengite mineral chemistry which does not vary significantly, and is more readily explained in terms of lithological type and bulk K. The more phengite-rich and potassic metacherts and

metapelites having higher excess argon concentrations in the grain boundary network than the lower potassium metabasites. This observation is consistent with the results of Foland (1979) who demonstrated that the concentration of excess argon found in biotites was higher in lithologies with higher bulk K.

2 High concentrations of excess argon have become incorporated into quartz, phengite and sodic-amphibole during the exhumation-related deformation event responsible for the formation of the penetrative foliation. This contrasts with the Alpine Dora Maira and Sesia Zone, within which excess argon became incorporated within minerals during peak HPLT metamorphism (Arnaud and Kelley, 1995; Reddy et al., 1996; Pickles et al., 1997). From the analysis of quartz it is apparent that this may have been accompanied by a minor fluid-phase containing chlorine. The concentration of excess argon inherent in the grain boundary network is likely to have been fortified by an additional pulse of excess argon for a duration of 1 Ma whilst the rocks were at temperatures of 330° to 300° C.

3 The transport of excess argon in the Tavsanli Zone cannot be attributed to the late-stage retrogressive foliation-parallel fluid influx which is observed within some metabasites in the Sivrihisar region. Many workers have attributed excess argon to extensive fluid alteration and greenschist-facies metamorphism (e.g. Wartho et al., 1996; von Blackenberg and Villa, 1988) indicating the widespread transport of 'imported' excess argon. Widespread excess argon enrichment in Caledonian eclogites in Norway occurred during a period of increased water activity associated with the eclogitisation of granulites (Boundy et al., 1997). In the Tavsanli Zone,

excess argon has been present in an essentially closed and low-fluid system for an indeterminate time period, the age of the protolith forming an upper limit of approximately 150 Ma. The concentration of excess argon in the grain boundary network is most likely related to the age of the protolith, which will determine the amount of argon which is recycled in the grain boundary network due to prograde breakdown reactions (Scaillet, 1996; Boundy et al., 1997). Rocks of the Tavsanli Zone have undergone a single metamorphic cycle (Sherlock et al., submitted a, b), and thus the problem of inherited trapped argon and memory effects encountered in polymetamorphic terranes (e.g. Scaillet, 1996; Boundy et al., 1997), is much less important.

4 Given the outcrop scale (approximately 100 m) and spatial distribution of adjacent lithologies (1 to 10 m) within the Tavsanli Zone, it is apparent that the mobility of excess argon in a low water activity environment may be less than has previously been suspected. Foland (1979) observed an upper limit of 10 m based on a study of excess argon contamination in biotites within granitic rocks. In the Tavsanli Zone rocks, the spatial distribution of lithologies and strong lithological control on the distribution of excess argon imply that argon mobility was restricted to a maximum of 5 m.

5 The small ^{40}Ar-^{39}Ar age ranges which have been obtained in the Tavsanli Zone HPLT metamorphic belt serve as an illustration of how the problem of excess argon in HPLT rocks may remain undetected and overlooked, whilst more elaborate tectonic models and mechanisms may be invoked to erroneously explain such data.

5.2 Flat plateau and impossible isochrons: apparent ^{40}Ar-^{39}Ar geochronology in a HP terrain

5.2.1 Introduction

'Excess argon' is the additional component of non-radiogenic ^{40}Ar which leads to ages older than the 'real' age, which has proved problematic in a large number of metamorphic terranes. Prior to laser-ablation techniques argon was without exception extracted by furnace step-heating, and the resulting age spectra used to determine a statistically meaningful age. Consequently until the high spatial resolution UVLAMP (Ultra Violet Laser Ablation MicroProbe) was applied to phengites from the Alpine Dora Maira (Arnaud and Kelley, 1995) the pervasive contamination by excess argon in the area was greatly underestimated. This has been corroborated by other techniques (e.g. Bowtell et al., 1994). The much cited ^{40}Ar-^{39}Ar plateau ages of up to 110 Ma for high-pressure metamorphism (e.g. Monié and Chopin, 1991; Scaillet et al., 1990, 1992), although convincingly flat, were probably misleading. It is now more generally accepted that flat plateau may not always reflect the 'real' age of metamorphism (e.g. Ruffét et al., 1995, 1997; Scaillet 1996; Sherlock et al., submitted a). In distinguishing meaningful from problematic age data the isochron approach has historically been used (e.g. Dalrymple and Lanphere, 1974; Lanphere and Dalrymple, 1978; Berger and York, 1981a). This approach enables us to identify the presence of a ^{40}Ar component which results in a deviation of the ^{40}Ar-^{36}Ar ratio from an atmospheric value of 295.5 (Steiger and Jager, 1977). Until now this has been considered extremely

valuable in the detection of excess argon. We present here a furnace step heating ^{40}Ar-^{39}Ar white mica plateau and inverse isochron diagram and Infra-Red laser spot ages which convincingly appear to reflect the 'real' age of a single high-pressure metamorphic event. When ^{40}Ar-^{39}Ar UVLAMP and Rb-Sr white mica ages from the same handsample are compared it is apparent that both the plateau age and the two 'isochrons' present potential flaws and are geologically meaningless.

5.2.2 Geochronological disagreement on a handsample scale.

Sample 96/134 from the Tavsanli Zone high-pressure metamorphic belt in NW Turkey, has yielded a range of isotopic ages for a single metamorphic event. Rb-Sr white mica ages of 79.7 ± 16 to 82.8 ± 1.7 Ma have been reported for high-pressure metamorphism (Sherlock et al., submitted a). Sample 96/134 yields a mineral age of 80.2 ± 1.6 Ma. ^{40}Ar-^{39}Ar UVLAMP analysis ranged from 78 ± 2 Ma to 109 ± 3 Ma.

5.2.3 Results

5.2.3.1 Furnace step-heated phengite

Figure 5.22 illustrates the convincing plateau age of 107 ± 2 Ma from a step-heated mica separate from 96/134, which is consistent with many of the oldest ^{40}Ar-^{39}Ar UVLAMP data for the sample, but is 25 Ma older than the Rb-Sr age. The ages of all seven steps fall within error of one another at the 1 sigma level, and

comprise 94 % of the total ^{39}Ar released (see Table F.1, Appendix F). This exceeds the generally accepted criteria for a plateau age of 3 concordant steps representing a significant proportion of total ^{39}Ar released (e.g. Dalrymple and Lanphere, 1974; Lanphere and Dalrymple, 1978; Berger and York, 1981a) which for most is approximately 50 %.

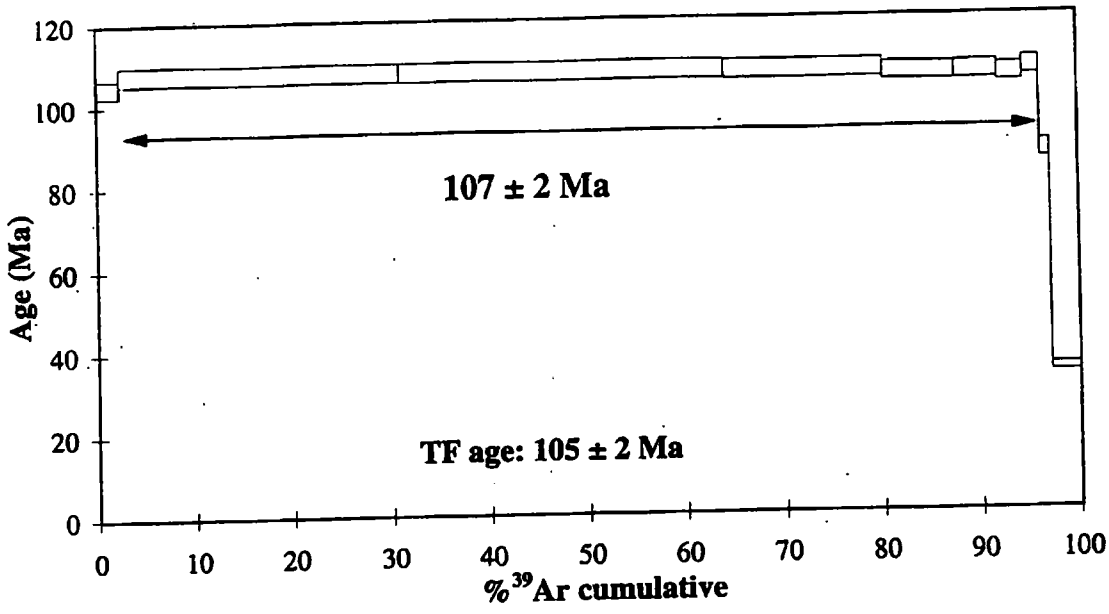

Figure 5.22: Flat age spectra for phengite sample 96/134 with a plateau age of 107 ± 2 Ma on the basis of 94% of the total ^{39}Ar released: total fusion age of 105 ± 2 Ma.

On an inverse isochron diagram the line of best fit drawn through the five points which naturally appear to define an 'isochron' - line *a* on Figure 5.23 - intercepts the y-axis at 0.00513, which is a ^{40}Ar-^{36}Ar ratio of 195 ± 24, far less than even the lowest recorded. The intercept age of 111 ± 2 Ma is within error of the plateau age but 31 Ma older than the Rb-Sr age.-Accounting for the sixth point - shaded circle on Figure 5.23 - has a significant effect on the 'isochron', and increases the MSWD from 0.1 to 2.6. On this scale the intercept on the y-axis is 0.0033 equal to the value for air. 'Isochrons' may be drawn to intercept the x-axis at a range of ages

depending on where the best fit of the five clustered points is assumed. Figure 5.23 depicts the two end-member intercept ages from the apparent range - 107.5 ± 2 Ma and 104.5 ± 2 Ma - lines *b* and *c* respectively. Both are within error of one another at the 1 sigma level, intercept the y-axis at the value for the air ratio, and are 27.5 Ma older than the Rb-Sr age. The fourth 'isochron' in Figure 5.23 - line *d* - is a line which intercepts the y-axis at the value for air, is the 'best fit' for all six data points, and has an intercept age of 107.5 ± 2 Ma.

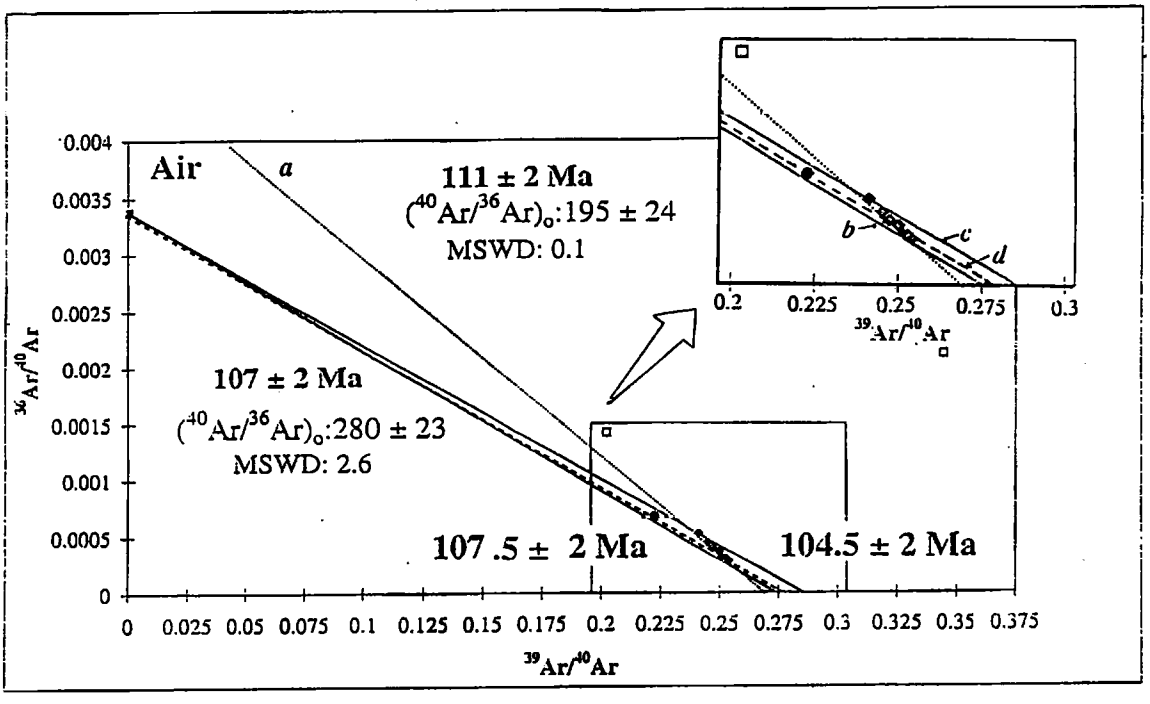

Figure 5.23: Inverse isochron correlation diagram for phengite sample 96/134, with end-members of all 'best fit' lines. Shaded squares are the five points which readily defined an 'isochron', the shaded circle is a sixth point which when taken into account increases the MSWD significantly though introduces a plausible, if incorrect, ^{40}Ar/^{36}Ar ratio. Open squares are discounted points.

The plateau and isochron for 96/134 phengite in Figure 5.23 would historically have been considered sufficient evidence for the 'real' age of high-pressure metamorphism for the Tavsanli Zone.

5.2.3.2 Infra-red laser whole rock analyses

Sample 96/75 is a fine-grained HPLT rock from the Tavsanli Zone. Whole rock laser spot ages gave an age range of 87 ± 4 to 100 ± 3 Ma (Table F.2, Appendix F). This sample has the assemblage phengite + quartz + lawsonite + chloritoid, and in the absence of any other K-bearing phases the whole rock ages are interpreted as white mica ages. The whole rock ages are 7 to 20 Ma older than Rb-Sr ages for samples from the same area and are attributed to excess argon contamination. Figure 5.24 is an inverse isochron correlation diagram illustrating results from sample 96/75. Line *e* is the line of best fit which takes into account all eight points. The interception on the y-axis at 0.0035 exceeds the value for air. Line *f* is made to intercept air when the shaded point is neglected resulting in an increased MSWD from 2.0 to 2.3. The intercept ages for lines *e* and *f* are 96 ± 1 and 98 ± 1 Ma, 16 and 18 Ma older than the Rb-Sr age from the same area.

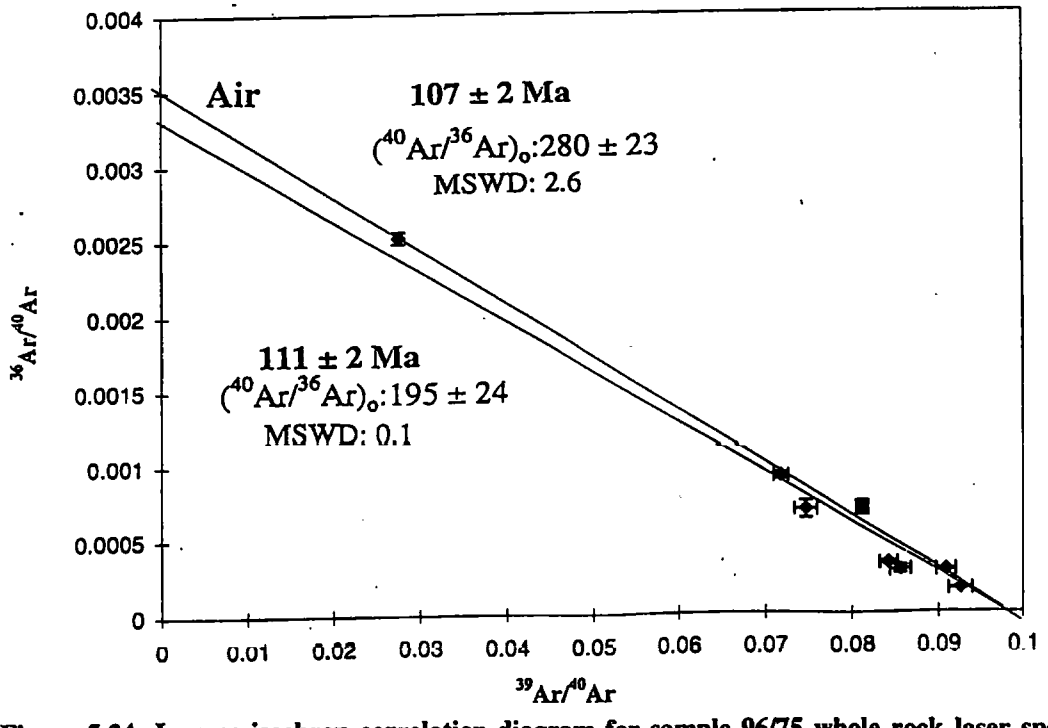

Figure 5.24: Inverse isochron correlation diagram for sample 96/75 whole rock laser spot analyses, with two 'best fit' lines depicted – one fitting all data points, a second neglecting the point with the lowest ^{39}Ar-^{40}Ar ratio.

5.2.4 Discussion

Figures 5.24 to 5.26 are the required graphical representation to prove and disprove the validity of both the 107 ± 2 Ma plateau and the IR laser spot ages. This raises a number of key issues for discussion.

1 *The plateau age is correct and is supported by the inverse isochron correlation diagram.* This assumes that the 'isochron' passes through the value for air on the y-intercept, disproving the presence of excess argon, and has an intercept age of 107 ± 2 Ma. The most immediate point to be addressed is why phengite ^{40}Ar-^{39}Ar ages are 27 Ma *older* than Rb-Sr ages for the same mica. One possibility is that the Rb-Sr age is wrong, however there is no *a priori* reason to suspect the Rb-Sr ages. The other consideration is that the ^{40}Ar-^{39}Ar closure temperature (T_C) for phengite is significantly higher than for muscovite white mica. This has already been examined in several HP metamorphic terranes (Chopin and Maluski, 1980; Monié and Chopin, 1991). T_C for sample 96/134 is approximately 380° C, calculated using the kinetic data of Hames and Bowring (1994) and the equations of Dodson (1973), and is some 120° C lower than for the Rb-Sr T_c of 550 ° C. However the paucity of diffusion kinetic data for argon in phengites precludes an adequate determination of the T_C for high-pressure white micas, and the estimation of 380° C for phengites in 96/134 may be entirely unrealistic. No definitive conclusion can presently be drawn, however, other constraints can be used to discard geological impossibilities. If the ^{40}Ar-^{39}Ar phengites ages are real, based on the P-T history and an average cooling rate and it is possible to constrain the T_C

for phengite based on the ^{40}Ar-^{39}Ar age of 107 Ma and the Rb-Sr age of 80 Ma. Most agree that cooling rates following peak pressure are generally quite rapid. If a conservative estimate of 10° C/Ma is taken, then the 27 Ma difference of age would suggest a closure temperature for the phengites of approximately 800° C. This is impossible to reconcile with the maximum temperature estimate of 550° C proposed for the Tavsanli Zone (Sherlock et al., submitted a). A cooling rate of 1° C/Ma would separate Rb-Sr and ^{40}Ar-^{39}Ar systems by only 20° C but this requires a thermal stasis of almost 30 Ma which is difficult to reconcile with the geodynamics of the Tavsanli Zone.

2 *Both the plateau age and the 'isochron' are incorrect and have no geological meaning.* Several studies have proved the existence of excess argon in some of the most debated samples in the Alps, and have suggested that this is a widely spread phenomenon in HP terranes (Arnaud and Kelley, 1995; Scaillet, 1996). However one has to explain why in our case especially, the plateau and isochron ages appear to be so exact. Inherent to the plateau approach is the fact that each step is corrected for air, assuming that all argon which is not radiogenic in each temperature step is polluted by argon solely in the ratio of ^{40}Ar-^{36}Ar = 295.5. Graphically this corresponds in the isochron diagram to draw lines from the air intercept on the y-axis down through each step/point to the x-axis. Typically most phengites are K-rich and are very rich in radiogenic argon providing they exceed 30 Ma in age. In this case most points on the isochron diagram are clustered near the x-axis. This cluster is typically smaller than the error bars associated with spectroscopic analysis, and the scale on the ^{40}Ar-^{39}Ar transforms large age

variations into small ratio deviations. Consequently contamination by excess ^{40}Ar may well go unnoticed in a sample whilst having a significant effect on the age of each step. If the excess argon or the radiogenic component are homogeneously distributed throughout the phengite then all points will remain clustered thus preventing any valid 'isochron' without an extensive re-scaling of the x-axis. In terms of the radiogenic component this is dependent only upon the homogeneous distribution in K over the sample. Most HP environments are likely to develop reservoirs of high ^{40}Ar concentrations and high ^{40}Ar-^{36}Ar, firstly because metamorphism often affects the base of the continental crust where age integrated growth of ^{40}Ar may be very efficient. Additionally in many examples fluid flow is reduced during high-pressure metamorphism which will restrict the extensive redistribution argon (Philippot, 1993). Thus most HP terranes are likely to develop the kind of artefacts that will typically be neglected by the classical statistical techniques used to assess meaningful ^{40}Ar-^{39}Ar ages. In our case it is possible to intercept the y-axis at any desired value and calls into question the validity of the diagram.

5.2.5 Conclusions

We would like to again stress that the use of plateau ages, not least during the analysis of high-pressure metamorphic terrains, must be rigorously examined in each individual case, preferably in the context of an independent geochronometer. The statistical tools have not been created in the forecast of such difficult applications, following the development of new sampling techniques. Failure to do

so will most likely lead to the generation of incorrect ages, and then to the production of erroneous tectonothermal modelling. We suggest that the use of the isochron in ^{40}Ar-^{39}Ar geochronology cannot always be relied upon to prove or disprove the presence of excess argon, and therefore cannot ultimately be used to prove or disprove the validity of a plateau age. Ultimately new diagnostic tools must be proposed as well as kinetic data for the diffusion of argon in high silica micas.

CHAPTER SIX

SYNTHESIS

6.0 Introduction

In chapters 3, 4 and 5 chemical and isotopic analyses from the Tavsanli Zone HPLT rocks have been presented and discussed within their individual contexts. This final chapter will briefly address the results in terms of the original aims and objectives of this thesis as set out in Chapter 1. By integrating detailed metamorphic petrology and geochronology it has been possible to further our understanding of a relatively little studied HPLT belt as part of a much larger-scale Tethyan evolution. The application of three different ^{40}Ar-^{39}Ar geochronological techniques has enabled a detailed study of argon geochronology in HPLT rocks, paying particular attention to the problem of excess argon.

6.1 The Pressure-Temperature-time evolution and exhumation of the HPLT Tavsanli Zone

The rocks of the Orhaneli, Tavsanli and Sivrihisar regions have undergone a single, clockwise Franciscan-type P-T path. Sediments and volcanic rocks underwent an initial static recrystallisation event at low temperature during subduction prior to peak metamorphic conditions. Peak metamorphic conditions are not uniform across the Tavsanli Zone. In the Orhaneli and Tavsanli regions peak conditions are within the lawsonite-blueschist sub-facies, with pressures and temperatures of up to 20 kbar and 400° C. In the Sivrihisar region peak metamorphic conditions were in the low-temperature eclogite sub-facies with minimum pressures of 24 kbar and maximum temperatures of 500° C. Peak metamorphism occurred between the onset of subduction which is estimated on the basis of palaeomagnetic data to be approximately 100 Ma, and white mica crystalisation at approximately 80 Ma. The exhumation of Tavsanli and Sivrihisar rocks is estimated to have started at approximately 80 Ma.

Initially exhumation was rapid, orthogonal, and in a syn-subduction exhumation setting, achieved by the mechanical exhumation back up the subduction zone by subcretion to crustal levels of approximately 36 km. Retrograde refrigeration resulted from the underplating of the cool descending slab. A slower period of exhumation occurred from approximately 72 Ma, corresponding to slowing subduction which ceased by approximately 65 Ma, when the oblique northeast-directed convergence of

the African and European plates became northward-directed orthogonal convergence and continent-continent collision ensued. During this period of continued orthogonal crustal shortening the HPLT rocks were tectonically exhumed, most likely by southward-directed thrusting. It is at this time that the Tavsanli Zone was thrust southwards over the Afyon Zone, synchronous with the southward-directed thrusting of the peridotite sheets over the Tavsanli Zone. In terms of the Alpine-Himalayan chain and the Alpine orogeny, the Tavsanli Zone HPLT rocks are some of the oldest. The equivalent Alpine HPLT event in the Alpine Dora Maira and Sesia Zones are 35 to 40 Ma and approximately 60 Ma respectively; in the Attic-Cycladic belt of Greece HPLT metamorphism took place at around 40 Ma, and at the Himalayan end of the chain collision was approximately 50 Ma. The Tavsanli Zone HPLT rocks most likely represent the deeply subducted remnants of a promontory or microplate, which underwent HPLT metamorphism some 20 to 30 Ma earlier than surrounding counterparts due to the diachronous closure of Tethys.

6.2 Geochronology and excess argon in the Tavsanli Zone

In comparing the results of the Rb-Sr and ^{40}Ar-^{39}Ar geochronological techniques applied to Tavsanli Zone HPLT white micas, it has become apparent that excess argon has affected the rocks within the Tavsanli Zone. Within Chapters 4 and 5, ^{40}Ar-^{39}Ar white mica ages of 72 Ma to 129 Ma are reported, which are both older and younger than the 79 to 82 Ma Rb-Sr white mica ages from the same regions, and in many cases

the same handsamples and outcrops. The maximum apparent ^{40}Ar-^{39}Ar ages obtained are younger than the protolith, which had a late-Jurassic age. During the single metamorphic cycle potassium in rocks of the Tavsanli Zone has decayed to produce ^{40}Ar which did not equilibrate over distances of greater than 5 m. Phengite crystallisation occurred in this closed system and thus incorporated variable amounts of excess ^{40}Ar. The initial concentration of excess ^{40}Ar in the grain boundary network corresponded to lithological type such that the higher bulk-K metapelites and metacherts contained higher concentrations of excess ^{40}Ar than the lower-K metabasites. The narrow but anomalously old ^{40}Ar-^{39}Ar phengite age ranges are a function of the protolith age, and therefore a combination of whole rock potassium content and the amount of time for $^{40}Ar^*$ to build up.

6.3 The advantages and pitfalls of the Infra-red laser, UVLAMP and furnace step-heating ^{40}Ar-^{39}Ar techniques applied to HPLT rocks

In trying to understand the argon isotopic evolution in the Tavsanli Zone the high spatial resolution UVLAMP technique is more suited than either the Infra-red laser or furnace step-heating techniques. The advantage of the UVLAMP over the infra-red laser is twofold. Firstly the ultra-violet laser may ablate areas down to 10 μm in size, and is limited purely by the need for sufficient argon over and above a blank correction within the ablated region to allow analysis. The infra-red laser produces laser pits in excess of 50μm and will average any isotopic heterogeneities which may occur on

lesser scales. Given the fine-grain sizes of the minerals analysed from the Tavsanli Zone a laser pit of 50 μm or more it becomes difficult to avoid ablating adjacent minerals. Secondly the ultra-violet laser is readily absorbed by both mafic and felsic/transparent minerals, whereas the infra-red laser is more readily absorbed by mafic minerals. The much broader beam size of the infra-red laser compared with the ultra-violet laser has been exploited for step-heating mineral separates such as the Sivrihisar granodiorite hornblende described within Chapter 4. This allows the low-grade alteration products often associated with amphiboles to be outgassed at low temperature or low laser power, so that they may be discounted and not affect the final plateau age of the mineral. The disadvantage of this approach, which is inherent in any bulk analysis, is the averaging of isotopic heterogeneities inherent in similar minerals in rocks such as those analysed from the Tavsanli Zone. The phengite and sodic-amphibole separates which have been furnace step-heated and described in Chapters 4 and 5 serve to illustrate this. Seemingly good plateaux from both phengites and sodic-amphiboles are geologically meaningless due to the averaging of the heterogeneously distributed excess ^{40}Ar component, within each grain. The phengite plateaux imply that excess argon is homogeneously distributed within the phengite mineral lattices. However, with the UVLAMP intra-grain analyses it is apparent that this is not the case and the exemplary plateaux are an artefact of white mica behaviour *in vaccuo*. The sodic-amphibole plateaux are also geologically meaningless, and given the low-K content of the mineral and the estimated excess ^{40}Ar component the results reflect phengite inclusions or intergrowths, which are unavoidable in a bulk separate analysis technique. With the UVLAMP it is possible to avoid inclusions and intergrowths

providing they are optically distinguishable. Given that excess argon is more difficult to distinguish with either the infra-red laser, or a bulk furnace step-heating approach, more emphasis is placed on the inverse isochron correlation diagram which is described in the second part of Chapter 5. Here a case is presented whereby a furnace step-heated phengite plateau age and a series of infra-red laser spots from a single sample, both yield inverse isochron correlation diagrams which give no indication of the presence of excess argon. This emphasises the point that a careful choice of argon extraction technique and careful scrutiny of results is imperative in attempting to understand such a complex region.

6.4 Isotopic and chemical disequilibrium: Low temperatures and 'dry' rocks

Many of the complexities of the argon systematics described in Chapters 4 and 5 and outlined above, have resulted from the low temperatures and the dry nature of the Tavsanli Zone HPLT rocks throughout their evolution. The problems incurred are numerous. Low temperatures are responsible for the fine mineral grain sizes experienced. The major element chemical heterogeneity resulting in the complex zoning patterns observed in minerals is described in Chapter 3. Disequilibrium of argon isotopes as described in Chapter 5. The problems of analysis and interpretation resulting from the major element chemical heterogeneities are reflected in the problems of applying thermobarometric techniques. It is unlikely that the required assemblages

were ever fully in equilibrium causing problems when applying both conventional thermobarometric techniques and internally consistent thermodynamic data sets and using the Thermocalc approach described within Chapter 3. The results are only valid if the assumptions of equilibrium is valid, which in the case of the Tavsanli Zone HPLT rocks is hampered by mineral disequilibria. Rocks of the Sivrihisar region may have reached the coesite stability field and evidence has been presented both for and against. With such low temperatures and 'sluggish' reactions kinetics, it is likely that even if the rocks did achieve pressures greater than 25 kbar within the observed temperature range, the quartz-coesite transition was not kinetically favoured.

The generally 'dry' conditions under which the Tavsanli Zone HPLT rocks have evolved are also partially responsible for the major element chemical disequilibrium, though have had more dramatic effects on the argon isotope systematics. The excess argon within the rocks has been able to build up within the grain boundary network during the evolution of the rocks, and in the absence of a fluid influx has not become mobile. With the introduction of fluid the excess argon within the grain boundary network would have been mobilised, and the excess argon concentration differences observed between different lithologies would have been averaged. Had a major fluid influx been introduced along major structures and derived from either adjacent tectonic units or the mantle, the *in situ*-derived concentration of excess argon within the grain boundary network may be enriched from this external source and result in much higher apparent ages which in themselves are undoubtedly geologically meaningless and a result of excess argon.

CHAPTER SEVEN

CONCLUSIONS AND FUTURE WORK

7.0 Introduction

Chapter Seven outlines the principal results of this thesis, as described in detail in Chapters 3 to 5 and briefly in Chapter 6. The final section of this chapter outlines ideas for future work which have arisen during the course of this thesis.

7.1 Metamorphic evolution

1 The Tavsanli Zone followed a single clockwise Pressure-Temperature evolution, culminating in peak pressures and temperatures which increase from west to east in the Tavsanli Zone.

2 Peak metamorphic conditions reached a maximum of 20 kbars and 400° C in the Tavsanli region, and a minimum of 24 kbars and maximum of 450° C in the Sivrihisar region.

3 The differences in peak metamorphic conditions between the west and east regions of the Tavsanli Zone reflect different structural levels in the

subducting slab; the rocks of the Sivrihisar region record higher pressures and temperatures since they were situated lower down in the descending slab than the rocks of the Tavsanli or Orhaneli regions.

4 The HPLT rocks did not experience overprinting at higher temperatures and lower pressures. Due to the refrigeration effects of syn-subduction exhumation the rocks of the Orhaneli and Tavsanli regions remained within the lawsonite-blueschist sub-facies. The rocks of the Sivrihisar region also experienced the low-temperature eclogite sub-facies.

5. The rocks of the Sivrihisar region may have reached the coesite stability field, but no relict coesite has been confirmed within this study.

6 The first reported occurrence of oscillatory zoning in lawsonite has been identified in metabasite rocks from the Sivrihisar region and is a primary metamorphic feature. Cr^{3+}-Al^{3+} substitution has been brought about by protolith-derived magmatic chromite and local fluid conditions.

7.2 Geochronology and exhumation

7 Rb-Sr dating indicates that white mica crystallisation took place between 78.5 ± 1.6 and 82.8 ± 1.7 Ma which is considered to reflect the onset of exhumation.

8 The Tavsanli Zone rocks underwent initial rapid exhumation at a rate of 3.6 mma^{-1} between 80 Ma and approximately 72 Ma, followed by a period of slower exhumation at a rate of 1.5 mma^{-1} between approximately 72 Ma and 53 Ma.

9 Initial rapid exhumation was synchronous with subduction and achieved by underplating and ascent back up the subduction zone; the slower period of exhumation from the base of the continental crust to the surface was achieved by southward-directed thrusting within a continent-continent collision setting following the cessation of subduction.

10 The Sivrihisar granodiorite was intruded at 52 Ma, the same time as the Orhaneli granodiorite.

7.3 Excess argon

11 Excess argon is prevalent within the regions studied in the Tavsanli Zone and is responsible for the wide range of apparent ^{40}Ar-^{39}Ar white mica ages which are both older and younger than Rb-Sr white mica ages.

12 Excess argon is likely to have been produced *in situ* within an effectively closed low-water system. In the absence of an externally-driven method for its removal, the excess argon has been able to concentrate within the grain boundary network.

13 According to the results of DIFFARG, the concentration of excess argon within the grain boundary network at the time of phengite growth must have an apparent age of 8 Ma.

14 The more K-rich metapelite and metachert lithologies contain higher concentrations of excess argon than the less potassic metabasite lithology, resulting in higher apparent phengite ages in the metapelite and metachert samples.

15 Excess argon is present within both phengite and K-free minerals, with the exception of garnet.

16 The majority of the ^{40}Ar-^{39}Ar ages within the Tavsanli Zone rocks are only slightly older than their Rb-Sr counterparts. This indicates that there is only a small quantity of excess argon, which is probably related to the young Tavsanli Zone protolith. The maximum age of the protolith is Upper Jurassic and there are no ^{40}Ar-^{39}Ar ages older than this from the Tavsanli Zone.

7.4 The application of ^{40}Ar-^{39}Ar geochronology to HPLT rocks: UVLAMP, Infra-red laser and furnace step-heating techniques

17 The UVLAMP is an important tool in undertaking detailed intra-grain analyses of grains as a result of both the high spatial resolution and the

ability to analyse a range of mineral types. With the UVLAMP it has been possible to assess the origin and evolution of excess argon within the Tavsanli Zone.

18 The furnace step-heating ^{40}Ar-^{39}Ar technique produces high-precision ages from lower-K minerals, though the analysis of bulk mineral separates in the absence of comparative Rb-Sr ages would not allow the detection of excess argon within the Tavsanli Zone.

19 The furnace step-heating of low-K sodic-amphiboles has been unsuccessful in the Tavsanli Zone samples since it is impossible to avoid inclusions and micro-intergrowths.

20 Results obtained using both the Infra-red laser and by furnace step-heating and plotted on an inverse isochron correlation diagram in Chapter 5 display no evidence of excess argon contamination, highlighting an inherent flaw in using this approach to identify the presence of excess argon.

7.5 Future work

1 The paucity of diffusion data for argon in high-silica white micas is such that the solubility and closure temperature of argon in phengite may only be estimated on the basis of argon diffusion data in lower pressure

muscovite, which in turn is poorly characterised. Within the second part of Chapter 5 a scenario is discussed in an attempt to explain a ^{40}Ar-^{39}Ar phengite age which is 27 Ma *older* than the Rb-Sr age from the same handsample. The argument for a much higher closure temperature for argon in phengite is discounted on the grounds that it would need to be in the realms of 800° C given the thermal history of the rock. In this case it is possible to state that the apparent age cannot be attributed to closure temperature differences. In examples such as the Greek Cyclades where errors on ^{40}Ar-^{39}Ar and Rb-Sr ages overlap, and excess argon has been generally dismissed, it may be necessary to consider the potential differences in closure temperature between muscovite and high-pressure white micas.

2 A detailed quantitative study of the relationship between bulk potassium content and apparent phengite age in HPLT rocks would improve the more qualitative approach to the excess argon. A simple XRF study of a number of well-characterised samples covering all the lithological types would complement the data described in Chapter 5.

3 In terms of the tectonic evolution of Turkey the relationship between the Tavsanli Zone and the Afyon Zone should be more fully explored. The Afyon Zone is said to contain relic HPLT minerals which have been overprinted by higher-temperature greenschist-facies minerals. It is possible that the Afyon Zone is another thrust slice formed in the same subduction zone with the Tavsanli Zone.

4 The Orhaneli granodiorite and the Sivrihisar granodiorite are contemporaneous. A detailed geochemical study may reveal something of the thermal conditions at the base of the continental crust prior to 52 Ma, and, therefore, something of the origins of the linear belt of granodiorites.

5 One of the prinicipal problems encountered during the investigation of P-T conditions is the problem of accurately determining the Fe^{2+}/Fe^{3+} ratios in minerals, especially sodic-pyroxene. It is possible to estimate the Fe^{3+} component empirically but a comprehensive investigation using Mossbauer Spectroscopy would provide a definitive answer. A limited pilot study is in operation on the Tavsanli Zone HPLT rocks but the restriction of the bulk sampling technique is insufficient in such strongly zoned minerals. The application of a high spatial resolution laser technique would allow the investigation of Fe^{2+}/Fe^{3+} in strongly zoned minerals and avoid the 'averaging' effect inherent in most bulk sampling techniques, and enable a more accurate determination of the pressures and temperatures of metamorphism.

APPENDIX A

^{40}Ar-^{39}Ar TECHNIQUES

A.1.0 The $^{40}Ar/^{39}Ar$ technique

The ^{40}Ar-^{39}Ar technique is a refinement of the K-Ar technique which has been extensively applied to geological problems since its first development in 1963 (Turner and Merrihue, 1963; Merrihue and Turner, 1966). The following sections give a brief comparison of the ^{40}Ar-^{39}Ar and K-Ar techniques, an overview of the ^{40}Ar-^{39}Ar technique and the different methods of argon extraction adopted within this study.

A.1.1 Comparison of K-Ar and ^{40}Ar-^{39}Ar dating techniques

Both K-Ar and 40Ar-39Ar dating techniques are based upon the radioactive decay of unstable 40K to radiogenic daughter 40Ar*. This occurs by positron emission (β^+) and electron capture to excited states followed by γ decay and decay to the ground state or electron capture direct to the ground state. ^{40}K decays not only to ^{40}Ar but also to ^{40}Ca which comprises almost 89% of the decay. K-Ca dating is possible but rarely used since ^{40}Ca is sufficiently abundant to make it difficult to

distinguish the radiogenic ^{40}Ca. ^{40}Ar is trace and inert and radiogenic levels normally exceed background levels.

The way in which the K is measured is the principal difference between K-Ar and ^{40}Ar-^{39}Ar dating. K-Ar requires the measurement of K and Ar from separate aliquots of the same sample. K is measured as total K and the amount of parent ^{40}K calculated from the known $^{40}K/K$ present day ratio in nature (0.0001167). The measurement is generally carried out by flame photometry, though isotope dilution can be used in order to achieve higher precision (Renne et al., 1997). Argon isotopic analysis is carried out by mass spectrometry using a calibrated ^{38}Ar spike from which the absolute amount of ^{40}Ar is determined.

The ^{40}Ar-^{39}Ar technique is an advance since it is possible to measure the ratio of the daughter to parent in a single analysis. The K is measured by the transformation of ^{39}K to ^{39}Ar by neutron bombardment in a nuclear reactor. Argon isotopes ^{40}Ar, ^{39}Ar, ^{38}Ar, ^{37}Ar and ^{36}Ar are then measured using noble gas mass spectrometry. Smaller samples may be measured by this technique and the ratios can be measured more precisely than separate determinations of K and Ar thus providing a more precise age determination. The second advantage of ^{40}Ar-^{39}Ar over K-Ar is the ability to identify excess ^{40}Ar by the inverse isochron correlation diagram which highlights mixing trends between radiogenic and excess or atmospheric argon components.

A.1.2 Principles of the ^{40}Ar-^{39}Ar technique

A comprehensive account of the subject is provided by McDougall and Harrison (1988) with further discussions within Kelley (1995). The ^{40}Ar-^{39}Ar technique was first described by Merrihue and Turner (1966). Its basis lies in the formation of ^{39}Ar from ^{39}K by the irradiation of K-bearing samples by neutron bombardment in a nuclear reactor by the reaction:

$$^{39}_{19}K(n,p)^{39}_{18}Ar \qquad \text{E.1}$$

^{39}Ar is radioactive and decays to ^{39}K by beta emission with a half life of 269 years and is corrected for. The $^{40}K/K$ ratio is known and essentially constant in nature (0.0001167, Steiger and Jäger, 1977). Thus the $^{40}Ar^*/^{39}Ar$ ratio can be calculated and this is proportional to the $^{40}Ar^*/^{40}K$ ratio in the sample and can therefore be used to calculate the age of the sample. The amount of ^{39}Ar produced from ^{39}K during neutron irradiation was formulated by Mitchell (1968) to be:

$$^{39}Ar = {}^{39}K\Delta T\int\Phi(\varepsilon)\sigma(\varepsilon)d\varepsilon \qquad \text{E.2}$$

^{39}Ar is the number of atoms produced from ^{39}K in the sample, ^{39}K is the original number of atoms of ^{39}K present, ΔT is the duration of the irradiation, $\Phi(\varepsilon)$ is the neutron flux density at energy ε, and $\sigma(\varepsilon)$ is the neutron capture cross section of ^{39}K for neutrons of energy ε for the neutro in/proton out reaction (E.2).

The standard equation for the K-Ar decay scheme is fully derived in McDougall and Harrison (1988). The age equation is:

$$t = \frac{1}{\lambda}\ln\left(1+\frac{\lambda}{\lambda e+\lambda' e}\frac{^{40}Ar^*}{^{40}K}\right) \qquad \text{E.3}$$

where t is the age of the sample, λ is the combined decay constant for ^{40}K, λe and $\lambda' e$ are the decay constants for electron capture to an excited state and a ground state respectively, $^{40}Ar^*/^{40}K$ is the ratio of radiogenic daughter to parent. Rearranging E.3 to show the number of $^{40}Ar^*$ atoms present in the sample due to decay of ^{40}K yields:

$$^{40}Ar^* = {}^{40}K \frac{\lambda e + \lambda' e}{\lambda} \left[\left(e^{\lambda t} \right) - 1 \right] \qquad \text{E.4}$$

If equations E.2 and E.4 are combined for a sample of age t then the $^{40}Ar^*/^{39}Ar$ ratio is:

$$\frac{^{40}Ar^*}{^{39}Ar} = \frac{^{40}K}{^{39}K} \frac{\lambda e + \lambda' e}{\lambda} \frac{1}{\Lambda T} \frac{\left[\left(e^{\lambda t} \right) - 1 \right]}{\int \Phi(\varepsilon) \sigma(\varepsilon) d\varepsilon} \qquad \text{E.5}$$

This term can be simplified by introducing by introducing a dimensionless irradiation related parameter, J:

$$J = \frac{^{39}K}{^{40}K} \frac{\lambda}{\lambda e + \lambda' e} \Lambda T \int \Phi(\varepsilon) \sigma(\varepsilon) d\varepsilon \qquad \text{E.6}$$

Standard minerals of known age are used to monitor the neutron flux in the reactor and the apparent ages obtained from them is used to determine the J-value. Standards used within this study are reported in the appropriate sections of Chapters 4 and 5. Substituting equation E.6 into E.5 and rearranging leads to the standard ^{40}Ar-^{39}Ar age equation:

$$t = \frac{1}{\lambda} \ln \left(1 + J \frac{^{40}Ar^*}{^{39}Ar} \right) \qquad \text{E.6}$$

Equation E.6 is similar to that for the K-Ar scheme E.1. The calculation of a ^{40}Ar-^{39}Ar age is possible given the J value which is calculated from mineral standards after irradiation. Measured ^{40}Ar comprises radiogenic and non-radiogenic (excess,

inherited and atmospheric). Atmospheric non-radiogenic argon may be corrected for since the $^{40}Ar/^{36}Ar$ ratio of the atmosphere is constant and has been measured at 295.5. Thus the daughter/parent ratio can be determined:

$$\frac{^{40}Ar^*}{^{39}Ar} = \left(\frac{^{40}Ar}{^{39}Ar}\right)_m - 295.5\left(\frac{^{36}Ar}{^{39}Ar}\right)_m \qquad \text{E.7}$$

Subscript *m* denotes the measured ratio.

A.1.3 Interference reactions

Neutron bombardment during irradiation induces a number of reactions in addition to the production of ^{39}Ar from ^{39}K. The neutron bombardment of K, Ca Cl and Ar nuclei produce a number of different argon isotopes which are outlined in Table A.1.1.

Table A.1.1: Reactions producing argon isotopes in neutron irradiated samples (from McDougall and Harrison, 1988).

The most important reactions involve Ca and K and data from irradiated samples are corrected to account for these. Correction factors used in this study are described in the appropriate sections of Chapters 4 and 5.

A.1.4 Argon extraction techniques

A.1.4.1 Furnace step-heating

Incremental step-heating was first applied by Turner et al. (1966) to extraterrestrial samples. The technique involves incrementally increasing the temperature of a double vacuum furnace (Staudacher et al., 1978) which contains the sample. Argon is released from the sample in a series of steps, with deeper or more strongly retained argon released from the mineral lattice as the temperature increases. If $^{40}Ar^*$ and K have remained in the sample since the time of initial cooling then the $^{40}Ar^*/^{39}Ar$ ratios and therefore ages for each step should remain constant. The limitations of the technique are briefly outlined in Chapter 2.

A.1.4.2 Laser extraction techniques

Laser extraction techniques have the advantage of being able to make detailed studies of the intra-grain isotopic heterogeneities which are 'averaged' by the furnace step-heating technique on hydrous minerals, in addition to overcoming the behavioural problems suffered by minerals *in vacuo*. Two main types of lasers are

used, continuous wave (CW) and pulsed. CW is the most commonly used since they can be used to both slowly heat and instantaneously melt material. It is also possible to focus CW lasers in order to carry out high spatial resolution work, resulting in laser pits of between 50 μm and 250 μm in diameter. Low mineral absorption as briefly described in Chapter 6 is a particular problem of CW lasers, when absorption is low the sample may take several seconds to melt during which time heating and argon loss may take place in the surrounding minerals. An additional problem is reflectance or refraction within the mineral and melting inclusions or adjacent minerals up to 500 μm from the laser spot. Pulsed laser output comprises a series of nano- to micro-second pulses. Instantaneous melting is achieved by pulses of high power densities which last for a few nano-seconds to hundreds of micro-seconds. In such pulsed-lasers there is a threshold where lasing will not occur, below which an alternative to both the CW and early pulsed lasers, Q-switched ultra-violet systems may be used; 'Q-switching' generates very short pulses of light a few nanoseconds in length by storing energy in the laser and releasing it rapidly. Such lasers achieve very short pulse lengths and short wavelengths resulting in a small spot size and avoiding large-scale heating. The UV is also strongly absorbed by all silicate minerals except quartz.

A.1.4.2.1 Infra-red laser probe

In this study a focussed infra-red laser has been used to carry out *in situ* single spot analyses of phengites and sodic-amphiboles, whole rock spot analyses of very fine-grained samples, and step-heating of a bulk hornblende separate. The main

drawback of this technique is the laser spot size which is limited to a minimum of around 50 μm, such that intra-grain isotopic heterogeneities may not be solved and in many cases some argon is extracted from beyond the limit of the laser pit, typically distances equalling 10 % of the width of the laser pit width, from adjacent minerals.

The Spectron Laser Systems SL902 CW Nd YAG laser used in these experiments produces a continuous wavelength infrared beam with a wavelength of 1064 nm. The beam has an output power of around 15 W in TEM 00 mode and is directed using high reflectance oxide coated mirrors into a customised Leica Metallux 3 microscope. Within the microscope the beam is focussed at the sample surface via the microscope objective lens to a spot size of around 25 μm. The sample may be observed using a CCD camera, coaxial with the laser beam. The gases released by laser ablation are cleaned using two SAES AP 10 getters (one operated at 400° C and other at room temperature) and after 5 minutes, equilibrated via automated valves into a MAP 215-50 noble gas mass spectrometer. Average blank levels were $^{40}Ar = 7 \times 10^{-5}$, $^{39}Ar = 2 \times 10^{-6}$, $^{36}Ar = 1 \times 10^{-6}$ (all cc STP).

A.1.4.2.2 Ultra-violet laser probe

This technique was developed by Kelley et al. (1994). UV analysis allows extraction of mineral samples which do not absorb IR wavelengths such as plagioclase and K-feldspar, and also allows high spatial resolution analysis of all minerals. There is also no heating outside the visible laser spots and thus there is

unlikely to be contamination from inclusions or adjacent minerals. The direct correlation of *in situ* argon analyses with positon within mineral grains is made possible (Kelley et al., 1994; Reddy et al., 1996; Pickles et al., 1997).

The laser port is fitted with a UV grade fused-silica window which has a high transmission coefficient for light at 266 nm. A 1 mm thick sapphire window is placed between the laser port and the sample to prevent ablated material from coating the outer window. A Spectron Laser Systems SL401 with two temperature and angle controlled KD*P crystals is used as the source of UV light. The laser produces pulsed light at with a wavelength of 1064 nm (IR) which is frequencey doubled by the two KD*P crystals to 532 nm then 266 nm (UV). The wavelengths are separated using a Pellin Brocca prism, and the resulting UV laser pulses have an energy of up to 20 mJ per pulse, for a pulse length of 10 ns at a repetition rate of 10 Hz. High reflectance oxide coated mirrors direct the light inot a customised Leica D M microscope. The beam is redirected within the microscope through a UV refracting objective lens and focussed to a spot size of 5 μm at the sample surface. A programmable automated stage allows the beam to be rastered across the sample, the gases released by laser ablation are cleaned using 2 SAES AP 10 getters (one operated at 400° C and one at room temperature) after 10 minutes, equilibrated via automated valves into a MAP 215-50 noble gas mass spectrometer. Average blank levels were $^{40}Ar = 3 \times 10^{-12}$, $^{39}Ar = 5 \times 10^{-13}$, $^{36}Ar = 1 \times 10^{-13}$ (all cc STP).

A.1.4.2.3 Furnace step-heating

The principal behind the technique has been outlined in A.1.4.1. Step-heating was carried out in a Modifications Ltd. Double vacuum resistance furnace which will heat to 1800° C (Staudacher et al., 1978). Temperature control is achieved by a Eurotherm controller linked to a W-Rh thermocouple which is situated in the bottom of a crucible, 1.5 ± 0.5 mm from the samples, the temperature is monitored at ± 10° C or better. During heating the gas is cleaned with a N_2 cold trap mounted on the furnace. On release from the furnace section of the extraction line the gas is transferred to a second section and cleaned by two SAES Zr-Al getters (one at 400° C, one at room temperature). The cleaned gas is analysed within a VG3600 noble gas mass spectrometer.

APPENDIX B

^{40}Ar-^{39}Ar DATA RELATING TO CHAPTER FOUR

B.1 UVLAMP analyses

	$^{40}Ar/^{39}Ar$	$^{38}Ar/^{39}Ar$ (X 100)	$^{37}Ar/^{39}Ar$ (X 100)	$^{36}Ar/^{39}Ar$ (X 100)	Total ^{39}Ar (x 10^{-12} cm^3, STP)	$^{40*}Ar/^{39}Ar$	Age (Ma)	± (2 σ)
96/12, Tavsanli								
Phengite	9.4133	0.9668	1.0269	1.1359	2.67	6.0582	88	3
Phengite	8.7612	1.4398	3.2079	0.1490	3.34	8.3199	82	1
Phengite	8.7311	0.9336	0.4189	0.4408	3.08	7.4292	82	2
Phengite	8.3626	1.4438	3.3075	0.0000	3.21	8.3630	78	3
Phengite	9.5343	1.0970	2.3138	0.0000	4.23	9.5341	89	1
Phengite	8.3540	0.7889	1.8711	0.4915	1.02	6.8996	78	5
Phengite	7.9870	0.1639	2.7354	0.0000	1.03	7.9772	75	6
Glaucophane	113.9021	195.0601	0.0001	92.5911	0.282	0.0000		
K380, Tavsanli								
Phengite1	14.5241	1.8132	1.1710	2.2901	0.04	7.7714	110	3
Phengite2	14.0900	0.6841	0.0000	0.0000	0.06	14.0901	107	3
Phengite3	15.1225	0.1052	0.0000	0.0000	0.05	18.3413	114	2
Phengite4	12.3331	1.6125	0.2965	0.3812	0.07	11.252	94	2
Phengite5	12.8510	0.4037	0.0000	1.4122	0.04	8.7003	98	3
Phengite6	12.3300	1.4413	0.0000	0.2713	0.08	11.5245	94	2
Phengite7	12.9403	0.6500	0.0000	0.7421	0.09	10.7612	98	1
Glaucophane	32.2500	6.8725	6.6900	13.4841	0.00	0.0000		
Glaucophane	536.9510	0.0000	0.0000	3.7001	0.00	0.0000		
96/198, Tavsanli								
Phengite1	11.9452	1.2964	0.0000	0.3838	2.26	10.8131	111	3
Phengite2	10.2820	2.1360	1.9861	0.5977	2.32	8.5187	96	3
Phengite3	10.2196	1.1152	0.0001	0.0000	2.62	10.2195	95	3
Phengite4	9.2631	1.3251	1.0623	2.1253	3.03	2.9918	86	3
Phengite5	9.9010	1.3298	0.0000	2.2654	2.75	3.2117	92	2
Phengite6	9.5496	2.2297	0.0000	0.0000	1.74	9.5492	89	2
Phengite7	9.1929	0.7209	1.5711	0.7769	2.62	6.9007	86	3
Phengite8	9.8616	1.4992	0.7101	1.0001	2.59	6.9081	92	3
Phengite9	10.0001	0.9992	0.0000	0.0000	2.47	10.0001	93	2
Glaucophane	10.3412	3.0938	2.8095	0.8471	0.00	0.0000		
96/120, Sivrihisar								
Phengite	10.8601	0.9110	0.1701	0.0600	1.34	10.6912	101	7
Phengite	10.1121	1.0100	0.0003	0.0000	0.01	10.4322	94	5
Phengite	11.3641	0.8702	0.1202	0.7921	3.44	9.0253	105	5
Phengite	9.2331	1.9000	6.4804	0.2314	1.33	8.5569	86	4
Phengite	10.2016	0.0545	4.1051	2.0855	1.02	4.0640	95	6
Glaucophane	149.0314	55.8816	447.0656	232.3512	0.00	0.0000		
Glaucophane	245.9400	0.0000	1333.3300	0.0000	0.00	393.69		
96/185, Tavsanli								
Phengite	9.9912	0.9163	0.0000	0.0000	1.86	10.8776	102	4
Phengite	11.5245	0.0000	0.4594	1.3806	1.73	7.4449	117	4
Phengite	11.6005	1.0497	2.0089	1.5502	2.89	7.0197	118	3
Glaucophane	0.0000	0.0000	0.0000	0.0000	0.00	422512	5687	2354
96/134, Sivrihisar								
Phengite1	10.7968	1.9988	0.0000	0.2309	3.49	10.1155	100	5
Phengite2	10.5541	2.2117	0.0000	0.0000	4.14	11.4322	98	3
Phengite3	11.7451	0.9077	2.9126	2.0727	4.15	5.6163	109	3
Phengite	11.3584	1.1216	6.4540	0.0214	3.14	11.2951	105	2
Phengite	10.9533	1.1662	2.7325	0.5281	2.31	9.3920	102	1
Phengite	9.9052	0.9441	0.6602	0.4263	2.18	8.6470	92	2
Phengite	11.3605	0.9647	2.2840	0.0000	2.58	11.3622	105	2
Phengite	8.3526	1.7009	0.0000	0.5847	1.88	6.6268	78	2
Glaucophane	0.0000	3.0910	2.8049	0.8422	0.03	0.0000		
96/158, Sivrihisar								
Phengite1	10.7042	1.4889	21.6801	6.1368	0.85	7.4312	100	5
Phengite2	8.5201	1.3241	1.4098	0.0000	1.29	8.5203	80	4
Phengite3	8.4463	1.9479	4.3241	1.2972	2.02	4.6141	79	3
Phengite4	8.1930	1.7593	0.0000	0.6819	1.98	6.1852	77	2
Phengite5	7.6968	1.4751	0.0000	1.0099	1.76	4.7114	72	3
Phengite6	8.5709	0.6571	1.8535	0.0000	1.91	8.5778	80	3

Phengite7	9.5857	0.8252	0.0000	0.0000	1.52	9.5961	89	3
Phengite8	9.3550	0.0000	0.0000	0.4769	1.94	7.9515	87	3
Phengite	10.9549	1.1266	7.5945	1.2835	2.69	7.1611	102	4
Phengite	11.5210	1.4676	0.0000	0.7544	3.48	9.2900	107	3
Phengite	10.5035	1.6081	1.3284	0.1066	4.81	10.1920	98	2
Phengite	8.8375	1.5273	3.2837	0.8928	2.47	6.2038	83	2
Phengite	9.1684	1.7672	0.4141	1.2438	3.13	5.4934	86	2
Glaucophane	11.7001	1.5576	0.0000	1.4272	2.14	7.4811	109	7
96/234, Orhaneli								
Phengite	8.2001	1.7801	3.8211	0.1710	3.77	7.6912	84	6
Phengite	10.3622	0.3920	0.0078	1.5874	3.59	5.7132	106	5
Phengite	12.1353	0.8122	10.0251	1.1725	2.05	8.6931	123	7
Phengite	12.1767	1.3036	0.0042	0.3213	3.47	11.2201	124	6
Phengite	12.1415	1.3435	1.5020	1.0900	3.38	8.9125	123	6
Phengite	9.9200	1.3401	0.0096	0.3731	2.88	8.8384	101	5
Phengite	11.0120	1.7001	0.0000	1.6110	2.38	6.2534	112	6
Phengite	9.8830	1.3802	0.0000	0.0000	2.59	7.5710	101	6

B.2 Infra-red laser spot analyses

	$^{40}Ar/^{39}Ar$	$^{38}Ar/^{39}Ar$ (X 100)	$^{37}Ar/^{39}Ar$ (X 100)	$^{36}Ar/^{39}Ar$ (X 100)	Total ^{39}Ar (x 10^{-12} cm^3, STP)	$^{40*}Ar/^{39}Ar$	Age (Ma)	± (2 σ)
K380, Tavsanli								
Phengite	15.6475	1.4107	2.5510	0.4608	4.58	14.2851	108	6
Phengite	13.9344	1.5461	0.0000	0.4994	10.51	12.4585	95	5
Phengite	16.0627	1.6107	5.1553	0.2421	6.90	15.3481	116	5
Phengite	34.8838	0.8474	0.0000	4.4383	1.51	21.7573	162	22
Phengite	17.6177	1.1045	0.0000	0.6995	9.01	15.5499	118	4
Phengite	23.6140	2.3525	9.7815	1.9101	2.86	17.9769	135	14
Phengite	14.0051	0.5609	0.0000	0.3510	3.60	12.9671	99	7
Phengite	16.5801	1.1520	0.0000	1.1672	3.24	13.1308	100	9
Phengite	16.5138	0.9222	0.0000	1.4819	3.12	12.1340	92	11
Phengite	33.4681	1.9597	0.0000	2.5537	4.30	25.9709	192	8
Phengite	23.7085	1.2260	0.4529	0.3062	10.95	22.8039	170	4
Phengite	13.7907	1.1722	0.0000	0.0290	8.85	12.9339	98	13
Phengite	17.9079	1.3405	0.0000	0.0429	11.75	16.6401	126	4
96/48, Akcakaya								
Whole rock	5.6901	0.7352	11.6910	0.3901	36.93	4.5222	59	5
Whole rock	5.8823	1.8136	17.1823	0.0000	139.18	6.5831	61	4
Whole rock	6.0625	0.8719	13.3802	0.0000	199.36	7.0216	63	9
Whole rock	6.0400	0.0000	14.3230	1.4601	68.89	1.7402	62	7

B.3 Infra-red laser step-heating analyses

	$^{40}Ar/^{39}Ar$	$^{38}Ar/^{39}Ar$ (X 100)	$^{37}Ar/^{39}Ar$ (X 100)	$^{36}Ar/^{39}Ar$ (X 100)	% ^{39}Ar released	$^{40*}Ar/^{39}Ar$	Age (Ma)	± (2 σ)
SivG								
Step1	317.6316	353.5151	0.0000	0.0000	0.03	11.5762	118	143
Step2	41.2235	58.5637	9.6001	6.1444	0.22	6.9553	72	40
Step3	7.9716	36.4333	26.1868	0.4109	1.98	5.6896	59	4
Step4	5.4377	39.2264	24.04048	0.1542	27.81	5.4063	56	1
Step5	5.1702	39.9177	23.9130	0.1139	40.53	5.1175	53	1
Step6	5.1191	40.3605	23.7173	0.0710	52.78	5.1627	53	2
Step7	5.1741	40.2142	25.7582	0.0350	56.81	4.8698	51	2
Step8	5.1061	41.2174	23.4630	0.0970	89.08	5.2473	54	1
Step9	5.0096	40.1157	23.7633	0.3076	92.54	3.8036	40	2
Step10	5.1786	42.5522	27.2805	0.1705	98.56	4.7558	49	1
Step11	5.1235	40.2160	33.1109	0.4913	100.00	2.2355	23	5

B.4 Furnace step-heating analyses

°C	$^{40}Ar/^{39}Ar$	$^{38}Ar/^{39}Ar$ (x 100)	$^{37}Ar/^{39}Ar$	$^{36}Ar/^{36}Ar$ (x 100)	% ^{39}Ar released	$^{40*}Ar/^{39}Ar$	Age (Ma)	± (1 σ)
96/134, Sivrihisar glaucophane								
800	5.77	1.91	0.59	0.54	41.46	4.51	133	3
850	7.91	1.97	2.50	0.78	66.24	5.90	172	3
900	9.16	2.13	6.26	1.20	76.74	6.27	183	4
950	10.25	2.24	6.85	1.73	82.22	5.88	171	6
1000	11.43	2.25	7.62	2.13	85.86	5.98	174	8
1050	12.14	2.30	5.29	2.31	90.01	5.96	174	8
1100	15.51	2.46	4.55	3.22	93.03	6.63	192	10
1400	37.12	3.90	1.63	11.54	100.00	3.81	113	11
96/12, Tavsanli glaucophane								
700	27.74	3.50	0.33	8.35	7.53	3.53	105	4
800	5.90	1.96	0.23	0.93	40.60	3.21	96	2
850	6.80	2.05	1.35	1.10	67.26	3.75	111	2
900	7.46	2.10	2.84	1.31	78.80	3.94	117	3
950	6.39	2.02	2.32	0.10	84.82	3.56	106	4
1000	5.06	1.89	1.37	0.63	89.46	3.35	100	5
1050	7.80	20.63	1.14	1.63	92.33	3.18	95	8
1100	23.16	3.05	1.30	6.82	93.86	3.51	104	15
1200	78.38	6.78	2.20	25.84	95.27	3.65	108	22
1400	59.87	5.68	1.69	19.61	100.00	3.16	95	9
96/12, Tavsanli phengite								
600	27.78	0.351	0.00	8.57	1.11	2.92	87	4
700	7.37	2.11	0.01	1.51	4.93	3.01	90	2
800	3.25	1.79	0.00	0.10	36.72	2.94	88	2
900	3.11	1.80	0.00	0.08	71.99	2.89	86	2
1000	3.15	1.79	0.00	0.09	87.95	2.89	86	2
1100	3.20	1.80	0.00	0.11	95.58	2.87	86	2
1200	3.76	1.84	0.00	0.33	98.60	2.80	84	2
1400	5.48	1.97	0.00	1.67	100.00	0.66	20	3

APPENDIX C

Rb-Sr ANALYTICAL DETAILS

C.1 Rb-Sr technical notes

Samples were crushed and sieved, and fines and very magnetic material removed from each fraction prior to mineral separation. Analyses were performed on 80-100 μm size fractions. Micas were separated by adherence to paper, other phases by standard magnetic and heavy liquid methods before final purification by hand-picking. Minerals were washed several times in methanol and water in an ultrasound bath. Samples were dissolved in hot HF + HNO_3 + $HClO_4$. Standard ion-exchange procedures were followed to separate Rb and Sr. Rb analyses were performed using a VG Micromass 30 mass spectrometer, Sr was analysed using VG Isomass 54E, both at the University of Leeds. Sr was corrected by reference to the NBS 987 standard. Errors in 87Sr/86Sr and 87Rb/86/Sr were assessed by replicate analysis of homogeneous natural mica samples which yielded 2-σ reproducibility of 0.005% in 87Sr/86Sr and 1.2% in 87Rb/86Sr. These errors were propagated through the age equation by a perturbation algorithm (Rees, 1984).

APPENDIX D

Rb-Sr DATA RELATING TO CHAPTER FOUR

D.1 Rb-Sr analyses

Sample	Rb ppm	Sr ppm	$^{87}Sr/^{86}Sr$	$^{87}Rb/^{86}Sr$	Age
96/12, Tavsanli					
Glaucophane	5.39	22.00	0.7062	0.70875	
Phengite	296.16	22.03	0.7490	39.06	78.5 ± 1.6
96/134, Sivrihisar					
Glaucophane	10.45	57.33	0.7073	0.53	
Phengite	292.45	7.25	0.8413	118.17	80.1 ± 1.6
Pyroxene	16.39	156.06	0.7062	0.30	
Lawsonite	15.49	645.08	0.7077	0.07	
69/198, Tavsanli					
Glaucophane	3.67	8.2	0.7095	1.30	
Phengite	256.23	8.28	0.8104	90.43	79.7 ± 1.6
96/158, Sivrihisar					
Phengite	223.16	59.93	0.7177	10.78	82.8 ± 1.7
Pyroxene	2.04	73.67	0.7051	0.08	

APPENDIX E

^{40}Ar-^{39}Ar DATA RELATING TO CHAPTER FIVE I

E.1 UVLAMP analyses from sample 96/234

96/234	$^{40}Ar/^{39}Ar$	$^{38}Ar/^{39}Ar$	$^{37}Ar/^{39}Ar$	$^{36}Ar/^{39}Ar$	^{39}Ar	$^{40}Ar^*/^{39}Ar$	Age (Ma)	± (2 σ)
Phengite 1 (T1)	12.1285	0.0081	10.0156	0.0116	0.0045	8.6871	123	7
Phengite 2 (T1)	12.1664	0.0130	0.0000	0.0032	0.0076	11.2165	124	6
Phengite 3 (T1)	12.1441	0.0134	1.4979	0.0109	0.0075	8.9101	123	6
Phengite 4 (T1)	10.3634	0.0139	0.0000	0.0158	0.0079	5.7083	106	5
Phengite 5 (T1)	9.9185	0.0134	0.0000	0.0037	0.0067	8.8284	101	5
Phengite 1 (T2)	12.2891	0.0101	0.0000	0.0410	0.0025	0.1691	125	9
Phengite 2 (T2)	11.0095	0.0170	0.0000	0.0161	0.0052	6.2499	112	6
Phengite 3 (T2)	9.7827	0.0161	14.1978	0.0116	0.0062	6.3645	100	6
Phengite 4 (T2)	9.8772	0.0107	9.4481	0.0140	0.0063	5.7438	101	5
Phengite 5 (T2)	9.3793	0.0137	3.8866	n.d.	0.0065	9.6825	96	5
Phengite 6 (T2)	9.2116	0.0113	7.7041	0.0104	0.0060	6.1386	94	5
Phengite 7 (T2)	9.8796	0.0138	0.0000	0.0078	0.0057	7.5713	101	6
Single phengite	15.3025	0.0153	0.0000	0.0000	0.0114	15.3025	154	7
Single phengite	8.1966	0.0177	3.8177	0.0017	0.0083	7.6945	84	6
Quartz 50µm A	223.7419	0.3990	336.6220	0.6874	0.0001	20.6169	1506	261
Quartz 100µm	5.6361	0.0000	54.3339	n.d.	0.0008	9.8748	58	43
Quartz 100µm	n.d.	0.0000	n.d.	0.3705	0.0000	n.d.	0	0
Quartz 50µm B	23.8345	0.0000	106.0801	0.2600	0.0004	n.d.	0	0
Quartz 100µm	10.7138	0.0195	0.0000	0.0086	0.0040	8.1799	109	6
Quartz 100µm	113.6479	0.1710	141.9973	0.0000	0.0002	113.6479	917	133

E.2 UVLAMP analyses from sample 96/198

96/198		$^{40}Ar/^{39}Ar$	$^{38}Ar/^{39}Ar$	$^{37}Ar/^{39}Ar$	$^{36}Ar/^{39}Ar$	^{39}Ar	$^{40}Ar^{*}/^{39}Ar$	Age (Ma)	± (2 σ)
Phengite 1	(T3)	10.8153	0.0525	0.0068	0.0042	0.0028	9.5662	101	4
Phengite 2	(T3)	11.9452	0.0000	0.0130	0.0038	0.0031	10.8131	111	3
Phengite 3	(T3)	10.2820	0.0199	0.0214	0.0060	0.0053	8.5187	96	3
Phengite 4	(T3)	10.2196	0.0000	0.0112	0.0000	0.0055	10.2195	95	3
Phengite 5	(T3)	9.2631	0.0506	0.0133	0.0213	0.0062	2.9918	86	3
Phengite 6	(T3)	9.9010	0.0000	0.0130	0.0227	0.0072	3.2117	92	2
Phengite 7	(T3)	9.5496	0.0000	0.0223	0.0000	0.0065	9.5492	89	2
Phengite 8	(T3)	9.1929	0.0157	0.0072	0.0078	0.0041	6.9007	86	3
Phengite 9	(T3)	9.8616	0.0071	0.0150	0.0100	0.0062	6.9081	92	3
Phengite 10	(T3)	10.0010	0.0000	0.0100	0.0000	0.0061	10.0006	93	2
Phengite 11	(T3)	9.6188	0.0000	0.0105	0.0106	0.0058	6.4895	90	2
Phengite 1	(T6)	10.9846	0.0000	0.0070	0.0336	0.0027	1.0544	102	4
Phengite 2	(T6)	10.7190	0.0566	0.0071	0.0125	0.0041	7.0285	100	3
Phengite 3	(T6)	10.1768	0.0000	0.0169	0.0199	0.0036	4.3102	95	3
Phengite 4	(T6)	11.3459	0.0000	0.0109	0.0007	0.0027	11.1422	105	4
Phengite 5	(T6)	10.3510	0.0000	0.0033	0.0398	0.0026	0.0000	96	4
Phengite 1	(T5)	10.0310	0.0000	0.0050	0.0136	0.0038	6.0000	93	3
Phengite 2	(T5)	11.2412	0.1029	0.0071	0.0004	0.0042	11.1137	104	3
Phengite 3	(T5)	10.9109	0.0000	0.0148	0.0107	0.0049	7.7588	101	3
Phengite 4	(T5)	10.2127	0.0008	0.0120	0.0211	0.0025	3.9916	93	3
Phengite 5	(T5)	10.9731	0.0287	0.0220	0.0095	0.0023	8.1675	102	5
Single phengite		10.9718	0.0158	0.0135	0.0068	0.0105	8.9499	102	2
Single phengite		10.2133	0.0182	0.0161	0.0000	0.0049	10.2132	95	4
Single phengite		10.0001	0.0339	0.0134	0.0123	0.0067	6.3583	93	3
Phengite 1	(T7)	10.4429	0.0427	0.0108	0.0074	0.0044	8.2704	97	2
Phengite 2	(T7)	10.4090	0.0262	0.0108	0.0000	0.0034	10.4102	97	4
Phengite 3	(T7)	10.2639	0.0000	0.0134	0.0174	0.0059	5.1197	96	3
Phengite 1	(T4)	10.1318	0.0284	0.0087	0.0064	0.0066	8.2508	94	2
Phengite 2	(T4)	10.0153	0.0330	0.0000	0.0057	0.0039	8.3413	93	4
Phengite 3	(T4)	11.3336	0.0044	0.0157	0.0267	0.0023	3.4344	105	5
Phengite 4	(T4)	10.6335	0.0000	0.0157	0.0004	0.0050	10.5047	99	3
Phengite 5	(T4)	10.5993	0.0000	0.0168	0.0088	0.0059	8.0014	99	2
Phengite 6	(T4)	10.7931	0.0153	0.0169	0.0000	0.0071	10.7925	100	3
Phengite 7	(T4)	13.2770	0.0018	0.0119	0.0160	0.0058	8.5398	123	7
Phengite 8	(T4)	10.4009	0.0000	0.0098	0.0000	0.0048	10.4006	97	3
Phengite A		11.3014	0.0715	0.0205	0.0122	0.0059	7.6937	105	2
Quartz 50µm A		n.d.	n.d.	n.d.	0.0000	0.0000	n.d.	0	0
Quartz 50µm B		32.3702	3.6742	1.8823	3.0879	0.0000	n.d.	0	0
Glaucophane A		52.9199	6.7475	2.5540	4.5797	0.0000	n.d.	0	0
Glaucophane B		n.d.	n.d.	n.d.	n.d.	0.0000	n.d.	0	0
Glaucophane C		93.4167	16.3333	0.0000	4.3167	0.0000	n.d.	726	876
Glaucophane D		n.d.	n.d.	n.d.	0.2583	0.0000	n.d.	n.d.	2173
Glaucophane		102.6667	18.1667	0.0000	0.9833	0.0000	n.d.	784	955

E.3 UVLAMP analyses from sample 96/185

96/185		$^{40}Ar/^{39}Ar$	$^{36}Ar/^{39}Ar$	$^{37}Ar/^{39}Ar$	$^{36}Ar/^{39}Ar$	^{39}Ar	$^{40}Ar^*/^{39}Ar$	Age (Ma)	± (2 σ)
Phengite 1	(T9)	10.6358	0.0076	n.d.	n.d.	0.0025	18.6901	99	7
Phengite 2	(T9)	9.5977	0.0202	n.d.	0.0096	0.0044	6.7599	90	4
Phengite 3	(T9)	9.8635	0.0131	n.d.	n.d.	0.0053	11.4220	92	4
Single phengite		9.8057	0.0023	n.d.	n.d.	0.0039	10.3941	91	5
Single phengite		9.6216	0.0145	0.0303	0.0301	0.0041	0.7404	90	5
Single phengite		10.7270	0.0059	0.0173	0.0168	0.0018	5.7525	100	3
Single phengite		11.2443	0.0084	0.0000	0.0053	0.0038	9.6764	104	2
Single phengite		9.7988	0.0096	0.0140	0.0023	0.0044	9.1265	91	2
Single phengite		11.2660	0.0140	0.0156	0.0248	0.0052	3.9475	105	3
Single phengite		10.2661	0.0077	0.0041	0.0065	0.0124	8.3562	96	2
Single phengite		10.4491	0.0139	n.d.	0.0035	0.0113	9.4059	97	1
Phengite 1	(T10)	9.9912	0.0092	n.d.	n.d.	0.0044	10.8776	93	3
Phengite 2	(T10)	11.5245	n.d.	0.0046	0.0138	0.0041	7.4449	107	4
Phengite 3	(T10)	11.6005	0.0105	0.2009	0.0155	0.0069	7.0197	108	3
Quartz 100µm A		4208.6667	7.3333	n.d.	6.3333	0.0000	2337.1667	5681	3562
Quartz 50µm B		2228.6667	n.d.	8.0000	10.8333	0.0000	n.d.	4601	5520
Quartz 100µm		55.7786	0.0816	0.0280	n.d.	0.0005	60.6002	467	44
Quartz 50µm		32.3702	n.d.	0.2353	n.d.	0.0001	233.4902	348	281
Glaucophane A		52.9199	0.5152	0.3636	n.d.	0.0000	382.3939	676	383
Glaucophane		175.1770	n.d.	n.d.	n.d.	0.0000	722.3707	1185	816
Glaucophane		25.5697	n.d.	6.6541	1.3888	0.0000	n.d.	229	203
Lawsonite A		12.6291	0.0213	7.1423	n.d.	0.0009	48.5482	117	17
Lawsonite B		24.0025	0.0000	5.3621	n.d.	0.0002	56.1904	216	30

E.4 UVLAMP analyses from sample K380

K380		$^{40}Ar/^{39}Ar$	$^{36}Ar/^{39}Ar$	$^{37}Ar/^{39}Ar$	$^{36}Ar/^{39}Ar$	^{39}Ar	$^{40}Ar^*/^{39}Ar$	Age (Ma)	± (2 σ)
Quartz 50µm		n.d.	n.d.	73.6147	3.3817	n.d.	0.0000	0	3838
Quartz 50µm		132.3680	0.1432	n.d.	n.d.	0.0002	88.5554	817	240
Quartz 50µm		n.d.	n.d.	n.d.	n.d.	0.0001	n.d.	0	972
Quartz 50µm		35.8560	n.d.	n.d.	0.0999	0.0005	3.4965	260	125
Phengite 1	(T8)	21.3297	0.0212	0.3822	0.0462	0.0043	11.1692	159	15
Phengite 2	(T8)	11.9234	0.0172	0.0395	0.0086	0.0035	7.7667	91	20
Phengite 3	(T8)	11.9084	0.0107	0.1753	n.d.	0.0046	14.0871	91	15
Phengite 4	(T8)	0.0728	0.0125	n.d.	n.d.	0.0073	18.3441	104	9
Phengite 5	(T8)	12.2513	0.0118	n.d.	0.0029	0.0104	11.2042	93	7
Phengite 6	(T8)	12.8243	0.0023	0.1381	0.0127	0.0078	8.6986	97	9
Phengite 7	(T8)	12.3108	0.0132	0.0440	0.0018	0.0110	11.5210	94	6
Glaucophane		17.2134	0.0222	0.0850	0.0110	0.0117	14.5099	130	6

E.5 UVLAMP analyses from sample 96/12

96/12		$^{40}Ar/^{39}Ar$	$^{38}Ar/^{39}Ar$	$^{37}Ar/^{39}Ar$	$^{36}Ar/^{39}Ar$	^{39}Ar	$^{40}Ar^{*}/^{39}Ar$	Age (Ma)	± (2 σ)
Single phengite		9.4133	0.0097	0.0103	0.0114	0.0063	6.0582	88	3
Single phengite		8.7612	0.0144	0.0321	0.0015	0.0079	8.3200	82	1
Single phengite		8.7311	0.0093	0.0042	0.0044	0.0073	7.4292	82	2
Single phengite		8.3626	0.0144	0.0331	0.0000	0.0076	8.3630	78	3
Single phengite		9.5343	0.0110	0.0231	0.0000	0.0100	9.5341	89	1
Phengite 1	(T11)	8.4840	0.0000	0.1813	0.0000	0.0024	8.4957	79	5
Phengite 2	(T11)	8.3470	0.0079	0.0187	0.0049	0.0024	6.8996	78	5
Phengite 3	(T11)	7.9755	0.0164	0.0274	0.0000	0.0025	7.9772	75	6
Glaucophane		n.d.	n.d.	n.d.	n.d.	0.0000	342.9354	0	0
Glaucophane		328.1779	28.2755	0.6258	0.0000	0.0001	1.1585	1818	826
Glaucophane		1622.6398	148.0435	3.7578	6.5217	0.0000	8.9656	4080	3724
Glaucophane		30.4180	0.0680	0.0000	3.3762	0.0001	n.d.	270	272
Glaucophane		294.0991	32.2973	2.5991	12.2072	0.0000	n.d.	1695	2940
Glaucophane		n.d.	n.d.	n.d.		0.0000	103.8157	0	0
Glaucophane		n.d.	0.1314	0.1565	n.d.	0.0000	n.d.	0	0
Glaucophane		17.1584	0.0000	0.3970	n.d.	0.0001	n.d.	157	130
Quartz 50µm		65.6211	0.1314	0.8106	n.d.	0.0000	n.d.	538	797

E.6 UVLAMP analyses from sample 96/153

96/153		$^{40}Ar/^{39}Ar$	$^{38}Ar/^{39}Ar$	$^{37}Ar/^{39}Ar$	$^{36}Ar/^{39}Ar$	^{39}Ar	$^{40}Ar^{*}/^{39}Ar$	Age (Ma)	± (2 σ)
Phengite 1	(T12)	10.8658	0.0135	0.8716	0.0052	0.0073	9.3228	111	3
Phengite 2	(T12)	10.8593	0.0055	1.0030	0.0016	0.0053	10.3801	111	4
Phengite 3	(T12)	11.7306	0.0143	n.d.	0.0019	0.0055	11.1681	119	4
Phengite 4	(T12)	10.9594	0.0214	2.4809	0.0159	0.0060	6.2515	112	4
Phengite 5	(T12)	9.8187	0.0039	1.0866	0.0258	0.0050	2.1982	100	4
Phengite 6	(T12)	11.7625	0.0125	n.d.	n.d.	0.0040	12.3850	120	4

E.7 UVLAMP analyses from sample 96/155

96/155		$^{40}Ar/^{39}Ar$	$^{38}Ar/^{39}Ar$	$^{37}Ar/^{39}Ar$	$^{36}Ar/^{39}Ar$	^{39}Ar	$^{40}Ar^{*}/^{39}Ar$	Age (Ma)	± (2 σ)
Single phengite		16.7837	0.0352	3.7396	0.4836	0.0003	n.d.	168	49
Single phengite		8.2243	0.0116	0.0000	0.0078	0.0103	5.9249	84	2
Phengite 1	(T13)	9.3876	0.0074	n.d.	n.d.	0.0053	9.9138	96	3
Phengite 2	(T13)	8.0759	0.0117	n.d.	0.0002	0.0076	8.0024	83	2
Phengite 3	(T13)	7.6089	0.0080	0.9812	0.0124	0.0087	3.9386	78	2
Phengite 4	(T13)	7.8691	0.0077	n.d.	n.d.	0.0077	8.2106	81	2
Phengite 5	(T13)	9.0777	0.0141	n.d.	0.0205	0.0035	3.0271	93	4
Single phengite		10.9320	0.0149	n.d.	0.0709	0.0013	n.d.	111	11
Single phengite		10.9481	0.0113	4.7428	n.d.	0.0052	12.9962	112	4
Single phengite		7.9868	0.0096	6.6113	0.0081	0.0067	5.6063	87	2
Garnet 100µm		n.d.	0.0041	n.d.	n.d.	n.d.	109.2919	0	0
Garnet 100µm		0.6781	0.1641	n.d.	n.d.	n.d.	92.3978	7	107

E.8 UVLAMP analyses from sample 96/117

96/117		$^{40}Ar/^{39}Ar$	$^{38}Ar/^{39}Ar$	$^{37}Ar/^{39}Ar$	$^{36}Ar/^{39}Ar$	^{39}Ar	$^{40}Ar^*/^{39}Ar$	Age (Ma)	± (2 σ)
Phengite 1	(T14)	8.5322	0.0054	0.1556	0.0039	0.0054	7.3885	80	4
Phengite 2	(T14)	8.6012	0.0101	0.1660	n.d.	0.0049	12.1697	80	5
Phengite 3	(T14)	8.7030	0.0119	0.1150	0.0069	0.0059	6.6536	81	4
Phengite 4	(T14)	8.3004	0.0118	0.1465	0.0133	0.0068	4.3721	78	4
Phengite 5	(T14)	9.1265	0.0056	0.0280	n.d.	0.0053	11.8622	85	5
Phengite 6	(T14)	8.7010	0.0147	0.0649	n.d.	0.0069	14.2534	81	4
Single phengite		8.8146	0.0126	0.0435	n.d.	0.0059	9.5606	82	40

E.9 UVLAMP analyses from sample 96/118

96/118		$^{40}Ar/^{39}Ar$	$^{38}Ar/^{39}Ar$	$^{37}Ar/^{39}Ar$	$^{36}Ar/^{39}Ar$	^{39}Ar	$^{40}Ar^*/^{39}Ar$	Age (Ma)	± (2 σ)
Single phengite		9.4923	0.0078	0.0227	n.d.	0.0063	9.8961	89	5
Phengite 1	(T15)	8.7130	0.0117	n.d.	0.0027	0.0042	7.9122	81	5
Phengite 2	(T15)	9.1047	0.0041	0.0990	0.0045	0.0047	7.7708	85	5
Phengite 3	(T15)	8.5280	0.0078	0.0759	0.0062	0.0051	6.7041	80	4
Phengite 4	(T15)	8.5034	0.0066	0.1643	0.0047	0.0044	7.1100	80	5
Phengite 5	(T15)	8.5238	0.0042	0.1854	0.0024	0.0045	7.8122	80	5
Phengite 6	(T15)	8.4499	0.0166	0.0803	0.0020	0.0055	7.8465	79	4
Phengite 7	(T15)	8.8506	0.0095	0.2141	0.0002	0.0042	8.7916	83	5
Single phengite		8.4414	0.0250	0.1475	0.0012	0.0042	8.0889	79	38
Single phengite		9.0977	0.0103	0.1432	n.d.	0.0073	9.7089	85	41
Single phengite		8.5946	0.0111	0.0305	n.d.	0.0095	10.0015	80	39

E.10 UVLAMP analyses from sample 96/158

96/158		$^{40}Ar/^{39}Ar$	$^{38}Ar/^{39}Ar$	$^{37}Ar/^{39}Ar$	$^{36}Ar/^{39}Ar$	^{39}Ar	$^{40}Ar^*/^{39}Ar$	Age (Ma)	± (2 σ)
Phengite 1	(T16)	10.7042	0.0149	0.2168	0.0614	0.0020	n.d.	100	5
Phengite 2	(T16)	8.5201	0.0132	0.0141	0.0000	0.0030	8.5209	80	4
Phengite 3	(T16)	8.4463	0.0195	0.0432	0.0130	0.0048	4.6130	79	3
Phengite 4	(T16)	8.1930	0.0176	0.0000	0.0068	0.0047	6.1780	77	2
Phengite 5	(T16)	7.6968	0.0148	0.0000	0.0101	0.0041	4.7126	72	3
Phengite 6	(T16)	8.5709	0.0066	0.0185	0.0000	0.0045	8.5720	80	3
Phengite 7	(T16)	9.5857	0.0083	0.0000	0.0000	0.0036	9.5857	89	3
Phengite 8	(T16)	9.3550	n.d.	0.0000	0.0048	0.0046	7.9457	87	3
Phengite 50µm		7.8474	0.0165	0.0000	0.0032	0.0069	6.9114	74	2
Phengite 50µm		8.5294	0.0166	0.0458	0.0104	0.0060	5.4706	80	2
Phengite 1	(T17)	9.3522	0.0163	0.5080	n.d.	0.0037	9.3829	87	4
Phengite 2	(T17)	8.7871	0.0142	0.2156	0.0063	0.0051	6.9341	82	3
Phengite 3	(T17)	9.1379	0.0134	0.0944	0.0057	0.0038	7.4391	85	3
Single phengite		10.9488	0.0113	0.0759	0.0128	0.0064	7.1560	102	4
Single phengite		11.5210	0.0147	0.0000	0.0075	0.0082	9.2918	107	3
Single phengite		10.5035	0.0161	0.0133	0.0011	0.0114	10.1884	98	2
Single phengite		8.8375	0.0153	0.0328	0.0089	0.0058	6.1994	83	2
Single phengite		9.1684	0.0177	0.0041	0.0124	0.0074	5.4930	86	2
Glaucophane 50µm		11.6974	0.0156	0.0000	0.0143	0.0051	7.4801	109	7
Garnet 100µm		n.d.	0.0041	n.d.	n.d.	n.d.	109.2919	0	0
Garnet 100µm		0.6781	0.1641	n.d.	n.d.	n.d.	92.3978	7	107

E.11 UVLAMP analyses from sample 96/135

96/135		$^{40}Ar/^{39}Ar$	$^{38}Ar/^{39}Ar$	$^{37}Ar/^{39}Ar$	$^{36}Ar/^{39}Ar$	^{39}Ar	$^{40}Ar^*/^{39}Ar$	Age (Ma)	± (2 σ)
Single phengite		11.3584	0.0112	0.0645	0.0002	0.0083	11.2951	105	2
Single phengite		10.9533	0.0116	0.0273	0.0053	0.0098	9.3920	102	1
Single phengite		9.9052	0.0094	0.0066	0.0043	0.0098	8.6470	92	2
Single phengite		11.3605	0.0096	0.0228	0.0000	0.0074	11.3622	105	2
Single phengite		8.3526	0.0170	0.0000	0.0058	0.0055	6.6268	78	2
Phengite 1	(T18)	10.7968	0.0200	0.0000	0.0023	0.0052	10.1155	100	5
Phengite 1	(T18)	10.5541	0.0221	0.0000	n.d.	0.0061	11.4322	98	3
Phengite 1	(T18)	11.7451	0.0091	0.0291	0.0207	0.0044	5.6163	109	3
Glaucophane		14.0000	0.0320	0.0000	2.6818	0.0001	n.d.	129	87
Glaucophane		67.6045	0.0680	0.0810	44.0032	0.0001	n.d.	552	469
Glaucophane		1068.8889	21.9259	0.0000	0.0000	0.0000	1068.722	3422	16047

APPENDIX F

^{40}Ar-^{39}Ar DATA RELATING TO CHAPTER 5 II

F.1 Furnace step-heating data for phengite sample 96/134

T (°C)	$^{40}Ar/^{39}Ar$	$^{38}Ar/^{39}Ar$	$^{37}Ar/^{39}Ar$	$^{36}Ar/^{39}Ar$ (10^{-3})	^{39}Ar (10^{-14}moles)	%^{39}Ar released	$^{40}Ar^*/^{39}Ar$	Age (Ma)	± (1 σ)
800	3.986	0.018	0.001	1.253	28.18	30.88	3.62	107.51	2.25
850	3.939	0.018	0.001	1.094	32.70	64.01	3.62	107.48	2.29
900	3.960	0.018	0.001	1.186	15.88	80.09	3.62	107.32	2.25
900	4.002	0.018	0.002	1.446	7.28	87.47	3.58	106.38	2.12
1000	4.046	0.018	0.004	1.588	4.34	91.86	3.59	106.45	2.18
1050	4.083	0.018	0.004	1.800	2.53	94.42	3.56	105.75	2.16
1100	4.498	0.017	0.005	3.041	1.67	96.11	3.62	107.32	2.20
1200	4.947	0.018	0.012	7.003	0.97	97.10	2.92	87.07	2.13
1400	2.903	0.019	0.029	6.133	2.86	100.00	1.13	34.15	0.92

F.2 Infra-red laser spot analyses for sample 96/75

	$^{40}Ar/^{39}Ar$	$^{38}Ar/^{39}Ar$	$^{37}Ar/^{39}Ar$	$^{36}Ar/^{39}Ar$	^{39}Ar	$^{40}Ar^*/^{39}Ar$	Age (Ma)	± (2 σ)
75	13.38799	0.016646	1.441724	0.009174	0.281222	10.677	124	2
75	11.8821	0.01338	0.385582	0.003975	0.686735	10.70739	110	1
75	10.33226	0.015405	0.580936	0.003606	0.377174	9.266759	96	1
75	10.61335	0.015409	0.809242	0.012917	0.294183	6.796343	99	1
75	36.34851	0.032888	2.884897	0.091573	0.078626	9.288805	318	3
75	10.80194	0.012799	0.309007	0.00168	0.845289	10.30553	100	2
75	11.0037	0.011356	0.202942	0.003065	0.691684	10.098	102	1
75	13.92799	0.015017	0.516988	0.012717	0.609824	10.17018	128	2
75	11.69171	0.013079	0.823328	0.003362	0.581434	10.69813	108	2
75	12.31924	0.013	0	0.008588	0.26259	9.781623	114	1

APPENDIX G

ELECTRON PROBE MICROANALYSIS

G.1 Cameca SX100

The electron probe microanalyser in the Dept. Earth Sciences at the Open University is a Cameca SX100 fitted with four wavelength-dispersive (WDS) spectrometers and an energy-dispersive spectrometer (EDS). Cameca software controls a fully automated system. Standards for each element, count times and detection limits in ppm are presented in Table G.1.1

Element	Standard	Conc. (Wt %)	Detection limit (ppm)
Na	jadeite-BM4	11.20	522
Mg	forsterite-BM4	25.52	713
Al	fspr-In5	9.83	536
Si	fspr-In5	30.10	799
K	fspr-In5	12.39	536
Ca	bustamite-ast3	13.56	575
Ti	rutile-BM4	59.95	1133
Cr	crocoite-ast3	16.09	627
Mn	bustamite-ast3	18.83	693
Fe	hematite-ast3	69.86	1293

Table G.1.1: Mineral standards used within this study.

APPENDIX H

ELECTRON MICROPROBE DATA

H.1 Sample 96/15

SiO_2	TiO_2	Al2O3	MgO	CaO	MnO	FeO	Total	Si	Ti	Al	Mg	Ca	Mn	Fe	Total
37.99	0.14	20.35	1.70	9.26	1.95	30.21	101.66	6.01	0.02	3.80	0.40	1.57	0.26	4.00	16.07
37.75	0.16	20.27	1.69	9.34	2.23	29.55	101.08	6.01	0.02	3.80	0.40	1.59	0.30	3.94	16.07
37.67	0.18	20.14	1.57	9.60	2.46	29.02	100.71	6.02	0.02	3.79	0.37	1.64	0.33	3.88	16.07
37.07	2.07	19.27	1.60	10.16	2.66	27.84	100.66	5.93	0.25	3.63	0.38	1.74	0.36	3.72	16.00
37.63	0.13	20.20	1.60	9.09	3.40	28.85	100.96	6.01	0.02	3.80	0.38	1.55	0.46	3.85	16.08
37.69	0.06	20.22	1.56	8.96	3.52	28.95	100.99	6.02	0.01	3.80	0.37	1.53	0.47	3.86	16.07
37.72	0.09	20.28	1.42	8.77	3.95	29.09	101.35	6.01	0.01	3.80	0.34	1.50	0.53	3.88	16.07
37.74	0.16	20.05	1.37	9.14	3.73	29.08	101.36	6.01	0.02	3.77	0.32	1.56	0.50	3.88	16.07
37.51	0.03	20.18	1.33	8.89	3.98	28.99	100.97	6.01	0.01	3.80	0.32	1.52	0.54	3.88	16.09
37.60	0.19	20.09	1.27	9.28	4.12	28.97	101.56	5.99	0.02	3.77	0.30	1.58	0.56	3.86	16.10
37.40	0.03	20.11	1.28	9.28	4.06	28.77	100.92	5.99	0.00	3.80	0.31	1.60	0.55	3.86	16.10
37.70	0.14	20.08	1.24	9.08	4.00	28.89	101.18	6.02	0.02	3.78	0.29	1.55	0.54	3.86	16.07
37.44	0.13	20.14	1.30	9.04	4.08	28.94	101.12	5.99	0.02	3.80	0.31	1.55	0.55	3.87	16.09

Table H.1.1: Garnet analyses from sample 96/15

SiO_2	Al_2O_3	MgO	MnO	FeO	Na_2O	K_2O	Total	Si	Al	Mg	Mn	Fe	Na	K	Total
52.47	21.39	4.29	0.00	4.75	0.12	11.06	94.21	7.19	3.45	0.87	0.00	0.54	0.03	1.94	14.05
52.88	20.88	4.40	0.06	4.92	0.03	11.04	94.37	7.24	3.37	0.90	0.01	0.56	0.01	1.93	14.01
52.16	21.24	4.25	0.04	5.11	0.16	10.79	93.90	7.18	3.45	0.87	0.01	0.59	0.04	1.90	14.05
52.99	21.83	4.40	0.00	4.72	0.15	10.92	94.50	7.22	3.43	0.89	0.00	0.54	0.04	1.90	14.03

Table H.1.2: Phengite analyses from sample 96/15

SiO_2	Al_2O_3	MgO	CaO	MnO	FeO	Na_2O	Total	Si	Al	Mg	Ca	Mn	Fe	Na	Total
54.75	4.86	7.42	13.70	0.00	12.64	6.50	99.86	2.04	0.21	0.41	0.55	0.00	0.39	0.47	4.08
54.96	5.18	7.39	12.97	0.00	12.72	6.75	100.00	2.05	0.23	0.41	0.52	0.00	0.40	0.49	4.09
54.70	4.92	7.45	13.54	0.00	12.85	6.64	100.13	2.04	0.22	0.41	0.54	0.00	0.40	0.48	4.09
54.97	5.85	7.03	13.02	0.01	12.29	7.20	100.35	2.04	0.26	0.39	0.52	0.00	0.38	0.52	4.10
54.75	5.10	7.60	13.83	0.05	12.54	6.54	100.42	2.03	0.22	0.42	0.55	0.00	0.39	0.47	4.09
55.01	6.15	6.86	12.73	0.04	12.19	7.21	100.25	2.04	0.27	0.38	0.51	0.00	0.38	0.52	4.09
54.82	4.41	7.59	13.55	0.07	13.27	6.44	100.15	2.05	0.19	0.42	0.54	0.00	0.41	0.47	4.09

Table H.1.3: Sodic-pyroxene analyses from sample 96/15

H.2 Sample 96/69

SiO_2	Al_2O_3	MgO	MnO	FeO	Na_2O	K_2O	Total	Si	Al	Mg	Mn	Fe	Na	K	Total
52.36	22.13	4.45	0.04	4.27	0.20	11.06	94.49	3.57	1.78	0.45	0.00	0.24	0.03	0.96	7.04
52.46	22.06	4.49	0.03	4.32	0.16	10.99	94.51	3.58	1.77	0.46	0.00	0.25	0.02	0.95	7.03
52.30	21.99	4.48	0.02	4.32	0.16	10.73	94.00	3.58	1.77	0.46	0.00	0.25	0.02	0.94	7.01
52.55	22.19	4.33	0.02	4.35	0.15	11.01	94.61	3.58	1.78	0.44	0.00	0.25	0.02	0.96	7.02
52.57	21.96	4.33	0.02	4.55	0.13	10.80	94.36	3.59	1.77	0.44	0.00	0.26	0.02	0.94	7.01
52.06	22.12	4.23	0.02	4.70	0.15	10.87	94.14	3.57	1.79	0.43	0.00	0.27	0.02	0.95	7.02
52.19	22.13	4.28	0.02	4.62	0.15	10.70	94.09	3.57	1.78	0.44	0.00	0.26	0.02	0.94	7.01
53.20	21.82	5.02	0.04	3.17	0.10	10.99	94.34	3.61	1.74	0.51	0.00	0.18	0.01	0.95	7.00
53.36	22.48	4.83	0.03	3.68	0.11	11.02	95.51	3.58	1.78	0.48	0.00	0.21	0.01	0.94	7.01
47.31	19.89	4.04	0.02	3.80	0.13	9.82	85.01	3.22	1.60	0.41	0.00	0.22	0.02	0.85	6.32

Table H.2.1: Phengite analyses from sample 96/69

SiO_2	Al_2O_3	MgO	CaO	MnO	FeO	Total	Si	Al	Mg	Ca	Mn	Fe	Total
35.63	20.36	1.07	7.79	9.65	24.58	99.39	2.92	1.97	0.13	0.69	0.67	1.69	8.08
35.80	20.48	1.11	7.73	10.03	24.34	99.57	2.93	1.98	0.14	0.68	0.70	1.67	8.08
35.54	20.23	1.09	7.64	10.39	24.03	98.99	2.93	1.96	0.13	0.68	0.73	1.66	8.09
35.71	20.17	1.10	7.56	10.72	23.86	99.21	2.94	1.95	0.14	0.67	0.75	1.64	8.08
35.56	20.27	1.08	7.71	11.00	23.50	99.36	2.92	1.96	0.13	0.68	0.77	1.61	8.09
36.32	20.32	1.08	7.72	11.12	23.69	100.31	2.95	1.95	0.13	0.67	0.77	1.61	8.07
36.23	20.44	1.07	7.65	11.08	23.51	100.07	2.95	1.96	0.13	0.67	0.76	1.60	8.07
36.47	20.51	1.10	7.63	10.82	23.47	100.20	2.96	1.96	0.13	0.66	0.74	1.59	8.05
34.32	18.50	0.99	7.34	10.03	22.80	94.33	2.97	1.89	0.13	0.68	0.74	1.65	8.07
33.31	17.87	0.95	7.41	10.03	22.36	92.11	2.96	1.87	0.13	0.71	0.76	1.66	8.10
33.56	18.16	0.95	7.70	10.56	23.05	94.06	2.93	1.87	0.12	0.72	0.78	1.69	8.12
34.86	19.75	0.99	7.93	10.93	23.97	98.54	2.90	1.94	0.12	0.71	0.77	1.67	8.12
34.79	19.73	0.99	7.89	10.80	23.79	98.07	2.91	1.94	0.12	0.71	0.77	1.66	8.12
35.16	19.65	1.03	7.82	10.69	23.86	98.44	2.92	1.93	0.13	0.70	0.75	1.66	8.10
35.12	19.65	1.02	7.72	10.79	23.80	98.53	2.92	1.93	0.13	0.69	0.76	1.65	8.10
35.03	19.56	1.03	7.76	10.63	23.73	97.83	2.93	1.93	0.13	0.70	0.75	1.66	8.10
34.92	19.59	1.03	7.69	10.45	23.81	97.56	2.93	1.94	0.13	0.69	0.74	1.67	8.10
34.74	19.59	1.00	7.59	10.52	23.58	97.33	2.92	1.94	0.13	0.68	0.75	1.66	8.10
34.43	19.61	0.95	7.75	10.59	24.11	97.53	2.90	1.95	0.12	0.70	0.76	1.70	8.12
34.79	19.40	0.98	7.66	10.23	24.31	97.47	2.93	1.92	0.12	0.69	0.73	1.71	8.11
34.47	19.34	0.96	7.82	10.27	24.20	97.15	2.91	1.93	0.12	0.71	0.74	1.71	8.12
34.76	19.58	1.00	7.74	10.38	24.53	98.24	2.91	1.93	0.13	0.69	0.74	1.71	8.12
35.68	19.98	0.99	7.60	10.34	24.38	99.05	2.94	1.94	0.12	0.67	0.72	1.68	8.08
35.41	20.07	1.03	7.55	10.18	24.30	98.63	2.93	1.96	0.13	0.67	0.71	1.68	8.09
34.96	19.80	1.01	7.69	10.01	24.22	97.90	2.92	1.95	0.13	0.69	0.71	1.69	8.09
33.81	18.65	0.95	7.42	9.84	23.94	94.77	2.93	1.90	0.12	0.69	0.72	1.73	8.11

Table H.2.2: Garnet analyses from sample 96/69

SiO_2	Al_2O_3	MgO	CaO	MnO	FeO	Na_2O	K_2O	Total	Si	Al	Mg	Ca	Mn	Fe	Na	K	Total
53.36	5.32	8.22	0.47	0.20	18.90	6.63	0.01	93.14	8.11	0.95	1.86	0.07	0.02	2.40	1.96	0.00	15.39
53.27	5.14	8.00	0.60	0.21	19.27	6.65	0.02	93.18	8.11	0.93	1.82	0.10	0.03	2.46	1.97	0.01	15.42
53.37	4.98	7.91	0.65	0.23	19.78	6.58	0.02	93.55	8.12	0.89	1.79	0.11	0.03	2.51	1.94	0.01	15.41
53.49	5.01	7.88	0.66	0.24	19.55	6.46	0.01	93.32	8.14	0.90	1.79	0.11	0.03	2.49	1.91	0.00	15.36
53.02	5.08	7.76	0.58	0.22	19.62	6.58	0.02	92.90	8.12	0.91	1.77	0.09	0.03	2.51	1.96	0.01	15.40
53.42	5.24	7.67	0.57	0.20	19.54	6.57	0.01	93.22	8.14	0.94	1.74	0.09	0.02	2.49	1.94	0.00	15.36
53.55	5.26	7.77	0.56	0.21	19.45	6.62	0.01	93.46	8.13	0.94	1.76	0.09	0.03	2.47	1.95	0.00	15.38
53.33	5.28	7.66	0.58	0.18	19.28	6.52	0.02	92.87	8.14	0.95	1.74	0.09	0.02	2.46	1.93	0.01	15.34
53.10	5.25	7.66	0.57	0.19	19.47	6.43	0.02	92.70	8.13	0.95	1.75	0.09	0.02	2.50	1.91	0.01	15.35
53.05	5.49	7.74	0.55	0.19	19.41	6.59	0.01	93.03	8.10	0.99	1.76	0.09	0.02	2.48	1.95	0.00	15.39
53.15	5.44	7.67	0.57	0.18	19.36	6.54	0.02	92.96	8.11	0.98	1.74	0.09	0.02	2.47	1.93	0.01	15.36
53.22	5.51	7.60	0.52	0.17	19.39	6.54	0.02	93.00	8.12	0.99	1.73	0.09	0.02	2.47	1.94	0.01	15.36
53.10	5.64	7.69	0.54	0.19	18.89	6.52	0.02	92.62	8.11	1.02	1.75	0.09	0.02	2.42	1.93	0.01	15.35
53.33	5.59	7.79	0.55	0.19	19.29	6.56	0.02	93.32	8.10	1.00	1.77	0.09	0.02	2.45	1.93	0.01	15.36
53.40	5.61	7.65	0.52	0.20	19.14	6.57	0.02	93.12	8.12	1.01	1.73	0.09	0.02	2.43	1.94	0.01	15.34
53.67	5.57	7.80	0.53	0.19	19.46	6.54	0.01	93.80	8.11	0.99	1.76	0.09	0.02	2.46	1.91	0.00	15.35
53.39	5.46	7.69	0.53	0.19	19.54	6.55	0.02	93.39	8.11	0.98	1.74	0.09	0.02	2.48	1.93	0.01	15.36
53.40	5.52	7.59	0.53	0.17	19.19	6.56	0.02	93.01	8.13	0.99	1.73	0.09	0.02	2.44	1.94	0.01	15.34
53.43	5.57	7.74	0.48	0.18	19.29	6.65	0.01	93.37	8.11	0.99	1.75	0.08	0.02	2.45	1.96	0.00	15.37
53.22	5.66	7.63	0.48	0.17	19.49	6.68	0.01	93.36	8.09	1.02	1.73	0.08	0.02	2.48	1.97	0.00	15.39
53.44	5.65	7.61	0.47	0.17	19.29	6.69	0.01	93.36	8.11	1.01	1.72	0.07	0.02	2.45	1.97	0.00	15.36
53.55	5.57	7.52	0.46	0.16	19.58	6.61	0.01	93.48	8.12	0.99	1.70	0.07	0.02	2.48	1.94	0.00	15.35
53.31	5.55	7.60	0.46	0.17	19.29	6.64	0.02	93.06	8.12	0.99	1.73	0.07	0.02	2.46	1.96	0.01	15.36
53.23	5.61	7.69	0.46	0.16	19.17	6.55	0.01	92.89	8.11	1.01	1.75	0.07	0.02	2.44	1.94	0.00	15.34
53.22	5.56	7.70	0.43	0.17	19.52	6.63	0.01	93.26	8.10	1.00	1.75	0.07	0.02	2.48	1.96	0.00	15.38
53.34	5.55	7.64	0.43	0.15	19.56	6.67	0.02	93.37	8.11	0.99	1.73	0.07	0.02	2.48	1.97	0.01	15.38
53.58	5.57	7.47	0.45	0.14	19.52	6.65	0.02	93.41	8.13	0.99	1.69	0.07	0.02	2.48	1.96	0.01	15.35
53.21	5.54	7.51	0.43	0.14	19.29	6.71	0.02	92.86	8.12	0.99	1.71	0.07	0.02	2.46	1.98	0.01	15.36
53.40	5.56	7.48	0.43	0.14	19.49	6.63	0.01	93.16	8.12	0.99	1.70	0.07	0.02	2.48	1.96	0.00	15.34
53.43	5.58	7.57	0.44	0.13	19.22	6.54	0.01	92.92	8.14	1.00	1.72	0.07	0.02	2.45	1.93	0.00	15.32
53.43	5.56	7.53	0.43	0.14	19.22	6.57	0.02	92.91	8.14	1.00	1.71	0.07	0.02	2.45	1.94	0.01	15.34
53.32	5.60	7.65	0.43	0.13	19.32	6.74	0.01	93.22	8.11	1.01	1.73	0.07	0.02	2.46	1.98	0.00	15.37
54.07	5.71	7.67	0.43	0.15	19.22	6.58	0.01	93.88	8.14	1.01	1.72	0.07	0.02	2.42	1.92	0.00	15.31
53.52	5.64	7.70	0.45	0.15	19.23	6.66	0.02	93.40	8.11	1.01	1.74	0.07	0.02	2.44	1.96	0.01	15.36
53.52	5.60	7.75	0.45	0.14	19.12	6.55	0.02	93.18	8.12	1.00	1.75	0.07	0.02	2.43	1.93	0.01	15.34
52.86	5.48	7.56	0.46	0.14	18.88	6.51	0.02	91.92	8.14	0.99	1.74	0.07	0.02	2.43	1.94	0.01	15.34
52.54	5.56	7.54	0.45	0.15	18.93	6.46	0.02	91.67	8.11	1.01	1.74	0.07	0.02	2.44	1.93	0.01	15.34
52.68	5.50	7.65	0.46	0.15	18.94	6.47	0.01	91.86	8.12	1.00	1.76	0.07	0.02	2.44	1.93	0.00	15.35
53.28	5.57	7.64	0.43	0.13	18.99	6.49	0.01	92.56	8.14	1.00	1.74	0.07	0.02	2.43	1.92	0.00	15.31

Table H.2.3: Sodic amphibole analyses from sample 96/69

SiO_2	Al_2O_3	MgO	CaO	MnO	FeO	Na_2O	Total	Si	Al	Mg	Ca	Mn	Fe	Na	Total
55.463	6.076	4.771	9.392	0.249	14.456	8.447	98.888	2.04	0.284	0.282	0.399	0.008	0.479	0.649	4.142
55.097	6.418	5.076	9.19	0.33	14.181	8.656	98.976	2.036	0.296	0.296	0.385	0.011	0.463	0.656	4.144
55.304	6.471	4.807	8.95	0.325	14.432	8.805	99.112	2.029	0.302	0.283	0.379	0.011	0.477	0.675	4.157
55.29	6.32	4.88	9.18	0.30	14.36	8.64	98.99	2.04	0.29	0.29	0.39	0.01	0.47	0.66	4.15

Table H.2.4: Sodic-pyroxene analyses from sample 96/69

SiO_2	Al_2O_3	MgO	CaO	MnO	FeO	Total	Si	Al	Mg	Ca	Mn	Fe	Total
37.28	22.12	0.00	22.56	0.27	13.49	95.71	3.37	2.36	0.00	2.18	0.02	1.02	8.95
37.66	22.51	0.01	22.89	0.23	12.51	95.81	3.38	2.38	0.00	2.20	0.02	0.94	8.92
37.05	22.26	0.02	21.83	0.71	13.03	94.90	3.37	2.39	0.00	2.13	0.05	0.99	8.94
37.66	22.17	0.00	22.56	0.43	13.74	96.55	3.38	2.34	0.00	2.17	0.03	1.03	8.95
37.36	22.98	0.01	22.19	0.68	12.49	95.71	3.36	2.44	0.00	2.14	0.05	0.94	8.92
37.45	22.35	0.01	23.10	0.26	13.13	96.30	3.36	2.37	0.00	2.22	0.02	0.99	8.95
37.32	22.36	0.02	22.19	0.93	12.98	95.79	3.37	2.38	0.00	2.15	0.07	0.98	8.95
37.70	22.59	0.00	22.94	0.44	12.85	96.52	3.37	2.38	0.00	2.20	0.03	0.96	8.94
37.22	22.07	0.01	23.05	0.30	13.55	96.20	3.35	2.35	0.00	2.23	0.02	1.02	8.97
37.72	22.23	0.03	23.30	0.15	13.17	96.61	3.38	2.35	0.00	2.23	0.01	0.99	8.95

Table H.2.5: Epidote analyses from sample 96/69

H.3 Sample 96/149

SiO_2	Al_2O_3	MgO	CaO	MnO	FeO	Total	Si	Al	Mg	Ca	Mn	Fe	Total
37.82	20.60	1.47	10.88	3.54	26.27	100.75	3.00	1.93	0.17	0.93	0.24	1.74	8.03
38.12	21.21	2.85	10.41	1.84	26.65	101.14	2.99	1.96	0.33	0.87	0.12	1.75	8.03
37.91	21.15	3.33	9.83	1.32	26.96	100.63	2.98	1.96	0.39	0.83	0.09	1.77	8.03
37.94	21.12	3.35	9.56	1.40	27.36	100.84	2.98	1.96	0.39	0.80	0.09	1.80	8.03
37.94	21.10	3.27	9.06	1.46	27.85	100.74	2.99	1.96	0.38	0.77	0.10	1.83	8.03
37.76	21.10	2.98	9.55	1.93	27.07	100.56	2.98	1.96	0.35	0.81	0.13	1.79	8.03
37.91	21.09	2.62	10.91	2.44	25.56	100.56	2.99	1.96	0.31	0.92	0.16	1.69	8.03
38.22	21.07	2.78	10.06	2.31	26.42	100.96	3.00	1.95	0.32	0.85	0.15	1.73	8.02
37.58	20.81	3.01	9.21	1.86	27.58	100.14	2.99	1.95	0.36	0.78	0.13	1.83	8.04
37.85	21.09	2.96	9.13	1.93	28.06	101.24	2.98	1.95	0.35	0.77	0.13	1.85	8.03
37.65	21.15	2.92	9.26	1.81	27.84	100.87	2.97	1.97	0.35	0.78	0.12	1.84	8.03
37.52	21.05	2.87	9.03	1.81	28.16	100.47	2.98	1.97	0.34	0.77	0.12	1.87	8.04
37.93	20.99	2.85	9.40	1.79	27.84	100.90	2.99	1.95	0.34	0.79	0.12	1.84	8.03
37.75	20.99	2.77	9.67	1.77	27.70	100.71	2.98	1.96	0.33	0.82	0.12	1.83	8.04
37.93	20.88	2.81	9.13	1.73	28.20	100.86	2.99	1.94	0.33	0.77	0.12	1.86	8.03
37.74	21.03	2.76	9.97	1.71	27.45	100.81	2.98	1.96	0.32	0.84	0.11	1.81	8.04
37.89	20.81	2.66	10.03	1.72	27.33	100.58	2.99	1.94	0.31	0.85	0.11	1.81	8.02
37.88	21.04	2.68	9.92	1.81	27.45	100.85	2.99	1.96	0.32	0.84	0.12	1.81	8.03
37.87	20.87	2.77	9.61	1.78	27.63	100.57	2.99	1.95	0.33	0.81	0.12	1.83	8.03
37.73	20.98	2.68	9.60	1.72	27.62	100.55	2.99	1.96	0.32	0.81	0.11	1.83	8.02
37.72	21.04	2.78	9.55	1.79	27.51	100.46	2.99	1.96	0.33	0.81	0.12	1.82	8.03
37.69	21.02	2.78	9.64	1.73	27.47	100.45	2.99	1.96	0.33	0.82	0.12	1.82	8.03
37.89	20.96	2.81	10.53	1.61	26.74	100.74	2.99	1.95	0.33	0.89	0.11	1.76	8.03
37.79	21.03	2.88	9.76	1.81	27.10	100.49	2.99	1.96	0.34	0.83	0.12	1.79	8.03
37.79	21.00	2.78	10.74	1.75	26.62	100.79	2.98	1.95	0.33	0.91	0.12	1.76	8.04
37.99	20.83	2.56	10.45	2.26	26.45	100.79	3.00	1.94	0.30	0.88	0.15	1.74	8.02
37.75	20.99	1.96	11.56	3.46	24.89	100.64	2.99	1.96	0.23	0.98	0.23	1.65	8.03
37.80	20.82	2.25	10.98	2.82	25.76	100.49	2.99	1.94	0.26	0.93	0.19	1.71	8.03
38.01	20.86	2.56	10.22	2.25	26.53	100.66	3.00	1.94	0.30	0.86	0.15	1.75	8.02
38.09	21.17	2.96	9.68	1.62	27.51	101.08	2.99	1.96	0.35	0.82	0.11	1.81	8.03
38.09	20.97	3.27	9.49	1.37	27.39	100.74	2.99	1.94	0.38	0.80	0.09	1.80	8.02
38.14	20.95	3.22	9.96	1.31	27.07	100.78	3.00	1.94	0.38	0.84	0.09	1.78	8.03
37.78	21.04	3.21	9.50	1.37	27.51	100.60	2.98	1.96	0.38	0.80	0.09	1.82	8.03

Table H.3.1: Garnet analyses from sample 96/149

SiO_2	Al_2O_3	MgO	CaO	MnO	FeO	Na_2O	K_2O	Total	Si	Al	Mg	Ca	Mn	Fe	Na	K	Total
56.07	0.98	16.29	9.71	0.40	11.65	1.39	0.07	96.56	8.06	0.17	3.49	1.50	0.05	1.40	0.39	0.01	15.05
58.13	7.86	10.58	1.18	0.00	13.32	6.37	0.02	97.46	8.12	1.29	2.20	0.18	0.00	1.56	1.73	0.01	15.09
57.55	6.96	10.88	1.75	0.01	13.89	5.88	0.03	96.96	8.13	1.16	2.29	0.26	0.00	1.64	1.61	0.01	15.10
56.74	0.71	17.21	10.43	0.39	11.14	1.13	0.07	97.80	8.04	0.12	3.63	1.58	0.05	1.32	0.31	0.01	15.06
55.18	4.45	9.10	14.97	0.00	10.84	5.22	0.00	99.75	7.84	0.74	1.93	2.28	0.00	1.29	1.44	0.00	15.51
55.11	6.53	7.81	12.55	0.12	10.75	6.20	0.00	99.07	7.83	1.09	1.66	1.91	0.01	1.28	1.71	0.00	15.48
50.73	6.18	5.85	9.94	0.01	12.89	2.84	0.11	88.55	8.03	1.15	1.38	1.68	0.00	1.71	0.87	0.02	14.85
58.19	9.44	10.89	1.22	0.08	11.29	6.40	0.00	97.51	8.04	1.54	2.24	0.18	0.01	1.31	1.72	0.00	15.04
58.42	10.47	10.71	1.08	0.08	10.43	6.59	0.02	97.80	8.02	1.69	2.19	0.16	0.01	1.20	1.75	0.01	15.02
57.91	10.50	11.00	1.73	0.05	10.12	6.25	0.04	97.59	7.96	1.70	2.25	0.25	0.01	1.16	1.67	0.01	15.01
58.09	10.04	10.93	1.61	0.09	10.99	6.24	0.00	97.98	7.99	1.63	2.24	0.24	0.01	1.27	1.66	0.00	15.03
57.88	7.97	11.13	1.73	0.05	13.02	6.09	0.03	97.89	8.06	1.31	2.31	0.26	0.01	1.52	1.65	0.01	15.12

Table H.3.2: Sodic-amphibole analyses from sample 96/149

SiO_2	Al_2O_3	MgO	CaO	MnO	FeO	Na_2O	Total	Si	Al	Mg	Ca	Mn	Fe	Na	Total
55.38	6.31	8.05	13.39	0.10	10.04	6.05	99.32	2.04	0.28	0.44	0.53	0.00	0.31	0.43	4.04
55.20	6.25	7.91	13.30	0.09	9.92	6.13	98.83	2.05	0.27	0.44	0.53	0.00	0.31	0.44	4.03
55.17	5.94	8.17	13.46	0.09	9.95	5.87	98.69	2.05	0.26	0.45	0.54	0.00	0.31	0.42	4.03
55.35	5.81	8.31	13.80	0.11	10.23	5.96	99.60	2.04	0.25	0.46	0.55	0.00	0.32	0.43	4.04
55.75	6.99	7.97	13.10	0.03	9.51	6.48	99.83	2.04	0.30	0.44	0.51	0.00	0.29	0.46	4.04
55.18	6.31	7.99	13.54	0.07	9.95	6.35	99.52	2.04	0.28	0.44	0.54	0.00	0.31	0.46	4.05
55.24	5.68	8.37	14.28	0.06	10.24	6.01	99.95	2.04	0.25	0.46	0.56	0.00	0.32	0.43	4.05
55.06	5.17	8.91	14.92	0.03	10.27	5.40	99.82	2.03	0.23	0.49	0.59	0.00	0.32	0.39	4.05
55.04	4.69	9.32	15.35	0.03	10.22	5.17	99.85	2.03	0.20	0.51	0.61	0.00	0.32	0.37	4.05
55.15	4.67	9.40	15.30	0.09	10.18	5.23	100.05	2.03	0.20	0.52	0.61	0.00	0.31	0.37	4.05
55.29	6.45	8.03	13.15	0.06	10.00	6.58	99.63	2.04	0.28	0.44	0.52	0.00	0.31	0.47	4.06
55.25	6.66	7.73	12.83	0.09	10.29	6.70	99.70	2.03	0.29	0.42	0.51	0.00	0.32	0.48	4.06
55.16	6.55	7.75	12.60	0.01	10.56	6.71	99.34	2.04	0.29	0.43	0.50	0.00	0.33	0.48	4.06
55.36	6.69	7.74	13.02	0.10	10.28	6.66	99.88	2.04	0.29	0.42	0.51	0.00	0.32	0.47	4.06
55.15	6.40	8.06	13.37	0.09	10.35	6.50	99.91	2.03	0.28	0.44	0.53	0.00	0.32	0.46	4.07
55.07	6.18	7.68	12.98	0.03	10.93	6.62	99.61	2.04	0.27	0.42	0.52	0.00	0.34	0.48	4.06
55.19	5.78	8.28	13.55	0.08	10.48	6.10	99.46	2.04	0.25	0.46	0.54	0.00	0.32	0.44	4.05
55.19	6.26	8.01	13.16	0.02	10.49	6.05	99.20	2.04	0.27	0.44	0.52	0.00	0.32	0.43	4.04
55.24	5.31	8.83	14.24	0.09	10.19	5.58	99.49	2.04	0.23	0.49	0.56	0.00	0.32	0.40	4.04
55.06	6.38	7.89	13.14	0.06	10.42	6.43	99.38	2.04	0.28	0.44	0.52	0.00	0.32	0.46	4.06

Table H.3.3: Sodic-pyroxene analyses from sample 96/149

SiO_2	Al_2O_3	MgO	MnO	FeO	Na_2O	K_2O	Total	Si	Al	Mg	Mn	Fe	Na	K	Total
52.32	21.90	4.36	0.03	4.13	0.20	10.22	93.23	3.59	1.77	0.45	0.00	0.24	0.03	0.90	6.98
52.77	20.81	4.70	0.07	3.90	0.12	11.23	93.71	3.62	1.69	0.48	0.01	0.23	0.02	0.98	7.03
51.01	21.58	5.44	0.00	4.34	0.15	10.38	93.05	3.53	1.76	0.56	0.00	0.25	0.02	0.92	7.05
52.13	22.09	4.19	0.10	4.30	0.16	10.65	93.78	3.58	1.78	0.43	0.01	0.25	0.02	0.93	7.00
52.67	21.72	4.40	0.04	4.22	0.15	10.52	93.84	3.60	1.75	0.45	0.00	0.24	0.02	0.92	6.99

Table H.3.4: Phengite analyses from sample 96/149

SiO_2	Al_2O_3	MgO	CaO	MnO	FeO	Na_2O	Total	Si	Al	Mg	Ca	Mn	Fe	Na	Total
38.18	23.26	0.03	23.21	0.05	12.46	0.01	97.20	3.37	2.42	0.00	2.20	0.00	0.92	0.00	8.92
37.80	24.12	0.03	23.47	0.07	11.26	0.00	96.74	3.34	2.51	0.00	2.22	0.00	0.83	0.00	8.91
38.45	26.81	0.15	23.10	0.10	7.73	0.01	96.35	3.33	2.74	0.02	2.14	0.01	0.56	0.00	8.80

Table H.3.5: Epidote analyses from sample 96/149

H.4 Sample 96/158

SiO_2	Al_2O_3	MgO	MnO	FeO	Na_2O	K_2O	Total	Si	Al	Mg	Mn	Fe	Na	K	Total
51.54	22.04	4.27	0.01	4.3	0.13	10.9	93.36	3.56	1.79	0.44	0	0.25	0.02	0.96	7.02
51.73	22.51	4.26	0.01	3.88	0.15	11.16	93.9	3.55	1.82	0.43	0	0.22	0.02	0.98	7.03
51.56	22.38	4.32	0.02	3.84	0.15	10.78	93.21	3.55	1.82	0.44	0	0.22	0.02	0.95	7.01
51.51	21.99	4.28	0	4.05	0.13	11	93.14	3.56	1.79	0.44	0	0.23	0.02	0.97	7.03
51.44	22.34	4.11	0.01	4.2	0.14	10.76	93.18	3.55	1.82	0.42	0	0.24	0.02	0.95	7.02
52.88	21.55	4.52	0.03	4.61	0.12	10.67	94.51	3.6	1.73	0.46	0	0.26	0.02	0.93	7
51.59	22.55	4.18	0.02	4.06	0.17	10.98	93.74	3.54	1.83	0.43	0	0.23	0.02	0.96	7.03
52.08	22.32	4.29	0.02	4.2	0.14	11.1	94.3	3.56	1.8	0.44	0	0.24	0.02	0.97	7.03
52.01	22.5	4.25	0.01	3.92	0.15	10.87	93.9	3.56	1.82	0.43	0	0.23	0.02	0.95	7.01
51.79	22.71	4.16	0	4.12	0.15	10.95	94.06	3.54	1.83	0.42	0	0.24	0.02	0.96	7.02
52.04	22.66	4.33	0.01	3.95	0.15	10.66	93.98	3.55	1.82	0.44	0	0.23	0.02	0.93	7
52.07	22.09	4.37	0.02	4.25	0.12	11.09	94.16	3.56	1.78	0.45	0	0.24	0.02	0.97	7.03
51.96	22.37	4.28	0.02	3.91	0.13	10.91	93.76	3.56	1.81	0.44	0	0.23	0.02	0.95	7.01
51.66	22.58	4.18	0	3.97	0.14	11.09	93.8	3.54	1.83	0.43	0	0.23	0.02	0.97	7.03
51.64	22.48	4.27	0	4.1	0.14	10.89	93.71	3.55	1.82	0.44	0	0.24	0.02	0.95	7.02
51.94	22.52	4.29	0	3.92	0.14	10.79	93.81	3.56	1.82	0.44	0	0.23	0.02	0.94	7.01
52.37	22.24	4.35	0	4.03	0.13	10.9	94.21	3.57	1.79	0.44	0	0.23	0.02	0.95	7.01
51.7	22.44	4.1	0	4.36	0.15	10.96	93.93	3.55	1.82	0.42	0	0.25	0.02	0.96	7.02
51.95	22.44	4.26	0.02	3.88	0.14	11.07	93.96	3.56	1.81	0.43	0	0.22	0.02	0.97	7.02
52.1	22.41	4.36	0.01	4	0.15	11.06	94.26	3.56	1.8	0.45	0	0.23	0.02	0.96	7.02
51.73	22.6	4.1	0.01	4.27	0.16	11.05	94.11	3.54	1.82	0.42	0	0.24	0.02	0.97	7.02

Table H.4.1: Phengite analyses from sample 96/158

SiO_2	Al_2O_3	MgO	CaO	MnO	FeO	Na_2O	Total	Si	Al	Mg	Ca	Mn	Fe	Na	Total
55.12	6.13	7.43	12.81	0.06	11.43	6.87	99.85	2.04	0.27	0.41	0.51	0.00	0.35	0.49	4.07
55.03	4.93	8.13	13.91	0.07	12.17	6.31	100.56	2.04	0.21	0.45	0.55	0.00	0.38	0.45	4.08
55.38	4.96	8.42	14.14	0.06	11.75	6.03	100.74	2.04	0.22	0.46	0.56	0.00	0.36	0.43	4.07
54.47	5.98	7.98	13.05	0.06	10.55	6.46	98.54	2.04	0.26	0.45	0.52	0.00	0.33	0.47	4.07
55.34	5.95	7.80	13.17	0.06	11.34	6.69	100.38	2.04	0.26	0.43	0.52	0.00	0.35	0.48	4.07
55.01	5.29	7.89	13.26	0.08	12.24	6.56	100.33	2.04	0.23	0.44	0.53	0.00	0.38	0.47	4.08
55.59	6.17	8.09	13.36	0.05	10.71	6.69	100.68	2.03	0.27	0.44	0.52	0.00	0.33	0.47	4.07
55.67	6.59	7.82	12.78	0.08	10.67	7.07	100.68	2.03	0.28	0.43	0.50	0.00	0.33	0.50	4.07
55.44	5.71	7.99	13.32	0.06	11.69	6.64	100.86	2.04	0.25	0.44	0.52	0.00	0.36	0.47	4.08
54.80	4.64	8.41	14.22	0.07	12.18	6.04	100.37	2.03	0.20	0.47	0.57	0.00	0.38	0.44	4.08

Table H.4.2: Sodic-pyroxene analyses from sample 96/158

SiO_2	Al_2O_3	MgO	CaO	MnO	FeO	Total	Si	Al	Mg	Ca	Mn	Fe	Total
38.22	21.20	1.81	9.04	2.92	28.32	101.69	3.00	1.97	0.21	0.76	0.20	1.86	8.01
38.07	21.19	1.81	9.23	2.85	28.54	101.77	2.99	1.97	0.21	0.78	0.19	1.88	8.02
37.91	21.02	1.82	9.35	2.85	28.38	101.38	2.99	1.96	0.21	0.79	0.19	1.88	8.03
37.73	21.12	1.81	8.87	2.76	28.92	101.24	2.99	1.97	0.21	0.75	0.19	1.91	8.03
37.94	21.09	1.83	8.91	2.84	28.82	101.49	2.99	1.96	0.22	0.75	0.19	1.90	8.02
37.68	21.05	1.81	8.79	2.81	28.73	101.24	2.98	1.97	0.21	0.74	0.19	1.90	8.02
37.51	20.99	1.80	8.86	2.86	28.85	101.01	2.98	1.97	0.21	0.75	0.19	1.92	8.03
37.78	21.01	1.81	8.81	2.88	28.85	101.21	2.99	1.96	0.21	0.75	0.19	1.91	8.02
37.59	20.94	1.77	8.81	2.87	29.00	101.05	2.99	1.96	0.21	0.75	0.19	1.93	8.03
37.96	20.92	1.77	8.80	2.87	28.96	101.35	3.00	1.95	0.21	0.75	0.19	1.92	8.02
37.90	21.15	1.81	8.59	2.94	29.05	101.49	2.99	1.97	0.21	0.73	0.20	1.92	8.02
37.38	21.05	1.80	8.66	2.94	29.21	101.08	2.97	1.97	0.21	0.74	0.20	1.94	8.04
37.38	20.89	1.79	8.72	2.87	28.63	100.33	2.99	1.97	0.21	0.75	0.20	1.91	8.03
37.35	21.06	1.79	8.94	2.87	28.78	101.28	2.96	1.97	0.21	0.76	0.19	1.91	8.03
37.45	21.05	1.75	8.90	2.81	28.69	100.68	2.98	1.98	0.21	0.76	0.19	1.91	8.03
37.49	20.98	1.72	8.77	2.99	28.82	100.88	2.98	1.97	0.20	0.75	0.20	1.92	8.03
37.47	20.88	1.71	8.60	3.04	28.68	100.99	2.98	1.96	0.20	0.73	0.20	1.91	8.02
37.66	20.93	1.76	8.69	3.09	28.70	101.14	2.99	1.96	0.21	0.74	0.21	1.91	8.02
37.72	20.85	1.83	8.83	3.11	28.68	101.17	2.99	1.95	0.22	0.75	0.21	1.90	8.03
37.20	20.95	1.79	8.93	3.04	28.94	101.09	2.96	1.97	0.21	0.76	0.20	1.93	8.05
37.44	20.97	1.74	8.89	3.10	28.61	100.92	2.98	1.97	0.21	0.76	0.21	1.90	8.03
37.33	20.89	1.71	8.84	3.13	28.59	100.66	2.98	1.97	0.20	0.76	0.21	1.91	8.04
37.31	20.73	1.72	9.02	3.24	28.65	100.86	2.98	1.95	0.20	0.77	0.22	1.91	8.04
37.30	20.86	1.74	8.97	3.16	28.45	100.68	2.98	1.96	0.21	0.77	0.21	1.90	8.03
37.61	20.82	1.74	9.19	3.18	28.51	101.14	2.99	1.95	0.20	0.78	0.21	1.89	8.03
37.62	20.94	1.73	9.15	3.30	28.28	101.08	2.99	1.96	0.20	0.78	0.22	1.88	8.03
37.36	20.86	1.75	8.93	3.44	28.42	100.81	2.98	1.96	0.21	0.76	0.23	1.89	8.03
37.30	20.82	1.74	8.52	3.52	28.77	100.71	2.98	1.96	0.21	0.73	0.24	1.92	8.04
37.81	20.75	1.80	8.45	3.54	28.62	101.03	3.00	1.94	0.21	0.72	0.24	1.90	8.02
37.32	20.85	1.71	8.41	3.63	28.55	100.71	2.98	1.96	0.20	0.72	0.25	1.91	8.03
37.15	20.72	1.72	8.45	3.75	28.73	100.57	2.98	1.96	0.21	0.73	0.26	1.93	8.05
37.62	20.80	1.72	8.44	3.88	28.45	101.02	2.99	1.95	0.20	0.72	0.26	1.89	8.03
37.18	20.72	1.65	8.59	3.96	28.06	100.41	2.98	1.96	0.20	0.74	0.27	1.88	8.04
37.37	20.71	1.65	8.65	3.94	27.97	100.33	2.99	1.95	0.20	0.74	0.27	1.87	8.02
37.16	20.85	1.57	8.91	4.09	28.07	100.66	2.97	1.97	0.19	0.77	0.28	1.88	8.04
37.50	20.77	1.57	8.94	4.32	27.61	100.79	2.99	1.95	0.19	0.77	0.29	1.84	8.03
37.30	20.77	1.53	8.94	4.32	27.76	100.66	2.98	1.96	0.18	0.77	0.29	1.86	8.04
37.10	20.77	1.55	8.97	4.42	27.50	100.40	2.97	1.96	0.19	0.77	0.30	1.85	8.04
37.16	20.82	1.48	8.98	4.51	27.62	100.97	2.96	1.96	0.18	0.77	0.31	1.84	8.04
37.24	20.81	1.42	8.79	4.51	27.91	100.79	2.98	1.96	0.17	0.75	0.31	1.87	8.04
37.10	20.82	1.50	8.52	4.65	27.74	100.37	2.98	1.97	0.18	0.73	0.32	1.86	8.03
37.19	20.72	1.48	8.44	4.81	27.87	100.85	2.97	1.95	0.18	0.72	0.33	1.86	8.04
37.45	20.67	1.46	8.57	4.67	27.96	100.83	2.99	1.95	0.17	0.74	0.32	1.87	8.03
36.98	20.77	1.39	8.35	4.86	27.61	100.55	2.97	1.96	0.17	0.72	0.33	1.85	8.03
37.19	20.77	1.42	8.64	4.92	27.74	100.80	2.98	1.96	0.17	0.74	0.33	1.86	8.04
37.21	20.79	1.40	8.46	4.78	27.73	100.42	2.99	1.97	0.17	0.73	0.32	1.86	8.03
37.22	20.87	1.35	8.77	4.80	27.74	100.92	2.97	1.97	0.16	0.75	0.32	1.85	8.03
37.08	20.84	1.36	8.78	4.77	27.55	100.45	2.97	1.97	0.16	0.75	0.32	1.85	8.03
37.10	20.82	1.36	8.73	4.81	27.45	100.61	2.97	1.97	0.16	0.75	0.33	1.84	8.03
37.17	20.78	1.27	8.83	4.95	27.26	100.70	2.97	1.96	0.15	0.76	0.34	1.82	8.03
36.92	20.21	1.24	9.16	4.94	26.79	100.10	2.97	1.92	0.15	0.79	0.34	1.80	8.02
37.41	20.77	1.27	8.72	5.06	27.31	100.89	2.99	1.95	0.15	0.74	0.34	1.82	8.02
36.58	20.81	1.27	8.55	5.25	27.29	99.92	2.96	1.98	0.15	0.74	0.36	1.85	8.05
36.91	20.58	1.22	8.36	5.20	27.19	99.52	2.99	1.97	0.15	0.73	0.36	1.84	8.03
36.89	20.74	1.25	8.29	5.28	27.19	99.69	2.98	1.97	0.15	0.72	0.36	1.84	8.03
37.33	20.71	1.21	8.69	5.27	27.06	100.78	2.99	1.95	0.14	0.74	0.36	1.81	8.02
37.11	20.68	1.21	8.68	5.43	27.04	100.68	2.97	1.95	0.14	0.74	0.37	1.81	8.03
36.97	20.69	1.27	8.49	5.63	27.13	100.41	2.97	1.96	0.15	0.73	0.38	1.82	8.04
37.07	20.68	1.27	8.34	5.73	26.92	100.19	2.98	1.96	0.15	0.72	0.39	1.81	8.03
37.10	20.77	1.25	8.25	5.70	27.29	100.43	2.98	1.97	0.15	0.71	0.39	1.83	8.03
37.03	20.62	1.28	8.25	5.82	27.22	100.42	2.98	1.95	0.15	0.71	0.40	1.83	8.03
37.25	20.64	1.28	8.46	5.73	26.89	100.31	2.99	1.95	0.15	0.73	0.39	1.81	8.03
37.09	20.93	1.53	8.61	4.31	27.66	100.25	2.98	1.98	0.18	0.74	0.29	1.85	8.03
37.23	21.04	1.70	8.76	3.32	28.35	100.71	2.97	1.98	0.20	0.75	0.23	1.89	8.03
37.01	21.20	1.96	9.08	1.55	29.36	100.24	2.96	2.00	0.23	0.78	0.11	1.96	8.04
37.38	21.11	2.04	9.08	1.56	29.18	100.41	2.98	1.98	0.24	0.77	0.11	1.94	8.03
37.29	20.86	1.99	9.33	1.58	29.30	100.44	2.98	1.96	0.24	0.80	0.11	1.96	8.04
37.70	21.03	1.79	9.98	1.67	28.49	100.90	2.99	1.96	0.21	0.85	0.11	1.89	8.02
37.44	21.15	1.80	9.95	1.65	28.42	100.68	2.97	1.98	0.21	0.85	0.11	1.89	8.03
37.46	21.05	1.85	10.05	1.42	28.43	100.36	2.98	1.97	0.22	0.86	0.10	1.89	8.03
37.22	20.96	1.83	10.24	1.54	28.43	100.34	2.97	1.97	0.22	0.88	0.11	1.90	8.04
37.14	20.91	1.73	10.09	1.62	28.71	100.29	2.97	1.97	0.21	0.86	0.11	1.92	8.04
37.45	20.98	1.72	10.16	1.65	28.41	100.43	2.98	1.97	0.20	0.87	0.11	1.89	8.03
37.25	20.99	1.72	10.30	1.70	28.29	100.30	2.97	1.97	0.20	0.88	0.11	1.89	8.03
37.29	21.01	1.65	10.45	1.63	28.12	100.43	2.97	1.97	0.20	0.89	0.11	1.87	8.03
37.46	21.04	1.70	10.47	1.62	28.33	100.91	2.97	1.97	0.20	0.89	0.11	1.88	8.03
37.75	20.94	1.67	10.46	1.59	28.28	100.76	2.99	1.96	0.20	0.89	0.11	1.88	8.02
37.53	21.21	1.67	10.49	1.62	28.34	101.34	2.96	1.97	0.20	0.89	0.11	1.87	8.03
37.30	20.99	1.72	10.46	1.60	28.27	100.59	2.97	1.97	0.20	0.89	0.11	1.88	8.04
37.65	20.86	1.67	10.56	1.59	28.31	100.74	2.99	1.95	0.20	0.90	0.11	1.88	8.05
37.22	21.05	1.66	10.18	1.59	28.54	100.55	2.96	1.98	0.20	0.87	0.11	1.90	8.04
37.22	20.95	1.70	9.97	1.61	28.78	100.71	2.96	1.97	0.20	0.85	0.11	1.92	8.03

Table H.4.3: Garnet analyses from sample 96/158

H.5 Sample 96/159

SiO_2	Al_2O_3	MgO	CaO	MnO	FeO	Total	Si	Al	Mg	Ca	Mn	Fe	Total
36.91	20.56	1.92	9.11	0.64	31.03	100.26	2.96	1.95	0.23	0.78	0.04	2.09	8.06
37.04	20.48	1.96	9.19	0.63	31.05	100.47	2.97	1.94	0.23	0.79	0.04	2.08	8.06
37.00	20.52	1.93	9.13	0.63	30.74	100.24	2.97	1.94	0.23	0.79	0.04	2.06	8.05
36.75	20.45	1.88	9.26	0.71	30.71	100.24	2.96	1.94	0.23	0.80	0.05	2.06	8.06
37.02	20.51	1.90	9.21	0.73	30.88	100.70	2.96	1.94	0.23	0.79	0.05	2.07	8.06
37.44	20.56	1.92	9.41	0.84	30.36	100.59	2.99	1.93	0.23	0.80	0.06	2.03	8.04
36.88	20.59	1.90	9.47	0.83	30.49	100.34	2.96	1.95	0.23	0.81	0.06	2.05	8.06
37.13	20.54	1.90	9.51	1.06	30.15	100.38	2.97	1.94	0.23	0.82	0.07	2.02	8.05
36.99	20.67	1.86	9.33	1.16	30.14	100.21	2.97	1.95	0.22	0.80	0.08	2.02	8.05
37.13	20.67	1.88	9.43	1.22	30.12	100.57	2.97	1.95	0.23	0.81	0.08	2.01	8.05
37.03	20.76	1.97	9.29	1.03	30.07	100.65	2.96	1.95	0.23	0.80	0.07	2.01	8.05
37.13	20.76	1.99	9.44	1.00	30.16	100.58	2.97	1.95	0.24	0.81	0.07	2.01	8.05
37.41	20.73	1.94	9.36	1.02	30.17	100.72	2.98	1.95	0.23	0.80	0.07	2.01	8.04
37.10	20.71	1.92	9.57	1.00	29.89	100.61	2.96	1.95	0.23	0.82	0.07	2.00	8.05
37.19	20.80	1.88	9.74	1.06	29.66	100.76	2.96	1.95	0.23	0.83	0.07	1.98	8.05
37.23	20.76	1.89	9.88	1.13	29.75	100.81	2.97	1.95	0.23	0.84	0.08	1.98	8.06
37.17	20.79	1.89	9.98	1.15	29.35	100.63	2.96	1.95	0.23	0.85	0.08	1.96	8.05
37.51	20.71	1.86	9.91	1.17	29.44	101.07	2.98	1.94	0.22	0.84	0.08	1.95	8.03
37.14	20.70	1.83	10.04	1.43	29.34	100.57	2.97	1.95	0.22	0.86	0.10	1.96	8.05
37.20	20.68	1.73	9.88	1.54	29.20	100.80	2.96	1.94	0.21	0.84	0.11	1.95	8.04
37.64	20.72	1.69	10.05	1.68	28.93	100.78	2.99	1.94	0.20	0.86	0.11	1.92	8.03
37.19	20.75	1.57	10.35	1.96	28.68	100.68	2.97	1.95	0.19	0.89	0.13	1.91	8.05
37.09	20.72	1.58	10.39	2.01	28.67	100.64	2.96	1.95	0.19	0.89	0.14	1.92	8.06
37.17	20.78	1.52	10.47	2.04	28.54	100.58	2.97	1.96	0.18	0.90	0.14	1.91	8.05
37.34	20.69	1.51	10.57	2.07	28.30	100.58	2.98	1.95	0.18	0.90	0.14	1.89	8.04
37.34	20.85	1.47	10.83	2.01	28.03	100.68	2.97	1.96	0.17	0.92	0.14	1.87	8.04
37.07	20.86	1.43	11.07	2.02	27.99	100.52	2.96	1.97	0.17	0.95	0.14	1.87	8.06
37.01	20.78	1.45	11.45	2.05	27.78	100.61	2.96	1.96	0.17	0.98	0.14	1.85	8.06
37.37	20.80	1.34	11.82	2.00	27.39	100.91	2.97	1.95	0.16	1.01	0.14	1.82	8.05
37.27	20.93	1.32	12.00	1.96	27.10	101.16	2.96	1.96	0.16	1.02	0.13	1.80	8.05
37.47	20.89	1.24	12.35	2.32	26.54	100.87	2.97	1.95	0.15	1.05	0.16	1.76	8.04

Table H.5.1: Garnet analyses from sample 96/159

SiO_2	Al_2O_3	MgO	MnO	FeO	Na_2O	K_2O	Total	Si	Al	Mg	Mn	Fe	Na	K	Total
54.15	21.96	4.95	0.02	4.18	0.08	11.31	96.65	3.60	1.72	0.49	0.00	0.23	0.01	0.96	7.02
54.75	22.30	4.98	0.00	3.93	0.10	11.19	97.26	3.61	1.73	0.49	0.00	0.22	0.01	0.94	7.00
54.18	22.97	4.88	0.01	4.00	0.13	11.24	97.40	3.57	1.78	0.48	0.00	0.22	0.02	0.95	7.02
54.63	22.60	4.91	0.01	3.94	0.12	11.24	97.44	3.60	1.75	0.48	0.00	0.22	0.01	0.94	7.00
54.35	22.34	4.81	0.01	4.18	0.11	11.17	96.99	3.60	1.74	0.48	0.00	0.23	0.01	0.94	7.01
52.97	22.85	4.39	0.01	4.38	0.15	11.13	95.88	3.56	1.81	0.44	0.00	0.25	0.02	0.95	7.03
53.89	22.34	4.86	0.01	4.01	0.08	11.30	96.48	3.59	1.75	0.48	0.00	0.22	0.01	0.96	7.02
52.44	22.23	4.54	0.00	4.45	0.14	11.20	95.00	3.56	1.78	0.46	0.00	0.25	0.02	0.97	7.04
53.00	22.41	4.51	0.02	4.55	0.13	11.12	95.74	3.57	1.78	0.45	0.00	0.26	0.02	0.95	7.03
52.77	22.14	4.54	0.00	4.89	0.10	11.28	95.72	3.56	1.76	0.46	0.00	0.28	0.01	0.97	7.04
53.80	22.14	4.81	0.01	4.41	0.17	11.03	96.38	3.59	1.74	0.48	0.00	0.25	0.02	0.94	7.02

Table H.5.2: Phengite analyses from sample 96/159

SiO_2	Al_2O_3	MgO	CaO	MnO	FeO	Na_2O	Total	Si	Ti	Al	Mg	Ca	Mn	Fe	Na	Total
54.39	4.19	8.92	13.78	0.24	10.83	5.62	97.98	2.05	0.00	0.19	0.50	0.56	0.01	0.34	0.41	4.06
53.37	5.03	8.00	12.44	0.16	10.71	6.30	98.95	2.00	0.08	0.22	0.45	0.50	0.00	0.33	0.46	4.04
55.19	4.64	8.76	13.60	0.17	10.79	5.85	99.10	2.05	0.00	0.20	0.49	0.54	0.00	0.34	0.42	4.05
55.62	4.34	11.28	12.32	0.17	9.97	5.00	98.78	2.06	0.00	0.19	0.62	0.49	0.01	0.31	0.36	4.03
55.27	4.93	8.89	13.51	0.19	10.41	5.96	99.16	2.05	0.00	0.22	0.49	0.54	0.01	0.32	0.43	4.06
55.27	4.87	8.92	13.87	0.21	10.50	5.95	99.60	2.05	0.00	0.21	0.49	0.55	0.01	0.33	0.43	4.06
55.55	4.68	9.15	13.81	0.19	10.36	5.80	99.34	2.05	0.00	0.20	0.51	0.55	0.01	0.32	0.42	4.03
54.06	4.83	8.88	13.74	0.20	10.10	5.67	97.54	2.04	0.00	0.21	0.50	0.56	0.01	0.32	0.42	4.06

Table H.5.3: Sodic-pyroxene analyses from sample 96/159

REFERENCES

Altherr R, Schleistedt M, Okrusch M, Siedel E, Kreuzer H, Harre W, Lenz H, Wendt I, Wagner GA (1979) Geochronology of high pressure rocks on Sifnos (Cyclades, Greece). *Contrib. Mineral. Petrol.*, 70: 245-255.

Andersen TB, Jamtveit B (1990) Uplift of deep crust during orogenic extensional collapse: a model based on field studies in the Sogn-Sunnfjord region of Western Norway. *Tectonics*, 9: 1097-1111.

Arnaud NO, Brunel M, Cantagrel JM, Tapponier P (1993) High cooling and denudation rates at Konur Shan, Eastern Pamir (Xinjiang, China) revealed by ^{40}Ar-^{39}Ar alkali feldspar thermochronolgy. *Tectonics,* 12: 1335-1346.

Arnaud NO, Kelley SP (1995) Evidence for excess argon during high pressure metamorphism in the Dora Maira Massif (western Alps, Italy), using an ultra-violet laser ablation microprobe ^{40}Ar-^{39}Ar technique. *Contrib. Mineral. Petrol.*, 121: 1-11.

Arnaud AO, Kelley SP (1997) Argon behaviour in gem-quality orthoclase from Madagascar: Experiments and some consequences for ^{40}Ar-^{39}Ar geochronology.*Geochim. Cosmochim. Acta.*, 61: 3227-3255.

Avigad D (1996) Pre-collisional ductile extension in the internal western Alps (Sesia Zone, Italy). *Earth Planet. Sci. Lett.*, 137: 175-188.

Bauer WH (1978) Crystal structure refinement of lawsonite. *Am. Min.*, 63: 311-5.

Beaumont C, Ellis S, Hamilton J (1996) Mechanical model for subduction -collision tectonics of Alpine-type compressional orogens. *Geology*, 24: 8: 675-678.

Berger GW, York D (1981a) Geothermometry from ^{40}Ar-^{39}Ar dating experiments. *Geochim. Cosmochim. Acta*, 45: 39-44.

Biino GG, Compagnoni R (1992) Very high pressure metamorphism of the Brossasco coronite metagranite, southern Dora Maira massif, western Alps. *Schweiz Min. Pet. Mitt.*, 72: 347-363.

Bingöl E (1976) Evolution geotectonique de l'Anatolie de l'Ouest, *Bull. Geol. Soc. Fr.*, 18: 235-254.

von Blackenberg F, Villa IM (1988) Argon retentivity and argon excess in amphiboles from the garbenschists of the western Tauern Window, Eastern Alps. *Contrib. Mineral. Petrol.*, 100: 1-11.

Bohlen SR, Boettcher AL (1982) The quartz-coesite transformation: a pressure determination and the effects of other components. *J. Geophys. Res.*, 87: 7073-7078.

Bose K, Ganguly J (1995) Quartz-coesite transition revisited: reversed experimental determination at 500°-1200° C and retrieved thermochemical properties. *Am. Min.*, 80: 231-238.

Boundy TM, Hall CM, Li G, Essene EJ, Halliday AN (1997) Fine-scale isotopic heterogeneities and fluids in the deep crust: a ^{40}Ar-^{39}Ar laser ablation and TEM study of muscovites from a granulite-eclogite transition zone. *Earth Planet. Sci. Lett.*, 148: 223-242.

Bowen NL (1928) The Evolution of Igneous Rocks. Princeton University Press, Princeton, New Jersey.

Bowtell SA, Cliff RA, Barnicoat AC (1994) Sm-Nd isotopic evidence on the age of eclogitization in the Zermatt-Saas ophiolite. *J. Met. Geol.*, 12: 187-196.

Bröcker M, Kreuzer H, Matthews A, Okrusch M (1993) ^{40}Ar-^{39}Ar and oxygen isotope studies of polymetamorphism from Tinos Island, Cycladic blueschist belt. *J. Met. Geol.*, 11: 223-40.

Bröcker M, Franz L (1998) Rb-Sr isotope studies on Tino Island (Cyclades, Greece): additional time constraints for metamorphism, extent of infiltration-controlled overprinting and deformational activity. *Geol. Mag.*, 135: 369-382.

Carswell DA, O'Brien PJ, Wilson RN, Zhai M (1997) Thermobarometry of phengite-bearing eclogites in the Dabie Mountains of central China. *J. Met. Geol.*, 15: 239-252.

Cawthorn RG, Collerson KD (1974) The recalculation of pyroxene end-member parameters and the estimation of ferrous and ferric iron content from electron microprobe analyses. *Am. Min.*, 59: 1203-1208.

Chao ETC, Shoemaker EM, Madsden BM (1960) First natural occurrence of coesite. *Science*, 132: 220-222.

Chinner GA (1960) Pelitic gneisses with varying ferrous/ferric ratios from Glen Clova, Angus, Scotland. *J. Petrology.* 1, 178-217.

Chopin C (1984) Coesite and pure pyrope in high-grade blueschists of the western Alps: a first record and some consequences. *Contrib. Mineral. Petrol.*, 86: 107-118.

Chopin C (1987) Very-high-pressure metamorphism in the western Alps - implications for subduction of continental crust. *Phil. Trans. Roy. Soc. Lond.*, 321: 183-197.

Chopin C, Maluski H (1980) ^{40}Ar-^{39}Ar dating of high-pressure metamorphic micas from the Gran Paradiso area (western Alps): evidence against the blocking temperature concept. *Contrib. Mineral. Petrol.*, 74: 109-22.

Chopin C, Brunet F, Gebert W, Medenbach O, Tillmanns E (1993) Bearthite, $Ca_2Al(PO_4)_2OH$, a new mineral from high pressure terranes of the western Alps. *Schweiz Min. Pet. Mitt.*, 73: 1-9.

Cloos M (1982) Flow melanges: Numerical modelling and geologic constraints on their in the Franciscan subduction complex, California. *Geol. Soc. Am. Bull.*, 93: 330-345.

Cogolu E (1967) Etude petrographique de la region de Mihaliccik. *Schweiz Min. Pet. Mitt.*, 47: 683-824.

Cogolu E, Krummenacher D (1967) Problemes geochronometriques dans la partie NW de l'Anatolie Centrale (Turquie). *Schwiez Min. Pet. Mitt.* 47: 825-833.

Coleman RG, Wang X (1995) Eds: *Ultrahigh pressure metamorphism.* Cambridge University Press. pp. 528.

Comodi P, Zanazzi, PF (1996) Effects of temperature and pressure on the structure of lawsonite. *Am. Min.*, 81: 833-41.

Cumbest RJ, Johnson EL, Onstott TC (1994) Argon composition of metamorphic fluids: implications for ^{40}Ar-^{39}Ar geochemistry. *Geol. Soc. Am. Bull.*, 106: 942-951.

Dahl PS (1996) The crystal chemical basis for Ar retention in micas: inferences from interlayer partitioning and implications for geochronology. *Contrib. Mineral. Petrol.*, 123: 22-39.

Dalrymple GB, Lanphere MA (1974) ^{40}Ar-^{39}Ar age spectra of some undisturbed terrestrial samples. *Geochim. Cosmochim. Acta*, 38: 715-738.

Davies JH, von Blackenberg F (1995) Slab breakoff: a model of lithosphere detachment and its test in the magmatism and deformation of collisional orogens. *Earth Planet. Sci. Lett.*, 129: 85-102.

van Der Molen I, van Roermund HLM (1986) The pressure path of solid inclusions in minerals: the retention of coesite inclusions during uplift. *Lithos*, 19: 317-324.

Dewey JF, Helman ML, Turco E, Hutton DW, Knott SD (1989) Kinematics of the western Mediterranean. In: Coward MP, Dietrich D, Park RG (Eds) Alpine Tectonics. *Geol. Soc. Lond. Spec. Pub.*, 45: 265-284.

Dewey JF (1988) The extensional collapse of orogens. *Tectonics*, 7: 1123-1139.

Dodson MH (1973) Closure temperature in cooling geochronological and petrological systems. *Contrib. Mineral. Petrol.*, 40: 259-274.

Draper G, Bone R (1981) Denudation rates, thermal evolution and preservation of blueschist terranes. *J. Geology,* 89: 601-613.

Droop GTR (1987) A general equation for estimating Fe^{3+} concentrations in ferromagnesian silicates and oxides from microprobe analyses using stoichiometric criteria. *Min. Mag.*, 51: 431-435.

Duchene S, Lardeaux J-M, Albarede F (1997) Exhumation of eclogites: insights from depth-time path analysis. *Tectonophysics,* 280: 125-140.

Ellis DJ, Green DH (1979) An experimental study of the effect of Ca upon garnet-clinopyroxene Fe-Mg exchange equilibria. *Contrib. Mineral. Petrol.*, 71: 13-22.

England PC (1981) Metamorphic pressure estimates and sediment volumes for the Alpine orogeny: An independent control on geobarometers*? Earth Planet. Sci. Lett.*, 56: 387-397.

England PC, Holland TJB (1979) Archimedes and the Tauern eclogites: the role of buoyancy in the preservation of exotic eclogite blocks. *Earth Planet. Sci. Lett.*, 44: 287-294.

England PC, Houseman GA (1988) The mechanics of the Tibetan plateau. *Phil. Trans. R. Soc. Lond.*, 326: 301-320.

England PC, Molnar P (1990). Surface uplift, uplift of rocks, and exhumation of rocks. *Geology*, 18: 1173-1177.

England PC, Thompson AB (1984) Pressure-temperature-time paths of regional metamorphism I. Heat transfer during the evolution of thickened crust. *J. Petrology,* 25: 894-892.

Ernst WG (1971) Petrologic reconnaissance of Franciscan metagraywackes from the Diablo Range, central California Coast Ranges. *J. Petrology*, 12: 413-437.

Ernst WG (1977) Mineral parageneses and plate tectonic settings of relatively high-pressure metamorphic belts. *Fortschritte der Mineralogie*, 54: 192-222.

Ernst WG (1988) Tectonic history of subduction zones inferred from retrograde blueschist P-T paths. *Geology*, 16: 1081-1084.

Ernst WG, Peacock SM (1996) A Thermotectonic model for preservation of ultrahigh-pressure phases in metamorphosed continental crust. In: *Geophysical Monograph 96, Subduction: Top to Bottom.* Am. Geophys. U. pp 171-178.

Evans BW (1990) Phase relations of epidote blueschists. *Lithos*, 25: 3-23.

Foland KA (1979) Limited mobility of argon in a metamorphic terrain. *Geochim. Cosmochim. Acta*, 43: 793-801.

Gautier Y (1984) *Deformations et metamorphismes associes a la fermeture Tethysienne en Anatolie Centrale (region de Sivrihisar, Turquie).* PhD Thesis, Universite de Paris-sud: pp. 235.

Gebauer D, Schertl HP, Brix M, Schreyer W (1997) 35 Ma old ultrahigh-pressure metamorphism and evidence for very rapid exhumation in the Dora Maira Massif, Western Alps. *Lithos*, 41: 5-24.

Green DH, Hellman PL (1982) Fe-Mg partitioning between coexisting garnet and phengite at high pressures, and comments on a garnet-phengite geothermometer. *Lithos*, 15: 253-266.

Greenwood HJ (1975) Buffering of pore fluids by metamorphic reactions. *Am. J. Sci.*, 275: 573-593.

Görür N, Monod O, Okay AI, Sengör AMC, Tüyüz O, Yiitbap E, Sakync M, Akkök R (1997) Palaeogeographic and tectonic position of the Carboniferous rocks of the western Pontides (Turkey) in the frame of the Variscan belt. *Bull. Geol. Soc. Fr.*, 168: 197-205.

Hacker BR, Peacock SM (1995) Creation, preservation and exhumation of UHPM rocks. In Coleman RG, Wang X (Eds) *Ultrahigh Pressure Metamorphism.* Cambridge University Press, New York 159-181.

Hames, WE., Bowring, SA. (1994) An empirical study of the argon diffusion geometry in muscovite. *Earth Planet. Sci. Lett.*, 124: 161-169.

Harris NBW, Kelley SP, Okay AI (1994) Post-collision magmatism and tectonics in northwest Anatolia. *Contrib. Mineral. Petrol.*, 117: 241-252.

Heizler MT, Harrison TM (1988) Multiple-trapped argon isotope components revealed by ^{40}Ar-^{39}Ar isochron analysis. *Geochim. Cosmochim. Acta*, 52: 1295-1303.

Henjes-Kunst F, Kreutzer H (1982) Isotopic dating of pre-Alpidic rocks from the island of Ios (Cyclades, Greece). *Contrib. Mineral. Petrol.*, 80: 245-253.

Henry C, Michard A, Chopin C (1993) Geometry and structural evolution of the ultra-high pressure and high-pressure rocks from the Dora Maira massif, western Alps, Italy. *J. Struct. Geol.*, 15: 965-981.

Hodges KV, Hames WE, Bowring SA (1994) $^{40}Ar/^{39}Ar$ gradients in micas from a high-temperature low-pressure metamorphic terrain: Evidence for very slow cooling and implications for the interpretation of age spectra. *Geology,* 22: 55-58.

Holland TJB (1980) The reaction albite = jadeite + quartz determined experimentally in the range 600° -1200° C. *Am. Min.,* 65: 129-134.

Holland TJB, Powell R (1998) A internally consistent thermodynamic data set for phases of petrological interest. *J. Met. Geol.,* 16: 309-343.

Hynes A, Arkani-Hamed J, Greiling R (1996) Subduction of continental margins and uplift of high-pressure metamorphic rocks. *Earth Planet. Sci. Lett.,* 140: 13-25.

Inger S, Ramsbotham W, Cliff RA, Rex D (1996) Metamorphic evolution of the Sesia-Lanzo Zone, western Alps: Time constraints from multi-system geochronology. *Contrib. Mineral. Petrol.*, 126: 152-168.

Jamtveit JB (1991) Oscillatory zonation patterns in hydrothermal grossular-andradite garnet. Nonlinear dynamics in regions of immiscibility. *Am. Min.*, 76: 1319-27.

Jamtveit BJ, Wogelius RA, Fraser DG (1993) Zonation patterns of skarn garnets: records of hydrothermal system evolution. *Geology,* 21: 113-6.

Jenkin GRT (1997) Do cooling paths derived from mica Rb-Sr data reflect true cooling paths? *Geology,* 25: 907-910

Kaya O (1972) Aufbau und Geschichte einer anatolischen Ophiolith Zone. *Zeitschrift de Deutschen Geologischen Gesellschaft*, 123: 423-432

Kaya O (1981) Preliminary study on the paragenetic relationships in the polymetamorphic blueschist rocks of the Tavsanli Area, West Anatolia. *Aegean Earth Sci.*, 1: 27-43.

Kelley SP, Arnaud AO, Turner SP (1994) High spatial resolution ^{40}Ar-^{39}Ar investigations using an ultra-violet laser probe extraction technique. *Geochim. Cosmochim. Acta,* 58: 3519-3525.

Kelley SP, Reddy SM, Maddock R (1994) Laser-probe ^{40}Ar-^{39}Ar investigation of a pseudotachylyte and its host rock from the Outer Isles thrust, Scotland. *Geology,* 22: 443-446.

Krogh EJ, Raheim A (1978) Temperature and pressure dependence of Fe-Mg partitioning between garnet and phengite with particular reference to ecolgites. *Contrib. Mineral. Petrol.,* 66: 75-80.

Krogh, EJ (1988) The garnet-clinopyroxene Fe-Mg geothermometer - a reinterpretation of existing experimental data. *Contrib. Mineral. Petrol.*, 99: 44-48.

Kulaksiz S (1981) Geology of the region northwest of Sivrihisar. *Yerbilimleri,* 8: 103-124.

Lanphere M, Dalrymple GB (1971) A test of the ^{40}Ar-^{39}Ar age spectrum technique on some terrestrial minerals. *Earth Planet. Sci. Lett.*, 12: 359-372.

Lanphere M, Dalrymple GB (1978) The use of ^{40}Ar-^{39}Ar data in evaluation of disturbed K-Ar systems: *U. S. Geological Survey Open-file Report* 78-701: 241-243.

Lappin MA, Smith DC (1978) Mantle-equilibrated orthopyroxene eclogite pods from the basal gneisses in the Selje district, western Norway. *J. Petrology,* 19: 530-584.

Leake BE, 21 others (1997) Nomenclature of amphiboles; Report of the Subcommittee on Amphiboles of the International Mineralogical Association Commission on New Minerals and Mineral Names. *Min. Mag,* 61: 295-321.

Li S, Wang S, Chen Y, Liu D, Qiu J, Zhou H, Zhang Z (1994) Excess argon in phengite from eclogite: evidence from dating eclogite minerals by Sm-Nd, Rb-Sr and ^{40}Ar-^{39}Ar methods. *Chem. Geol. (Isotope Geosci),* 112: 343-350.

Lisenbee A (1971) The Orhaneli ultramafic-gabbro thrust sheet and its surroundings. In: *Geology and History of Turkey: Tripoli, Libya, Petroleum Exploration Institute of Libya,* Cambell AS (Ed). 349-360.

Livermore RA, Smith AG (1985) Some boundary conditions for the evolution of the Mediterranean region. In: (Eds: Stanley DJ, Wezel SC) *Geological Evolution of the Mediterranean Basin.*, 84-98. Springer-Verlag, Berlin.

Lunel T (1967) *Geology of Subren-Karaalan area, Eskisehir county (Turkey).* PhD Thesis, Bristol University.

Maluski H, Vergely P, Bavay D, Bavay Ph, Katsikatsos G (1981) ^{40}Ar-^{39}Ar dating of glaucophanes and phengites in southern Euboa (Greece). *Bull. Soc. Geol. Fr.,* 7: 469-476.

Maluski H, Bonneau M, Kienast JR (1987) Dating the metamorphic events in the Cycladic area: ^{40}Ar-^{39}Ar data from metamorphic rocks of the island of Syros (Greece). *Bull. Soc. Geol. Fr.,* 8: 833-842.

Massonne HJ, Schreyer W (1987) Phengite barometry based on the limiting assemblage with K feldspar, phlogopite and quartz. *Contrib. Mineral. Petrol.*, 96: 212-224.

McDougall I, Harrison TM (1988) *Geochronology and Thermochronology by the ^{40}Ar-^{39}Ar Method.* Oxford Univeristy Press.

Menard T, Spear FS (1996) Interpretation of plagioclase zonation in calcic pelitic schist, South Strafford, Vermont, and the effects on thermobarometry. *Can. Min.*, 34: 133-46.

Merrihue C, Turner G (1966) Potassium-argon dating by activation with fast neutrons. *J. Geophys. Res.*, 71: 2852-2857.

Mevel C, Kienast JR (1980) Chromian jadeite, phengite, pumpellyite and lawsonite in a high-pressure metamorphosed gabbro from the French Alps. *Min. Mag.*, 43: 979-84.

Mitchell JG (1968) The 40Ar-39Ar method for potassium-argon age determination. *Geochim. Cosmochim. Acta*, 32: 781-790.

Monie P, Chopin C (1991) ^{40}Ar-^{39}Ar dating in a coesite-bearing eclogite and related units, Dora Maira massif, western Alps. *Eur. J. Mineral.*, 3: 239-262.

Monod O, Andrieux J, Gautier Y, Kienast JR (1991) Pontides-Taurides relationships in the region of Eskischir (NW Turkey). *Bull. Tech. Univ. Istanbul*, 44: 257-272.

Okay AI (1980a) Mineralogy, petrology and phase relations of glaucophane-lawsonite zone blueschists from the Tavsanli region, northwest Turkey. *Contrib.Mineral. Petrol.*, 72: 243-255.

Okay AI (1980b) Lawsonite zone blueschists and a sodic amphibole producing reaction in the Tavsanli Region, Northwest Turkey. *Contrib. Mineral. Petrol.*, 75: 179-186.

Okay AI (1982) Incipient blueschist metamorphism and metasomatism in the Tavsanli region, northwest Turkey. *Contrib. Mineral. Petrol.*, 79: 361-367.

Okay, AI (1984) Distribution and characteristics of the northwest Turkish blueschists. In: The Geological Evolution of the Eastern Mediterranean (Eds: Robertson, AHF. & Dixon, JE). *Geol. Soc. Spec. Publ.*, 17: 455-466.

Okay AI (1986) High-pressure low-temperature rocks of Turkey. *Geol. Soc. Am. Mem.*, 164: 333-347.

Okay AI (1989) Tectonic units and sutures in the Pontides, northern Turkey. In: Sengor AMC (Ed): *Tectonic evolution of the Tethyan region*, 109-113. Dordrecht: Kluwer.

Okay AI (1993) Petrology of a diamond and coesite-bearing terrain: Dabie Shan, China. *Eur. J. Mineral.*, 5: 659-675.

Okay AI, Kelley SP (1994) Jadeite and chloritoid schists from northwest Turkey: tectonic setting, petrology and geochronology. *J. Metamorphic Geol.*, 12: 155-166.

Okay AI, Monie P (1997) Early Mesozoic subduction in the Eastern Mediterranean: evidence from a Triassic eclogite in northwest Turkey. *Geology*, 25: 595-598.

Okay AI, Tuyuz O (in press) Tethyan sutures of northern Turkey. *J. Geol. Soc. Lond. Spec. Pub.*

Okay AI, Xu S, Sengör AMC (1989) Coesite from the Dabie Shan eclogites, central China. *Eur. J. Mineral.*, 1: 595-598.

Okay AI, Satir M, Maluski H, Siyako M, Monie P, Metzger R, Akyuz S (1996) Paleo- and Neo-Tethyan events in northwest Turkey: Geologic and geochronologic constraints. In: (Eds: Yin A, Harrison TM) *The Tectonic evolution of Asia*, 420-441. Cambridge University Press.

Okay AI, Harris NBW, Kelley SP (1998) Blueschist exhumation along a Tethyan suture in northwest Turkey. *Tectonophysics*, 285: 275-299.

Pankhurst RJ, Moorbath S, Rex DC, Turner G (1973) Mineral age patterns ca. 3700 My old rocks from West Greenland. *Earth Planet. Sci. Lett.*, 20: 157-170.

Pawley AR (1994) The pressure and temperature stability of lawsonite: implications for H_2O recycling in subduction zones. *Contrib. Mineral. Petrol.*, 118: 99-108.

Phillipot P (1993) Fluid-melt-rock interaction in mafic eclogites and coesite-bearing metasediments: Constraints on volatile recycling during subduction. *Chem. Geol.*, 108: 93-112.

Pickles CS, Kelley SP, Reddy SM, Wheeler J (1997) Determination of high spatial resolution argon isotope variations in metamorphic biotites. *Geochim. Cosmochim. Acta.*, 61: 3809-3834.

Platt JP (1986) Dynamics of orogenic wedges and the uplift of high-pressure metamorphic rocks. *Geol. Soc. Am. Bull.*, 97: 1037-1053.

Platt JP (1987) The uplift of high-pressure low-temperature metamorphic rocks. *Phil. Trans. R. Soc. Lond.*, A321: 87-103.

Platt JP (1993) Exhumation of high-pressure rocks: a review of concepts and processes. *Terra Nova*, 5: 199-133.

Platt JP, England PC (1994) Convective removal of lithosphere beneath mountain belts: thermal and mechanical consequences. *Am. J. Sci.*, 294: 307-336.

Pognante U (1989) Tectonic implications of lawsonite formation in the Sezia Zone (Western Alps). *Tectonophysics*, 162: 219-227.

Pognante U (1991) Petrological constraints on eclogite- and blueschist-facies metamorphism and P-T-t paths in the Western Alps. *J. Met. Geol.*, 9: 5-17.

Powell R (1985) Regression diagnostics and robust regression in geothermometer/geobarometer calibration: the garnet-clinopyroxene geothermometer revisited. *J. Met. Geol.*, 3: 327-342.

Reddy SM, Kelley SP, Wheeler J (1996) A ^{40}Ar-^{39}Ar laser probe study of micas from the Sesia Zone, Italian Alps: Implications for metamorphic and deformation histories. *J. Met. Geol.*, 14: 493-508.

Reddy SM, Kelley SP, Magenis L (1997) A microstructural and argon laserprobe study of shear zone development at the western margin of the Nanga-Parbat-Haramosh Massif, Western Himalaya. *Contrib. Mineral. Petrol.*, 28: 16-29.

Rees CE (1984) Error propagation calculations. *Geochim. Cosmochim. Acta.* 48: 2309-2311.

Renne PR, Sharp WD, Deino AL, Orsi G, Civetta L (1997) ^{40}Ar-^{39}Ar dating into the historical realm: Calibration against Pliny the Younger. *Science,* 277: 1279-1280

Ricou LE (1994) Tethys reconstructed - plates, continental fragments and their boundaries since 260 Ma from central America to south eastern Asia. *Geod. Acta.*, 7: 169-218.

Rubie DC (1984) A thermal-tectonic model for high-pressure metamorphism and deformation in the Sesia Zone, western Alps. *J. Geology*, 92: 21-36.

Ruffét G, Féraud G, Balevre M and Kienast J-R (1995) Plateau ages and excess argon in phengites: an ^{40}Ar-^{39}Ar laser probe study of Alpine micas (Sesia Zone, Western Alps, northern Italy). *Chem. Geol. (Isot. Geosci. Sect.),* 121: 327-3543.

Ruffét G, Gruau G, Ballevre M, Féraud G and Philippot P (1997) Rb-Sr and ^{40}Ar-^{39}Ar laser probe dating of high-pressure phengites from the Sezia zone (Western Alps): underscoring of excess argon and new age constraints on the high-pressure metamorphism. *Chem. Geol. (Isot. Geosci. Sect.),* 141: 1-18.

Scaillet S, Feraud G, Lagabrielle Y, Ballevre M, Ruffet G (1990) ^{40}Ar-^{39}Ar laser probe dating by step-heating and spot-fusion of phengites from the Dora Maira nappe of the Western Alps, Italy. *Geology,* 18: 741-744.

Scaillet S, Feraud G, Lagabrielle Y, Ballevre M, Amouric M. (1992) Mg/Fe and [(Mg,Fe)Si-Al2] compositional control on argon behaviour in high-pressure white micas: a ^{40}Ar-^{39}Ar continuous laser probe study from the Dora-Maira nappe of the internal Western Alps, Italy, II. *Geochim. Cosmochim. Acta,* 56: 2851-2872.

Scaillet S (1996) Excess ^{40}Ar transport scale and mechanism in high-pressure phengites: A case study from an eclogitised metabasite of the Dora-Maira nappe, western Alps. *Geochim. Cosmochim. Acta,* 60: 1075-1090.

Schliestedt M (1990) Occurrences and stability conditions of low-temperature eclogites. In: (Ed: Carsell DA) *Eclogite Facies Rocks.* Chapman and Hall. 160-179.

Schmidt MW (1995) Lawsonite: Upper pressure stability and formation of higher density hydrous phases. *Am. Min.,* 80: 1286-92.

Sengör AMC (1979) The North Anatolian Transform Fault: its age offset and tectonic significance. *J. Geol. Soc. Lond.,* 136: 269-282.

Sengör AMC (1984) The Cimmeride orogenic system and the tectonics of Eurasia. *Geol. Soc. Am. Spec. Pap.,* 195: 1-82.

Sengör AMC (1987) Tectonics of the Tethysides: orogenic collage development in a collisional setting. *Ann. Rev. Earth Planet. Sci. Lett.,* 15: 213 244.

Sengör AMC, Yilmaz Y (1981) Tethyan evolution of Turkey: a plate tectonic approach. *Tectonophysics,* 75: 181-241.

Servais M (1981) Donnees preliminaires sur la zone de suture mediotethysienne dans la region d'Eskisehir (NW Anatolie). *Comptes Rendus des Seances de L'Academie des Sciences, Paris,* 293: 83-86.

Sherlock SC, Arnaud NO (submitted). Flat plateau and impossible isochrons: apparent ^{40}Ar-^{39}Ar geochronology in a HP terrain. *Submitted to Geochim. Cosmochim. Acta,*

Sherlock SC, Kelley SP (submitted) Excess argon in the Tavsanli Zone of NW Turkey: a UVLAMP study of phengite and K-free minerals. *Submitted to Chem. Geol,*

Sherlock SC, Okay AI (submitted) Oscillatory zoned chrome lawsonite in the Tavsanli Zone of Northwest Turkey. *Submitted to Min. Mag.,*

Sherlock SC, Kelley SP, Inger S, Harris NBW and Okay AI (submitted a). ^{40}Ar-^{39}Ar and Rb-Sr geochronology of high-pressure metamorphism and exhumation history of the Tavsanli Zone, NW Turkey. *Submitted to Contrib. Mineral. Petrol.,*

Sherlock SC, Harris NBW, Okay AI (submitted b) Thermobarometry and P-T evolution of Tethyan high- pressure metamorphism: the Tavsanli Zone of NW Turkey. *Submitted to J. Met. Geol.,*

Shore M, Fowler AD (1996) Oscillatory zoning in minerals: A common phenomenon. *Can. Min.,* 34: 1111-26.

Sisson VB, Onstott TC (1986) Dating blueschist metamorphism: A combined ^{40}Ar-^{39}Ar and electron microprobe approach. *Geochim. Cosmochim. Acta,* 50: 2111-2117.

Smith AG (1973) The so-called Tethyan ophiolites. In: (Eds: Tarling DH, Runcorn SK) *Implications of Continental Drift to the Earth Sciences,* 977-986. Academic Press, Cambridge.

Smith DC (1984) Coesite in clinopyroxene in the Caledonides and its implications for geodynamics. *Nature,* 310: 641-644.

Sobolev NV, Shatskii VS, Vavilov MA, Goryainov SV (1991) Coesite inclusion in zircon from diamond-containing gneisses of Kokchetav Massif - 1st find of coesite in metamorphic rocks in the USSR. *Doklady Akademii Nauk SSSR,* 1: 184-188

Stampfli GM (1996) The Intra-Alpine terrain: A Palaeotethyan remnant in the Alpine Variscides. *Ec. Geol. Helv.,* 89: 13-42.

Staudacher Th, Jessberger EK, Dörflinger D, Kiko J (1978) A refined ultra-high vacuum furnace for the rare gas analysis. *J. Phys E: Sci. Instrum.,* 11: 781-784.

Steiger RH, Jäger E (1977) Subcommission on geochronology: Convention on the use of decay constants in geo- and cosmochronology. *Earth Planet. Sci. Lett.,* 36: 359-362.

Tetley NW (1978) *Geochronology by the ^{40}Ar-^{39}Ar technique using HIFAR reactor.* PhD thesis, Australia National University, Canberra.

Thompson AB, England PC (1984) Pressure-Temperature-time paths of regional metamorphism II: Their inference and interpretation using mineral assemblages in metamorphic rocks. *J. Petrology,* 25: 929-955.

Thompson AB, Schulmann K, Jezek J (1997) Extrusion tectonics and elevation of lower crustal metamorphic rocks in convergent orogens. *Geology,* 25: 491-494.

Tilton GR, Schreyer W and Schertl HP (1989) Pb-Sr-Nd isotopic behaviour of deeply subducted crustal rocks from the Dora Maira massif, Western Alps, Italy, II: what is the age of metamorphism? *Contrib. Mineral. Petrol.,* 108: 22-23.

Tilton GR, Schreyer W, Schertl HP (1991) Pb-Sr-Nd isotopic behaviour of deeply subducted crustal rocks from the Dora Maira Massif, Western Alps, Italy. II. What is the age of the ultra-high pressure metamorphism? *Contrib. Mineral. Petrol.,* 108: 22-33.

Turner G, Miller JA, Grasty RL (1966) The thermal history of the Bruderheim meteorite. *Earth Plnet. Sci. Lett.,* 1: 155-157.

Wain A (1997) Neew evidence for coesite in eclogite and gneisses: defining an ultrahigh-pressure province in the Western Gneiss region of Norway. *Geology,* 25: 927-930.

Wang X, Liou JG, Mao HK (1989) Coesite-bearing eclogites from the Dabie Mountains in central China. *Geology,* 17: 1085-1088.

Wartho J-A, Rex DC, Guise PG (1996) Excess argon in amphiboles linked to greenschist facies alteration in the Kamila Amphibolite Belt, Kohistan island arc system, northern Pakistan: Insights from ^{40}Ar-^{39}Ar step-heating and acid-leaching experiments. *Geol. Mag.,* 133: 595-609.

Waters DJ, Martin HN (1993) Geobarometry of phengite-bearing eclogites. *Terra Abstracts*, 5: 410-411.

Wendt AS, D'Arco P, Goffé B, Oberhänsli R (1993) Radial cracks around α-quartz inclusions in almandine: constrains on the metamorphic history of the Oman mountains. *Earth Planet. Sci. Lett.*, 114: 449-461.

Wheeler J (1996) DIFFARG: a program for simulating argon diffusion profiles in minerals. *Comp. Geosci.*, 22: 919-929.

Wickmann FE (1947) The crystal structure of lawsonite $CaAl_2(Si_2O7)(OH)_2.H_2O$ *Arkiv. Kem. Min. Geol.*, 25: 1-7.

Wijbrans JR, McDougall I (1986) ^{40}Ar-^{39}Ar dating of white micas from an Alpine high-pressure metamorphic belt on Naxos (Greece): the resetting of the argon isotopic system. *Contrib. Mineral. Petrol.*, 93: 187-194.

Wijbrans JR, McDougall I (1988) Metamorphic evolution of the Attic Cycladic Metamorphic belt on Naxos (Cyclades, Greece) utilizing ^{40}Ar-^{39}Ar age spectrum measurements. *J. Met. Geol.*, 6: 571-594.

Wijbrans JR, Schliestedt M, York D (1990) Single grain argon laser probe dating of phengites from the blueschist to greenschist transition on Sifnos (Cyclades, Greece). *Contrib Mineral Petrol,* 104: 582-593.

Wijbrans JR, Vanwees JD, Stephenson RA, Cloetingh SAPL (1993) Pressure-temperature-time evolution of the high-pressure metamorphic complex of Sifnos, Greece. *Geology*, 21: 443-446.

Yardley BWD, Rochelle CA, Barnicoat AC, Lloyd GE (1991) Oscillatory zoning in metamorphic minerals: an indicator of infiltration metasomatism. *Min. Mag.*, 55: 357-65.

York D, Hall CM, Yanase Y (1981) 40Ar-39Ar dating of terrestrial minerals with a continous laser. *J. Geophys. Res.*, 8: 1136-1138.